



# DESIGN AND OPTIMIZATION OF MODULAR LATTICE STRUCTURES FOR AEROSPACE APPLICATIONS

Enrico Stragiotti

François-Xavier Irisarri<sup>1</sup>, Cédric Julien<sup>1</sup> and Joseph Morlier<sup>2</sup>

1: ONERA - The French Aerospace Lab  
DMAS - Département matériaux et structures  
92320 Châtillon, France  
[{francois-xavier.irisarri, cedric.julien}@onera.fr](mailto:{francois-xavier.irisarri, cedric.julien}@onera.fr)

2: ICA - Institut Clément Ader  
ISAE - SUPAERO  
31400 Toulouse, France  
[joseph.morlier@isae-supero.fr](mailto:joseph.morlier@isae-supero.fr)  
February 6, 2024

PhD manuscript

ONERA – ISAE Supaero

## **Colophon**

This document was typeset with the help of KOMA-Script and L<sup>A</sup>T<sub>E</sub>X using the kaobook class.

ONERA – ISAE Supaero

# CONTENTS

<b>Contents</b>	<b>iii</b>
<b>List of Figures</b>	<b>vii</b>
<b>List of Tables</b>	<b>xiv</b>
<b>List of Abbreviations</b>	<b>xvi</b>
<b>Abstract</b>	<b>1</b>
<b>Introduction</b>	<b>3</b>
<b>1 Literature review</b>	<b>7</b>
1.1 An introduction to structural optimization . . . . .	7
1.1.1 Optimizers . . . . .	9
1.2 Ultra-lightweight structures optimization approaches . . . . .	11
1.2.1 Density-based topology optimization . . . . .	13
1.2.2 Feature-Mapping topology optimization . . . . .	16
1.2.3 Truss topology optimization (TTO) . . . . .	16
1.3 Modular structures and cellular materials . . . . .	20
1.3.1 Modular structures and cellular materials optimization . . . . .	24
1.3.2 Multi-scale structures optimization . . . . .	25
1.3.3 Full-scale structures optimization . . . . .	27
<b>2 Evaluating discretization approaches for ultralight structure optimization</b>	<b>29</b>
2.1 The formulation of a shared problem: volume minimization with stress constraints . . . . .	29
2.1.1 Density-based topology optimization minimum volume formulation . . . . .	29
2.1.2 Truss Topology Optimization (TTO) minimum volume formulation . . . . .	36
2.2 Comparison between density-based topology optimization and TTO . . . . .	38
2.2.1 Definition of a test case for the comparison . . . . .	38
2.2.2 Numerical application . . . . .	39
2.2.3 Discussion . . . . .	46
2.3 Conclusion . . . . .	49
<b>3 Enriching the classic TTO formulation with advanced mechanical constraints</b>	<b>51</b>
3.1 Advanced mechanical constraints . . . . .	51
3.1.1 Minimum slenderness constraints . . . . .	52
3.1.2 Local and topological buckling constraints . . . . .	53
3.1.3 Kinematic compatibility constraints . . . . .	55
3.2 Optimization formulation and solving strategy . . . . .	56
3.2.1 Optimization strategy . . . . .	57
3.2.2 First step: SLP optimization . . . . .	57
3.2.3 Handling local minima: reinitialization strategy . . . . .	59

3.2.4	Second step: NLP optimization . . . . .	61
3.3	Numerical application . . . . .	62
3.3.1	L-shaped beam . . . . .	64
3.3.2	Ten-bar truss . . . . .	65
3.3.3	2D cantilever beam . . . . .	68
3.3.4	Simply supported 3D beam . . . . .	71
3.3.5	Ten-bar truss with multiple load cases . . . . .	73
3.4	Conclusion . . . . .	76
<b>4</b>	<b>Optimizing modular structures</b>	<b>77</b>
4.1	Formulation of a modular structure optimization algorithm . . . . .	77
4.1.1	Variable linking . . . . .	78
4.1.2	Topological buckling of modular structures . . . . .	79
4.1.3	Optimization formulation . . . . .	80
4.1.4	Sensitivity analysis . . . . .	81
4.2	Optimization of modular structures using the variable linking approach . . . . .	82
4.2.1	On the equivalence of multi-load cases and modular structures . . . . .	82
4.2.2	Parametric study on the number of subdomains and the complexity of the module . . . . .	84
4.2.3	Comparison with the optimized octet-truss . . . . .	92
4.2.4	Using multiple module topologies . . . . .	95
4.3	Conclusion . . . . .	98
<b>5</b>	<b>Optimizing the layout of the modules in space</b>	<b>101</b>
5.1	Optimizing the modules' layout using a modified DMO algorithm . . . . .	101
5.1.1	Definition of the subdomains cross-sectional areas . . . . .	101
5.1.2	Variables penalization schemes . . . . .	102
5.1.3	The optimization formulation and resolution algorithm . . . . .	104
5.1.4	Optimization initialization: a clustering algorithm to identify similarly behaving subdomains . . . . .	106
5.2	Numerical optimization of the topology and layout of modular structures . . . . .	108
5.2.1	Layout optimization of fixed topology modules . . . . .	109
5.2.2	Modules and layout optimization . . . . .	112
5.2.3	A benchmark case study: a simply supported modular bridge . . . . .	115
5.2.4	Simply supported 3D beam . . . . .	120
5.3	Conclusion . . . . .	121
<b>6</b>	<b>Design of real-size aeronautical wing structures</b>	<b>123</b>
6.1	3D CRM wingbox with multiple load cases . . . . .	123
6.1.1	Advanced thresholding . . . . .	124
6.1.2	Numerical optimization of the CRM wingbox . . . . .	125
6.2	NACA 0012 modular drone wing . . . . .	134
6.2.1	Modular ground structure generation for irregular volumes . . . . .	134
6.2.2	Numerical optimization of the modular NACA 0012 drone wing . . . . .	135
6.3	Conclusion . . . . .	143

<b>Conclusion and perspectives</b>	<b>145</b>
<b>Communications</b>	<b>151</b>
<b>Bibliography</b>	<b>153</b>
<b>Appendix</b>	<b>177</b>
<b>Sensitivity analysis of the modular structure optimization algorithm</b>	<b>179</b>
1 Optimization formulation, objective function and constraints . . . . .	179
2 Common derivatives . . . . .	180
3 Gradient . . . . .	181
4 Jacobian matrix . . . . .	181
5 Hessian matrix . . . . .	183



# LIST OF FIGURES

1	(a) The transonic truss-braced wing called ALBATROS by ONERA [1, 2]; (b) the Blended-Wing Body (BWB) zero-e demonstrator by Airbus [3]. . . . .	3
2	Modular lattice structures present multiple properties that could be applied to the aerospace domain; (a) small two-dimensional components are reversibly assembled to build large three-dimensional structures [5]; (b) the assembly phase of modular lattice structures is done by fully robotic means in the NASA's Automated Reconfigurable Mission Adaptive Digital Assembly Systems (ARMADAS) project [6]. . . . .	4
1.1	Visual representation of (a) size, (b) shape, and (c) topology optimization [7]. . . . .	7
1.2	The domain $\Omega$ is discretized using $N_e = N_x N_y$ continuous 4-nodes elements. . . . .	13
1.3	Comparison between SIMP model with the Hashin-Strikman upper bound, considering an isotropic material with a Poisson ratio of 1/3 mixed with void. The Hashin-Strikman upper bound is illustrated with microstructures approaching the specified bounds. [57]. . . . .	14
1.4	Kernel of the 2D convolution operator. . . . .	14
1.5	Component (a) and density (b) plot of a short cantilever beam optimized using the component-based topology optimization method Generalized Geometry Projection (GGP) [78]. . . . .	16
1.6	The TTO algorithm is divided into four principal steps: (a) specification of the design space, loads, and boundary conditions; (b) discretization of the design space; (c) the ground structure is generated depending on the desired connectivity level; (d) resolution of the optimization problem and plot of the solution [83]. . . . .	17
1.7	The domain $\Omega$ is discretized using a set of straight members connecting a set of nodes. This framework is known as the ground structure. . . . .	18
1.8	The optimal structures found by Truss Topology Optimization (TTO) tend at Michell-like structures, made up of a very large number of infinitesimal struts [91]. . . . .	20
1.9	The natural evolution process frequently generates lattice materials and modular structures; (a) The spore-bearing gills of a Hypholoma fasciculare [103], (b) SEM image of a leaf microstructure [104], (c) architected material of the wing of a dragonfly [105], (d) internal structure of a human bone [106]. . . . .	21
1.10	Density versus yield strength Ashby chart. Exploiting the architecture of the material as a variable to design new metamaterials, empty spaces of the graph can be filled (see dots) [99]. . . . .	22
1.11	A stretch-dominated and a bending-dominated Representative Volume Element (RVE). Bending-dominated cells act as a mechanism if the joints cannot withstand moments. The scaling laws are different for the two structural families [99]. . . . .	22
1.12	Vickers Wellingtons, bombers utilized during World War II, remained operational despite sustaining extensive damage, thanks to their modular fuselage. When one of the ribs was damaged, the load was redistributed to the others, allowing the structure to remain functional [123]. . . . .	23

1.13	The different length scales present in a lattice structure [117]. The size of the module (shown in subfigure A) is comparable with the dimensions of the wing, especially in the thickness. We therefore talk about lattice structure and not material. . . . .	23
1.14	Graphical representation of the asymptotic homogenization method used to retrieve the equivalent mechanical properties of a periodic cell [141]. . . . .	26
1.15	In the study of Zhang <i>et al.</i> [110] the same test case is optimized using a hierarchical optimization method and a different number of microstructures. Here we show the multi-scale optimized structures using 3 and 19 different microstructures. The structure with 19 microstructures is 10 % stiffer compared to the one with 3. . . . .	26
1.16	Three structures with the same volume are optimized for compliance minimization using three different methods: on the left, a classic mono-scale topology optimization algorithm. Middle: the variable linking method is used to enforce the pattern repetition on the structure. On the right an optimized structure with local volume constraints. The algorithms used to optimize the last two structures belong to the family of <i>full-scale</i> methods. [128]. . . . .	27
2.1	A four-node quadrilateral element. GP is the Gaussian integration point for which the equivalent stress is evaluated. . . . .	31
2.2	On the left, plot of the L-shape beam test case, on the right the graphical representations of the two discretizations used, the continuous (above) composed of $600 \times 600$ quadrilateral elements, and the truss-like (below) discretized using $33 \times 33$ nodes and a fully connected ground structure. The images represent a coarser discretization for visual clarity. . . . .	39
2.3	(a-d) Topology of the optimized structures for different values of the material allowable $\sigma_L = 10.00, 2.00, 0.40, and }0.25$ , showing a volume fraction of $V_f = 1.60\%, 4.04\%, 18.03\%$ and $34.71\%$ , respectively. (e-h) Von Mises stress distribution for the optimized structures. . . . .	40
2.4	The intermediate resulting structure for $\sigma_L = 0.2$ with $V_f = 48.08\%$ after 7500 optimization iterations. . . . .	42
2.6	Linear (a) and logarithmic (b) plot of the volume fraction $V_f$ and the compliance $C$ with respect to the maximum material allowable $\sigma_L$ for the continuous mesh structures. Areas in red represent the zones outside the domains of applicability of the applied method. . . . .	43
2.5	The optimized structure for $\sigma_L = 10.0$ with $V_f = 1.60\%$ . Some of the structure's features present not even a fully-dense element in their thickness. . . . .	43
2.7	Topology (a) and stress distribution (b) plot for the TTO optimized structure of the L-shape beam test case with varying values of the material allowable $\sigma_L$ on a $33 \times 33$ nodes ground structure. The structure topology is invariant with respect to the value of $\sigma_L$ . . . . .	44
2.8	Optimized structure obtained using a fully connected ground structure with $13 \times 13$ nodes and 7705 candidates. . . . .	44
2.9	Linear (a) and logarithmic (b) plot of the volume fraction $V_f$ and the compliance $C$ with respect to the value of the maximum material allowable $\sigma_L$ for the TTO optimized structures. Areas in red represent the zones outside the domains of applicability of the truss discretization. . . . .	45
2.10	Compliance $C$ versus maximum material allowable $\sigma_L$ plot for the density-based topology optimization and the TTO algorithms. . . . .	46

2.11	Maximum material allowable $\sigma_L$ versus volume fraction $V_f$ plot for the density-based topology optimization and the TTO algorithms. . . . .	47
2.12	Compliance $C$ versus volume fraction $V_f$ plot for the density-based topology optimization and the TTO algorithms. . . . .	47
2.13	Computational time $t$ versus volume fraction $V_f$ plot for the density-based topology optimization and the TTO algorithms. . . . .	48
3.1	The three ground structures loaded in compression are used to highlight the topological buckling problem in TTO. (a) Two-bar ground structure loaded in compression; (b) single bar ground structure; (c) overlap of the $a$ and $b$ ground structures. . . . .	54
3.2	Flowchart of the two-step optimization strategy used to solve Problem $\mathbb{P}_1$ . . . . .	58
3.3	Linearization of the local buckling constraints for a single bar. . . . .	59
3.4	The linearized buckling constraints (blue dashed line) limit the design space of successive iterations when evaluated on compressive bars with very small areas. Additionally, the gradient of the linearized buckling constraint tends to 0. . . . .	59
3.5	The reinitialization strategy modifies the linearization point of the members with a small area to promote their reintroduction in the optimization problem. . . . .	60
3.6	Flowchart of the Sequential Linear Programming (SLP) strategy with reinitialization used to solve Problem $\mathbb{P}_2$ . . . . .	61
3.7	Boundary conditions of the L-shaped beam test case. . . . .	64
3.8	Topology of the optimized truss structures for different material admissibles $\sigma_L = 1.0, 0.8, 0.3$ and $0.2$ with a minimum slenderness limit $\lambda < 15$ . . . . .	64
3.9	The ten-bar truss ground structure and load case. . . . .	65
3.10	Scatter plot of the four benchmarked optimization algorithms on the ten-bar truss. The 2S-5R shows a 100 % convergence rate to the lightest structure found. The dashed lines represent the mean of the distributions. . . . .	66
3.11	Volume convergence history for the proposed two-step resolution strategy with one step of reinitialization (2S-1R) for the initialization point $a_s^0$ . The reinitialization strategy permits to jump from the local minimum (b), with $V = 87857$ , to the lighter structure (d), with $V = 85534$ . Only the SLP step is plotted because the solution is statically determinate and kinematic compatibility constraints are already satisfied. In red the members loaded in tension, in blue the members loaded in compression. . . . .	67
3.12	The 2D cantilever beam load case with a first-order connectivity ground structure. The total number of candidate members is $N_{el} = 90$ . . . . .	68
3.13	(a) Non-Linear Programming (NLP) optimized design of the 2D cantilever beam with a volume of $V = 80.67$ and high number of active and crossing bars $N_{el} = 66$ ; (b) 2S-5R solution $V = 77.78$ with $N_{el} = 31$ . In red the members loaded in tension, in blue the members loaded in compression. . . . .	69
3.14	Left: scatter plot of three of the four benchmarked optimization algorithms on the 2D cantilever beam compared to the solution by Achtziger [189]. The dashed lines represent the mean of distributions. Right: histogram of the distribution of the results of the optimization algorithms. . . . .	70
3.15	The simply supported 3D beam example with the load case and boundary conditions. In blue we plot the symmetry planes. . . . .	71

3.16	Ground structure composed of $N_{el} = 496$ elements of the symmetric portion used to optimize the simply supported 3D beam. . . . .	71
3.17	Orthographic views of the topology of the optimized simply supported 3D beam. (a) XZ plane (b) YZ plane (c) XY plane (d) auxiliary perspective view. . . . .	72
3.18	Maximum stress constraint value (a) and buckling constraint value (b) plotted on the optimized topology of the simply supported 3D beam. . . . .	72
3.19	Ground structure of the ten-bar truss with two applied load cases $P_1$ and $P_2$ . . . . .	74
3.20	Maximum stress constraint value (left) and buckling constraint value (right) plotted on the optimized design of the multiple load cases ten-bar truss. . . . .	74
3.21	Iteration history of the ten-bar truss with multiple load cases example solved with the 2S-5R algorithm; (a) objective function history for the SLP and NLP step (b) constraint violation for the NLP step. . . . .	76
4.1	Notations used for the definition of the variable linking approach used to apply the modularity constraints. . . . .	78
4.2	Notations used for the evaluation of the sensitivities for the optimization of modular structures based on the variable linking scheme. . . . .	82
4.3	Boundary conditions of the multi-subdomains (a) and the multi-load cases (b) test cases.	83
4.4	Optimized structures of the multi-subdomains (a) and the multi-load cases (b) test cases. The resulting module topology is equal for the two cases. In red the bars are in a tensile state, and in blue the bars are in a compressive state. . . . .	84
4.5	Symmetric boundary conditions of the simply supported 3D beam. In gray are the symmetry planes of the test case. . . . .	84
4.6	Perspective view of the monolithic simply supported 3D beam optimized structure with $V = 9.907 \text{ cm}^3$ . . . . .	84
4.7	Influence of the number of subdomains on the volume of the optimized modular structure.	85
4.8	Influence of the number of subdomains on the computational time of the optimization.	85
4.9	Rendering of the optimized structures with $6 \times 2 \times 3$ (a-e), $12 \times 4 \times 6$ (b-f), $18 \times 6 \times 9$ (c-g), and $30 \times 10 \times 15$ (d-h) subdomains. The module presents a $2 \times 2 \times 2$ complexity. . . . .	87
4.10	Influence of the number of subdomains on the loading metrics $\varphi$ and $\psi$ of the optimized structures. . . . .	87
4.11	Stress (a-c) and local buckling (b-d) failure criteria plotted on the monolithic and the $12 \times 4 \times 6 - 3 \times 3 \times 3$ cases. . . . .	88
4.12	Rendering of the optimized structures with $2 \times 2 \times 2$ (a-e), $3 \times 3 \times 3$ (b-f), $4 \times 4 \times 4$ (c-g), and $5 \times 5 \times 5$ (d-h) module complexity. The number of subdomains is $6 \times 2 \times 3$ . . . . .	89
4.13	Influence of the module complexity on the volume of the optimized modular structure.	90
4.14	Influence of the module complexity on the computational time of the optimization. . .	90
4.15	Influence of the module complexity on the loading metrics $\varphi$ and $\psi$ of the optimized structures. . . . .	90
4.16	Main effects plot of volume (a) and computational time (b) as a function of the independent variables. . . . .	91
4.17	Design of experiments (DOE) response curves and isocurves plot for the volume (a-b) and computational time (c-d). . . . .	92
4.18	Rendering of a single octet-truss module. . . . .	93

4.19	Comparison of the octet-truss structures (a-c-e-g) and the TTO structures (b-d-f-h) for two different numbers of subdomains, $6 \times 2 \times 3$ and $12 \times 4 \times 6$ . . . . .	94
4.20	Graphical representation of the given module layout for the simply supported 3D beam.	95
4.21	Orthographic views of the topology of the optimized modular simply supported 3D beam. (a) XZ plane (b) YZ plane (c) XY plane (d) auxiliary perspective view. . . . .	96
4.22	Comparison of the volume and computational time of the structure with multiple modules with the monolithic and the fully modular structures. . . . .	96
4.23	Stress (a-c) and local buckling (b-d) failure criteria plotted on the multiple and single module modular structures. . . . .	97
5.1	A modular cantilever beam with $N_{\text{sub}} = 8$ . The subdomains' topology is defined as the weighted sum of two modules' topologies. . . . .	102
5.2	A dual-phase RAMP interpolation scheme is used to penalize the intermediate weights and promote 0-1 designs. . . . .	103
5.3	The stress values of the initial ground structure evaluated using a Finite Element Method (FEM) analysis are used to identify similar behaving subdomains. The sets are calculated using the k-means clustering technique with $N_T$ number of clusters. . . . .	107
5.4	The proposed starting point for the first step of the optimization: a fully connected ground structure with uniform cross-sectional areas and a biased $\alpha_{\text{init}}$ distribution, as suggested by the k-means clustering. . . . .	108
5.5	Boundary conditions of the 2D cantilever beam divided in $24 \times 12$ subdomains. In the upper part of the image, the ground structure of the module composed of $\bar{n} = 6$ elements is shown. . . . .	109
5.6	Monolithic optimized structure labeled R1 for the cantilever beam 2D test case with a maximum cross-sectional area $a_{\max} = 0.6$ . This solution represents the lower bound solution for this test case with a volume $V = 832.8$ . . . . .	110
5.7	Fully-modular structure labeled R2 in which every subdomain is populated with a fixed given module. The structural volume is $V = 9832.9$ . . . . .	110
5.8	Optimization of the fixed module topology of the 2D cantilever beam. (a-d) show the solution M1, obtained without penalizing intermediate weights with a final volume $V = 8808.6$ ; (e-h) show the solution M2, in which the RAMP interpolation helps to reduce intermediate weights. The final structural volume is $V = 3414.2$ . . . . .	111
5.9	Two different examples of the optimization of a modular 2D cantilever beam using $N_T = 2$ fixed topology modules. (a-b) show the topology and the module layout of the structure obtained using two modules with identical topology, but different cross-sectional areas, while the solution shown in (c-d) is obtained using two modules with identical cross-sectional areas, but different topologies. In (a) and (c) red bars are loaded in tension, while blue bars are loaded in compression. . . . .	112
5.10	Optimized topology of the modular structure (a) and the module (b) for the 2D cantilever beam optimized using a single module ( $N_T = 1$ ). Red bars are loaded in tension, while blue bars are loaded in compression. . . . .	112
5.11	Similarly stressed subdomains are identified using the k-means clustering algorithm to suggest a starting point for the first step of the proposed optimization algorithm. In the figure, we show the resulting distribution for $N_T = 2$ and $N_T = 5$ , obtained from the Finite Element Analysis (FEA) stress. . . . .	113

5.12	Influence of the number of modules $N_T$ on the volume $V$ and the loading metric $\psi$ of the optimized 2D cantilever beam. . . . .	113
5.13	Visual representation of the optimized modular 2D cantilever beam together with the corresponding module topologies for (a) $N_T = 2$ and (b) $N_T = 5$ . . . . .	114
5.14	Optimized 2D cantilever beam obtained using the variable linking formulation with fixed modules' layout and $N_T = 5$ . The modules' layout is obtained using the k-means clustering technique. The final volume is $V = 1727.314$ . . . . .	114
5.15	Bailey bridge placed on construction site road over Orava river (Slovakia) [218]. . . . .	115
5.16	Graphical representation of the 2D Bailey bridge test case. The structure is divided into $N_{\text{sub}} = 10$ . The bridge is symmetric, and we are here optimizing only the right part of it. . . . .	115
5.17	Visual comparison of the 2D Bailey bridge test case without local buckling constraints proposed by Tugilimana <i>et al.</i> [158] obtained for different number of modules $N_T$ . The images (a-j) represent the optimized structures in [158], while the images (k-t) show the structures obtained with the proposed optimization method. Different colors are used to highlight different modules. . . . .	117
5.18	Normalized volume values plotted against the number of modules $N_T$ for the simply supported modular bridge. The buckling constraints do not influence the trend of the beneficial effect of using multiple modules $N_T$ on the structure. . . . .	118
5.19	Visual representation of the optimized structures obtained for different values of $N_T$ for the 2D Bailey bridge test case with local buckling constraints. . . . .	119
5.20	Study of the influence of the parameters $N_{\text{sub}}$ and $N_T$ on the volume and the topology of the 2D Bailey bridge test case. . . . .	119
5.21	Normalized volume values plotted against the number of subdomains $N_{\text{sub}}$ for different values of $N_T$ . . . . .	120
5.22	Symmetric boundary conditions of the simply supported 3D beam. In gray are the symmetry planes of the test case. . . . .	120
5.23	Rendering of the optimized simply supported 3D beam with $N_T = 1$ (a,d), $N_T = 2$ (b,e), and $N_T = 3$ (c,f). . . . .	121
5.24	Perspective view of the monolithic simply supported 3D beam optimized structure with $V = 9.907 \text{ cm}^3$ . . . . .	121
6.1	(a) Ground structure of the CRM-315 test case; (b) Ground structure of the CRM-2370 test case. The cross-sectional areas shown in the two sub-figures represent the starting point of the optimizations. . . . .	125
6.2	Optimized topology of the CRM-315 with 257 active bars. . . . .	125
6.3	Iteration history of the CRM-315 test case solved with the 2S-5R algorithm. (a) objective function history for the SLP and NLP step. The sharp increases in the objective function during the SLP step correspond to the reinitialization calls. (b) constraint violation for the NLP step. . . . .	127
6.4	Undeformed (gray) and deformed (black) shapes of the optimized CRM-315 structures with a half wing span of 29.4 m for different values of maximum Z displacement $Z_{t,\ell}$ of the wing tip constraints for the LC_1 load case. (a) $Z_{t,\ell} = 1 \text{ m}$ ; (b) $Z_{t,\ell} = 2 \text{ m}$ ; (c) $Z_{t,\ell} = 3 \text{ m}$ ; (d) no maximum displacement constraints. . . . .	128

6.5 Undeformed (gray) and deformed (black) shapes of the optimized CRM-315 structures with four different materials for the LC_1 load case; (a) aluminum with $Z_t = 4.10$ m; (b) titanium with $Z_t = 5.97$ m; (c) inox steel with $Z_t = 1.70$ m; (d) pultruded CFRP with $Z_t = 5.31$ m. . . . .	130
6.6 Environmental and economic cost of the CRM-315 structure optimized using four different materials: aluminum, titanium, inox steel, and pultruded CFRP. . . . .	130
6.7 Maximum stress constraint value (left) and buckling constraint value (right) plotted on the deformed shape of the optimized design (undeformed shape in light grey) of CRM-2370 for the three load cases: +2.5 g maneuver (a), -1 g maneuver (b), and cruise with gust (+1.3 g) (c). The maximum z tip deflection is 4.167 m, -2.953 m, and 1.948 m, respectively. . . . .	132
6.8 Iteration history of the CRM-2370 example solved with the 2S-5R algorithm. (a) objective function history for the SLP and NLP step. The sharp increases in the objective function during the SLP step correspond to the reinitialization calls. (b) constraint violation for the NLP step. . . . .	133
6.9 Normalized buckling and maximum stress constraint values for the optimized CRM-2370 structure after the SLP and the NLP optimization steps. . . . .	133
6.10 The Digital Morphing Wing Platform developed at NASA [125]. . . . .	134
6.11 Ground structure generation flow chart of the proposed algorithm used to discretize irregular volumes and maximize the modular part. . . . .	136
6.12 (a) wingbox type and (b) section type ground structures used for the optimization of the NACA 0012 drone wing. . . . .	137
6.13 Rendering of the complete ground structure used for the optimization of the NACA 0012 drone wing seen from different viewing angles. This ground structure is formed by the superposition of two conformal ground structures: the wingbox and the section type. .	137
6.14 Subfigures (a) to (d) present different views on the resulting optimized structure obtained for configuration A with $N_T = 3$ different topologies for the wingbox and the section type modules. The structure has a total mass of $M = 29.5$ g and a mass density of $\bar{\rho} = 6.93$ kg/m <sup>3</sup> ; (e) and (f) illustrates the modules' layout in the structure for the wingbox and section modules type; (g) and (h) present the modules' topology for the wingbox and section modules type. . . . .	139
6.15 Rendering of the wingbox type subdomains of the resulting optimized structure obtained for configuration A with $N_T = 1$ . The most voluminous bars could be lightened by splitting them into shorter components, reducing the free buckling length. . . . .	140
6.16 Visual representation of the ground structure of the 20 wingbox type submodules of configuration B. . . . .	141
6.17 Evolution of the mass of the NACA 0012 drone wing structure for configuration A and B and different number of modules' topologies $N_T$ . . . . .	141

6.18 Subfigures (a) presents the resulting optimized structure obtained for configuration B with $N_T = 3$ different topologies for the wingbox and the section type modules. The structure has a total mass of $M = 22.9$ g and a mass density of $\bar{\rho} = 5.38$ kg/m <sup>3</sup> ; (b) and (c) illustrates the modules' layout in the structure for the wingbox and section modules type; (d) and (e) present the modules' topology for the wingbox and section modules type. . . . .	142
---	-----

## LIST OF TABLES

1.1 Vocabulary used in this document to write about lattice materials and modular structures. The adjectives architected and lattice are the only one that are used for both materials and structures. . . . .	24
2.1 Material data used for the optimizations. The value of the maximum material allowable $\sigma_L$ is used as the parameter to generate multiple optimized topologies. The Poisson module is used only in density-based topology optimization. . . . .	39
2.2 Numerical results of the topology optimization method of the L-shape beam load case with varying material allowable $\sigma_L$ on a $600 \times 600$ elements mesh. Numbers in red highlight the results that have not converged. . . . .	42
2.3 Numerical results of the TTO method of the L-shape beam test case with varying values of the material allowable $\sigma_L$ on a $33 \times 33$ nodes ground structure. Numbers in red highlight the results that lie outside the domains of applicability of the optimization method. . .	44
3.1 Non-exhaustive list of the existing research in Truss Topology Optimization (TTO) with their corresponding scientific contributions. . . . .	52
3.2 Values and description of the parameters used for the SLP and NLP optimizations. . .	63
3.3 Material data used for the optimizations. . . . .	64
3.4 Numerical comparison of the effect of the minimum slenderness constraint on the optimization of the 2D L-shaped beam. . . . .	65
3.5 Material data used for the ten-bar truss optimization. . . . .	65
3.6 Numerical comparison of the four optimization algorithms on the ten-bar truss for 50 different initial points. The 2S-5R algorithm shows a 100 % convergence rate to the lightest structure found. The iteration count and time are from the first initialization point $a_s^0$ . .	66
3.7 Material data used for the 2D cantilever beam optimization. . . . .	68
3.8 Numerical comparison of the 2D cantilever beam of the four algorithms for 100 random initial points. The 2S-5R algorithm shows a good balance between the volume, complexity, and dispersion of the solutions. . . . .	69
3.9 Optimal values of the member forces, areas, and volumes of the 2D cantilever beam. .	69
3.10 Material data used for the simply supported 3D beam optimization. . . . .	71
3.11 Numerical results of the optimization of the simply supported 3D beam. . . . .	72
3.12 Material data used for the ten-bar truss optimization. . . . .	73
3.13 Numerical comparison of the four optimization algorithms on the ten-bar truss for 50 different initial points. . . . .	73

3.14 Comparison of the results of the SLP step and NLP step for the multiple load cases ten-bar truss. . . . .	75
3.15 Optimal values of the member forces, areas, and volumes of the members of the ten-bar truss with multiple load cases. . . . .	75
 4.1 Reminder of the parameters used to set the reinitialization parameters for the modular optimization. The full list of values and tolerances used for the setup of the optimization algorithm can be found in Table 3.2. . . . .	82
4.3 . . . . .	83
4.2 Material data used for the modular bridge section 2D structure. . . . .	83
4.4 Material data used for the simply supported 3D beam optimization. . . . .	84
4.5 Numeric results of the parametric study on the influence of the number of subdomains on the optimized structures. . . . .	86
4.6 Numeric results of the parametric study on the influence of the module complexity on the optimized structures. . . . .	89
4.7 Coefficients of the quadratic function used to model how the volume $V$ varies with the number of subdomains $N_{\text{sub}}$ and the module complexity $\bar{n}$ . . . . .	91
4.8 Coefficients of the quadratic function used to model how the computational time $t$ varies with the number of subdomains $N_{\text{sub}}$ and the module complexity $\bar{n}$ . . . . .	91
4.9 Numerical results of the comparison between octet-truss and TTO structures. . . . .	93
4.10 Numerical results of the comparison between the structure with multiple modules with the monolithic and the fully modular structures. . . . .	98
 5.1 Material and geometrical data used for the 2D cantilever beam optimization. The Young's module is not listed as in this problem we temporarily overlook compatibility. . . . .	109
5.2 Performance parameters evaluated for the two reference cases R1 and R2. . . . .	110
5.3 Numeric results of the parametric study on the influence of the number of modules on the optimized 2D cantilever beam. . . . .	113
5.4 Material data used for the 2D Bailey bridge without local buckling constraints test case to compare with the work of Tugilimana <i>et al.</i> [158]. The Young's module is not listed as in this problem the authors overlook compatibility and buckling constraints. . . . .	116
5.5 Material data used for the 2D Bailey bridge with local buckling constraints test case. .	118
5.6 Material data used for the simply supported 3D beam optimization. . . . .	120
5.7 Numeric results of the parametric study on the influence of the number of modules $N_T$ on the simply supported 3D beam. . . . .	121
 6.1 Material data used for the CRM optimization. . . . .	124
6.2 Numerical results of the optimization of the CRM with two different ground structures. .	127
6.3 Numerical results of the optimization of the CRM-315 model with three different maximum displacement constraints ( $Z_{t,\ell} = 1 \text{ m}$ , $Z_{t,\ell} = 2 \text{ m}$ , $Z_{t,\ell} = 3 \text{ m}$ ) and no maximum displacement constraints. . . . .	128
6.4 Material data of the four materials used for the CRM-315 optimization. . . . .	129
6.5 Numerical results of the CRM-315 optimized using four different materials. . . . .	129
6.6 Number of active mechanical failure constraints for the CRM-2370 optimized design per type of constraint (rows) and per load case (columns). . . . .	131
6.7 Material data of the Ultem 2200 used for the NACA 0012 optimization. . . . .	134

6.8	Numeric results of the parametric study on the influence of the number of modules $N_T$ on the NACA 0012 drone wing. . . . .	137
1	Reminder of the indexes used for the sensitivity analysis of the layout and topology optimization of modular structures. . . . .	179

## LIST OF ABBREVIATIONS

<b>AD</b>	Alternate Directions
<b>AI</b>	Artificial Intelligence
<b>BESO</b>	Bi-directional ESO
<b>BWB</b>	Blended-Wing Body
<b>CFRP</b>	Carbon Fiber Reinforced Polymer
<b>CONLIN</b>	CONvex LINearization
<b>CRM</b>	NASA Common Research Model
<b>DMO</b>	Discrete Material Optimization
<b>DOE</b>	Design of experiments
<b>DOFs</b>	Degrees Of Freedom
<b>DSI</b>	Degree of Static Indeterminacy
<b>ESO</b>	Evolutionary Structural Optimization
<b>FEA</b>	Finite Element Analysis
<b>FEM</b>	Finite Element Method
<b>GA</b>	Genetic Algorithm
<b>GBMMA</b>	Gradient Based MMA
<b>GCMMA</b>	Globally Convergent MMA
<b>GGP</b>	Generalized Geometry Projection
<b>GP</b>	Geometry Projection
<b>HAR</b>	High Aspect Ratio
<b>HS</b>	Hashin-Shtrikman
<b>KS</b>	Kreisselmeier-Steinhauser
<b>LP</b>	Linear Programming
<b>MIL</b>	Mixed-Integer Linear Optimization
<b>MILP</b>	Mixed-Integer Linear Programming
<b>MIP</b>	Mixed-Integer Programming
<b>MMA</b>	Method of Moving Asymptotes
<b>MMC</b>	Moving Morphable Components
<b>MPVCs</b>	Mathematical Programs with Vanishing Constraints
<b>NAND</b>	Nested Analysis and Design
<b>NLP</b>	Non-Linear Programming
<b>OC</b>	Optimality Criteria
<b>RAMP</b>	Rational Approximation of Material Properties

<b>RVE</b>	Representative Volume Element
<b>SA</b>	Simulated Annealing
<b>SAND</b>	Simultaneous Analysis and Design
<b>SIMP</b>	Solid Isotropic Material with Penalization Method
<b>SLA</b>	Stereolithography
<b>SLP</b>	Sequential Linear Programming
<b>SLSQP</b>	Sequential Least Square Quadratic Programming
<b>SQP</b>	Sequential Quadratic Programming
<b>TTO</b>	Truss Topology Optimization



## ABSTRACT

In the aerospace industry, an ongoing demand exists for lighter aerostructures, motivated by the imperative to enhance fuel efficiency and overall performance. For that reason, the aerospace sector is currently witnessing two innovative shifts: the transition to hydrogen-powered and electric planes, directing engineering efforts toward cleaner and more sustainable aviation technologies. These changes offer opportunities to deviate from the classic tube-and-wing configuration and explore inventive concepts like the flying wing or transonic truss-braced wings. One promising approach to meet these requirements is the utilization of lattice structures. These structures not only offer ultralight properties but also modularity. Modular designs bring numerous advantages, including the ability to assemble large structures from smaller and easier-to-manufacture repeating modules, on-field reparability, and rapid assembly for temporary structures. The objective of this thesis is to develop a design and optimization algorithm for ultralight and modular aerostructures. In the initial phase, we reviewed existing literature to identify the most suitable algorithm basis for optimizing monolithic (non-modular) structures. After a thorough comparison, we selected the Truss Topology Optimization (TTO) approach, an optimization method based on the use of bars as the discretizing element of the structure. However, the classic TTO formulation has limitations, such as the inability to address buckling constraints, consider multiple load cases, and ensure mechanical compatibility. To overcome these challenges, we proposed an innovative two-step optimization algorithm. In this approach, a relaxed problem is utilized to generate an initial solution, serving as the starting point for the optimization using a complete formulation. The second part of the thesis focuses on adapting the proposed monolithic formulation to incorporate modular constraints. Initially, the emphasis is on optimizing the topology of a fully modular structure, where a single module is repeated throughout the entire design. We evaluate how hyperparameters, such as the number of subdomains and module complexity, affect the mechanical performance of the structure. Subsequently, we delve into a more complex scenario, optimizing multiple module topologies and their layout within the structure. This is achieved through a Discrete Material Optimization (DMO) approach, employing a gradient-based optimizer. By addressing the challenges of lightweight design and modularity in aerostructures, this research aims to contribute to the ongoing evolution of aerospace technologies and advance the efficiency and performance of future aircraft.



# INTRODUCTION

*Scientists study the world as it is,  
Engineers create the world that never has been.*

— Theodore von Kármán

## TOWARDS LIGHTER STRUCTURES

In the aerospace industry, an ongoing demand exists for lighter aerostructures, motivated by the need to enhance fuel efficiency and overall performance. This emphasis on lighter structures and materials not only reduces operational costs for airlines but also aligns with a broader commitment to sustainability, mitigating fuel consumption and carbon emissions. Furthermore, the aerospace sector is currently witnessing two innovative shifts: the transition to hydrogen-powered and electric planes, directing engineering efforts toward cleaner and more sustainable aviation technologies. These changes offer opportunities to deviate from the classic tube-and-wing configuration and explore inventive concepts like the flying wing Blended-Wing Body (BWB), in which the fuselage and the wing blend to form an aircraft in which the fuselage, widened and integrated into the wing, also contributes significantly to the lift. Another explored configuration is the use of transonic truss-braced wings, with the goal of direct reduction in the aerodynamic drag by using a High Aspect Ratio (HAR) strut-braced wing configuration (see examples in Fig. 1). Regardless of the specific configuration, a highly probable shared goal is the necessity to design lightweight dry wings—i.e., with no fuel tanks inside—with high aspect ratios and thin profiles.



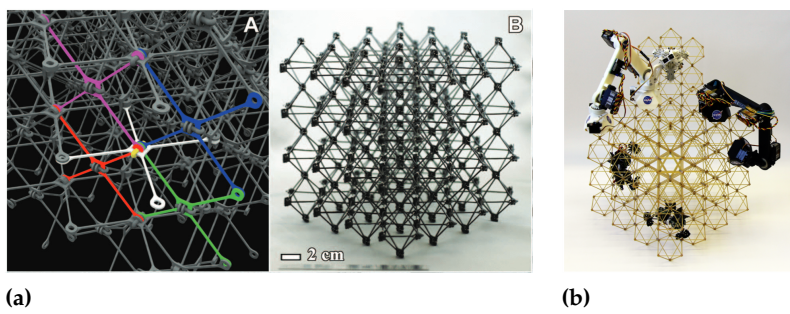
(a)



(b)

**Figure 1:** (a) The transonic truss-braced wing called ALBATROS by ONERA [1, 2]; (b) the Blended-Wing Body (BWB) zero-e demonstrator by Airbus [3].

**Figure 2:** Modular lattice structures present multiple properties that could be applied to the aerospace domain; (a) small two-dimensional components are reversibly assembled to build large three-dimensional structures [5]; (b) the assembly phase of modular lattice structures is done by fully robotic means in the NASA's Automated Reconfigurable Mission Adaptive Digital Assembly Systems (ARMADAS) project [6].



Lattices emerge as a promising solution to fulfill these requirements. These structures consist of interconnected elements resulting in an arrangement of material and void spaces, recognized for their remarkable strength-to-weight ratio. Depending on their scale, lattice structures are categorized into two main types: lattice materials and lattice structures. Lattice materials, prevalent in research, are typically fabricated using additive manufacturing techniques and are primarily used to create individual structural components. Conversely, lattice structures, due to their larger size, are impractical to manufacture using additive methods alone. Instead, they are assembled from smaller components to form larger structures. The process of going from materials to structures is not only accompanied by a change in manufacturing processes but also an evolution in the issue of connections i.e., moving from the problem of connecting the structural component made of lattice material to its environment, to the problem of linking the constituent elements of the lattice structure.

When lattice structures present a repetitive pattern, they not only possess the inherent ultralight properties typical of such structures but also provide the advantages of modularity. Modular lattices offer numerous benefits, including the ability to construct large structures using smaller, more readily manufactured repeating modules (see Fig. 2a). Other notable properties include on-field reparability, improved damage resistance, fast assembly for temporary structures, and possibility to repurpose the repetitive components compared to conventional monolithic material systems [4]. Additionally, recent research opens up the possibility of a fully robotic assembly phase, permitting faster and more reliable assembly (see Fig. 2b). These features are crucial to assess whether lattice structures can challenge the classic composite materials in aerospace applications.

4. Belvin et al. (2016), 'In-Space Structural Assembly'

Given these beneficial properties, ONERA, the French aerospace research agency, initiated the STARAC research project to investigate modular lattice structures more comprehensively. This thesis is conducted within this research effort, in a unit dedicated to developing design and optimization methods for such structures.

## OBJECTIVE

Optimizing modular lattice structures involves four main dimensions: material, module shape, layout, and topology. Material optimization focuses on improving mechanical properties by tailoring the material distribution within lattice constituents, while shape optimization fine-tunes the repeating module geometry. Layout optimization arranges modules in space, defining their presence or absence in the design region, and topology optimization refines the overall arrangement and connections of bars within each module. Navigating these dimensions enables engineers to tailor lattice structures for a balance between weight, strength, and functionality. However, the abundance of design choices poses a significant challenge due to the lack of an optimized design method. Using available tools, it is possible to create oversized structures using modern robotic means. However, achieving better results is complex and requires leveraging numerical optimization tools to explore the design space. It is these tools, and even more importantly, the necessary methods, that are lacking. Thus, the challenge of this research lies not in designing modular lattice structures, but rather in realizing their full potential.

This thesis aims to develop an optimization methodology tailored for lightweight and modular aerospace structures. The methodology development involves working on problem formulation, theorize a resolution method, implementing it numerically, and validating the results against existing literature. The aim of the thesis is broad and complex, involving several interrelated subproblems. Initially, the focus is on optimizing lattices without modularity while considering mechanical failure constraints. Subsequently, attention shifts to incorporating modularity into the optimization process and assessing its impact on mass and performance. Further, efforts are directed towards optimizing the arrangement of repeating modules alongside their individual designs. Finally, the methodology is extended to the scale of a full wing for aerospace applications.

## OUTLINE OF THE THESIS

Chapter 1 provides a review of structural optimization algorithms, especially focusing on ultralight weight and modular cases. The chapter introduces the density-based topology optimization and the Truss Topology Optimization (TTO) methods that will be utilized throughout the document. Chapter 2 presents two equivalent formulations: one for density-based topology optimization and another for the TTO method. It then conducts an in-depth comparison of the resulting optimized structures, focusing on those with volume fractions below 5 %. The numerical analysis reveals shorter computational times and improved performance with the TTO approach,

particularly in modeling lightweight structures, thus validating its selection. Chapter 3 introduces additional features with respect to the classic TTO formulation, such as local buckling constraints, minimum slenderness limits, consideration of multiple load cases, and ensuring mechanical compatibility for complex structures. Some of these constraints have been studied in the literature, but they have never been comprehensively considered in a single volume minimization formulation. Due to the inherent multimodality of the problem, a two-step optimization algorithm is introduced, utilizing a relaxed problem to generate an initial approximate solution for subsequent optimization using a complete non-linear formulation. In an effort to minimize the impact of the initial starting point on optimization outcomes, a heuristic is formulated to reintroduce candidates into the optimization process when it converges to local minima. Chapter 4 explores how to formulate a modular optimization problem within the TTO framework, employing the full-scale variable linking approach. This approach optimizes the topology of a single module that is repeated throughout the entire design region to create modular structures. The chapter evaluates the impact of hyperparameters, such as the number of subdomains and the choice of the module ground structure, on the mechanical performance of the structure. A Design of experiments (DOE), based on the chapter's results, helps formulating a guide on choosing hyperparameters for optimization. In Chapter 5 we complicate the optimization by introducing multiple modules into the process. Each module is optimized independently, as well as the selection of the active module in each subdomain. This optimization, inherently more complex, involves optimizing not only the modules' topology but also the layout of the modules within the structure. A modified Discrete Material Optimization (DMO) approach is employed, utilizing a gradient-based optimizer, while the starting point is determined by employing k-means clustering on the stress distribution of the optimization starting point. In Chapter 6 the proposed optimization methodologies are applied to more ambitious aerospace cases that require some minor methodological adaptations. First, the monolithic TTO algorithm is used to reduce the mass of the wingbox of the NASA Common Research Model (CRM), a standard benchmark for aeronautic research. The test case is subjected to real-world multiple load cases (+2.5g, -1g, and cruise maneuver loads) associated with some corresponding safety factors. The optimization is conducted using different materials and discretizations, resulting in lighter structures with less computational effort compared to the literature. Later, the modular formulation presented in Chapter 5 is used on a drone-sized wing based on the 0012 NACA wing profile, validating the ability of the proposed modular optimization methodology to work on real-world test cases. Additionally, follow-up scientific perspectives are discussed.

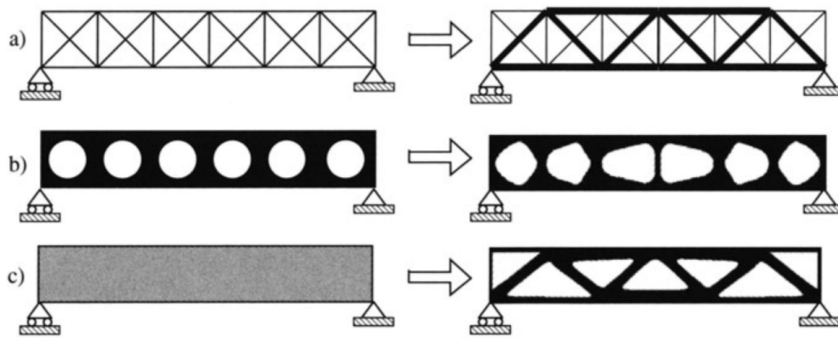
# LITERATURE REVIEW

This thesis focuses on numerical optimization in the structural engineering domain. Consequently, it requires familiarity with existing optimization methods and contemporary engineering practices. The purpose of this chapter is to provide the reader with a non-exhaustive historical overview of structural optimization, particularly in the context of ultralight and modular structures. Additionally, we introduce crucial concepts and terminology that will be employed consistently throughout the document.

## 1.1 AN INTRODUCTION TO STRUCTURAL OPTIMIZATION

Structural optimization is a multidisciplinary field within engineering that aims to systematically improve structural performance—considering factors like mass, stiffness, and dynamic response—by optimizing their shape, material distribution, and overall design. Historically, structural optimization algorithms are categorized into three families: sizing, shape, and topology optimization. Sizing optimization concentrates on determining the optimal distribution of variables, where both the design and state variable domains are known *a priori* and remain constant during optimization. In contrast, shape optimization aims to discover the optimal shape of a predefined domain, treating the domain itself as a design variable allowing for flexibility in shaping the structure. Topology optimization goes further, involving the determination of features like the number, location, and shape of holes, as well as the connectivity of the structural domain. This approach offers a more comprehensive exploration of possibilities in structural design. A visual representation of the three families is provided in Fig. 1.1.

Structural optimization involves using mathematical algorithms, computational models, and iterative analyses to explore and refine design



1.1 AN INTRODUCTION TO STRUCTURAL OPTIMIZATION	7
1.2 ULTRA-LIGHTWEIGHT STRUCTURES OPTIMIZATION APPROACHES . . . . .	11
1.3 MODULAR STRUCTURES AND CELLULAR MATERIALS . . . . .	20

**Figure 1.1:** Visual representation of (a) size, (b) shape, and (c) topology optimization [7].

solutions. For that reason, we introduce the basic concepts and terminology behind numerical optimization. In numerical optimization, algorithms are employed to minimize or maximize a specific function by adjusting various design variables. The problem may or may not be subject to constraints. Formulating an optimization problem is a crucial step to prevent common conceptual errors, such as confusing constraints with objective functions. An incorrect problem formulation can lead to a failed solution or yield a mathematical optimum that lacks feasibility from an engineering perspective.

The most general formulation of an optimization problem is written as:

$$\begin{aligned} \min_x \quad & f(\mathbf{x}) \\ \text{by varying} \quad & \mathbf{x} \in [l^-, l^+] \\ \text{s.t.} \quad & g_e(\mathbf{x}) = 0 \\ & g_i(\mathbf{x}) > 0, \end{aligned} \tag{1.1}$$

where  $f(\mathbf{x})$  is the objective function to minimize,  $\mathbf{x}$  is the vector of design variables bounded between  $l^-$  and  $l^+$ , and  $g_e$  and  $g_i$  represent the equality and inequality constraints, respectively.

**OBJECTIVE FUNCTION** In numerical optimization, the objective function  $f(\mathbf{x})$  represents the scalar that we aim to minimize. Should the goal be to maximize a function, one can achieve this by minimizing the opposite of that function, maintaining adherence to the convention. Common objective functions in structural design include the minimization of volume or structural compliance. The objective function can take the form of an explicit function or result from a highly complex computational procedure. The selection of the objective function is crucial to propose a design that is feasible from an engineering perspective, regardless of the precision of the optimization scheme employed.

Optimization problems are categorized in the literature based on how the objective function is with respect to design variables, whether linear, quadratic, or generally non-linear. It is possible to concurrently optimize multiple objective functions, but this usually results in a family of optimum designs with differing emphases on the various objectives called the Pareto front. When possible, it is more straightforward to convert these diverse objectives into constraints [8].

8. Martins et al. (2021), 'Engineering Design Optimization'

**DESIGN VARIABLES** The design variables  $\mathbf{x}$  are the parameters that the optimizer algorithm changes to minimize the objective function. Design variables could be continuous or discrete if only some distinct values are allowed (for example, only a certain size for a hole in a structural analysis). The optimization problem formulation allows for

the lower and upper boundary for each design variable known in the literature as variable bounds.

**CONSTRAINTS** The constraints are functions used to restrict the design variables in some way. They serve the purpose of preventing the algorithm from converging to a numerical minimum that is not feasible due to physical and engineering constraints. Similar to the objective function, constraint functions can take on linear, quadratic, or generally non-linear forms, and different algorithms must be applied accordingly.

Constraint functions can be further classified into two types: equality constraints (*ge*), which arise when the design variables are restricted to be equal to a fixed quantity, and inequality constraints (*gi*), which come into play when the design variables are required to be greater than or equal to a certain quantity.

### 1.1.1 OPTIMIZERS

The field of numerical optimizers is extensive. For that reason, our focus here will be specifically on algorithms employed in structural optimization. Various algorithm types have been applied to address structural optimization problems, predominantly categorized into three main families: optimality criteria, metaheuristic algorithms, and gradient-based strategies.

Optimality Criteria (OC) refer to mathematical conditions or rules used to assess and guide the modification of a design or structure to achieve the desired performance [9, 10]. In the context of topology optimization, OC are primarily applied in compliance minimization problems, as each element contributes independently to the overall compliance. Bendsøe used OC to seek the stiffest plate i.e. compliance minimization—that can be made of a given amount of material and, together with Kikuchi [11], they used OC to obtain optimal shape design of structural elements based on boundary variations without the use of remeshing. Later, Bendsøe and Sigmund [12, 13] introduced a heuristic update scheme for isotropic materials, while Allaire *et al.* [14] demonstrated the convergence proof for both isotropic and anisotropic materials using the Alternate Directions (AD) approach. In both methods mechanical analysis provides essential information for solving closed-form conditions, allowing iterative updates of variables until convergence is achieved. Recently, OC methods gained interest again thanks to the reduced calculation time [15, 16] obtained using a modified Anderson acceleration strategy [17].

Metaheuristic (or gradient-free) algorithms offer a broader range of options compared to their gradient-based counterparts. While gradient-based algorithms typically conduct local searches, possess

9. Prager et al. (1968), 'Problems of Optimal Structural Design'
10. Prager (1968), 'Optimality Criteria in Structural Design'
11. Bendsøe et al. (1988), 'Generating optimal topologies in structural design using a homogenization method'
12. Bendsøe (1995), 'Optimization of Structural Topology, Shape, and Material'
13. Sigmund (2001), 'A 99 line topology optimization code written in Matlab'
14. Allaire et al. (1996), 'The homogenization method for topology and shape optimization. Single and multiple loads case'
15. Li et al. (2020), 'Accelerated fixed-point formulation of topology optimization'
16. Ferrari et al. (2020), 'A new generation 99 line Matlab code for compliance topology optimization and its extension to 3D'
17. Anderson (1965), 'Iterative Procedures for Nonlinear Integral Equations'

- 18. Conn et al. (2009), 'Introduction to Derivative-Free Optimization'
- 19. Audet et al. (2017), 'Derivative-Free and Blackbox Optimization'
- 20. Simon (2013), 'Evolutionary optimization algorithms'
- 21. Balamurugan et al. (2011), 'A two phase approach based on skeleton convergence and geometric variables for topology optimization using genetic algorithm'
- 22. Sigmund (2011), 'On the usefulness of non-gradient approaches in topology optimization'
- 23. Luh et al. (2009), 'Structural topology optimization using ant colony optimization algorithm'
- 24. Luh et al. (2011), 'A binary particle swarm optimization for continuum structural topology optimization'
- 25. Stolpe (2004), 'Global optimization of minimum weight truss topology problems with stress, displacement, and local buckling constraints using branch-and-bound'
- 26. Mattheck et al. (1990), 'A new method of structural shape optimization based on biological growth'
- 27. Xie et al. (1993), 'A simple evolutionary procedure for structural optimization'
- 28. Manickarajah et al. (1998), 'An evolutionary method for optimization of plate buckling resistance'
- 29. Young et al. (1999), '3D and multiple load case bi-directional evolutionary structural optimization (BESO)'

mathematical justification, and operate deterministically, metaheuristic algorithms are simpler and usually take much less developer time to use, and are perfect candidates for smaller problems. They find very diverse application cases and are useful when the design space is discrete, with multiple objective functions, or highly non-linear with many local minima (multimodal). The works authored by Conn *et al.* [18] and Audet and Hare [19] offer a comprehensive exploration of gradient-free optimization algorithms. Evolutionary algorithms, a prominent category, simulate natural selection by retaining the fittest solutions in each generation while introducing mutations or cross-overs for improvement. A review of these optimization methods is given in the following reference [20]. These algorithms, also called Genetic Algorithm (GA), are employed for example by Balamurugan *et al.* [21] for compliance minimization, showcase versatility but face challenges with combinatorial considerations as the number of design variables increases [22]. Particle swarm and ant colony algorithms, inspired by nature, provide alternative strategies with randomness and new search directions. However, these non-gradient methods require regularization schemes for topology optimization, as outlined by Luh, Lin, and others [23, 24]. Targeting the resolution of Mixed-Integer Programming (MIP) problems, branch-and-bound algorithms divide the feasible set of the original problem into subsets through a process known as branching. These subsets are then further segmented to refine the partition of the feasible set. For each subset, lower bounds and optionally upper bounds on the objective function value are determined, a process referred to as bounding. Typically, the lower bounding problems are convex problems that can be efficiently solved to global optimality. Stolpe [25] addresses a volume minimization problem on a truss using a continuous branch-and-bound method, ensuring convergence to a globally optimal solution. The Evolutionary Structural Optimization (ESO) framework, initially a metaheuristic, removes less solicited elements iteratively [26, 27]. These methods offer freedom in optimization and improved convergence to local minima, especially in handling various optimization problems like buckling [28]. The ESO algorithm has been enhanced by the Bi-directional ESO (BESO) framework [29], which allows both removal and addition of elements.

Gradient-based algorithms in optimization leverage local information at a trial point to comprehend the shape of the local objective function in the neighborhood. This insight is crucial for determining the optimal direction to minimize the objective function. Typically, only the Jacobian (first derivative) is utilized, though more advanced algorithms incorporate the Hessian (second derivative). The computational demand for gradient calculation often constitutes the most resource-intensive aspect of the optimization loop. When constraints are present, solving the problem directly on the analytic response surface of the objective function becomes impractical. Consequently,

the approach involves creating local approximations of the problem at the current design point using gradient information. These approximations are designed so that specialized algorithms can efficiently solve them. The categorization of gradient-based algorithms is often based on how this local approximation is constructed.

The most used approximations in structural optimization includes among others Sequential Linear Programming (SLP), Sequential Quadratic Programming (SQP) and Sequential Least Square Quadratic Programming (SLSQP) [30], Method of Moving Asymptotes (MMA) [31] and its amelioration Globally Convergent MMA (GCMMA) [32] and Gradient Based MMA (GBMMA) [33], and CONvex LINearization (CONLIN) [34]. Specialized algorithms for solving the approximated problems are, among others, the primal-dual method and interior-point method.

An interior-point method is a numerical optimization algorithm used to solve constrained optimization problems. The key idea behind interior-point methods is to transform the constrained optimization problem into a sequence of unconstrained problems, allowing for efficient iterative solutions. The method introduces a barrier function that penalizes points outside the feasible region, effectively creating a "barrier" against leaving that region. This barrier function is incorporated into the objective function, and as the optimization progresses, it guides the search towards the interior of the feasible region. The term "interior point" originated from early methods that relied on interior penalty techniques, assuming the initial point was feasible. Nevertheless, contemporary interior-point methods such as the open source IPOPT [35] are more versatile and can start from infeasible points. Rojas Labanda and Stolpe conducted a benchmark of various optimization algorithms and structural optimization formulations using a compliance minimization problem. Their findings highlight the efficacy of employing interior-point algorithms such as IPOPT in topology optimization problems [36].

## 1.2 ULTRA-LIGHTWEIGHT STRUCTURES OPTIMIZATION APPROACHES

Two of the most frequently employed formulations for structural optimization are the minimization of volume while adhering to stress constraints and the minimization of compliance under volume constraints. Historically, the volume minimization formulation has been used in the first works of structural optimization of truss structures [37–39]. The problem was initially formulated in terms of member forces, ignoring the kinematic compatibility to obtain a Linear Programming (LP) problem. The formulation was modeled using the Simultaneous Analysis and Design (SAND) approach, in which the equations of nodal equilibrium are treated as equality constraints, and

30. Kraft (1988), 'A software package for sequential quadratic programming'

31. Svanberg (1987), 'The method of moving asymptotes—a new method for structural optimization'

32. Svanberg (2002), 'A Class of Globally Convergent Optimization Methods Based on Conservative Convex Separable Approximations'

33. Bruyneel et al. (2002), 'A family of MMA approximations for structural optimization'

34. Fleury et al. (1986), 'Structural optimization'

35. Wächter et al. (2006), 'On the implementation of an interior-point filter line-search algorithm for large-scale nonlinear programming'

36. Rojas Labanda et al. (2015), 'Benchmarking optimization solvers for structural topology optimization'

37. Dorn et al. (1964), 'Automatic design of optimal structures'

38. Chan (1964), 'Optimum structural design and linear programming'

39. Hemp (1973), 'Optimum Structures'

- 40.** Sankaranarayanan et al. (1994), 'Truss topology optimization with simultaneous analysis and design'
- 11.** Bendsøe et al. (1988), 'Generating optimal topologies in structural design using a homogenization method'
- 41.** Bendsøe (1989), 'Optimal shape design as a material distribution problem'
- 42.** Sigmund (1994), 'Materials with prescribed constitutive parameters'
- 43.** Zhang et al. (2006), 'Scale-related topology optimization of cellular materials and structures'
- 44.** Collet et al. (2018), 'Topology optimization for microstructural design under stress constraints'
- 45.** Borrvall et al. (2003), 'Topology optimization of fluids in Stokes flow'
- 46.** Bruyneel et al. (2005), 'Note on topology optimization of continuum structures including self-weight'
- 47.** Sigmund (2009), 'Manufacturing tolerant topology optimization'
- 48.** Brackett et al. (2011), 'Topology Optimization for Additive Manufacturing'
- 49.** Sigmund (1997), 'On the Design of Compliant Mechanisms Using Topology Optimization\*
- 50.** Bruns et al. (2001), 'Topology optimization of non-linear elastic structures and compliant mechanisms'
- 51.** Wang et al. (2020), 'Space-time topology optimization for additive manufacturing'
- 52.** Allaire et al. (2002), 'A level-set method for shape optimization'
- 53.** Wang et al. (2003), 'A level set method for structural topology optimization'
- 54.** Allaire et al. (2004), 'Structural optimization using sensitivity analysis and a level-set method'
- 1:** This proposition holds when referring to the end of the 1980s when computational power was scarce compared to what we have today.
- 8.** Martins et al. (2021), 'Engineering Design Optimization'
- 55.** Tortorelli et al. (1994), 'Design sensitivity analysis'
- 7.** Bendsøe et al. (2004), 'Topology Optimization'

where both nodal displacements and the cross-sectional areas of truss members serve as design variables [40]. These methods are known in the literature as layout optimization or Truss Topology Optimization (TTO).

However, to attain greater design freedom, the structure optimization field later transitioned from truss structures to continuous discretization (also called density methods). While truss structures offered simplicity and ease of analysis, they imposed limitations on the design due to their discrete member configurations and their inability to transmit moments, handle torsional effects, and represent complex structural elements such as plates or volumes. The continuous mesh offered instead more versatility [11, 41], and has since been used for multiple different applications, e.g. the design of optimized repetitive metamaterials [42–44], fluids optimization [45], modelization of self-weight of the structure [46], the simulation of advanced manufacturing constraints [47, 48], the design of compliant mechanism [49, 50], or the optimization for additive manufacturing [51]. Other than the density methods, other ways to deal with topology optimization exist, like level-set methods [52–54]. The SAND approach is, however, incompatible with density methods due to its excessive number of variables<sup>1</sup>. Given this limitation, a new approach was required to better handle the complexity of continuous meshes.

In the density-based Nested Analysis and Design (NAND) approach, the nodal displacement (state) variables are eliminated from the optimization problem through a process where the structural equilibrium equation is solved every iteration of the optimization loop instead of being used as a constraint of the optimization. This results in an independent nested phase where the state equation of structural equilibrium is solved separately from the optimization algorithm. This creates a dense coupling between displacement and material density variables, necessitating a computationally expensive sensitivity analysis within the nested algorithm, typically employing the adjoint method (more information about the adjoint method on the following resources [8, 55]). Nevertheless, if the problem is reformulated as a compliance minimization with volume constraints, the problem is self-adjoint and the adjoint algorithm is no longer necessary to evaluate the gradient sensitivities [7], and this reduces considerably the computational times.

Both the TTO methods based on the ground structure and the density-based topology optimization approaches are good candidates for the optimization of ultra-light structures. We review here their main characteristics and numerical properties, starting from density-based approaches.

### 1.2.1 DENSITY-BASED TOPOLOGY OPTIMIZATION

Let  $\Omega \in \mathbb{R}^2$  be a rectangular domain of dimensions  $X$  and  $Y$ , containing respectively  $N_x$  and  $N_y$  linear 4-nodes elements, for a total of  $N_e = N_x N_y$  elements and  $M$  nodes (see Fig. 1.2). The objective of the optimization is the minimization of the compliance  $C$  of the structure, equivalent to finding the structure with the least possible nodal displacement with respect to a defined set of boundary conditions.

**COMPLIANCE MINIMIZATION FORMULATION** The Problem  $\mathbb{T}_0$  is stated in terms of the density design variables  $\rho$  for a single load case as follows:

$$\begin{aligned} \min_{\rho} \quad & C = \sum_i \mathbf{u}_{e,i}^T \mathbf{K}_{e,i} \mathbf{u}_{e,i} = \mathbf{f}^T \mathbf{u} \quad \forall i \in [0, \dots, N_e] \\ \text{s.t.} \quad & \frac{1}{V_p} \frac{\sum_i (\bar{\rho}_i v_i)}{V_0} - 1 \leq 0 \quad \forall i \in [0, \dots, N_e] \quad (\mathbb{T}_0) \\ & \mathbf{K}\mathbf{u} = \mathbf{f} \\ & 0 \leq \rho_i \leq 1. \quad \forall i \in [0, \dots, N_e] \end{aligned}$$

The design variables  $\rho$  are defined for every element of the structure as  $\rho = [\rho_1, \rho_2, \dots, \rho_{N_e}]^T$ , with  $\rho_i \in [0, 1]$ ,  $\forall i \in [0, \dots, N_e]$ . The physical densities  $\bar{\rho}$  are related to the design variable  $\rho$  through density filtering and threshold projection [56], as explained later in the document.  $V_p \in [0, 1]$  is the prescribed volume fraction that acts as the constraint of the minimization problem, while  $v_i$  represents the area of the  $i$ -th element and  $V_0$  is the total area of the domain  $\Omega$ .  $\mathbf{K}\mathbf{u} = \mathbf{f}$  is the state equation of the problem and defines the elastic response of the structure to an external nodal load  $\mathbf{f} = [f_1, f_2, \dots, f_{2M}]^T$ . The global stiffness matrix  $\mathbf{K}$  is assembled from the element stiffness matrix  $\mathbf{K}_{e,i}$  and  $\mathbf{K}_{e,i} = E_i \mathbf{K}_{e,0}$  where  $\mathbf{K}_{e,0}$  represents the element stiffness matrix relative to the chosen type of element (linear or quadratic) and  $E_i(\bar{\rho}_i)$  the Young's modulus of the  $i$ -th element.

The material scheme used to interpolate between void and full material is the well-known Solid Isotropic Material with Penalization Method (SIMP) [41, 57] approach. It is governed by the equation:

$$E_i(\bar{\rho}_i) = E_{\min} + \bar{\rho}_i^p (E_0 - E_{\min}), \quad (1.2)$$

where the parameter  $p$  penalizes the intermediate densities and pushes the result to a black-and-white result.  $E_0$  is the Young's modulus of the dense material and  $E_{\min}$  is a small value used to avoid the global stiffness matrix  $\mathbf{K}$  from being singular when  $\bar{\rho}_i = 0$ .

The SIMP exponent  $p$  is constrained to be greater than or equal to 1. From a physical perspective, the extreme case of  $p = 1$  makes sense only in a two-dimensional optimization context, where it becomes

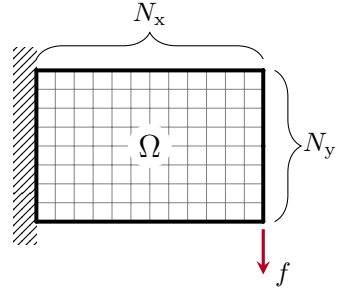


**Figure 1.2:** The domain  $\Omega$  is discretized using  $N_e = N_x N_y$  continuous 4-nodes elements.

56. Wang et al. (2011), 'On projection methods, convergence and robust formulations in topology optimization'

41. Bendsøe (1989), 'Optimal shape design as a material distribution problem'

57. Bendsøe et al. (1999), 'Material interpolation schemes in topology optimization'

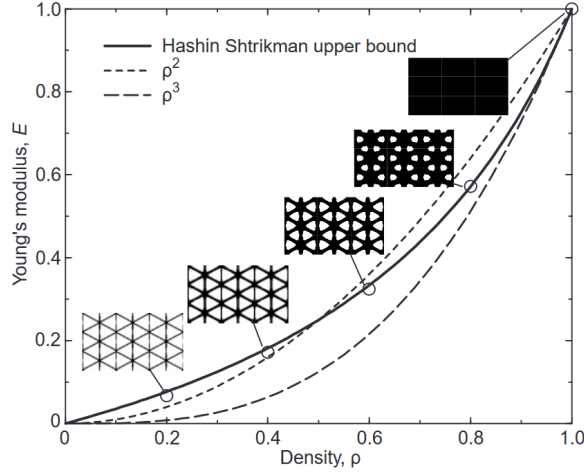


**Figure 1.3:** Comparison between SIMP model with the Hashin-Shtrikman upper bound, considering an isotropic material with a Poisson ratio of 1/3 mixed with void. The Hashin-Shtrikman upper bound is illustrated with microstructures approaching the specified bounds. [57].

58. Hashin et al. (1963), 'A variational approach to the theory of the elastic behaviour of multiphase materials'  
 57. Bendsøe et al. (1999), 'Material interpolation schemes in topology optimization'

59. Díaz et al. (1995), 'Checkerboard patterns in layout optimization'  
 49. Sigmund (1997), 'On the Design of Compliant Mechanisms Using Topology Optimization'  
 60. Sigmund (1994), 'Design of Material Structures using Topology Optimization'  
 61. Sigmund (2007), 'Morphology-based black and white filters for topology optimization'

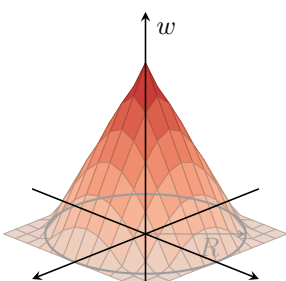


**Figure 1.4:** Kernel of the 2D convolution operator.

equivalent to optimizing membrane thickness. When  $p > 1$ , the interpolation results in an equivalent homogenized stiffness tensor for intermediate densities, determined by the material-to-void ratio  $\rho$ . This mirrors microstructures conforming to the Hashin-Shtrikman (HS) conditions, which estimate the theoretical lower and upper bounds for the elastic modulus of a homogeneous, isotropic mixture of different materials based on their elastic modulus and volume fractions [58]. If the exponent  $p$  exceeds 3, Bendsøe [57] mathematically proves that the equivalent homogenized stiffness tensor adheres to the upper bound of the HS conditions (refer to Fig. 1.2). It is important to note that in the mono-scale topology optimization context, deviating from the HS bounds for intermediate densities is allowed. The objective is to drive the density distribution towards a black-and-white result with minimal intermediate densities, without concerning whether the equivalent homogenized stiffness tensor can be replicated by a real microstructure.

**SPATIAL FILTERING AND PROJECTION** Multiple approaches have been developed to solve the problems linked to mesh discretization, such as mesh dependency or the checkerboard problem [59]. Filtering the sensitivity information of the optimization problem proved to be an effective approach to guarantee independence from mesh resolution [49, 60]. Another possibility is instead to directly filter the density field  $\rho$  using the 2D convolution operator [61]. The weight function  $w$  (or kernel) of the convolution is defined as:

$$w(d_j) = R - d_j, \quad j \in \mathbb{N}_{i,R} \quad (1.3)$$

where  $\mathbb{N}_{i,R}$  represent the set of elements lying within a circle of radius  $R$  centered on the  $i$ -th element and  $d_j$  is the distance of the  $j$ -th element to the center of the filter (see Fig. 1.4).

The filtered values  $\tilde{\rho}$  of the design variable  $\rho$  are calculated as:

$$\tilde{\rho}_i = \frac{\sum_{j \in \mathbb{N}_{i,R}} w(d_j) v_j \rho_j}{\sum_{j \in \mathbb{N}_{i,R}} w(d_j) v_j}. \quad (1.4)$$

As the filtering phase produces a large number of gray elements, a projection technique based on the  $\tanh$  function is implemented [56] to evaluate the value of the physical density  $\bar{\rho}$  of the structure:

$$\bar{\rho}_j = \frac{\tanh(\beta\eta) + \tanh(\beta(\tilde{\rho}_j - \eta))}{\tanh(\beta\eta) + \tanh(\beta(1 - \eta))}, \quad (1.5)$$

where  $\beta$  is a parameter that defines the slope of this approximation function: the larger the value of  $\beta$ , the fewer elements with intermediate density are present in the structure topology.  $\eta$  is the threshold value of the projection. The key characteristic of Equation 1.5 is its smoothness over the defined interval, permitting easy differentiation and rendering it ideally suited for gradient descent optimization algorithms.

In the domain of structural topology optimization, it is a widely adopted strategy to employ continuation methods. Introduced in the 90s [62, 63], they are used to converge towards more optimized structures. These methods solve a sequence of problems with increasing values of the SIMP material penalization parameter  $p$ . Many researchers such as Bendsøe and Sigmund [7] and Rozvany [64] consider, among others, continuation methods as a standard procedure in topology optimization. However, this approach comes at the expense of an increased number of iterations and, consequently, augmented computational time [65]. In an effort to mitigate this drawback, Rojas Labanda and Stolpe [66] have derived an automatic penalization scheme. This innovative scheme aims to reduce both the objective function value and the number of iterations, providing an improvement over the classical formulation with a fixed penalty parameter. While the literature is predominantly focused on the continuation scheme on the SIMP material penalization parameter  $p$ , it is worth noting that similar techniques could be employed for other optimization parameters e.g. the filter radius  $R$  or the projection parameter  $\beta$ .

While density-based topology optimization offers tremendous benefits in terms of weight reduction and structural efficiency, it is important to acknowledge the challenges associated with manufacturing such designs. The intricate and complex geometries generated through the optimization can pose difficulties in the fabrication process, often requiring advanced manufacturing techniques, specialized equipment, and specific constraints in the optimization [48, 67, 68]. Additionally, the computational time required for generating such optimized designs, particularly for low-volume fractions typical of the aerospace

<sup>56</sup>. Wang et al. (2011), 'On projection methods, convergence and robust formulations in topology optimization'

<sup>62</sup>. Allaire et al. (1993), 'A Numerical Algorithm for Topology and Shape Optimization'

<sup>63</sup>. Allaire et al. (1993), 'Topology Optimization and Optimal Shape Design Using Homogenization'

<sup>7</sup>. Bendsøe et al. (2004), 'Topology Optimization'

<sup>64</sup>. Rozvany (2009), 'A critical review of established methods of structural topology optimization'

<sup>65</sup>. Petersson et al. (1998), 'Slope constrained topology optimization'

<sup>66</sup>. Rojas-Labanda et al. (2015), 'Automatic penalty continuation in structural topology optimization'

<sup>48</sup>. Brackett et al. (2011), 'Topology Optimization for Additive Manufacturing'

<sup>67</sup>. Zhou et al. (2002), 'Progress in Topology Optimization with Manufacturing Constraints'

<sup>68</sup>. Liu et al. (2018), 'Current and future trends in topology optimization for additive manufacturing'

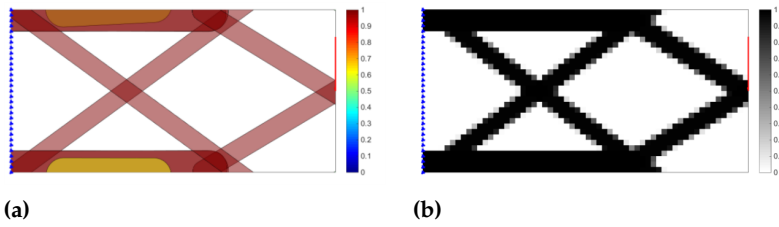


**Figure 1.5:** Component (a) and density (b) plot of a short cantilever beam optimized using the component-based topology optimization method GGP [78].

- 69. Aage et al. (2017), 'Giga-voxel computational morphogenesis for structural design'
- 70. Salazar de Troya et al. (2018), 'Adaptive mesh refinement in stress-constrained topology optimization'
- 71. Zhang et al. (2020), 'Adaptive mesh refinement for topology optimization with discrete geometric components'
- 72. Sigmund et al. (2016), 'On the (non-)optimality of Michell structures'
- 73. Wein et al. (2020), 'A review on feature-mapping methods for structural optimization'
- 74. Guo et al. (2014), 'Doing Topology Optimization Explicitly and Geometrically—A New Moving Morphable Components Based Framework'
- 75. Zhang et al. (2017), 'A new three-dimensional topology optimization method based on moving morphable components (MMCs)'
- 76. Norato et al. (2015), 'A geometry projection method for continuum-based topology optimization with discrete elements'
- 77. Zhang et al. (2016), 'A geometry projection method for the topology optimization of plate structures'
- 78. Coniglio et al. (2020), 'Generalized Geometry Projection'
- 79. Kazemi et al. (2020), 'Multi-material topology optimization of lattice structures using geometry projection'
- 80. Cheng et al. (1997), ' $\epsilon$ -relaxed approach in structural topology optimization'
- 81. Rozvany (2001), 'On design-dependent constraints and singular topologies'
- 82. Gao et al. (2015), 'Topology optimization of continuum structures under buckling constraints'

domain, can be significant [69], impacting the overall efficiency of the design process. This remains true even with the use of adaptive meshes [70, 71]. Even if the freedom of the design space offered by continuous meshes is high, it is known that at very low volume fractions (e.g. ultralight structures), and, especially if buckling constraints and manufacturing considerations (e.g. minimum length scale), are taken into account, the optimal topology resembles a truss-like structure [72]. As a result, a distinct branch of continuous topology optimization has emerged specifically tailored for optimizing truss-like structures, known as feature-mapping topology optimization (also called topology optimization with explicitly defined components).

### 1.2.2 FEATURE-MAPPING TOPOLOGY OPTIMIZATION

Topology optimization methods using explicitly defined components have been developed to permit an easier interpretation of the solution, finding the optimal shape, size, and connectivity of components projected over a finite element continuous mesh (see Fig. 1.5). Two main feature-mapping methods applied to topology optimization have been developed [73], the Moving Morphable Components (MMC) approach [74, 75] and the Geometry Projection (GP) approach [76, 77], later combined in a unique methodology called Generalized Geometry Projection (GGP) [78]. Recently, the GP approach has been used to optimize light lattice structures, proving the effectiveness of the method to provide easy-to-interpret solutions [79]. Nevertheless, the optimization is still based on a density field projected on a continuous mesh, that needs to be refined to correctly discretize low-volume fraction structures. Additionally, truss structure design naturally depends on constraints on maximum allowable stress and buckling which are all known for being difficult to implement on topology optimization using the Nested Analysis and Design (NAND) formulation. This is principally due to the singular optima (or topologies) phenomenon [80, 81] and the pseudo-modes of buckling of low-density elements [82].

### 1.2.3 TRUSS TOPOLOGY OPTIMIZATION (TTO)

Truss Topology Optimization (TTO) focuses on optimizing the topology of the truss structure itself, instead of operating on a continuous mesh. It involves selecting the cross-sectional areas and the connectivity of a discrete and dense mesh called ground structure, aiming to

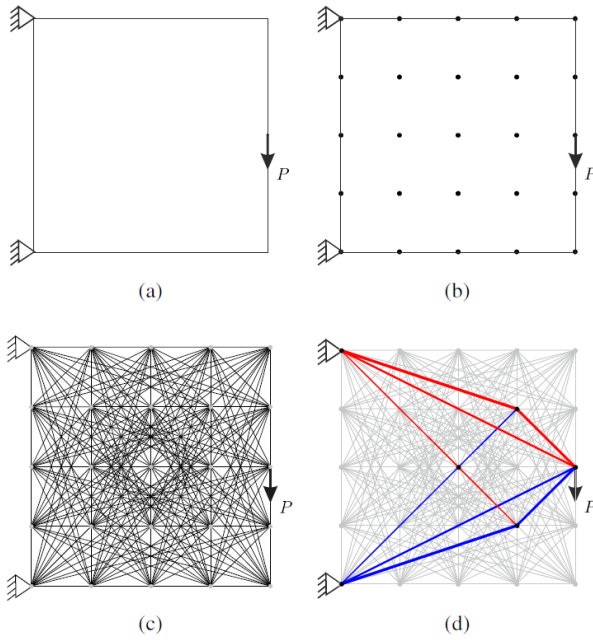


**Figure 1.6:** The TTO algorithm is divided into four principal steps: (a) specification of the design space, loads, and boundary conditions; (b) discretization of the design space; (c) the ground structure is generated depending on the desired connectivity level; (d) resolution of the optimization problem and plot of the solution [83].

minimize weight while satisfying structural constraints. The process is graphically presented in Fig. 1.6.

In the early works, the TTO problem was formulated in terms of member forces [37, 39] with plastic material modelization, ignoring the kinematic compatibility to obtain a LP problem. Formulated using the SAND approach, the equations of structural mechanics of the problem are imposed as constraints of the optimization and, contrary to NAND approaches, are not explicitly solved. Formulated that way, it is trivial to add maximum stress constraints compared to an equivalent NAND formulation. However, the SAND formulation with plastic material modelization only correctly predicts the mechanical behavior of statically determinate structures or mechanisms [84, 85]. Moreover, adding local buckling constraints to the optimization formulation is fundamental, as ultralight truss structures are often dominated by this mode of failure [72]. Multiple works in the field of truss structure optimization have focused on addressing these two crucial challenges [86–88].

**CLASSICAL MICHELL STRUCTURES** The characteristics of this class of truss structures are described by some simple criteria that date to the end of the 19th and the beginning of the 20th century. When a structure is statically determinate — i.e. the structure is not a mechanism, and it is not over-constrained by the supports — the Maxwell theorem [89] states that:

$$\sum_{\forall i | q_i > 0} \ell_i q_i + \sum_{\forall i | q_i < 0} \ell_i q_i = \text{const.} \quad (1.6)$$

where  $\ell_i$  and  $q_i$  represent the length and the axial force of the  $i$ -th member, respectively. The constant value at the right of Equation 1.6

- 37. Dorn et al. (1964), 'Automatic design of optimal structures'
- 39. Hemp (1973), 'Optimum Structures'

- 84. Kirsch (1989), 'Optimal topologies of truss structures'
- 85. Rozvany et al. (1995), 'Layout Optimization of Structures'
- 72. Sigmund et al. (2016), 'On the (non-)optimality of Michell structures'
- 86. Kirsch (1980), 'Optimal design of trusses by approximate compatibility'
- 87. Cheng (1995), 'Some aspects of truss topology optimization'
- 88. Achtziger (1999), 'Local stability of trusses in the context of topology optimization Part I'
- 89. Maxwell (1870), 'I.—On Reciprocal Figures, Frames, and Diagrams of Forces'

depends on the nature of the boundary conditions and the material used. The Maxwell theorem dictates that any increment in compression forces must be counterbalanced by an equivalent increase in tension forces when the structure remains topologically unchanged. So for statically determinate structures the structure layout is not influenced by the ratio between  $\sigma_c$  and  $\sigma_t$ , Young's modulus  $E$  of the material, nor the force magnitude.

[90.](#) Michell (1904), 'The limits of economy of material in frame-structures'

[39.](#) Hemp (1973), 'Optimum Structures'

[37.](#) Dorn et al. (1964), 'Automatic design of optimal structures'

[38.](#) Chan (1964), 'Optimum structural design and linear programming'

[39.](#) Hemp (1973), 'Optimum Structures'

The first use of the ground structure in structural optimization is by Dorn et al. [37]

Starting from Maxwell's findings, Michell theorized two further criteria for optimal truss structures [90] valid when the maximum allowable stress is equal in tension and compression ( $\sigma_t = \sigma_c$ ) and when the supports of the structure are statically determinate. The first one states that all the members of an optimal structure should present internal stress equal in magnitude to the maximum allowable value of the material – i.e. the structure is *fully stressed*. The second criterion asserts that the strain of all the members of the structure should be equal and there should be no other point having a strain higher than this value. As formulated, these two criteria are known as the Michell criteria. The second criterion was later generalized by Hemp [39] as:

$$-\frac{1}{\sigma_c} \leq \varepsilon \leq \frac{1}{\sigma_t}. \quad (1.7)$$

Compared to the second Michell criterion, Equation 1.7 permits the correct identification of the minimum volume structure even when different strength values for compression and tension and different support types are taken. These criteria are known as the Michell-Hemp criteria.

**PLASTIC MATERIAL FORMULATION** The rigid-plastic formulation characterizes the material as entirely rigid up to the point of reaching the yield stress, denoted as  $\sigma_y$ , and subsequently assumes a constant stress level of  $\sigma_y$  once that threshold is exceeded. This formulation is a clear consequence of the application of the Michell-Hemp criteria and has thus been used in the very first work of TTO [37–39].

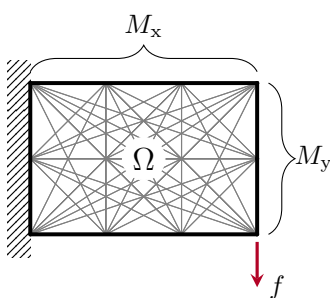


**Figure 1.7:** The domain  $\Omega$  is discretized using a set of straight members connecting a set of nodes. This framework is known as the ground structure.

**THE GROUND STRUCTURE APPROACH** The ground structure is a framework composed of various structural members that connect specified points or nodes in two- or three-dimensional space (see Fig. 1.7). These members can take the form of beams, columns, wires, or bar elements, depending on the specific structural requirements, but the most used is historically the bar element. Since the nodes within the ground structure are considered pin-joints, all straight members exclusively face either tension or compression loads.

Depending on how the connectivity of the grid of nodes is, we can experience very different ground structures. In a fully connected ground structure, every node within the system is linked to every other

node, resulting in a dense and redundant structural configuration. The number of bars  $N_{\text{el}}$  of a fully connected ground structure can be determined using the following formula:

$$N_{\text{el}} = \frac{M \cdot (M - 1)}{2}, \quad (1.8)$$

where  $M$  represents the number of nodes of the structure.

In classic works, the ground structure is used as the start of the optimization, where the optimized structure is obtained as a subset of the initial ground structure, but multiple alternative approaches have been proposed since then, e.g. starting from a very coarse ground structure that is enriched during the analysis [91], or giving the nodes of a coarse ground structure the possibility to move, during [92–94], or after the optimization, simultaneously reducing the number of active members of the solution [95, 96]. Recently, a hybrid method based on the projection of explicitly defined components on a discrete ground structure has been proposed, easing the interpretation of the stiffening pattern of the optimized truss [97].

**OPTIMIZATION FORMULATION** The volume minimization formulation with maximum stress constraints is stated in terms of members' cross-sectional areas  $\alpha$  and member forces  $q$  as follows:

$$\begin{aligned} \min_{\alpha, q} \quad & V = \ell^T \alpha \quad (\text{Volume minimization}) \\ \text{s.t.} \quad & Bq = f \quad (g_{\text{eq}}) \\ & -\sigma_c \alpha \leq q \leq \sigma_t \alpha \quad (g_{\text{st,c}}, g_{\text{st,t}}) \\ & \alpha \geq 0, \end{aligned} \quad (\mathbb{P}_0)$$

where  $B$  is a  $N_{\text{dof}} \times N_{\text{el}}$  matrix containing the direction cosines of the  $i$ -th member with respect to the  $i$ -th degree of freedom to calculate the nodal force equilibrium constraints  $g_{\text{eq}}$ , and where  $N_{\text{dof}}$  is the number of Degrees Of Freedom (DOFs), equal to  $2M$  or  $3M$  for a two- or a three-dimensional load case, respectively.  $q = [q_1, q_2, \dots, q_{N_{\text{el}}}]^T$  is the vector containing the internal member forces, with a positive sign when in tension, caused by the external load  $f = [f_1, f_2, \dots, f_{N_{\text{dof}}}]^T$ . The state variable  $\alpha = [\alpha_1, \alpha_2, \dots, \alpha_{N_{\text{el}}}]^T$  represents the cross-sectional area of the  $N_{\text{el}}$  members of the structure.  $\sigma_c$  and  $\sigma_t$  are the compressive and tensile maximum allowable stresses of the material, respectively, used in the stress constraints  $g_{\text{st,c}}$  and  $g_{\text{st,t}}$ . This formulation takes into account only the linear behavior of the structure and is equivalent to the original and well-studied member force formulation [7, 37]. As such,  $\mathbb{P}_0$  is a linear (and thus convex) formulation that can be efficiently solved using LP optimization algorithms.

The resolution of Problem  $\mathbb{P}_0$  frequently produces complex structures made up of a multitude of small members that tend to the shapes of

91. Gilbert et al. (2003), 'Layout optimization of large-scale pin-jointed frames'

92. Pedersen (1973), 'Optimal Joint Positions for Space Trusses'

93. Achtziger (2007), 'On simultaneous optimization of truss geometry and topology'

94. Descamps et al. (2013), 'A lower-bound formulation for the geometry and topology optimization of truss structures under multiple loading'

95. He et al. (2015), 'Rationalization of trusses generated via layout optimization'

96. Lu et al. (2023), 'Reducing the number of different members in truss layout optimization'

97. Savine et al. (2021), 'A component-based method for the optimization of stiffener layout on large cylindrical rib-stiffened shell structures'

7. Bendsøe et al. (2004), 'Topology Optimization'

37. Dorn et al. (1964), 'Automatic design of optimal structures'

90. Michell (1904), 'The limits of economy of material in frame-structures'

98. Parkes (1975), 'Joints in optimum frameworks'

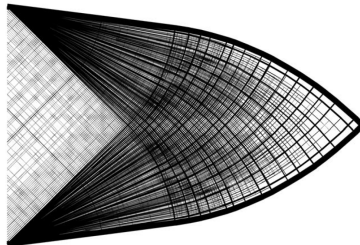


**Figure 1.8:** The optimal structures found by TTO tend at Michell-like structures, made up of a very large number of infinitesimal struts [91].

99. Schaedler et al. (2016), 'Architected Cellular Materials'

100. Kohn et al. (1986), 'Optimal design and relaxation of variational problems'

101. Allaire et al. (1999), 'On optimal microstructures for a plane shape optimization problem'

102. Fleck et al. (2010), 'Microarchitected materials'

2: The HS bounds are the tightest bounds possible from the range of composite moduli for a two-phase isotropic mixture. In lattices, usually, the second material is void.

107. Dai et al. (2008), 'Size effects of basic cell in static analysis of sandwich beams'

108. Kalamkarov et al. (2009), 'Asymptotic Homogenization of Composite Materials and Structures'

109. Coelho et al. (2016), 'Scale-size effects analysis of optimal periodic material microstructures designed by the inverse homogenization method'

110. Zhang et al. (2018), 'Multiscale concurrent topology optimization for cellular structures with multiple microstructures based on ordered SIMP interpolation'

Michell structures (see Fig 1.8) [90]. While it is known that these structures are nearly optimal, one would want to limit the complexity of the resulting structure. Substituting  $\ell$  with  $\tilde{\ell} = [\ell_1 + s, \ell_2 + s, \dots, \ell_{Nel} + s]^T$  in the objective function of  $\mathbb{P}_0$ , one would penalize the appearance of small members [98].  $\tilde{\ell}$  is called augmented member length and  $s$  the joint cost. This approach mimics the mesh-independency regularization filter of topology optimization, avoiding the inevitable apparition of structures with tiny features when a fine mesh is adopted.

### 1.3 MODULAR STRUCTURES AND CELLULAR MATERIALS

Historically, material properties were modified by manipulating chemical composition, microstructure, and production processes [99]. Another possible way to enhance material properties involves tailoring the spatial arrangement of solids and voids within the material. Referred to as architected (or lattice) materials, this concept has gained significant traction in research, particularly with recent advancements in additive manufacturing. These materials, often observed in natural structures like bone microstructures or birds' beaks (refer to Fig. 1.9 for additional examples), have garnered interest due to the recognition that optimal structures exhibit stiffness across multiple scales [100, 101]. Additionally, Fleck et al. noted [102] that one reason for structural hierarchy in engineering is to augment buckling strength. Local buckling strength scales with the strut length  $\ell$  following  $\ell^{-2}$ , indicating that finer length scales contribute to higher buckling strength.

If we observe the Ashby material chart shown in Fig. 1.10, where the material yield strength  $\sigma_Y$  is plotted against density  $\rho$ , it becomes evident that numerous empty spaces exist. Besides some unattainable areas delineated by the HS bounds<sup>2</sup>, these empty spaces can be filled by lattice materials, extending the property space of actual materials.

Up to this point, we discussed materials, implicitly assuming that the bounding volume in which we find the arrangement of solids and voids, called Representative Volume Element (RVE), is small compared to the macrostructure. However, it is possible to differentiate between a lattice material and a lattice structure exactly based on the size of the RVE with respect to the considered structure. In a modular lattice structure, there is no clear physical scale separation between the RVE and the structure, indicating that the RVE mechanical characteristics are manifested at both the micro and macro scales. However, defining a specific threshold to distinctly categorize the two is challenging, as the transition from lattice material to lattice structure can be gradual and context-dependent [107–110].

Lattices can be categorized as open- or closed-wall based on the topology they show. Despite the use of closed-wall lattices potentially

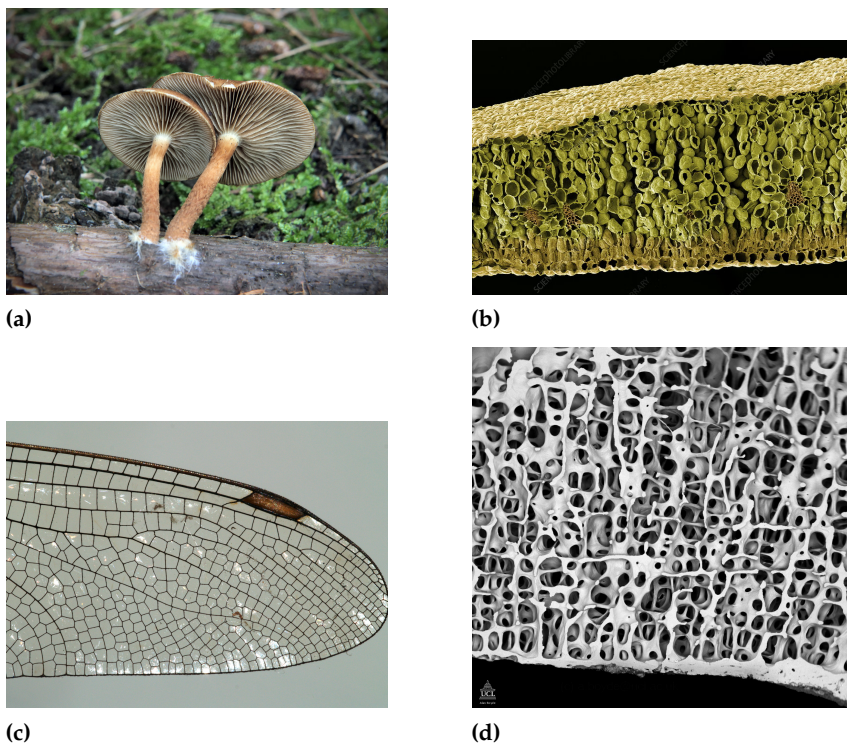


**Figure 1.9:** The natural evolution process frequently generates lattice materials and modular structures; (a) The spore-bearing gills of a *Hypholoma fasciculare* [103], (b) SEM image of a leaf microstructure [104], (c) architected material of the wing of a dragonfly [105], (d) internal structure of a human bone [106].

resulting in stiffer structures, the preference for open-cell configurations is well-articulated by Sigmund *et al.* [72]. They emphasize that the outcome of minimum compliance topology optimization studies should inherently be of sheet type when using density methods unless explicit constraints favoring open-wall structures are specified. These constraints include considerations of structural and microstructural stability, as the load required to initiate buckling in a slender strut of an open-cell lattice is significantly higher than that of a comparable closed-cell lattice [111]. Consequently, open-cell structures are less prone to buckling. Additionally, the porosity of open-wall cells allows for the passage of flow, making them suitable for applications such as heat exchangers or promoting bone regrowth in biomedical scaffolds. From a manufacturing perspective, open-cell designs are preferable, as very thin walls are challenging to manufacture. The transparency inherent in open-cell structures is advantageous for tasks such as repair and health monitoring. Finally, an open-cell design is considered elegant and aesthetic, as it embodies Michell-like structures, which are described as "inarguably beautiful" and "look elegant and efficient" by Sigmund *et al.* [72].

72. Sigmund et al. (2016), 'On the (non-)optimality of Michell structures'

111. Deshpande et al. (2001), 'Foam topology'

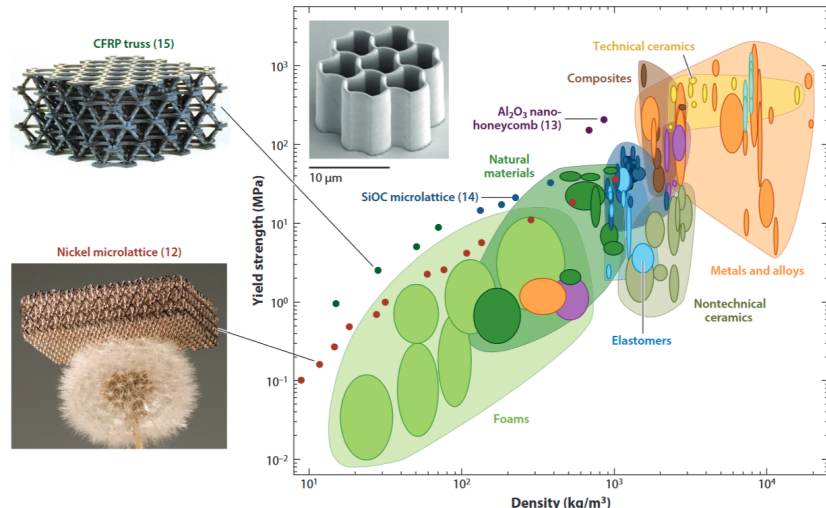


**Figure 1.10:** Density versus yield strength Ashby chart. Exploiting the architecture of the material as a variable to design new metamaterials, empty spaces of the graph can be filled (see dots) [99].

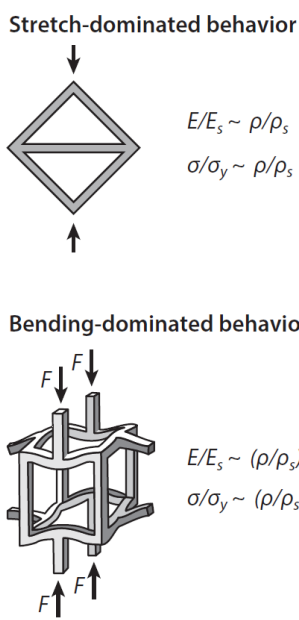


**Figure 1.11:** A stretch-dominated and a bending-dominated RVE. Bending-dominated cells act as a mechanism if the joints cannot withstand moments. The scaling laws are different for the two structural families [99].

112. Ashby (2006), 'The properties of foams and lattices'

113. Evans et al. (2010), 'Concepts for Enhanced Energy Absorption Using Hollow Micro-Lattices'

114. Schaedler et al. (2014), 'Designing Metallic Microlattices for Energy Absorber Applications'

115. Ozdemir et al. (2016), 'Energy absorption in lattice structures in dynamics'

Lattices are further categorized into stretching- and bending-dominated based on the failure mode they show when loaded. A stretching-dominated lattice is characterized as a lattice in which its constitutive struts exclusively experience tension and compression loads. In such a structure, the nodal stiffness does not contribute to the overall structural stiffness, and the truss undergoes collapse primarily through the stretching of its struts. Deshpande *et al.* [111] noted that freezing the joints of a stretching-dominated truss has minimal impact on its macroscopic stiffness or strength. Despite the bending of the struts, the frame remains stretching-dominated, and the collapse load is predominantly determined by the axial strength of the struts. Consequently, if an open-cell lattice is stretching-dominated, it can effectively be treated as a connected set of pin-jointed struts.

The relative density of the lattice is defined as:

$$\bar{\rho} = \frac{\rho_l}{\rho} \quad (1.9)$$

where  $\rho_l$  and  $\rho$  represent the density of the lattice and the dense material, respectively [112]. A stretching-dominated lattice exhibits approximately 10 times greater stiffness and 3 times greater strength than a bending-dominated lattice at  $\bar{\rho} = 0.1$ , as illustrated in Figure 1.11. Nevertheless, when subjected to compression, stretching-dominated lattices display a softening post-yield response attributed to the buckling of struts, rendering them less suitable for energy absorption tasks. In contrast, bending-dominated lattices showcase a more favorable energy-absorbing behavior, characterized by a plateau-like response. Bending-dominated lattices are often named foams [112].

Lattice structures and materials exhibit a wide range of promising applications. They showcase notable energy-absorbing properties, particularly when designed as being bending-dominated [113–115]. This quality positions lattices as potential candidates for novel design

schemes in aerodynamics, thanks to their remarkable aeroelastic properties [116, 117]. Additionally, lattices have proven to be compelling choices for constructing biomedical scaffolds, promoting bone ingrowth [118–120]. Furthermore, lattice materials demonstrate excellent heat exchanger properties, attributed to their high surface-to-volume ratio and the turbulent mixing flow they induce when a fluid passes through [121, 122].

An interesting class of architected materials is represented by modular lattices, alternatively referred to in the literature as cellular architected materials. The defining feature of lattice materials is to exhibit a repetitive cell (also called module when dealing with lattice structures and not materials) that is replicated throughout space. This characteristic allows for the establishment of a systematic and reproducible unit that captures the essential structural and material properties of the lattice. The study of the repetitive nature of the RVE i.e., the part of the structural domain that is populated with a cell, permits a comprehensive understanding of the cellular lattice's behavior, enabling researchers to analyze and predict its mechanical, thermal, and other pertinent properties with a high degree of accuracy [124].

Modular structures show additional captivating properties that demonstrate their versatility. Firstly, modular structures can be purposefully designed for reversible assembly, introducing the concept of rapid assembly and easily repairable structures (see Fig. 1.13). Various approaches, such as utilizing fasteners [5, 117, 125], or incorporating snap-fit joints [126], have been proposed to realize this idea. Furthermore, modular structures inherently exhibit damage tolerance [127, 128] e.g., in a skin-lattice design, the skin is non-load-bearing, ensuring that skin damage does not lead to progressive structural failure. Additionally, in cases of rib damage, the affected rib can be isolated from the load without compromising the integrity of the entire structure (refer to Fig. 1.12). Lastly, modular structures pave the way for extensive utilization of robotics in both the manufacturing [129] and assembly phases [6, 130–132].

There is no consensus on the terminology of lattice materials and

116. Opgenoord et al. (2018), 'Aeroelastic Tailoring using Additively Manufactured Lattice Structures'

117. Cramer et al. (2019), 'Elastic shape morphing of ultralight structures by programmable assembly'

118. Hutmacher (2000), 'Scaffolds in tissue engineering bone and cartilage'

119. Mota et al. (2015), 'Additive manufacturing techniques for the production of tissue engineering constructs'

120. Nikolova et al. (2019), 'Recent advances in biomaterials for 3D scaffolds'

121. Lu et al. (1998), 'Heat transfer in open-cell metal foams'

122. Wadley et al. (2007), 'Thermal Applications of Cellular Lattice Structures'



**Figure 1.12:** Vickers Wellingtons, bombers utilized during World War II, remained operational despite sustaining extensive damage, thanks to their modular fuselage. When one of the ribs was damaged, the load was redistributed to the others, allowing the structure to remain functional [123].

124. Bensoussan et al. (1978), 'Asymptotic analysis for periodic structures'



**Figure 1.13:** The different length scales present in a lattice structure [117]. The size of the module (shown in subfigure A) is comparable with the dimensions of the wing, especially in the thickness. We therefore talk about lattice structure and not material.

**Table 1.1:** Vocabulary used in this document to write about lattice materials and modular structures. The adjectives architected and lattice are the only one that are used for both materials and structures.

Description	Material (Scale separation)	Structure (No scale separation)
Whole domain	Macrostructure	Structure
Properties are dictated by the spacial arrangement of voids and solids	Lattice, architected	Lattice, architected
Properties are dictated by the stochastic spacial arrangement of voids and solids	Cellular	Modular
Repetitive entity	Cell, microstructure	Module
Part of the domain where the repetitive entity is placed	RVE	Subdomain

- 5. Cheung et al. (2013), 'Reversibly Assembled Cellular Composite Materials'
- 117. Cramer et al. (2019), 'Elastic shape morphing of ultralight structures by programmable assembly'
- 125. Jenett et al. (2017), 'Digital Morphing Wing: Active Wing Shaping Concept Using Composite Lattice-Based Cellular Structures'
- 126. Dong et al. (2015), 'Mechanical response of Ti-6Al-4V octet-truss lattice structures'
- 127. Stolpe (2019), 'Fail-safe truss topology optimization'
- 128. Wu et al. (2021), 'Topology optimization of multi-scale structures'
- 129. Hunt et al. (2019), 'WrapToR composite truss structures'
- 6. Costa et al. (2020), 'Algorithmic Approaches to Reconfigurable Assembly Systems'
- 130. Gershenfeld et al. (2015), 'Macro-fabrication with Digital Materials'
- 131. Jenett et al. (2017), 'BILL-E: Robotic Platform for Locomotion and Manipulation of Lightweight Space Structures'
- 132. Niehs et al. (2020), 'Recognition and Reconfiguration of Lattice-Based Cellular Structures by Simple Robots'
- 133. Opgenoord (2018), 'Transonic Flutter Prediction and Aeroelastic Tailoring for Next-Generation Transport Aircraft'
- 134. Park et al. (2022), 'Design Optimization of Lattice Structures under Compression'

structures, leading to confusion with multiple names in the literature. Some define a "cellular structure" as one comprising nodes and struts connecting those nodes, where all struts may have different cross-sectional areas [133, 134]. When a cellular structure exhibits a repeating pattern, it is referred to as a "lattice structure". Conversely, others use "cellular" and "lattice" interchangeably when discussing materials and structures that shows a stretch dominated behaviour [111, 112]. In such cases, the opposite of a lattice material is often termed a "foam" i.e. a bending-dominated architected material [111]. Additionally, there is often ambiguity between the terms "material" and "structure," despite their distinct concepts. For example, many works describe lattice structures as RVEs with homogenized mechanical properties [135, 136].

To address these issues, we opted to establish clarity by using different terminology depending on whether we are discussing materials (with scale separation) or structures (without scale separation). This approach helps to eliminate any confusion in this thesis. The chosen terminology is presented in Table 1.1.

### 1.3.1 MODULAR STRUCTURES AND CELLULAR MATERIALS OPTIMIZATION

The initial density-based topology optimization method, as seen in Bendsøe and Kikuchi's foundational work [11], employed numerical homogenization to model a meta-material consisting of infinitesimally small square cells with square holes. Notably, this marked the advent of multi-scale optimization, driven by the observation that optimal stiffness for a structure encompasses various scales [100, 101].

In the 1990s, the focus shifted from homogenization algorithms to mono-scale algorithms, where the optimization involved a homogeneous distribution of an isotropic material [41, 137]. This shift was primarily caused by the manufacturing challenges associated with producing multi-scale meta-materials. Subsequently, these approaches evolved into what is now known as density-based topol-

ogy optimization. Mono-scale methods, where the design domain discretization results in structures at a single scale, can achieve theoretical stiffness-optimal structures spanning multiple scales with fine mesh discretization and careful continuation techniques. Bendsøe and Kikuchi's original work and homogenization-based algorithms have gained recently more interest due to the advances in additive manufacturing technologies. Contemporary studies are combining asymptotic homogenization and topology optimization to optimize multi-scale structures.

Modular structures and cellular materials are optimized through either a multi-scale or a full-scale approach. Multi-scale algorithms operate on structures with different physical scales between the micro- and macro-levels, assuming periodic boundary conditions for the RVE. Doing that allows for the use of a material model with micro-structure properties evaluated using asymptotic homogenization. In contrast, full-scale methods represent mono-scale approaches where modular optimization is achieved by controlling the layout locally. In these full-scale approaches, both analysis and optimization are conducted at the full resolution of the domain. For a more in-depth exploration and comparison of full-scale and multi-scale approaches, interested readers can refer to the comprehensive review by Wu *et al.* [128].

### 1.3.2 MULTI-SCALE STRUCTURES OPTIMIZATION

Optimal structures span multiple scales, and using a finer mesh allows for detailed geometric improvements, potentially enhancing optimized structures. However, higher-resolution mono-scale approaches come with increased computational costs. To tackle this, multi-scale approaches like the hierarchical method by Rodrigues *et al.* [138] and de-homogenization techniques [139, 140] have been introduced.

The hierarchical optimization framework consists of a master problem addressing the global spatial distribution of material and an inner problem tackling the optimal choice of material at the local level. This approach shifts the focus from a specific composite's material distribution problem to a more comprehensive challenge involving both topology and material optimal design. The idea is to use the homogenized microscale cell as the base material of the macroscale topology optimization. Fig. 1.14 gives a graphical representation of how asymptotic homogenization works. The equivalent elastic tensor  $\mathbf{C}^H$  is calculated using the following formula [142]:

$$\mathbf{C}^H = \frac{1}{|\Omega_m|} \int_{\Omega_m} (\varepsilon_m^0 - \varepsilon_m) \mathbf{C} (\varepsilon_m^0 - \varepsilon_m) d\Omega_m \quad (1.10)$$

where  $\Omega_m$  represents the RVE volume,  $\mathbf{C}$  is the base material elastic tensor and  $\varepsilon_m^0$  are called unit test strain and are defined as  $\varepsilon^{11} =$

- 111. Deshpande et al. (2001), 'Foam topology'
- 112. Ashby (2006), 'The properties of foams and lattices'
- 135. Xu et al. (2016), 'Design of lattice structures with controlled anisotropy'
- 136. Song et al. (2021), 'Investigation on the modelling approach for variable-density lattice structures fabricated using selective laser melting'
- 11. Bendsøe et al. (1988), 'Generating optimal topologies in structural design using a homogenization method'
- 100. Kohn et al. (1986), 'Optimal design and relaxation of variational problems'
- 101. Allaire et al. (1999), 'On optimal microstructures for a plane shape optimization problem'
- 41. Bendsøe (1989), 'Optimal shape design as a material distribution problem'
- 137. Zhou et al. (1991), 'The COC algorithm, Part II'
- 128. Wu et al. (2021), 'Topology optimization of multi-scale structures'
- 138. Rodrigues et al. (2002), 'Hierarchical optimization of material and structure'
- 139. Pantz et al. (2008), 'A Post-Treatment of the Homogenization Method for Shape Optimization'
- 140. Groen et al. (2018), 'Homogenization-based topology optimization for high-resolution manufacturable microstructures'
- 142. Guedes et al. (1990), 'Preprocessing and postprocessing for materials based on the homogenization method with adaptive finite element methods'

**Figure 1.14:** Graphical representation of the asymptotic homogenization method used to retrieve the equivalent mechanical properties of a periodic cell [141].

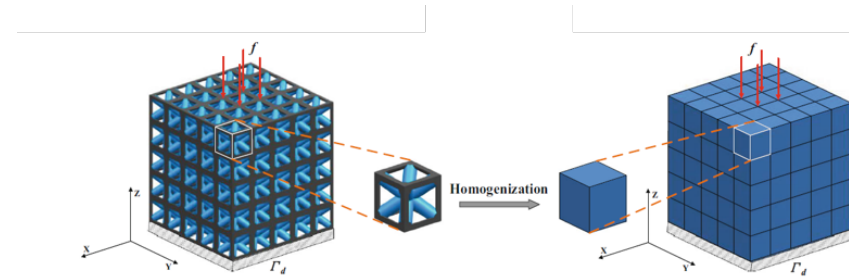
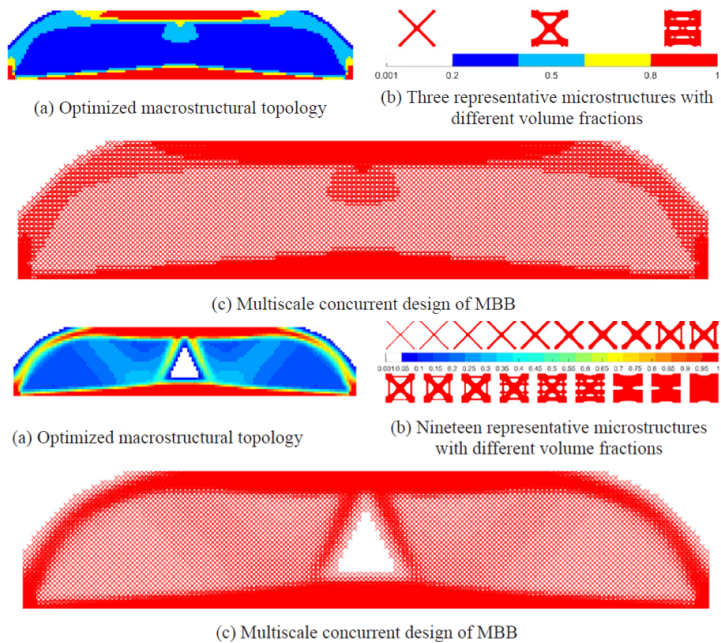


**Figure 1.15:** In the study of Zhang et al. [110] the same test case is optimized using a hierarchical optimization method and a different number of microstructures. Here we show the multi-scale optimized structures using 3 and 19 different microstructures. The structure with 19 microstructures is 10 % stiffer compared to the one with 3.



$(1, 0, 0)^T, \varepsilon^{22} = (0, 1, 0)^T, \varepsilon^{12} = (0, 0, 1)^T$ . An example of the results obtained using a hierarchical method is presented in Fig. 1.15.

- 140. Groen et al. (2018), 'Homogenization-based topology optimization for high-resolution manufacturable microstructures'
- 143. Allaire et al. (2019), 'Topology optimization of modulated and oriented periodic microstructures by the homogenization method'
- 144. Geoffroy-Donders et al. (2020), '3-d topology optimization of modulated and oriented periodic microstructures by the homogenization method'
- 145. Kumar et al. (2020), 'A density-and-strain-based K-clustering approach to microstructural topology optimization'
- 146. Xia et al. (2015), 'Multiscale structural topology optimization with an approximate constitutive model for local material microstructure'

De-homogenization is an approach where the optimization problem is initially solved solely on the macroscopic level using a homogenization method. Subsequently, an additional phase is introduced to obtain connected and physically realizable microstructures based on the obtained macroscopic result. In the macroscale optimization, multiple additional parameters are typically optimized concurrently with the density of the RVE. These parameters may include microstructure orientation, contributing to the creation of a smooth mapping function [140, 143–145]. An alternative approach involves approximating the material behavior through a reduced database model, as demonstrated by Xia and Breitkopf [146]. In this method, microstructural computations are performed offline, only once, to reduce the computational time of successive optimizations. Precomputed databases are often employed to obtain the full design for the parametrized lattice RVE, often using a polynomial model to interpolate between the database microstructures [147–149]. Recent approaches are now using Artificial Intelligence (AI) and deep learning to speed up the de-homogenization phase [150–153].

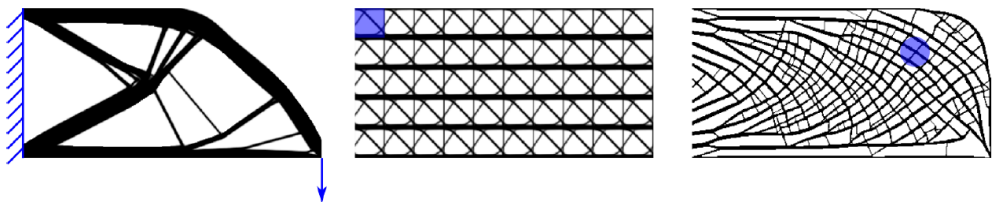


**Figure 1.16:** Three structures with the same volume are optimized for compliance minimization using three different methods: on the left, a classic mono-scale topology optimization algorithm. Middle: the variable linking method is used to enforce the pattern repetition on the structure. On the right an optimized structure with local volume constraints. The algorithms used to optimize the last two structures belong to the family of *full-scale* methods. [128].

In conclusion, despite maintaining the separation of the two physical scales during the optimization process, it is imperative to conduct a full-scale validation for all multi-scale methods, as highlighted in various studies [128, 140, 149, 154]. Additionally, the multi-scale optimization approaches in which the microstructure is aligned to local stress fields without constraints imposed by cell geometry or orientation [140], deliver good performance even for structures with less periodicity compared to a bulk distribution.

### 1.3.3 FULL-SCALE STRUCTURES OPTIMIZATION

Recent studies have focused on assessing homogenization predictions compared to mechanical responses, revealing up to a 20 % variation in the effective components of the stiffness tensor for a  $6 \times 6 \times 6$  cube when compared to homogenized models [109, 155]. This variability is attributed to the "boundary layer phenomenon" observed in the late 70s, challenging the assumptions of periodic boundary conditions and scale separability inherent in homogenization [108, 124]. To address these limitations, a new family of methodologies, known as full-scale approaches, has emerged. Unlike homogenization-based methods, full-scale approaches, such as pattern repetition (also known as variable linking) and local volume constraints, avoid reliance on homogenization. In pattern repetition, the initial design space is partitioned into repetitive domains that are optimized and constrained to ensure their uniformity [43]. In contrast, the local volume constraints method imposes an upper limit on the solid elements' fraction in a neighborhood radius centered at each point within the design domain. The objective is to generate porous structures aligned with principal stress directions. While experiencing a modest stiffness reduction compared to mono-scale designs, these structures demonstrate heightened resilience against variations in load angle, local material failure, and buckling [156].

Variable linking approach faces a common limitation, leading to compromised structural performance due to topological periodicity [43, 157]. This limitation arises as the design converges toward solutions influenced by the region with the highest compliance, resulting in suboptimal solutions for other regions where the same module de-

147. Wang et al. (2018), 'Concurrent topology optimization design of structures and non-uniform parameterized lattice microstructures'

148. Imediegwu et al. (2019), 'Multiscale structural optimization towards three-dimensional printable structures'

149. Duriez et al. (2021), 'A well connected, locally-oriented and efficient multi-scale topology optimization (EMTO) strategy'

150. Kim et al. (2021), 'Machine learning-combined topology optimization for functionary graded composite structure design'

151. White et al. (2019), 'Multiscale topology optimization using neural network surrogate models'

152. Chandrasekhar et al. (2021), 'Multi-Material Topology Optimization Using Neural Networks'

153. Wang et al. (2021), 'Enhancing Data-driven Multiscale Topology Optimization with Generalized Dehomogenization'

128. Wu et al. (2021), 'Topology optimization of multi-scale structures'

140. Groen et al. (2018), 'Homogenization-based topology optimization for high-resolution manufacturable microstructures'

149. Duriez et al. (2021), 'A well connected, locally-oriented and efficient multi-scale topology optimization (EMTO) strategy'

154. Sigmund (2022), 'On benchmarking and good scientific practise in topology optimization'

- 109.** Coelho et al. (2016), 'Scale-size effects analysis of optimal periodic material microstructures designed by the inverse homogenization method'
- 155.** Cheng et al. (2019), 'Functionally graded lattice structure topology optimization for the design of additive manufactured components with stress constraints'
- 108.** Kalamkarov et al. (2009), 'Asymptotic Homogenization of Composite Materials and Structures'
- 124.** Bensoussan et al. (1978), 'Asymptotic analysis for periodic structures'
- 43.** Zhang et al. (2006), 'Scale-related topology optimization of cellular materials and structures'
- 156.** Wu et al. (2018), 'Infill Optimization for Additive Manufacturing—Approaching Bone-Like Porous Structures'
- 43.** Zhang et al. (2006), 'Scale-related topology optimization of cellular materials and structures'
- 157.** Huang et al. (2008), 'Optimal design of periodic structures using evolutionary topology optimization'
- 158.** Tugilimana et al. (2019), 'An integrated design methodology for modular trusses including dynamic grouping, module spatial orientation, and topology optimization'
- 159.** Bakker et al. (2021), 'Simultaneous optimization of topology and layout of modular stiffeners on shells and plates'
- 160.** Tugilimana et al. (2017), 'Spatial orientation and topology optimization of modular trusses'
- 158.** Tugilimana et al. (2019), 'An integrated design methodology for modular trusses including dynamic grouping, module spatial orientation, and topology optimization'
- 161.** Liu et al. (2023), 'Layout optimization of truss structures with modular constraints'
- 162.** Stromberg et al. (2011), 'Application of layout and topology optimization using pattern gradation for the conceptual design of buildings'
- 163.** Wu et al. (2016), 'A System for High-Resolution Topology Optimization'
- sign is applied [158]. To address this, Bakker [159] identified two key approaches. The first involves extending the solution space by introducing additional module properties as design variables. For instance, allowing module rotations has proven effective, as it modifies the local material distribution and enhances structural performance [160]. Another possibility would be the use of multiple modules, permitting the subdomains to show a topology tailored to their loading condition [158, 161]. The second approach involves allowing the module unit to resize, providing flexibility in adapting to different regions within the global domain [162, 163]. These strategies offer ways to overcome the challenges associated with topological periodicity and achieve more optimized solutions for diverse regions within the structure.

# EVALUATING DISCRETIZATION APPROACHES FOR ULTRALIGHT STRUCTURE OPTIMIZATION

## 2

The process of topology optimization for a structure involves the selection and sizing of optimal elements within a predetermined set. As discussed in the previous chapter, in our context this set could be composed of either continuum elements (shell or volumetric) or truss-like elements. Based on the discretization choice we distinguish between density-based topology optimization and Truss Topology Optimization (TTO). This chapter aims to assess the suitability and the inherent advantages and disadvantages of both methods when optimizing ultralight structures i.e. structures that exhibit a low volume fraction, typically below 5%.

For this purpose, we initially formulate a volume minimization problem subject to maximum stress constraints for both discretizations in Section 2.1. Later, a two-dimensional test case, featuring identical dimensions, loads, and material properties is optimized using the density-based topology optimization and the TTO algorithms. The outcomes of the comparison of both optimization approaches are presented and discussed in Section 2.2.

### 2.1 THE FORMULATION OF A SHARED PROBLEM: VOLUME MINIMIZATION WITH STRESS CONSTRAINTS

Instead of focusing on the commonly used compliance minimization formulation in density-based topology optimization, our emphasis on the aerospace sector leans towards the volume minimization problem. Prioritizing volume minimization, directly linked to the more crucial mass minimization objective, is driven by economic, environmental, and performance considerations within the aerospace industry. This strategic approach supports industry goals of sustainability, efficiency, and technological advancement. Therefore, we have chosen to adopt the volume minimization optimization formulation for our study, and we will now implement it on both continuum and truss-like meshes.

#### 2.1.1 DENSITY-BASED TOPOLOGY OPTIMIZATION MINIMUM VOLUME FORMULATION

This section introduces the Nested Analysis and Design (NAND) volume minimization formulation for topology optimization on continuum meshes. We will begin by explaining important notations and concepts that are essential for developing the volume minimization formulation.

2.1 THE FORMULATION OF A SHARED PROBLEM: VOLUME MINIMIZATION WITH STRESS CONSTRAINTS . . . . .	29
2.2 COMPARISON BETWEEN DENSITY-BASED TOPOLOGY OPTIMIZATION AND TTO . . . . .	38
2.3 CONCLUSION . . . . .	49

Part of the content presented in this chapter has been published and showcased during a conference as: Stragiotti, E. et al. (2021) "Towards manufactured lattice structures: a comparison between layout and topology optimization", in *AeroBest 2021 International Conference on Multidisciplinary Design Optimization of Aerospace Systems*. Book of proceedings. Lisbon, Portugal: ECCOMAS [164].

**OBJECTIVE AND CONSTRAINT FUNCTIONS** The goal of the optimization is to minimize the volume fraction occupied by a structure under a specified load case. In this thesis, as we deal with two- and three-dimensional structures, we should differentiate between area and volume, but for the sake of generality, we talk about volume. The volume fraction of the structure, denoted as  $V_f$ , is expressed as the ratio between the structural volume  $V = \sum_{i \in \Omega} \bar{\rho}_i v_i$  and the total volume  $V_0$  of the domain  $\Omega$ :

$$V_f = \frac{V}{V_0} = \frac{1}{V_0} \sum_{i \in \Omega} \bar{\rho}_i v_i. \quad (2.1)$$

We assume that the elementary volume  $v_i$  occupied by the  $i$ -th element is equal for all the elements, and thus Equation 2.1 is simplified as follows:

$$V_f = \frac{1}{N_e} \sum_{i \in \Omega} \bar{\rho}_i. \quad (2.2)$$

The normalized local stress constraint  $g_{st}$  is formulated as:

$$g_{st} := \frac{\sigma_{VM,i}}{\sigma_L} - 1 \leq 0, \quad \forall i \in \Omega_{mat}(\rho) \quad (2.3)$$

where  $\Omega_{mat}(\rho) \subseteq \Omega$  represents the design-dependent set of elements with a non-zero density i.e., stress constraints are defined only for the active elements,  $\sigma_{VM,i}$  is the equivalent Von Mises stress for the  $i$ -th element, and  $\sigma_L$  is the maximum allowable of the material.

165. Achtziger et al. (2008), 'Mathematical programs with vanishing constraints'

166. Cheng et al. (1992), 'Study on Topology Optimization with Stress Constraints'

The first difficulty that arises using this formulation is that the stress constraints are defined only for the elements where  $\bar{\rho}_i > 0$ , while  $\bar{\rho}_i \in [0, 1]$ . Thus, the set of constraints changes during the optimization. This class of problems is called Mathematical Programs with Vanishing Constraints (MPVCs) [165] and is known for being difficult to solve with a gradient descent optimization algorithm. The original set of constraints  $g_{st}$  is then reformulated into an equivalent design-independent set of constraints  $\bar{g}$  as follows [166]:

$$\bar{g} := \bar{\rho}_i \left( \frac{\sigma_{VM,i}}{\sigma_L} - 1 \right) \leq 0, \quad \forall i \in \Omega. \quad (2.4)$$

**VON MISES STRESS EVALUATION** The evaluation of the equivalent stress of a two-dimensional element follows the formulation proposed by Von Mises. Let us take a four-node quadrilateral linear element with a single integration (or Gauss) point in the center and four  $2a$  equal-length sides (see Fig. 2.1). If bilinear shape functions are used to interpolate the displacement field, we can evaluate the deformations

at the integration point as:

$$\begin{pmatrix} \varepsilon_x \\ \varepsilon_y \\ \gamma_{xy} \end{pmatrix} = \mathbf{B}_s \mathbf{q}_s, \text{ with } \mathbf{B}_s = \frac{1}{4a} \begin{pmatrix} -1 & 1 & 1 & -1 & 0 & 0 & 0 & 0 \\ 0 & 0 & 0 & 0 & -1 & -1 & 1 & 1 \\ -1 & -1 & 1 & 1 & -1 & 1 & 1 & -1 \end{pmatrix}, \quad (2.5)$$

where  $\mathbf{q}_s = (u_1, u_2, u_3, u_4, v_1, v_2, v_3, v_4)^T$  represents the vector of the displacement degrees of freedom of the element.

The stress tensor is evaluated using the elasticity Hooke's law in 2D as follows:

$$\begin{pmatrix} \sigma_x \\ \sigma_y \\ \tau_{xy} \end{pmatrix} = \mathbf{C}_e \begin{pmatrix} \varepsilon_x \\ \varepsilon_y \\ \gamma_{xy} \end{pmatrix} \quad \text{with} \quad \mathbf{C}_e = \frac{E}{1-\nu^2} \begin{pmatrix} 1 & \nu & 0 \\ \nu & 1 & 0 \\ 0 & 0 & G \end{pmatrix}. \quad (2.6)$$

The equivalent Von Mises stress of the element can then be written as:

$$\langle \sigma_{VM} \rangle = \sqrt{\sigma_x^2 + \sigma_y^2 - \sigma_x \sigma_y + 3\tau_{xy}} \quad (2.7)$$

$$= \sqrt{\begin{pmatrix} \sigma_x & \sigma_y & \tau_{xy} \end{pmatrix} \begin{pmatrix} 1 & -1/2 & 0 \\ -1/2 & 1 & 0 \\ 0 & 0 & 3 \end{pmatrix} \begin{pmatrix} \sigma_x \\ \sigma_y \\ \tau_{xy} \end{pmatrix}} \quad (2.8)$$

$$= \sqrt{\mathbf{q}_s^T \mathbf{B}_s^T \mathbf{C}_e^T \mathbf{D}_{VM} \mathbf{C}_e \mathbf{B}_s \mathbf{q}_s}, \text{ with } \mathbf{D}_{VM} = \begin{pmatrix} 1 & -1/2 & 0 \\ -1/2 & 1 & 0 \\ 0 & 0 & 3 \end{pmatrix} \quad (2.9)$$

$$\langle \sigma_{VM} \rangle = \sqrt{\mathbf{q}_s^T \mathbf{S} \mathbf{q}_s}, \quad \text{with } \mathbf{S} = \mathbf{B}_s^T \mathbf{C}_e^T \mathbf{D}_{VM} \mathbf{C}_e \mathbf{B}_s. \quad (2.10)$$

in which we used the notation introduced by Verbart [167]  $\langle \dots \rangle$  to represent macroscopic (or homogenized) variables.

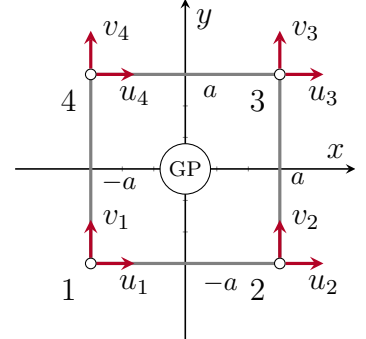


**Figure 2.1:** A four-node quadrilateral element. GP is the Gaussian integration point for which the equivalent stress is evaluated.

167. Verbart et al. (2017), 'A unified aggregation and relaxation approach for stress-constrained topology optimization'

**MICROSCOPIC AND MACROSCOPIC STRESS** In stress-constrained topology optimization, the element stress is usually evaluated using the microscopic stress formulation, assuming that there is no direct correlation between stress and density [168]. Indeed, the use of the macroscopic stress in volume minimization optimization problems creates an all-void design [169]. The properties that the microscopic stress should present are:

- (i) The stress criterion should be mathematically as simple as possible, as the relationship between Young's modulus and density. This permits a simple numerical implementation.
- (ii) To mimic the real physical behavior, the microscopic stress should be inversely proportional to density.

168. Duysinx et al. (1998), 'Topology optimization of continuum structures with local stress constraints'

169. Le et al. (2010), 'Stress-based topology optimization for continua'

<sup>167.</sup> Verbart et al. (2017), 'A unified aggregation and relaxation approach for stress-constrained topology optimization'

Equation 1.2 reads as follows:

$$E_i(\bar{\rho}_i) = E_{\min} + \bar{\rho}_i^p (E_0 - E_{\min})$$

where the parameter  $p$  is called SIMP penalization parameter, and it is used to reduce the quantity of intermediate densities, pushing the result to a black-and-white result.

<sup>167.</sup> Verbart et al. (2017), 'A unified aggregation and relaxation approach for stress-constrained topology optimization'

<sup>169.</sup> Le et al. (2010), 'Stress-based topology optimization for continua'  
<sup>170.</sup> Holmberg et al. (2013), 'Stress constrained topology optimization'  
<sup>171.</sup> Silva et al. (2019), 'Stress-constrained topology optimization considering uniform manufacturing uncertainties'

<sup>81.</sup> Rozvany (2001), 'On design-dependent constraints and singular topologies'

<sup>172.</sup> Stolpe (2003), 'On Models and Methods for Global Optimization of Structural Topology'

<sup>173.</sup> Sved et al. (1968), 'Structural optimization under multiple loading'

<sup>80.</sup> Cheng et al. (1997), ' $\varepsilon$ -relaxed approach in structural topology optimization'

- (iii) The microscopic stress should converge to a non-zero value at zero density. This requisite is deduced from investigations into the asymptotic stress behavior in thin layers [167].

The relation between stress and displacement is written as:

$$\langle \sigma_{VM} \rangle = C_e(\langle E \rangle) \langle \varepsilon \rangle, \quad (2.11)$$

where the variables between angular brackets  $\langle \dots \rangle$  represent macroscopic variables.

Combining (i) and (ii) with Equations 1.2, and 2.11, the microscopic stress can be written as:

$$\sigma_{VM} = \frac{\langle \sigma_{VM} \rangle}{\rho_e^q} = \rho_e^{p-q} C_e(E_0) \langle \varepsilon \rangle, \quad (2.12)$$

where the exponent  $q$  is a number greater than 1.

One possible choice that satisfy all the requirements is  $q = p$  [167, 169–171]. Thus, the microscopic stress is defined as:

$$\sigma_{VM} = C_e(E_0) \langle \varepsilon \rangle. \quad (2.13)$$

The significance of microscopic stress becomes evident when considering an element with intermediate density, that is physically realized by a porous microstructure. The microscopic stress presented in Equation 2.13 measures the stress in the material of the microstructure. It is grounded in the assumption that the macroscopic deformations of the homogenized element generate within the microstructure of the element a stress state that remains unaffected by the density of the element itself.

**CONSTRAINTS AGGREGATION AND RELAXATION** When optimizing a structure with stress constraints using a NAND formulation, two primary challenges commonly arise:

- (i) Is it known in the literature [81, 172] that stress-based topology optimization suffers from the *singular minima* (or *singularity*) problem: firstly observed on truss structure optimization [173], these *minima* are almost inaccessible to a standard gradient-based optimizer, often preventing it to reach the global optimum of the optimization [81]. This is because achieving the optimal solution to a problem using continuous design variables may necessitate passing through a state where the optimization constraints are violated, i.e. the *minimum* is on a lower dimension compared to the design space. This problem is often solved using a technique called *constraints relaxation* [80].
- (ii) The stress is a local measure, and thus a large set of constraints is generated when a reasonably fine mesh is used (one element,

one constraint). This problem is often solved using a technique called *constraints aggregation* or *global constraints* [174].

Following the work developed by Verbart *et al.* [167], the lower bound Kreisselmeier-Steinhauser (KS) function [175] is used to approximate the local relaxed stress constraint maximum. The authors showed that employing lower-bound KS aggregation functions to approximate the maximum operator in stress-constrained topology optimization ensures the relaxation and aggregation of the constraints simultaneously. The KS aggregated stress constraint function is defined as follows:

$$G_{\text{KS}}^{\text{L}} = \frac{1}{P} \ln \left( \frac{1}{N_e} \sum_{i \in \Omega} e^{P \bar{g}_i} \right). \quad (2.14)$$

Its main advantage over other different formulations is that it uses a single hyperparameter  $P$  to control the aggregation and the relaxation of the constraints simultaneously.

[174]. Silva et al. (2021), 'Local versus global stress constraint strategies in topology optimization'

[167]. Verbart et al. (2017), 'A unified aggregation and relaxation approach for stress-constrained topology optimization'

[175]. Kreisselmeier et al. (1979), 'Systematic Control Design by Optimizing a Vector Performance Index'

We remember that the stress constraints are defined as follows:

$$\bar{g} := \bar{\rho}_i \left( \frac{\sigma_{\text{VM},i}}{\sigma_{\text{L}}} - 1 \right) \leq 0.$$

**MINIMUM VOLUME FORMULATION** The NAND minimum volume formulation for continuous discretization is written combining Equations 2.2, and 2.14 as:

$$\begin{aligned} \min_{\rho} \quad & V = \frac{1}{N_e} \sum_{i \in \Omega} \bar{\rho}_i, && \text{(Volume minimization)} \\ \text{s.t.} \quad & G_{\text{KS}}^{\text{L}} = \frac{1}{P} \ln \left( \frac{1}{N_e} \sum_{i \in \Omega} e^{P \bar{g}_i} \right) \leq 0 && \text{(Stress constraints)} \quad (\mathbb{T}_1) \\ & \mathbf{K}\mathbf{u} = \mathbf{F} && \text{(FEM equation)} \\ & 0 \leq \rho_i \leq 1, \end{aligned}$$

The optimization is carried out using a gradient descent optimization algorithm for which the sensitivities are given in analytical form. Using analytic gradients is in general more efficient than finite differences as it avoids the need for multiple function evaluations, making the optimization process faster and more precise.

**SENSITIVITY ANALYSIS OF THE OBJECTIVE FUNCTION** Deriving Equation 2.2 with respect to  $\bar{\rho}$  we obtain:

$$\frac{\partial V}{\partial \bar{\rho}_i} = \frac{1}{N_e}. \quad (2.15)$$

The sensitivity of the objective function can then be evaluated using Equation 2.15 as follows:

$$\frac{dV}{d\rho_i} = \sum_{j \in \mathbb{N}_{i,R}} \frac{\partial V}{\partial \bar{\rho}_j} \frac{\partial \bar{\rho}_j}{\partial \bar{\rho}_i} \frac{\partial \bar{\rho}_i}{\partial \rho_i}. \quad (2.16)$$

Equation 1.4 reads:

$$\tilde{\rho}_i = \frac{\sum_{j \in \mathbb{N}_{i,R}} w(d_j) v_j \rho_j}{\sum_{j \in \mathbb{N}_{i,R}} w(d_j) v_j}.$$

Equation 1.5 reads:

$$\bar{\tilde{\rho}}_j = \frac{\tanh(\beta\eta) + \tanh(\beta(\tilde{\rho}_j - \eta))}{\tanh(\beta\eta) + \tanh(\beta(1 - \eta))}.$$

in which the derivative of the filtered density  $\tilde{\rho}$  with respect to the design variable  $\rho$  is written deriving Equation 1.4:

$$\frac{\partial \tilde{\rho}_i}{\partial \rho_j} = \frac{w(d_j) v_j}{\sum_{j \in \mathbb{N}_{i,R}} w(d_j) v_j}. \quad (2.17)$$

The sensitivity of the physical densities  $\bar{\tilde{\rho}}$  with respect to the filtered  $\tilde{\rho}$  can be written deriving Equation 1.5 as:

$$\frac{\partial \bar{\tilde{\rho}}_j}{\partial \tilde{\rho}_j} = \beta \frac{1 - \tanh^2(\beta(\tilde{\rho}_j - \eta))}{\tanh(\beta\eta) + \tanh(\beta(1 - \eta))}. \quad (2.18)$$

Using the chain rule it is possible to write:

$$\frac{\partial h}{\partial \rho_i} = \sum_{j \in \mathbb{N}_{i,R}} \frac{\partial h}{\partial \bar{\tilde{\rho}}_j} \frac{\partial \bar{\tilde{\rho}}_j}{\partial \tilde{\rho}_j} \frac{\partial \tilde{\rho}_j}{\partial \rho_i}, \quad (2.19)$$

where  $h$  represents a generic function.

**SENSITIVITY ANALYSIS OF THE CONSTRAINT FUNCTION** The sensitivity of the aggregated constraint function  $G_{KS}^L$  with respect to the design variable  $\rho$  is evaluated using:

$$\frac{dG_{KS}^L}{d\rho_i} = \sum_{j \in \mathbb{N}_{i,R}} \frac{\partial G_{KS}^L}{\partial \bar{\tilde{\rho}}_j} \frac{\partial \bar{\tilde{\rho}}_j}{\partial \tilde{\rho}_j} \frac{\partial \tilde{\rho}_j}{\partial \rho_i}. \quad (2.20)$$

we remember that

$$K(\bar{\tilde{\rho}})\mathbf{u} = f$$

As the constraint function  $G_{KS}^L = G(\bar{\tilde{\rho}}, \mathbf{u}(\bar{\tilde{\rho}}))$  is explicitly and implicitly (via the relationship with  $\mathbf{u}$ ) depending on  $\bar{\tilde{\rho}}$ , the first-order derivative is evaluated using the total derivative formula:

$$\frac{dG}{d\bar{\tilde{\rho}}_j} = \frac{\partial G}{\partial \bar{\tilde{\rho}}_j} + \frac{\partial G}{\partial \mathbf{u}} \frac{\partial \mathbf{u}}{\partial \bar{\tilde{\rho}}_j}. \quad (2.21)$$

As function  $G_{KS}^L$  depends on  $\mathbf{u}$  via the stresses  $\sigma_i$ , it is possible to write:

$$\frac{\partial G}{\partial \mathbf{u}} = \sum_{i \in \Omega} \left( \frac{\partial G}{\partial \sigma_i} \frac{\partial \sigma_i}{\partial \mathbf{u}} \right). \quad (2.22)$$

Combining Eq. 2.21 with Eq. 2.22, we obtain:

$$\frac{dG}{d\bar{\tilde{\rho}}_j} = \underbrace{\frac{\partial G}{\partial \bar{\tilde{\rho}}_j}}_A + \sum_{i \in \Omega} \left( \underbrace{\frac{\partial G}{\partial \sigma_i}}_B \underbrace{\frac{\partial \sigma_i}{\partial \mathbf{u}}}_C \right) \underbrace{\frac{\partial \mathbf{u}}{\partial \bar{\tilde{\rho}}_j}}_D. \quad (2.23)$$

We compute the four factors separately:

A – The first term represents the explicit relationship of  $G$  to the physical densities and its calculation is straightforward:

$$\frac{\partial G}{\partial \bar{\rho}_j} = \frac{1}{P} \frac{\left( \frac{\sigma_{VM,j}}{\sigma_L} - 1 \right) \frac{1}{N_e} P e^{P \bar{g}_j}}{\frac{1}{N_e} \sum_k e^{P \bar{g}_k}} = \left( \frac{\sigma_{VM,j}}{\sigma_L} - 1 \right) \frac{e^{P \bar{g}_j}}{\sum_k e^{P \bar{g}_k}}. \quad (2.24)$$

B – The second term can be calculated using the chain rule:

$$\frac{\partial G}{\partial \sigma_i} = \frac{\partial G}{\partial \bar{g}_i} \frac{\partial \bar{g}_i}{\partial \sigma_i} = \frac{1}{P} \frac{\frac{1}{N_e} P e^{P \bar{g}_i} \bar{\rho}_i}{\frac{1}{N_e} \sum_k e^{P \bar{g}_k} \sigma_L} = \frac{\bar{\rho}_i}{\sigma_L} \frac{e^{P \bar{g}_i}}{\sum_k e^{P \bar{g}_k}}. \quad (2.25)$$

C – We reformulate Equation 2.10 to be written in global coordinates instead of local:

$$\sigma_i^2 = q_s^T S q_s = u^T S_g u, \quad (2.26)$$

Equation 2.10 reads:

$$\langle \sigma_{VM} \rangle = \sqrt{q_s^T S q_s}.$$

where  $S_g$  represents the matrix  $S$  of Equation 2.10 written on global coordinates<sup>1</sup>. We can now differentiate Equation 2.26 with respect of the displacement field in global coordinates  $u$  to obtain:

$$\frac{\partial \sigma_i}{\partial u} = \frac{S_g u}{\sigma_i}. \quad (2.27)$$

Equations 2.25, and 2.27 are now combined to obtain the result of the product of the  $\mathbf{B}$  and  $\mathbf{C}$  terms. As a result, the derivatives of  $G$  with respect to  $u$ , are written as:

$$\frac{\partial G}{\partial u} = \frac{\bar{\rho}_j}{\sigma_L \sigma_j} e^{P \bar{g}_i} |S_j|_g u. \quad (2.28)$$

1: The matrix  $S_g$  can be calculated using the very same assembling approach used for the stiffness matrix  $K$  starting from the elemental stiffness matrix  $K_e$ . As the global stiffness matrix  $K$ ,  $S_g$  is symmetric and sparse.

D – To calculate the last term, we take the static equilibrium equation  $Ku = f$  and differentiate it with respect to the physical densities  $\bar{\rho}_j$ , obtaining:

$$\frac{\partial K}{\partial \bar{\rho}_j} u + K \frac{\partial u}{\partial \bar{\rho}_j} = 0 \iff \frac{\partial u}{\partial \bar{\rho}_j} = -K^{-1} \frac{\partial K}{\partial \bar{\rho}_j} u, \quad (2.29)$$

where

$$\frac{\partial K}{\partial \bar{\rho}_j} = (E_0 - E_{min}) p \bar{\rho}_j^{p-1} K_{e,j}. \quad (2.30)$$

Equation 2.30 represent the well-known first-derivative term of the global stiffness matrix  $K$  with respect to the physical densities  $\bar{\rho}_j$  when using Solid Isotropic Material with Penalization Method (SIMP) material scheme [7]. We obtain the last term:

$$\frac{\partial u}{\partial \bar{\rho}_j} = -K^{-1} \left( (E_0 - E_{min}) p \bar{\rho}_j^{p-1} K_{e,j} \right) u. \quad (2.31)$$

7. Bendsøe et al. (2004), 'Topology Optimization'

Combining Eq. 2.23, Eq. 2.24, Eq. 2.28, and Eq. 2.31, we finally obtain:

$$\frac{\partial G_{KS}^L}{\partial \bar{\rho}_j} = \left( \frac{\sigma_{VM,j}}{\sigma_L} - 1 \right) \frac{e^{P\bar{g}_j}}{\sum_k e^{P\bar{g}_k}} - K^{-1} \frac{\partial G}{\partial u} \left( \frac{\partial K}{\partial \bar{\rho}_j} \right) u. \quad (2.32)$$

2: More information about the adjoint method used to analytically calculate the first-order derivatives can be found on the Martins *et al.* book [8].

To avoid the explicit calculation of  $K^{-1}$  we use the *adjoint method*<sup>2</sup>. Here is the linear system that, once solved, permits to calculate  $\psi$ :

$$K\psi = \frac{\partial G}{\partial u} \iff \psi = K^{-1} \frac{\partial G}{\partial u}. \quad (2.33)$$

This formula is called *adjoint equation*. This equation is solved for  $\psi$  and the result used to evaluate:

$$\frac{\partial G_{KS}^L}{\partial \bar{\rho}_j} = \left( \frac{\sigma_{VM,j}}{\sigma_L} - 1 \right) \frac{e^{P\bar{g}_j}}{\sum_k e^{P\bar{g}_k}} - \psi \left( \frac{\partial K}{\partial \bar{\rho}_j} \right) u. \quad (2.34)$$

Solving linear system 2.33 instead of directly calculating the inverse matrix of  $K$  is more efficient from a performance perspective. The cost of solving a system using the Cholesky decomposition is  $\mathcal{O}(N^3/3)$ , while a matrix inversion is  $\mathcal{O}(N^3)$ .

where  $N$  represents the size of the square matrix describing the linear system. Equation 2.34 represents the first-order derivative equation used to evaluate the sensitivity of the constraint function  $G_{KS}^L$  with respect to the physical densities  $\bar{\rho}$ . The value of  $\psi$  is calculated every iteration solving the linear system 2.33.

### 2.1.2 TRUSS TOPOLOGY OPTIMIZATION (TTO) MINIMUM VOLUME FORMULATION

We are now shifting our focus from continuous structures to discrete truss systems, describing the Truss Topology Optimization (TTO) (also known in early literature as layout optimization), a structure optimization method that focuses on discrete structures. In his most used formulation, TTO aims at reducing structural volume while meeting stress criteria using a Simultaneous Analysis and Design (SAND) approach. The problem is already well-posed for the comparison with continuous discretization.

**OBJECTIVE AND CONSTRAINT FUNCTIONS** The goal of the optimization is to minimize the volume occupied by a structure under a specified load case. For a truss structure, we can write:

$$V = \ell^T a \quad (2.35)$$

in which  $\ell = [\ell_1, \ell_2, \dots, \ell_{Nel}]^T$  is the length vector of the member of the ground structure. The volume fraction is evaluated as the ratio  $V_f = \frac{V}{V_0}$ , where  $V_0$  represents the total volume of the design domain  $\Omega$ .

As the volume minimization problem is stated using the SAND approach, both the members' cross-sectional areas  $a$  and member

forces  $\mathbf{q}$  are design variables of the problem. For that reason, the stress constraints in tension and compression ( $g_{st,t}$  and  $g_{st,c}$ ) can be trivially written as:

$$-\sigma_c \mathbf{a} \leq \mathbf{q} \leq \sigma_t \mathbf{a} \quad (2.36)$$

in which  $\sigma_c$  and  $\sigma_t$  are the compressive and tensile maximum allowable stresses of the material.

**MINIMUM VOLUME FORMULATION** We recall the full volume minimization formulation here, stated in terms of members' cross-sectional areas  $\mathbf{a}$  and member forces  $\mathbf{q}$  as follows:

$$\begin{aligned} \min_{\mathbf{a}, \mathbf{q}} \quad & V = \tilde{\ell}^T \mathbf{a} \quad (\text{Volume minimization}) \\ \text{s.t.} \quad & \mathbf{B}\mathbf{q} = \mathbf{f} \quad (g_{eq}) \\ & -\sigma_c \mathbf{a} \leq \mathbf{q} \leq \sigma_t \mathbf{a} \quad (g_{st,c}, g_{st,t}) \\ & \mathbf{a} \geq 0, \end{aligned} \quad (\mathbb{P}_0)$$

where  $\tilde{\ell} = [\ell_1 + s, \ell_2 + s, \dots, \ell_{Nel} + s]^T$  is called augmented member length and  $s$  the joint cost, used to penalize the appearance of small members [98]. The listing and explanation of the other parameters is given in Section 1.2.3. This formulation takes into account only the linear behavior of the structure and is equivalent to the original and well-studied member force formulation [7, 37].

It is worth listing the key distinctions of the TTO formulation compared to the density-based topology optimization formulation described earlier in this chapter. Firstly, the TTO problem is formulated using the SAND approach, in which the equations of structural mechanics are treated as constraints in the optimization. Unlike NAND approaches, these equations are not explicitly solved. Consequently, concerns about the singularity of the stiffness matrix  $\mathbf{K}$  are avoided, and bars can potentially vanish from the structure during the optimization ( $\mathbf{a} = 0$ ). Secondly, the TTO problem is expressed in terms of members' cross-sectional areas  $\mathbf{a}$  and member forces  $\mathbf{q}$  with a plastic material model, disregarding kinematic compatibility to formulate a Linear Programming (LP) problem. Due to its linearity, this optimization problem is convex, ensuring that the solutions found are global optima. Moreover, the linear nature of the formulation  $\mathbb{P}_0$  makes it computationally efficient, even with a large number of design variables, when employing modern interior point optimizers. However, the SAND formulation with a plastic material model accurately predicts the mechanical behavior of only statically determinate structures or mechanisms [84, 85]. When dealing with more complex structures, such as those that are statically indeterminate due to symmetry or multiple load cases, explicit consideration of the linear kinematic constraints is necessary, leading to a loss of the linear property of the formulation.

98. Parkes (1975), 'Joints in optimum frameworks'

7. Bendsøe et al. (2004), 'Topology Optimization'

37. Dorn et al. (1964), 'Automatic design of optimal structures'

84. Kirsch (1989), 'Optimal topologies of truss structures'

85. Rozvany et al. (1995), 'Layout Optimization of Structures'

## 2.2 COMPARISON BETWEEN DENSITY-BASED TOPOLOGY OPTIMIZATION AND TTO

In the upcoming discussion, we will be comparing the optimized structures obtained using the density-based topology optimization and the TTO optimization algorithms. Our primary objective in this comparison is to choose the most appropriate method for our study by understanding the application limits inherent in these two structural discretization methods. If, indeed, we identify such limitations, the aim is to discern and define them. Such discussions have already been briefly addressed in the literature [41, 176], but treating the problem without providing numerical results as a basis for making the choice.

Since our interest is in ultralight structures, we are willing to compare the results of both optimization methods when dealing with different volume fractions on a common load case. The volume minimization formulation with stress constraints we use cannot, however, directly control the volume of the optimized structure. For that reason, we decided to adjust the material strength  $\sigma_L$  to influence the volume fraction of the optimized structure i.e. employing more resistant material results in a lower volume fraction and *vice versa*. For this comparative analysis, we have selected three key performance metrics: the volume fraction  $V_f$ , the structural compliance  $C$ , and the maximum material allowable – or strength  $\sigma_L$ . Among these, we classify stress limit as the active metric used to influence the optimization, while volume and compliance are the objective of the optimization and a passive metric, respectively. In addition to the aforementioned performance metrics, we will also track the execution time of the algorithms.

### 2.2.1 DEFINITION OF A TEST CASE FOR THE COMPARISON

The L-shape beam is one of the most used load case benchmarks for stress-based topology optimization [168, 169]. This choice is driven by the distinctive geometry of the problem, which generates a stress concentration at the sharp corner in the case of linear elasticity—a phenomenon approaching infinity. Consequently, optimized solutions often feature a large fillet, mitigating the intensity of the stress singularity. The geometric description of the test case is given in Fig. 2.2. The beam with dimensions  $L \times L$  presents a fixed support on the nodes in the top part and a load on the right extremity.

To permit the methods' comparison, the design domain  $\Omega$  is discretized using two distinct meshes: in the continuous case, we employ a mesh consisting of  $600 \times 600$  quadrilateral elements, totaling 270 000 elements. For this mesh, the load is distributed over multiple elements (5% of  $L$ ) to avoid local stress concentrations. Additionally, the stress constraints are not evaluated on the corresponding elements, and this

**41.** Bendsøe (1989), 'Optimal shape design as a material distribution problem'

**176.** Watts et al. (2019), 'Simple, accurate surrogate models of the elastic response of three-dimensional open truss micro-architectures with applications to multiscale topology design'

**168.** Duysinx et al. (1998), 'Topology optimization of continuum structures with local stress constraints'  
**169.** Le et al. (2010), 'Stress-based topology optimization for continua'

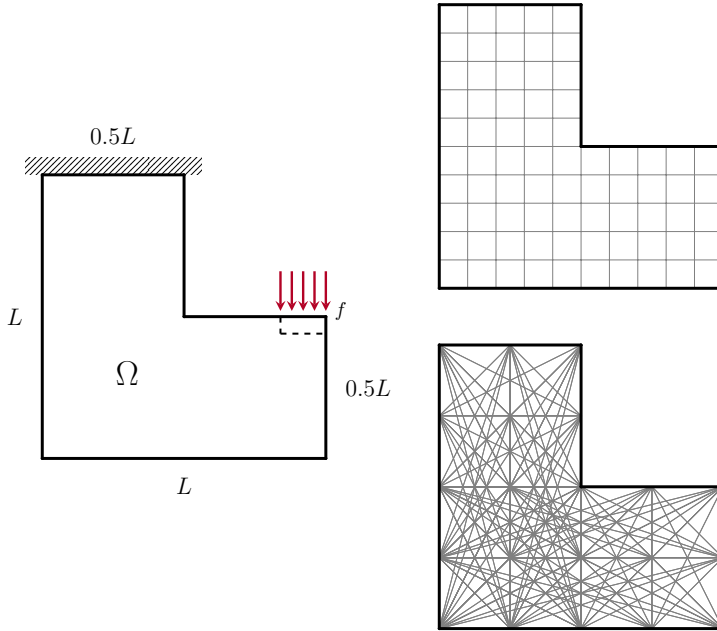


**Figure 2.2:** On the left, plot of the L-shape beam test case, on the right the graphical representations of the two discretizations used, the continuous (above) composed of  $600 \times 600$  quadrilateral elements, and the truss-like (below) discretized using  $33 \times 33$  nodes and a fully connected ground structure. The images represent a coarser discretization for visual clarity.

zone is considered outside of the design domain  $\Omega$ . Concerning the truss discretization for the TTO algorithm, we employ a mesh with  $33 \times 33$  nodes and a fully connected ground structure, comprising a total of 305 728 candidates. The load is applied only on one single node.

We employ the same isotropic material and structure dimensions for the two optimizations, and the complete data is resumed in Table 2.1. The value of the maximum material allowable  $\sigma_L$  is used to control, although not directly, the volume fraction of the solutions. For simplicity, all numeric values are assumed normalized and dimensionless.

### 2.2.2 NUMERICAL APPLICATION

The density-based topology optimization and the TTO have both been implemented using Python, employing different optimization algorithms. For density-based topology optimization, the chosen optimization algorithm is the Method of Moving Asymptotes (MMA), developed by Svanberg [31]. The parameter called *movelimit*<sup>3</sup> is set to 0.1 while the other algorithm's parameters are set to their default value. We chose to filter the density field  $\rho$  using the 2D convolution operator [61] and the projection technique based on the *tanh* function [56] precedently described. The radius of the filter is set to  $R = 5$  elements. Using the projection Equation 1.5 is not volume conservative for all values of  $\eta$ , and to stay conservative we use a volume-increasing filter [16]. The value of  $\eta = 0.4$  is then chosen. A continuation scheme for the projection parameter  $\beta$  is set to increase by one every 200 iterations and starting from 1, the number of maximum iterations is set to 7500, and the stopping criteria is calculated as  $\|\Delta x\|_2 / \sqrt{N_e}$  [16] on the absolute difference between two successive iterations of the physical densities  $\bar{\rho}$ , and it is set to  $10^{-4}$ . The aggregation parameter  $P$

Parameter	Value
$E$	1
$\nu$	0.3
$L$	100
$\sigma_L$	[0.20, 20]

**Table 2.1:** Material data used for the optimizations. The value of the maximum material allowable  $\sigma_L$  is used as the parameter to generate multiple optimized topologies. The Poisson module is used only in density-based topology optimization.

31. Svanberg (1987), 'The method of moving asymptotes—a new method for structural optimization'

3: More information on the implementation of the *movelimit* parameter can be found on the paper by Verbart [167].

61. Sigmund (2007), 'Morphology-based black and white filters for topology optimization'

56. Wang et al. (2011), 'On projection methods, convergence and robust formulations in topology optimization'

Equation 1.5 reads:

$$\bar{\bar{\rho}}_j = \frac{\tanh(\beta\eta) + \tanh(\beta(\bar{\rho}_j - \eta))}{\tanh(\beta\eta) + \tanh(\beta(1 - \eta))}.$$

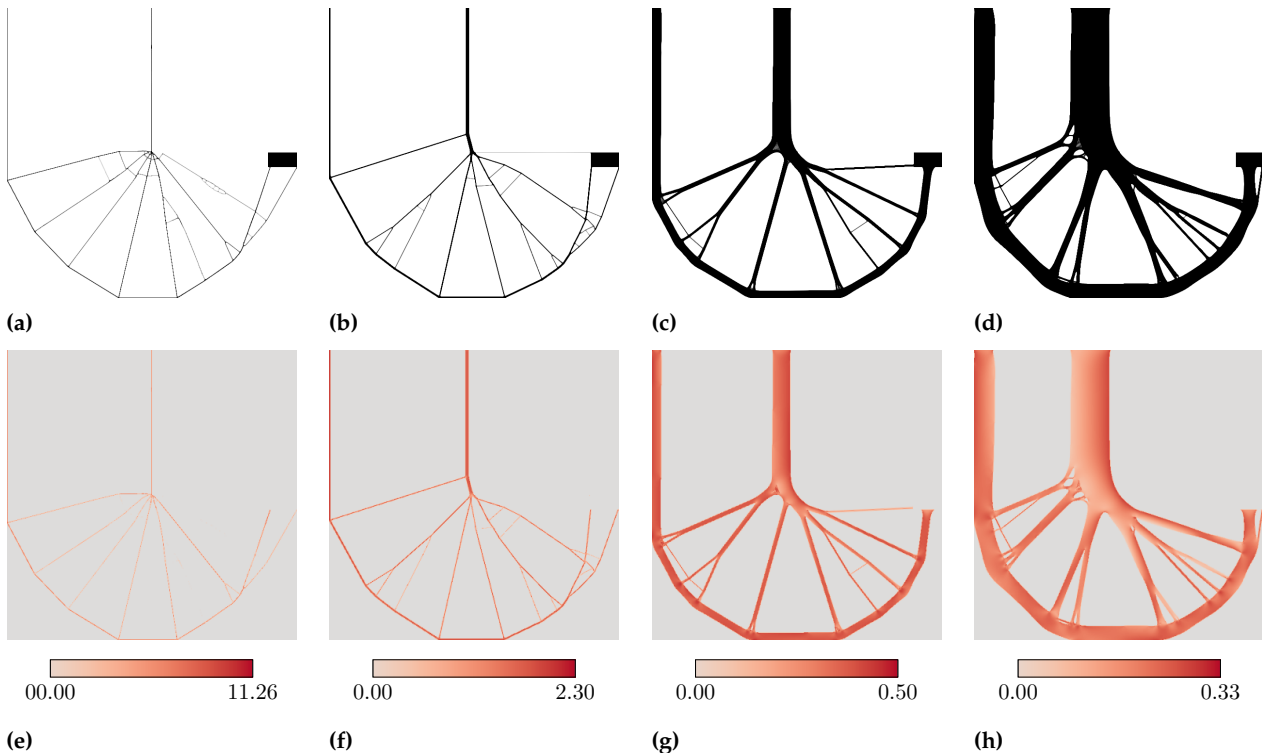


**Figure 2.3:** (a-d) Topology of the optimized structures for different values of the material allowable  $\sigma_L = 10.00, 2.00, 0.40$ , and  $0.25$ , showing a volume fraction of  $V_f = 1.60\%, 4.04\%, 18.03\%$  and  $34.71\%$ , respectively. (e-h) Von Mises stress distribution for the optimized structures.

16. Ferrari et al. (2020), 'A new generation 99 line Matlab code for compliance topology optimization and its extension to 3D'

177. Johnson (2007), 'The NLOpt nonlinear-optimization package'

178. Diamond et al. (2016), 'CVXPY: A Python-Embedded Modeling Language for Convex Optimization'

179. Domahidi et al. (2013), 'ECOS: An SOCP solver for embedded systems'

of the aggregation function  $G_{KS}^L$  is set to 32. The SIMP parameters of Equation 1.2 are set to  $E_0 = 1$ , and  $E_{min} = 10^{-9}$ . The value of the penalization parameter  $p$  is selected as  $p = 3$ . The optimization is carried out using the NLOpt Python optimization package [177], analytically evaluating the sensitivity using Equations 2.15, and 2.23.

The volume minimization TTO problem as formulated in  $\mathbb{P}_0$  represents a LP problem that can be efficiently solved by contemporary optimization algorithms. In this work, we used the Python package CVXPY 1.2.2 [178] with the ECOS 2.0.7 [179] solver. The joint cost  $s$  is set to 0.001 and the stopping criterion is chosen as  $\|\Delta x\|_\infty \leq 10^{-8}$ . As the formulation is linear, no sensitivity calculation is carried out.

The optimizations presented in this section are performed using a single core on a cluster equipped with an Intel® Xeon® CPU E5-2650 @ 2.20 GHz and using 8 GB of RAM.

**DENSITY-BASED TOPOLOGY OPTIMIZATION RESULTS** We generate multiple optimized structures with different volume fractions  $V_f$  by launching the optimization code for continuous mesh with different values of the material allowable  $\sigma_L$  spanning from 0.2 to 20.

The results obtained for  $\sigma_L = 10.00, 2.00, 0.40$  and  $0.25$  are shown in

Fig. 2.3. In the upper part of the figure (a-d), we see the topology of the optimized structures with an increasing volume fraction  $V_f$ . Interestingly, the topology of the solution remains almost unchanged, varying principally in the thickness of its members. We notice the classic large fillet around the corner that alleviates the local stress concentration. As the volume decreases, the optimized structure tends to a solution that resembles a truss-like structure, with a reducing fillet radius. In those cases, we know that the density-based topology optimization algorithm acts as a method for the layout of truss-like structures [11]. This effect is caused by the combination of different factors, such as the regularization filter, the mesh size, and the low volume fraction [72].

A summary of the numerical results is presented in Table 2.2. Firstly, we can observe how we successfully controlled the volume fraction  $V_f$  by modifying the material resistance  $\sigma_L$ , obtaining results that perfectly follow a monotonically decreasing function. Additionally, as expected, a more voluminous solution also exhibits a lower value of structural compliance. Next, we notice that the optimization processes exhibit long execution times, especially when dealing with extreme cases like low-material resistance and high-volume fractions. This effect is caused by the very fine mesh used to discretize the design domain  $\Omega$ , the sensitivity calculation using the adjoint method, and the increasing difficulty of satisfying the stress constraints. Furthermore, it is observed that the maximum stress exceeds the material allowable  $\sigma_L$ . This is because we are employing an aggregation function for the stress constraints that estimates the maximum value of the constraint across a group of elements. However, these aggregation methods do not perfectly align with the exact maximum value, which is a recognized limitation.

On top of volume fraction, compliance, and stress, we evaluate an additional metric specific to continuous meshes called the *greyness level* or *measure of non-discreteness* [61] to evaluate the quality of the solutions. It is defined as:

$$M_{nd} = \frac{\sum_e 4\bar{\rho}_e(1 - \bar{\rho}_e)}{n} \times 100\%, \quad (2.37)$$

where results near zero mean a completely black-and-white design. Observing the  $M_{nd}$  values in Table 2.2, we notice that all the optimized structures converged to nearly black-and-white solutions, confirming the correct numerical implementation of the problem.

In the lower part of Fig. 2.3 (e-f), we plot the equivalent Von Mises stress for every element of the solution with physical density  $\bar{\rho} > 0.5$ . Multiple interesting observations can be made. First, we notice that the stress distribution is almost uniform in the structure, and it tends to the value of the material allowable  $\sigma_L$  – i.e. we approach a *fully stressed*

11. Bendsøe et al. (1988), 'Generating optimal topologies in structural design using a homogenization method'

72. Sigmund et al. (2016), 'On the (non-)optimality of Michell structures'

61. Sigmund (2007), 'Morphology-based black and white filters for topology optimization'

**Table 2.2:** Numerical results of the topology optimization method of the L-shape beam load case with varying material allowable  $\sigma_L$  on a  $600 \times 600$  elements mesh. Numbers in red highlight the results that have not converged.

$\sigma_L$	max $\sigma_L$	$V_f$	$C$	$M_{nd}$	It.	Time
20.00	23.51	1.18 %	6992	1.91 %	1142	8 h 11 m
10.00	11.26	1.60 %	3837	2.19 %	1147	7 h 55 m
8.00	8.78	1.74 %	2766	1.95 %	792	5 h 39 m
6.00	7.15	1.89 %	2243	1.81 %	806	5 h 35 m
5.00	5.81	2.17 %	1823	1.81 %	849	5 h 53 m
4.00	4.69	2.67 %	1424	2.02 %	894	6 h 12 m
3.00	3.47	3.00 %	1133	1.64 %	993	6 h 45 m
2.00	2.30	4.04 %	781	1.45 %	1189	8 h 20 m
1.00	1.18	7.28 %	404	1.35 %	1621	11 h 41 m
0.90	1.06	8.09 %	365	1.31 %	1656	11 h 36 m
0.80	0.96	8.82 %	332	1.21 %	1937	15 h 21 m
0.70	0.84	10.05 %	292	1.09 %	1827	13 h 21 m
0.60	0.73	11.80 %	250	1.19 %	1955	14 h 21 m
0.50	0.61	14.18 %	213	1.06 %	2032	15 h 39 m
0.40	0.50	18.03 %	170	1.08 %	2259	17 h 6 m
0.35	0.44	21.12 %	148	1.15 %	2421	19 h 29 m
0.30	0.38	26.21 %	126	1.50 %	3100	24 h 46 m
0.25	0.33	34.71 %	104	1.04 %	3484	27 h 39 m
0.20	0.27	48.08 %	77	1.26 %	7500	91 h 46 m

Michell theorized two criteria for optimal truss structures [90] valid when the maximum allowable stress is equal in tension and compression ( $\sigma_t = \sigma_c$ ) and when the supports of the structure are statically determinate. The first one states that all the members of an optimal structure should present internal stress equal in magnitude to the maximum allowable value of the material – i.e. the structure is *fully stressed*. The second criterion asserts that the strain of all the members of the structure should be equal and there should be no other point having a strain higher than this value.

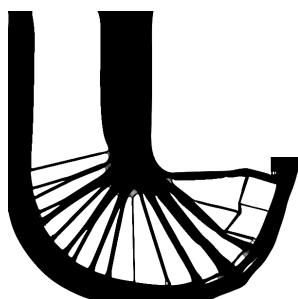


**Figure 2.4:** The intermediate resulting structure for  $\sigma_L = 0.2$  with  $V_f = 48.08\%$  after 7500 optimization iterations.

structure. Even if the geometric support of the theory is different, it looks like the topology-optimized structures follow the Michell criteria presented in Section 1.2.3 for optimal truss structures.

As previously mentioned, our focus lies in exploring the method's limits, particularly at the volume fraction boundaries. When dealing with low-resistance materials – i.e. materials that show a low  $\sigma_L$ , we encounter a scenario where no solution can be attained since no distribution can fulfill the imposed constraints. Throughout our research with this specific test case and mesh size, we did not produce any solutions with a volume fraction exceeding 50%, suggesting we have encountered a limitation of the problem. With this combination of material properties, loading conditions, geometry, and mesh, it appears that there is no feasible solution for  $V_f > 50\%$ . We notice that the calculation time has significantly increased with the increase of  $V_f$  because the algorithm needs more iterations to converge and faces greater difficulty in satisfying the stress constraints. Fig. 2.4 shows the topology of the non-converged solution with  $\sigma_L = 0.2$ ,  $V_f = 48.08\%$  and over five days of optimization.

Conversely, when dealing with excessively strong material – i.e. materials that show a high  $\sigma_L$ , the optimal scenario would demand such minimal material usage that certain sections of the structure become thinner than the width of a single element. In this case, the mesh used for discretization is too coarse to accurately represent the solution, and finer meshing becomes essential to capture the details of the optimized design. Fig. 2.5 shows the limit case when  $\sigma_L = 10.0$  and  $V_f = 1.60\%$ .

Finally, in Fig. 2.6 we show the plots summarizing our results, with

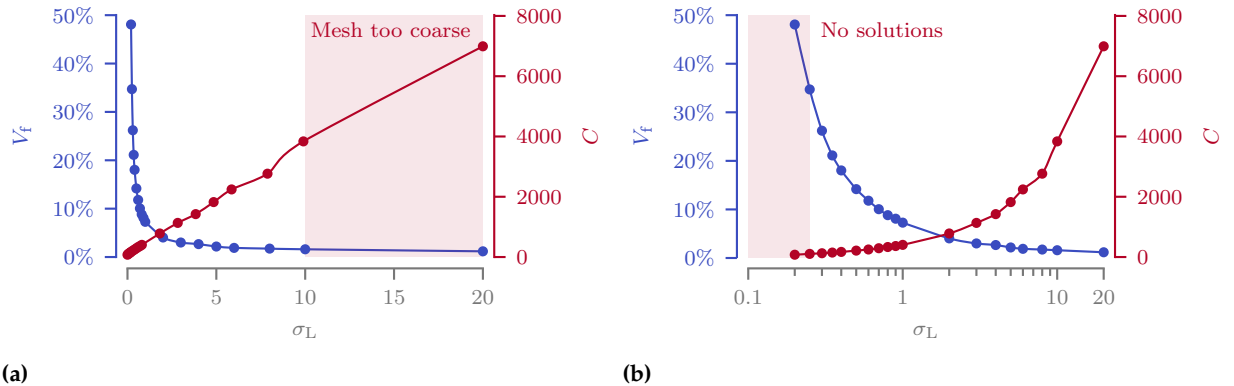


**Figure 2.6:** Linear (a) and logarithmic (b) plot of the volume fraction  $V_f$  and the compliance  $C$  with respect to the maximum material allowable  $\sigma_L$  for the continuous mesh structures. Areas in red represent the zones outside the domains of applicability of the applied method.

the method's limits highlighted. To effectively show the different orders of magnitude present in the plot, we have used both linear and logarithmic scales simultaneously. We notice that the volume fraction  $V_f$  follows a hyperbolic relationship, while compliance  $C$  exhibits a linear correlation with respect to the material allowable  $\sigma_L$ .

**TTO OPTIMIZATION RESULTS** In this section, we present the optimized structures of the TTO formulation with different values of the material allowable  $\sigma_L$  spanning from 0.2 to 20. Due to the inherent linearity of Formulation  $\mathbb{P}_0$ , the solutions exhibit several intriguing characteristics. Notably, in cases such as the tested L-shaped test case where the structures are not overconstrained and are not subject to asymmetric stress constraints, the formulation aligns with the Michell criteria. Consequently, the topology remains unchanged regardless of the imposed stress limit, and the stress distribution results in a fully stressed structure. Fig. 2.7 provides a visual representation of the optimized topology and the corresponding stress distribution for the different values of the material allowable  $\sigma_L$ . By examining the figure, it is evident that the node positions are constrained by the initial ground structure. The solution resembles half of a spoked wheel, with an irregular distribution of these spokes. One might expect a more evenly distributed arrangement of these spokes. Interestingly, no fillet is formed at the corner of the L-shaped beam. This observation is attributed to the modeling of truss nodes as frictionless joints that do not support moments. However, this aligns with our earlier findings in density-based topology optimization, where the fillet radius diminishes as the volume fraction decreases. Finally, it is crucial to note that in this simple test case with only a single load case, linear elasticity is inherently considered in the formulation. There is no need to explicitly account for it by imposing kinematic compatibility constraints, as highlighted in previous studies [7, 37, 39].

The following equation consistently holds for the optimized structures,

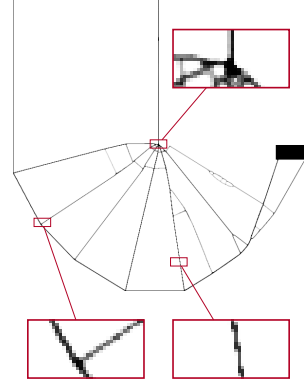


**Figure 2.5:** The optimized structure for  $\sigma_L = 10.0$  with  $V_f = 1.60\%$ . Some of the structure's features present not even a fully-dense element in their thickness.

7. Bendsøe et al. (2004), 'Topology Optimization'

37. Dorn et al. (1964), 'Automatic design of optimal structures'

39. Hemp (1973), 'Optimum Structures'

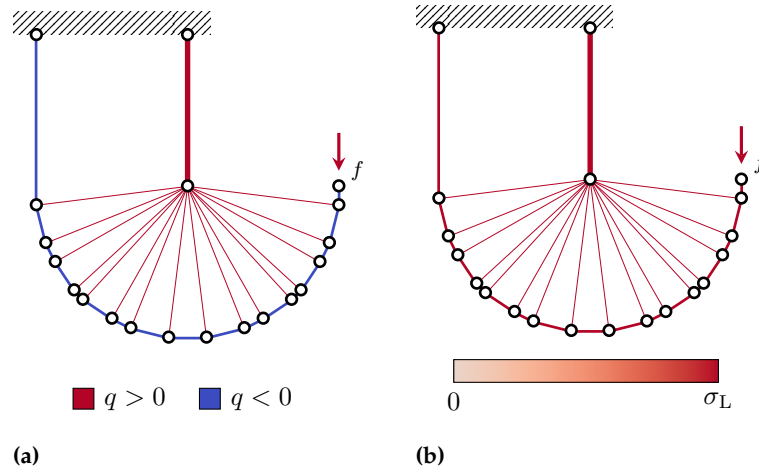


**Figure 2.7:** Topology (a) and stress distribution (b) plot for the TTO optimized structure of the L-shape beam test case with varying values of the material allowable  $\sigma_L$  on a  $33 \times 33$  nodes ground structure. The structure topology is invariant with respect to the value of  $\sigma_L$ .

**Table 2.3:** Numerical results of the TTO method of the L-shape beam test case with varying values of the material allowable  $\sigma_L$  on a  $33 \times 33$  nodes ground structure. Numbers in red highlight the results that lie outside the domains of applicability of the optimization method.

$\sigma_L$	$V_f$	$C$	Min $\lambda$	Time
50.0	0.12 %	23 282	111.7	1 m 6 s
20.0	0.31 %	9313	70.6	1 m 9 s
10.0	0.62 %	4656	49.9	1 m 18 s
8.0	0.78 %	3725	44.7	1 m 15 s
6.0	1.03 %	2794	38.7	1 m 10 s
5.0	1.24 %	2328	35.3	1 m 24 s
4.0	1.55 %	1863	31.6	1 m 18 s
3.0	2.07 %	1397	27.4	1 m 15 s
2.0	3.10 %	931	22.3	1 m 15 s
1.0	6.21 %	466	15.8	1 m 17 s
0.9	6.90 %	419	15.0	1 m 20 s
0.8	7.76 %	373	14.1	1 m 21 s
0.7	8.87 %	326	13.2	1 m 16 s
0.6	10.35 %	279	12.2	1 m 20 s
0.5	12.42 %	233	11.2	1 m 22 s

regardless of the value of  $\sigma_L$ :

$$V^* = \frac{fL}{\sigma_L} \cdot \Gamma, \quad (2.38)$$

180. Lewiński et al. (1994), 'Extended exact solutions for least-weight truss layouts—Part I'

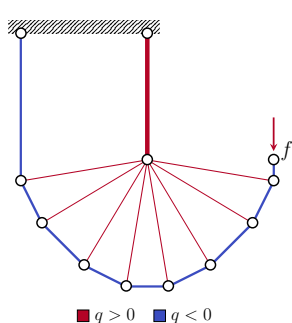


**Figure 2.8:** Optimized structure obtained using a fully connected ground structure with  $13 \times 13$  nodes and 7705 candidates.

where the volume multiplicative constant  $\Gamma$  depends on the load case and the ground structure used to discretize the design space  $\Omega$  [180]. For this specific test case with the  $33 \times 33$  nodes ground structure, we found  $\Gamma = 4.656$ . The execution time of the optimization is approximately 90 s and does not change with respect to the maximum stress  $\sigma_L$ . The full numerical results of the multiple optimizations can be found in Table 2.3.

It's worth noting that we have intentionally opted for a dense ground structure here to achieve an element count roughly equivalent to that of the continuous mesh case (305 728 and 270 000 for the TTO and the density-based topology optimization, respectively). We have utilized a fully connected ground structure with  $33 \times 33$  nodes, but we obtained satisfactory results with just  $13 \times 13$  nodes (see Fig. 2.8). In this case, we obtain a volume multiplicative constant  $\Gamma = 4.705$ ,

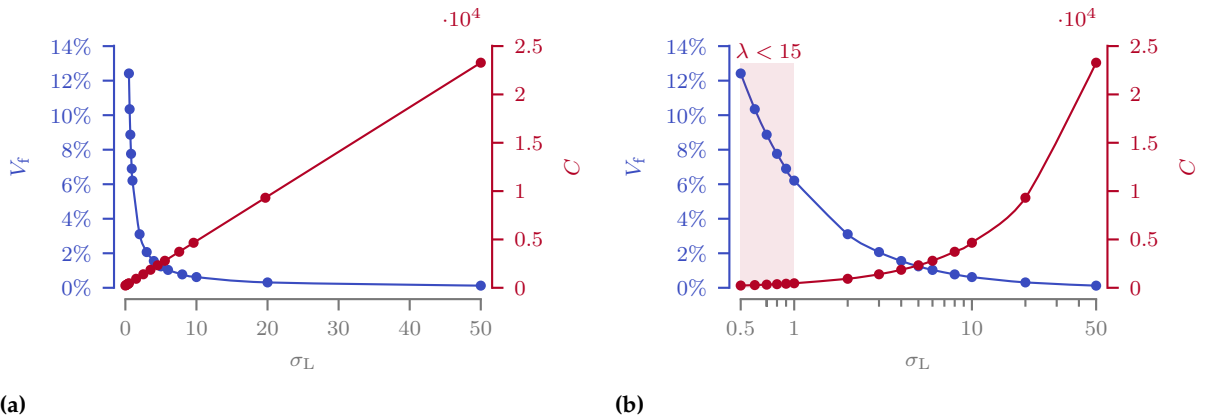


**Figure 2.9:** Linear (a) and logarithmic (b) plot of the volume fraction  $V_f$  and the compliance  $C$  with respect to the value of the maximum material allowable  $\sigma_L$  for the TTO optimized structures. Areas in red represent the zones outside the domains of applicability of the truss discretization.

signifying a 1.05 % increase compared to the  $33 \times 33$  case with  $\Gamma = 4.656$ . However, the element number is reduced by 97.4 % (305 728 versus 7705 candidates). The computational time for this simplified test case is below one second.

With this example, we notice that refining the continuous mesh and refining the ground structure are not equivalent operations. In one case, it allows for representing finer details, while in the other, it permits new shapes for the structure. The choice of the ground structure dictates the final form; it is more restrictive than merely allowing finer details. If bars are missing initially, they will not be added later on.

In assessing solution quality, we employ a distinct metric known as the slenderness ratio, denoted as  $\lambda$ , which represents the ratio between the length and the radius of gyration of the bars of the ground structure. In our specific case, we have established a minimum slenderness ratio of 15. For a bar with a circular cross-sectional area, this corresponds to a radius of  $R_\lambda$  for a bar length of  $7.5 R_\lambda$ . We highlighted in red the optimized structures that do not respect the minimum slenderness ratio in Table 2.3.

Lastly, Fig. 2.9 provides a visual summary of our findings, emphasizing in red the solutions that do not respect the minimum slenderness ratio  $\lambda < 15$ . To effectively show the different orders of magnitude present in the plot and how already done for the continuous mesh case, we have used both linear and logarithmic scales simultaneously. In this case, the compliance exhibits a perfectly linear relationship with respect to  $\sigma_L$ , while the volume follows a hyperbolic law in accordance with Equation 2.38.

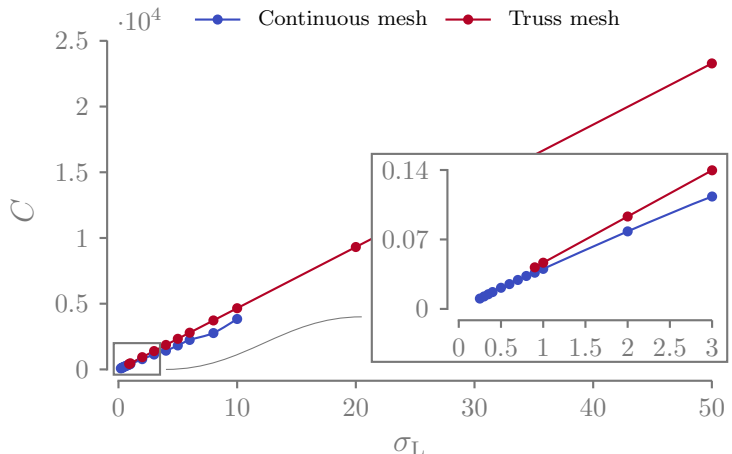


**Figure 2.10:** Compliance  $C$  versus maximum material allowable  $\sigma_L$  plot for the density-based topology optimization and the TTO algorithms.

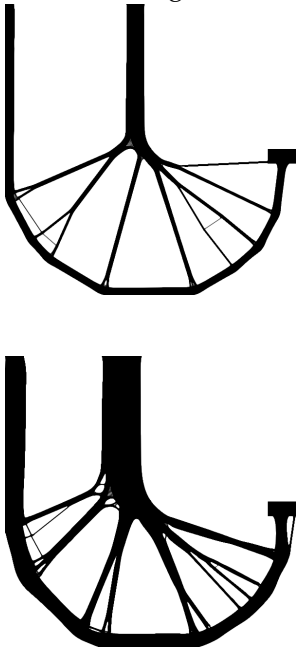
### 2.2.3 DISCUSSION

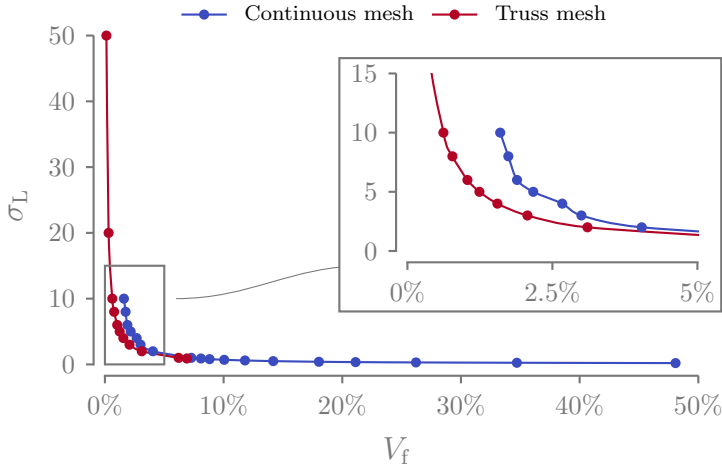
Up until now, we have discussed the results of the density-based topology optimization and the TTO algorithms separately. Here, we provide a comparative analysis by presenting a series of graphs showcasing the key performance indicators considered for both formulations: the maximum material allowable stress  $\sigma_L$ , the compliance  $C$ , the volume fraction  $V_f$ , and the computational time  $t$ . It is important to note that the data presented in these graphs excludes the values that fall outside the methods' limits, highlighted for the two different algorithms in the previous subsections.

Fig. 2.10 depicts the compliance  $C$  versus maximum material allowable  $\sigma_L$  graph for the L-shaped beam test case. It is evident that the truss discretization of TTO consistently exhibits lower compliance values for every considered material allowable and maintains a perfectly linear relationship, in contrast to the continuous discretization approach. We speculate that the difference may be attributed to the more complex formulation (non-linearity, use of the filter, and projection), potentially causing the continuous approach to converge to a local minimum. It is worth noting that the differences between the two methods reduce for small  $\sigma_L$  values.

In Fig. 2.11 we plot the different volume fractions obtained for a given material allowable (the axis in the graph are swapped as for us the most important figure of merit is the volume fraction). The density-based topology optimization yields structures that are more massive for a given material resistance. This outcome can be attributed not only to the aforementioned non-linearity in the formulation but also to another intriguing phenomenon. When dealing with high volume fractions (see e.g. Fig. 2.3c and d), we observe that the material that composes the “beams” of the structure is distributed across multiple elements, appearing somewhat “smeared”. In contrast, the truss representation concentrates all the structural mass along the line extending from one node to another, putting the material exactly

Recall of Fig. 2.3c and d:





**Figure 2.11:** Maximum material allowable  $\sigma_L$  versus volume fraction  $V_f$  plot for the density-based topology optimization and the TTO algorithms.

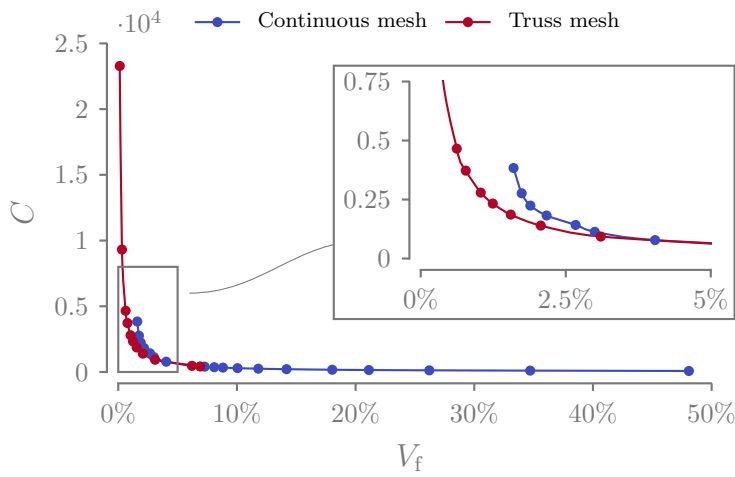


**Figure 2.12:** Compliance  $C$  versus volume fraction  $V_f$  plot for the density-based topology optimization and the TTO algorithms.

where needed and being, thus, numerically more efficient. This fact happens because the truss representation is an idealization, and it emphasizes the importance of ensuring that the chosen discretization remains within its applicable domain.

We can also observe that the truss representation serves as the lower limit of the topology optimization. We speculate that improving the convergence of the density-based topology optimization could potentially lead to results approaching those provided by the TTO algorithm. Interestingly, both discretizations follow a similar trend for high-volume fractions, despite the significant disparity in their physical description models. The very same trends can be observed watching the volume-compliance graph of Fig. 2.12.

Finally, in Fig. 2.13 we turn our attention to the computational time comparison between the two optimization methods. It is noteworthy that a consistent three-order of magnitude difference is observed between the two methods (days vs. minutes) for every value of  $V_f$ . Additionally, it's worth recalling that for this specific test case, employing an extremely fine ground structure is not always a necessity, as we were able to obtain similar results (slightly more than 1 % volume

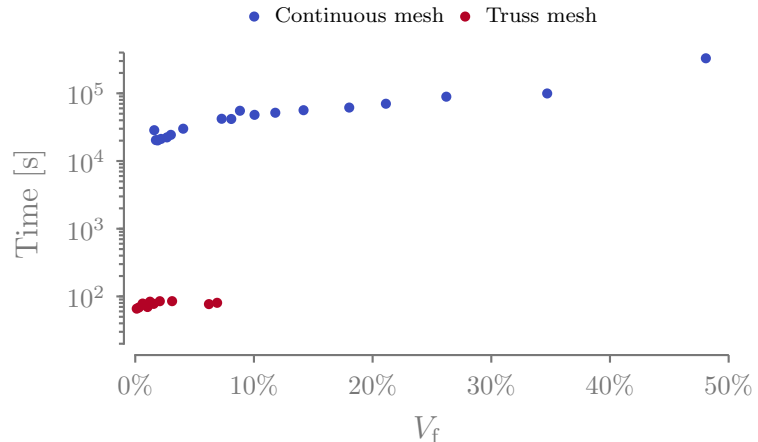


**Figure 2.13:** Computational time  $t$  versus volume fraction  $V_f$  plot for the density-based topology optimization and the TTO algorithms.

difference) with coarser ground structures (97 % fewer bars). This fact implies that the calculation time difference between density-based topology optimization and TTO could potentially be even bigger.

The notable difference in computation time for stress-based density-based topology optimization (which is not self-adjoint, in contrast to compliance minimization) points to the potential for exploring SAND approaches for density-based topology optimization. It's worth mentioning that SAND approaches typically lead to a substantial increase in the number of design variables<sup>4</sup>, but could be beneficial when advanced mechanical constraints are used. In TTO problems, this is less of a concern due to the use of the ground structure approach, which results in numerous cross-sectional area design variables and fewer displacement-related ones. This, however, does not hold when dealing with a continuous mesh. While preliminary studies in this direction have been conducted [181], they lie beyond the scope of this thesis and will not be further investigated.

4: In the SAND approach the displacements  $\mathbf{u}$  are no more evaluated using the linear Finite Element Method (FEM) equation  $\mathbf{K}\mathbf{u} = \mathbf{f}$ , but used as design variables of the optimization.

181. Munro et al. (2017), 'Local stress-constrained and slope-constrained SAND topology optimisation'

182. Bruggi et al. (2012), 'Topology optimization for minimum weight with compliance and stress constraints'

183. París et al. (2010), 'Block aggregation of stress constraints in topology optimization of structures'

184. Norato et al. (2022), 'A maximum-rectifier-function approach to stress-constrained topology optimization'

To sum up, the advantages of the TTO optimization algorithm become evident when considering the limitations of continuous discretization for optimizing ultralight structures. The first key drawback of density-based topology optimization is its increasing need for more elements to correctly discretize low-volume fraction structures, substantially augmenting computational time. Additionally, density-based topology optimization faces several numerical challenges, such as the need for constraint aggregation and relaxation. The optimization formulation proposed in this chapter addresses these problems but introduces another drawback: stress limit in optimized structures often exceed the specified allowable limit. To address this challenge, multiple approaches have been proposed within the aggregation framework to accurately account for the true constraint value, like using a set of active stress constraints [182], several aggregation clusters [183] or rectifier functions [184]. However, all of these strategies come at the cost of increased computation time. Furthermore, stress constraints in continuous discretization are often defined for equivalent von

Mises stress, making it more challenging to distinguish between asymmetric bounds for tension and compression. New failure criteria should then be implemented. Finally, the optimization of ultralight structures naturally tends to result in truss-like topologies regardless of the chosen optimization formulation. These structures are naturally subject to local buckling as a mode of failure [72], a phenomenon that is difficult to describe when using continuous elements.

While truss discretization offers advantages in terms of computational efficiency, it does come with certain limitations. In the minimum volume formulation, the problem is linear and cost-effective to solve. However, the linearity is lost when additional constraints, such as local buckling, are introduced. Moreover, as the FEM equation  $\mathbf{K}\mathbf{u} = \mathbf{f}$  is never explicitly solved during the optimization, the SAND formulation does not inherently account for the kinematic compatibility of the displacements and the forces of the problem. This limitation restricts its applicability to relatively simple problems, such as those presented in this chapter, where kinematic compatibility was inherently satisfied. Issues can arise, however, when dealing with complex scenarios involving multiple loads or constraints that may lead to statically indeterminate structures. These limitations are well-known in the literature of TTO and should be taken into account during the optimization if we decide to pursue the development of the optimization algorithm using the TTO framework.

## 2.3 CONCLUSION

Since the first developments of the topology optimization method, it has been recognized that "For moderately low volume fractions the lay-out of truss-like structures is predicted, but for very low volume fractions it is recommended that the traditional layout theory be employed..." [41]. However, the performance gap has never been quantified, nor has the domain of applicability been assessed. Additionally, it's important to note that these assumptions were primarily based on compliance formulations and not on volume minimization formulations, which are more pertinent to the aeronautical context.

In this chapter, we assessed the suitability of employing the TTO algorithm for the optimization of ultralight structures by quantifying the disparities between density-based topology optimization and TTO under the volume minimization under strength constraints formulation. We introduced a standardized two-dimensional test case, the L-shaped beam, commonly utilized in stress-based optimization scenarios. Multiple optimization runs are conducted for both discretization methods, employing various materials, and the results are subsequently compared, with a primary focus on volume fraction, compliance, stress, and computational time in the optimized structures.

**72.** Sigmund et al. (2016), 'On the (non-)optimality of Michell structures'

**41.** Bendsøe (1989), 'Optimal shape design as a material distribution problem'

The sensitivity calculation is easier, as the different design variables are not explicitly dependent on each other.

Considering the limitations encountered with the continuous approach, particularly at very low volume fractions, we opted to pursue our optimization algorithm development using the Truss Topology Optimization (TTO) framework. The use of a ground structure to discretize the design space is more coherent with the type of structures we are working on, and the use of the SAND approach permits us to drastically reduce the computational time and take into account additional constraints more easily. We also identified certain limitations inherent to truss discretizations, namely the need to take into account the kinematic compatibility of the structure and the local buckling failure mode, which will be addressed in the following chapter.

# ENRICHING THE CLASSIC TTO FORMULATION WITH ADVANCED MECHANICAL CONSTRAINTS

# 3

Chapter 2 highlighted some inherent limitations of the truss modeling and the conventional optimization formulation of Truss Topology Optimization (TTO). These limitations include the minimum slenderness problem and the absence of local buckling and kinematic compatibility constraints. The primary objective of this chapter is to propose a comprehensive formulation capable of addressing these shortcomings. As we will observe, the resulting formulation, if solved in its original form, tends to yield solutions characterized by numerous active and intersecting bars. To mitigate this, we propose a two-step optimization algorithm that offers a means to reduce the solution complexity. Additionally, we introduce a heuristic designed to reduce the influence of the starting point within this two-step optimization algorithm.

In Section 3.1, we detail and model the various mechanical constraints applied in the context of TTO. Subsequently, in Section 3.2, a comprehensive formulation is presented along with an accompanying optimization algorithm. Through the utilization of this optimization algorithm, we are able to maintain control over the complexity of the design. Finally, in Section 3.3, we put the proposed formulation to the test, applying it to various 2D and 3D test cases sourced from the literature, as well as novel cases. The objective is to assess its capabilities and numerical performance.

## 3.1 ADVANCED MECHANICAL CONSTRAINTS

This section aims to introduce additional mechanical constraints that will be utilized in this study, to reduce the need for post-processing at the end of the optimization process, just before the manufacturing phase begins. We begin by addressing the issue of minimum slenderness, a side constraint that is imposed on the cross-sectional area of the active members to guarantee that the solution adheres to the truss modeling. Subsequently, we address the local buckling constraints, a critical failure mode observed in ultra-light truss structures. Particular attention is devoted to examining the stability of nodes within what are known as compressive chains. The combination of local buckling and nodal stability, a phenomenon known in the literature as topological buckling, is discussed. Furthermore, as we want our formulation to be as versatile as possible, we explore the extension of these constraints to accommodate multi-load cases. A challenge arises from the fact that the resulting structures are frequently statically indeterminate. To address this, we introduce an additional mechanical constraint

3.1 ADVANCED MECHANICAL CONSTRAINTS . . . . .	51
3.2 OPTIMIZATION FORMULATION AND SOLVING STRATEGY . . . . .	56
3.3 NUMERICAL APPLICATION . . . . .	62
3.4 CONCLUSION . . . . .	76

Part of the content presented in this chapter has been published as:  
Stragiotti, E. et al. (2024) "Efficient 3D truss topology optimization for aeronautical structures", in *Structural and Multidisciplinary Optimization* [185].

**Table 3.1:** Non-exhaustive list of the existing research in Truss Topology Optimization (TTO) with their corresponding scientific contributions.

Authors	Stress	Local Buckling	Topological buckling	Kinematic compatibility	Multi-load cases	Minimum slenderness
Dorn et al. (1964) [37]	x	-	-	-	-	-
Hemp (1973) [39]	x	-	-	-	x	-
Reinschmidt et al. (1974) [186]	x	x	-	~	-	-
Kirsch (1980) [86]	x	-	-	x	-	-
Oberndorfer et al. (1996) [187]	x	x	-	-	-	-
Silva Smith (1997) [188]	x	x	~	-	x	-
Achtziger (1999a, 1999b) [88, 189]	x	x	x	-	x	-
Stolpe (2004) [25]	x	x	-	x	x	-
Pritchard et al. (2005) [190]	x	-	-	-	x	-
Tyas et al. (2006) [191]	x	x	x	-	x	-
Descamps et al. (2014) [192]	x	x	x	-	x	-
Schwarz et al. (2018) [193]	x	x	-	-	-	-
Cai et al. (2022) [194]	x	x	x	-	-	-
Present work	x	x	x	x	x	x

known as "kinematic compatibility" to ensure that the predicted force field aligns with the displacements of the structure.

In Table 3.1, we provide an overview of historical and contemporary research in the field of TTO, along with their respective scientific contributions. This serves to highlight the necessity for a more comprehensive formulation that incorporates these mechanical constraints, reducing the gap between the optimized design and the actual manufactured structure.

### 3.1.1 MINIMUM SLENDERNESS CONSTRAINTS

As previously discussed in Section 2.2.2, the TTO method shows numerous limitations due to its reliance on the truss model. Therefore, the resulting structures may not be acceptable if the model falls outside the bounds of this idealization. To better study this limit, as outlined in Section 2.2.2, we introduced a metric called bar slenderness, which is defined as follows:

$$\lambda = \frac{\ell}{R_g}, \quad (3.1)$$

where  $R_g$  represents the gyration radius of the cross-sectional area, defined as  $R_g = \sqrt{I/a_i}$ . The primary objective of this section is to introduce an upper limit constraint on the cross-sectional area design variable. This constraint prevents a bar from exceeding the bounds of its idealized model, thereby enhancing the optimization process's robustness.

Remembering that for a circular cross-section  $I = \pi r_i^4/4$ , we can write

$$R_{g,i} = \frac{r_i}{2}. \quad (3.2)$$

The minimum slenderness limit constraints  $g_{\text{slend}}$  are then stated as:

$$g_{\text{slend}} := a_i \leq \frac{4\pi\ell_i^2}{\lambda_{\max}}, \quad \forall i \in [1, \dots, N_{\text{el}}] \quad (3.3)$$

for a fixed  $\lambda_{\max}$ . In this thesis we set  $\lambda_{\max} = 15$ .

### 3.1.2 LOCAL AND TOPOLOGICAL BUCKLING CONSTRAINTS

Adding local buckling constraints to the optimization formulation is fundamental, as ultralight truss structures are often dominated by this mode of failure [72]. By imposing local buckling constraints over a TTO problem (where the lower bound for the members' cross-sectional areas is 0), the optimization domain becomes disjointed [87]. The solution is to be searched inside a degenerate space of the design space of the optimization, known in the literature as singular optimum [195]. Stolpe [196] showed how using the Simultaneous Analysis and Design (SAND) formulation with local buckling and kinematic compatibility constraints, it is possible to find well-optimized structures without the use of relaxation techniques. The authors, however, point out how the solution is still very sensitive to the initialization point of the Non-Linear Programming (NLP) formulation. The local buckling constraints  $g_{\text{buck}}$  are stated using Euler's critical load formula as:

$$g_{\text{buck}} := q_i + \frac{s_i a_i^2}{\ell_i^2} \geq 0 \quad \forall i \in [1, \dots, N_{\text{el}}], \quad (3.4)$$

where  $s_i$  is a parameter dependent on the member material and section topology as follows:

$$s_i = \pi^2 E \beta_i. \quad (3.5)$$

$\beta_i = I_i/a_i^2$  is a positive constant dependent on the moment of inertia and the section of the  $i$ -th bar, and  $E$  is Young's modulus of the material. Assuming that the shape of the cross-section is identical over the whole structure and is independent of  $a$ , it follows that  $\beta_i = \beta$  and  $s_i = s$ ,  $\forall i \in [1, \dots, N_{\text{el}}]$ .

Direct application of the local buckling constraint  $g_{\text{buck}}$  in the optimization formulation tends to create "chains" of unstable compressive members [12, 197, 198]. This problem is known in the literature as topological buckling [88], as the definition of the compressive chains is a function of the topology of the structure, and is one of the elements of the nodal stability of the structure. Additional forms of structure instability, such as global buckling [199–202] or the use of lateral perturbing forces to obtain nodal stability [191, 203] have been studied in the literature. However, since they are beyond the scope of this work, they will not be discussed further.

To illustrate the topological buckling phenomenon, we consider the

- 72. Sigmund et al. (2016), 'On the (non-)optimality of Michell structures'
- 87. Cheng (1995), 'Some aspects of truss topology optimization'
- 195. Guo et al. (2001), 'A new approach for the solution of singular optima in truss topology optimization with stress and local buckling constraints'
- 196. Stolpe et al. (2003), 'A note on stress-constrained truss topology optimization'
- 12. Bendsøe (1995), 'Optimization of Structural Topology, Shape, and Material'
- 197. Zhou (1996), 'Difficulties in truss topology optimization with stress and local buckling constraints'
- 198. Rozvany (1996), 'Difficulties in truss topology optimization with stress, local buckling and system stability constraints'
- 88. Achtziger (1999), 'Local stability of trusses in the context of topology optimization Part I'
- 199. Ben-Tal et al. (2000), 'Optimal Design of Trusses Under a Nonconvex Global Buckling Constraint'
- 200. Kočvara (2002), 'On the modelling and solving of the truss design problem with global stability constraints'
- 201. Neves et al. (1995), 'Generalized topology design of structures with a buckling load criterion'
- 202. Ferrari et al. (2021), 'Topology optimization with linearized buckling criteria in 250 lines of Matlab'
- 191. Tyas et al. (2006), 'Practical plastic layout optimization of trusses incorporating stability considerations'
- 203. Mela (2014), 'Resolving issues with member buckling in truss topology optimization using a mixed variable approach'

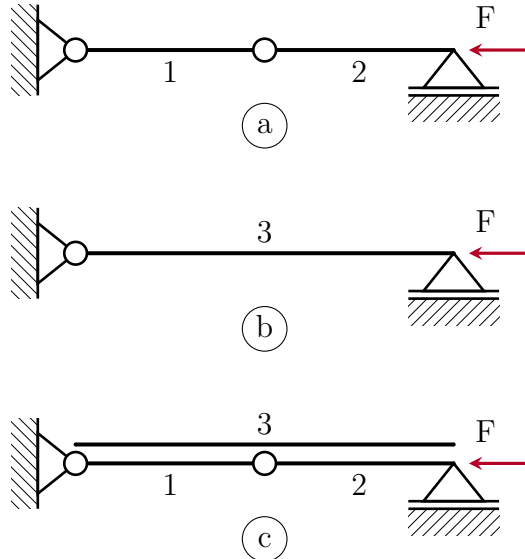


**Figure 3.1:** The three ground structures loaded in compression are used to highlight the topological buckling problem in TTO. (a) Two-bar ground structure loaded in compression; (b) single bar ground structure; (c) overlap of the *a* and *b* ground structures.

case shown in Fig. 3.1a. It consists of a ground structure with  $M = 3$  nodes and  $N_{\text{el}} = 2$  bars with length  $\ell_1 = \ell_2 = \ell$ , and a compressive load of magnitude  $F$  applied at the right-hand side node. For this trivial structure, we can state that  $q_1 = q_2 = F$  and thus  $a_1 = a_2 = a$ . We suppose here that the allowables of the material are such that the local buckling (and not the stress) is the most limiting failure criterion for the bars. Assuming that the shape of the section is equal, the local buckling constraints are written as:

$$q_i \geq -\frac{sa^2}{\ell^2}, \quad i \in [1, 2]. \quad (3.6)$$

However, the structure is unstable because the vertical force equilibrium equation evaluated on the central hinge is satisfied only in an ideal case where no structural imperfections are taken into account.

If the hinge between bars 1 and 2 is deleted, we obtain the structure pictured in Fig. 3.1b with  $\ell_3 = 2\ell$ . The local buckling constraints for bar 3 are thus:

$$q_3 \geq -\frac{sa_3^2}{(2\ell)^2}. \quad (3.7)$$

Combining Equations 3.6, 3.7 and observing that  $q_1 = q_2 = q_3 = F$ , it is now trivial to demonstrate that  $a_3 = 2a$ . Constraint 3.7 leads, then, to more voluminous structures compared to constraint 3.6. For that reason, even if we consider the ground structure given in Fig. 3.1c composed by the superposition of the ground structures given in Fig. 3.1a and Fig. 3.1b, the optimization with a uniform initialization tends to converge to the solution  $a^* = [a, a, 0]$ , unstable but lighter than the physical solution  $a_p^* = [0, 0, 2a]$ .

The easiest way to get rid of the instability of the compressive chains is to post-process the optimized structure and remove the unstable

hinges between the compressive bars. Doing that, the local buckling constraints are not satisfied anymore as the effective buckling length has increased. It is, then, necessary to calculate the section of the new compressive bars to comply with the newly introduced buckling constraints. As extensively shown by Achtziger [189], this post-processing phase leads to structures that are less optimal compared to the ones we could obtain if we take into account the topological buckling in the optimization in the first place.

For that reason, Achtziger proposes an update strategy to modify the length used to evaluate the critical buckling force of 3.4 as follows:

$$\ell_i^*(\boldsymbol{a}) := \begin{cases} \ell_i & \text{if } i \notin \mathcal{C}_{l,r}(\boldsymbol{a}) \\ \sum \ell_r \mid r \in \mathcal{C}_{l,r}(\boldsymbol{a}) & \text{otherwise,} \end{cases} \quad (3.8)$$

where  $r$  represents the  $r$ -th bar of the  $l$ -th compression chain of the structure. The topology-dependent set  $\mathcal{C}_{l,r}(\boldsymbol{a})$  is defined as the set of  $r$  member indexes of the  $l$ -th buckling chain. As internal forces on buckling chains are constant, only the buckling length of the first member of the chain ( $\ell_i^*(\boldsymbol{a})$  with  $i \in \mathcal{C}_{l,1}(\boldsymbol{a})$ ) is modified. Additionally, we add the following side constraints on the other members of the  $l$ -th chain to ensure feasibility:

$$a_r \geq a_{r=1} \quad r \in \mathcal{C}_{l,r}(\boldsymbol{a}), \quad \forall r \neq 1. \quad (3.9)$$

### 3.1.3 KINEMATIC COMPATIBILITY CONSTRAINTS

To optimize test cases that result in statically indeterminate structures, such as structures loaded with multiple load cases or imposed symmetries, we add an additional mechanical constraint called kinematic compatibility [84, 85]. Compatibility can be imposed as a nonlinear constraint in the optimization formulation [86], or can be taken into account by prestressing the initial structure [204].

The kinematic compatibility constraints restrict the displacement field  $\boldsymbol{U} = [U_1, \dots, U_{N_{\text{dof}}}]^T$  in such a way that strains  $\varepsilon_i$  and internal stresses  $\sigma_i$  comply with Hooke's law  $\sigma_i = E_i \varepsilon_i$  with  $i \in [1, \dots, N_{\text{el}}]$ . Recalling that in a truss the relationship between nodal displacements and member deformations is  $\boldsymbol{b}_i^T \boldsymbol{U} = \ell_i \varepsilon_i$  with  $\boldsymbol{b}$  as the  $i$ -th column of the  $\boldsymbol{B}$  matrix, we can formulate the kinematic compatibility constraints  $\boldsymbol{g}_{\text{comp}}$  as:

$$\boldsymbol{g}_{\text{comp}} := q_i - \frac{a_i E_i}{\ell_i} \boldsymbol{b}_i^T \boldsymbol{U} = 0 \quad \forall i \in [1, \dots, N_{\text{el}}]. \quad (3.10)$$

Kinematic compatibility constraints are non-linear as the design variable  $\boldsymbol{q}$  is dependent on  $\boldsymbol{a}$  and  $\boldsymbol{U}$ .

<sup>189</sup>. Achtziger (1999), 'Local stability of trusses in the context of topology optimization Part II'

<sup>84</sup>. Kirsch (1989), 'Optimal topologies of truss structures'

<sup>85</sup>. Rozvany et al. (1995), 'Layout Optimization of Structures'

<sup>86</sup>. Kirsch (1980), 'Optimal design of trusses by approximate compatibility'

<sup>204</sup>. Kirsch (1989), 'Effect of Compatibility and Prestressing on Optimized Trusses'

### 3.2 OPTIMIZATION FORMULATION AND SOLVING STRATEGY

In this section, we propose an innovative TTO formulation developed specifically to minimize the mass of 3D ultralight truss structures, taking into account maximum stress, topological buckling, kinematic compatibility, and minimum slenderness constraints. Combining Formulation  $\mathbb{P}_0$  with Equations 3.4, 3.3, 3.8, 3.9, and 3.10, Formulation  $\mathbb{P}_1$  is stated in terms of members' cross-sectional area  $a$ , member forces  $q$  and nodal displacements  $U$  as follows:

$$\begin{aligned}
 & \min_{\substack{\mathbf{a}, \mathbf{q}^0, \dots, \mathbf{q}^{N_p}, \\ \mathbf{U}^0, \dots, \mathbf{U}^{N_p}}} \quad V = \boldsymbol{\ell}^T \mathbf{a} \\
 & \text{s.t.} \quad \mathbf{B}\mathbf{q}^p = \mathbf{f}^p \quad \forall p \in [0, \dots, N_p] \\
 & \quad \mathbf{q}^p = \frac{aE}{\ell} \mathbf{b}^T \mathbf{U}^p \quad \forall p \in [0, \dots, N_p] \\
 & \quad \mathbf{q}^p \geq -\frac{s\mathbf{a}^2}{\ell^{*2}} \quad \forall p \in [0, \dots, N_p] \tag{\mathbb{P}_1} \\
 & \quad -\sigma_c \mathbf{a} \leq \mathbf{q}^p \leq \sigma_t \mathbf{a} \quad \forall p \in [0, \dots, N_p] \\
 & \quad a_r \geq a_{r=1} \quad r \in \mathcal{C}_{l,r}(\mathbf{a}) \\
 & \quad 0 \leq \mathbf{a} \leq \frac{4\pi\ell^2}{\lambda_{\max}}
 \end{aligned}$$

88. Achtziger (1999), 'Local stability of trusses in the context of topology optimization Part I'

40. Sankaranarayanan et al. (1994), 'Truss topology optimization with simultaneous analysis and design'

The formulation has been extended to multiple load cases given by  $N_p$  external loads vector  $\mathbf{f}^0, \dots, \mathbf{f}^{N_p}$  and the resulting internal forces  $\mathbf{q} = [\mathbf{q}^0, \dots, \mathbf{q}^{N_p}]$  and displacements  $\mathbf{U} = [\mathbf{U}^0, \dots, \mathbf{U}^{N_p}]$ . This proposed formulation expands the multiple load cases formulation of Achtziger [88] with kinematic compatibility constraints, permitting the correct evaluation of the mechanical state of statically indeterminate structures.

The formulation follows the SAND approach [40], where, in addition to the members' cross-sectional area  $a$ , the member forces  $q$  and the structure displacements  $U$  are used as state variables. One of the advantages of SAND approach is that the state variables are independent of each other and, thus, the sensitivity calculation of the constraints functions is usually simpler and leads to sparse partial derivatives. Additionally, compared to Nested Analysis and Design (NAND) formulations, the problem stays well-posed even if the cross-sectional area goes to 0. As the linear system  $KU = f$  is never explicitly solved during the optimization, it is not necessary to impose a lower bound on the members' cross-sectional area  $a$  to avoid a singular stiffness matrix. The last important advantage is that thanks to  $U$  being design variables, it is trivial to add bound constraints on the nodal displacements of the structure if needed.

### 3.2.1 OPTIMIZATION STRATEGY

Formulation  $\mathbb{P}_1$  presents multiple constraints and design variables for every physical bar of the ground structure. The quantity of constraints creates a highly multimodal problem and it proved to be hard for the optimizer to bring to zero the value of the cross-sectional areas. If a NLP optimizer is directly used on Formulation  $\mathbb{P}_1$ , the resulting structure will be composed of a multitude of intersecting bars. The optimizer is, thus, working like it is performing sizing optimization instead of topology optimization—i.e. in the final design all the members of the ground structure are active.

Inspired by the early works by Reinschmidt [186], we propose a novel two-step optimization strategy in which a first optimization solving a relaxed formulation is used to find a good starting point for the second optimization, solving the full Formulation  $\mathbb{P}_1$ . Doing that way, the first optimization explores extensively the relaxed and more regular design space and finds simpler structures, while the second optimization refines the solution imposing additional mechanical constraints. The complete solving strategy is graphically presented in Fig. 3.2.

186. Reinschmidt et al. (1974), 'Applications of linear programming in structural layout and optimization'

In the first step, Problem  $\mathbb{P}_1$  is relaxed: kinematic compatibility constraints are omitted. We call this relaxed Problem  $\mathbb{P}_2$ . Problem  $\mathbb{P}_2$  is solved using a Sequential Linear Programming (SLP) method by iteratively linearizing the local buckling constraints. A heuristic strategy called Reinitialization is iteratively used to reduce the influence of the starting point  $a_0$ . The resulting structure described by the design variables vector  $\tilde{x}^*$  is then post-processed, removing the members whose optimized area is below a fixed cross-sectional area threshold value. The structures generated by solving the relaxed Problem  $\mathbb{P}_2$  proved to be simpler i.e. fewer active members compared to directly solving  $\mathbb{P}_1$  with a NLP optimizer. If the solution is not statically indeterminate the optimization is completed as the kinematic compatibility constraints 3.10 are automatically satisfied and, thus, used to evaluate the optimal displacements.

Otherwise, a second step is needed. Firstly, the ground structure of the problem is simplified, removing all the members that do not appear in the solution of the relaxed Problem  $\mathbb{P}_2$  i.e. avoiding the reintroduction of members discarded by the SLP step. Then, the kinematic compatibility and the exact local buckling constraints are restored, and Problem  $\mathbb{P}_1$  is solved in its original form on the simplified ground structure using a NLP optimizer. The initial values for the cross-sectional areas are the solution  $\tilde{x}^*$  of Problem  $\mathbb{P}_2$ .

### 3.2.2 FIRST STEP: SLP OPTIMIZATION

The first step of the proposed optimization strategy is here described in detail. The relaxed Problem  $\mathbb{P}_2$  obtained by omitting 3.10 and the

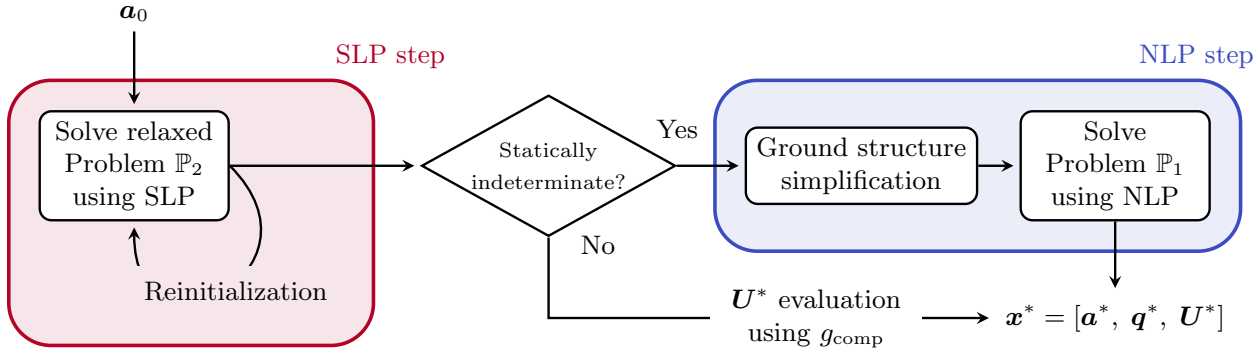


**Figure 3.2:** Flowchart of the two-step optimization strategy used to solve Problem  $\mathbb{P}_1$ .

displacements  $\mathbf{U}$  in Formulation  $\mathbb{P}_1$  is stated as:

$$\begin{aligned}
 & \min_{\mathbf{a}, \mathbf{q}^0, \dots, \mathbf{q}^p} \quad V = \ell^T \mathbf{a} \\
 \text{s.t.} \quad & \mathbf{B}\mathbf{q}^p = \mathbf{f}^p \quad \forall p \in [0, \dots, N_p] \\
 & \mathbf{q}^p \geq -\frac{s\mathbf{a}^2}{\ell^{*2}} \quad \forall p \in [0, \dots, N_p] \\
 & -\sigma_c \mathbf{a} \leq \mathbf{q}^p \leq \sigma_t \mathbf{a} \quad \forall p \in [0, \dots, N_p] \\
 & \mathbf{a}_r \geq \mathbf{a}_{r=1} \quad r \in \mathcal{C}_{l,r}(\mathbf{a}) \\
 & 0 \leq \mathbf{a} \leq \frac{4\pi\ell^2}{\lambda_{\max}}
 \end{aligned} \tag{\mathbb{P}_2}$$

[193] Schwarz et al. (2018), 'Efficient size and shape optimization of truss structures subject to stress and local buckling constraints using sequential linear programming'

Since the objective function and all of its constraints are linear, except for the buckling constraint, this problem is solved by iteratively linearizing the non-linear buckling constraints and using a SLP algorithm. Following the work of [193], the Euler's critical load is iteratively updated using a first-order Taylor expansion for every  $i$  member with cross-sectional area  $a_i^k$  at the iteration  $k$  in the neighborhood of the point  $P_k$  (see Fig. 3.3):

$$\tilde{q}_{i,k}^{\text{cr}} = q_{i,k}^{\text{cr}}(a_i^k) + (a_i^{k+1} - a_i^k) \left. \frac{\partial q_{i,k}^{\text{cr}}(a_i^k)}{\partial a} \right|_{a=a_i^k} \tag{3.11}$$

where  $a_i^{k+1}$  represent the design variable of the SLP at the current iteration and  $q_{i,k}^{\text{cr}}(a_i^k) = -s(a_i^k)^2/\ell_i^{*2}$  represents the Euler's critical load with cross-sectional area  $a_i^k$  and modified buckling length  $\ell_i^*$ .

The linearized local buckling constraints  $\tilde{g}_{\text{buck}}$  are then stated as:

$$q_i \geq \tilde{q}_{i,k}^{\text{cr}}, \text{ with } \tilde{q}_{i,k}^{\text{cr}} = -\frac{s a_i^k (2a_i^{k+1} - a_i^k)}{\ell_i^{*2}} \quad \forall i \in [1, \dots, N_{\text{el}}], \quad (\tilde{g}_{\text{buck}})$$

where superscript  $\sim$  indicates linearized functions and variables.

We can now state the relaxed linearized sub-problem  $\tilde{\mathbb{P}}_2$  obtained

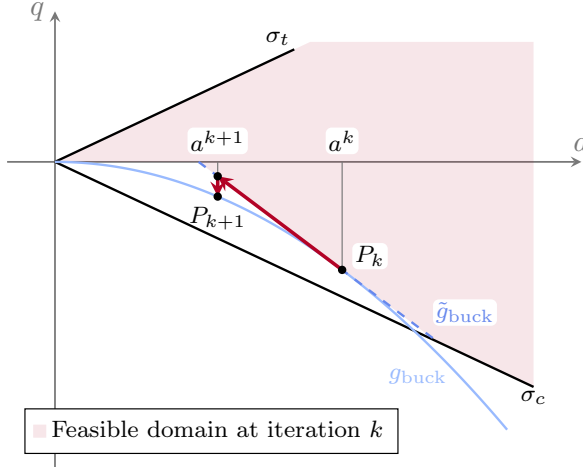


**Figure 3.3:** Linearization of the local buckling constraints for a single bar.

substituting 3.4 with  $\tilde{g}_{\text{buck}}$  in Formulation  $\mathbb{P}_2$ :

$$\begin{aligned}
 \min_{\boldsymbol{a}, q^0, \dots, q^P} \quad & V = \boldsymbol{\ell}^T \boldsymbol{a} \\
 \text{s.t.} \quad & \boldsymbol{B}\boldsymbol{q}^p = \boldsymbol{f}^p \quad \forall p \in [0, \dots, N_p] \\
 & \boldsymbol{q}^p \geq -\frac{s\boldsymbol{a}^k (2\boldsymbol{a}^{k+1} - \boldsymbol{a}^k)}{\ell^{*2}} \quad \forall p \in [0, \dots, N_p] \\
 & -\sigma_c \boldsymbol{a} \leq \boldsymbol{q}^p \leq \sigma_t \boldsymbol{a} \quad \forall p \in [0, \dots, N_p] \\
 & \boldsymbol{a}_r \geq \boldsymbol{a}_{r=1} \quad r \in \mathcal{C}_{l,r}(\boldsymbol{a}) \\
 & 0 \leq \boldsymbol{a} \leq \frac{4\pi\ell^2}{\lambda_{\max}}.
 \end{aligned} \tag{\tilde{\mathbb{P}}_2}$$

Since the objective function and all of its constraints are linear, we can approximate the solution of  $\mathbb{P}_2$  by iteratively solving the subproblem  $\tilde{\mathbb{P}}_2$ . At every iteration  $k$ , the vector of cross-sectional areas  $\boldsymbol{a}^k$  is used to evaluate the linearization point  $P_k$  and calculate the set of linearized buckling constraints  $\tilde{g}_{\text{buck}}$  (see Fig. 3.3). The sub-problem  $\tilde{\mathbb{P}}_2$  is, then, solved using a Linear Programming (LP) solver, and the updated vector of cross-sectional areas  $\boldsymbol{a}^{k+1}$  is used to evaluate the set of linearized buckling constraints of the  $k + 1$  iteration. These steps are repeated until convergence i.e. when  $\|\Delta\boldsymbol{x}\|_\infty \leq \text{tol}_{slp}$ , where  $\Delta\boldsymbol{x}$  represents the difference of the design variable vector  $\boldsymbol{x}$  between two successive iterations.

### 3.2.3 HANDLING LOCAL MINIMA: REINITIALIZATION STRATEGY

If at the end of iteration  $k - 1$  the cross-sectional area of bar  $i$ ,  $a_i^k$ , becomes very small, the gradient of the corresponding local buckling constraint at iteration  $k$  will tend towards 0 and the feasible domain will shrink (see Fig. 3.4). Any bar with near-zero sections will remain as such in future iterations since there is no incentive for the SLP optimizer to increase its value. This is one of the possible reasons why the SLP optimizer gets stuck in local minima.

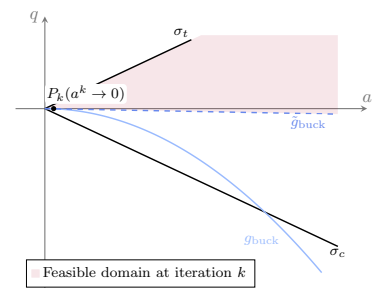


**Figure 3.4:** The linearized buckling constraints (blue dashed line) limit the design space of successive iterations when evaluated on compressive bars with very small areas. Additionally, the gradient of the linearized buckling constraint tends to 0.

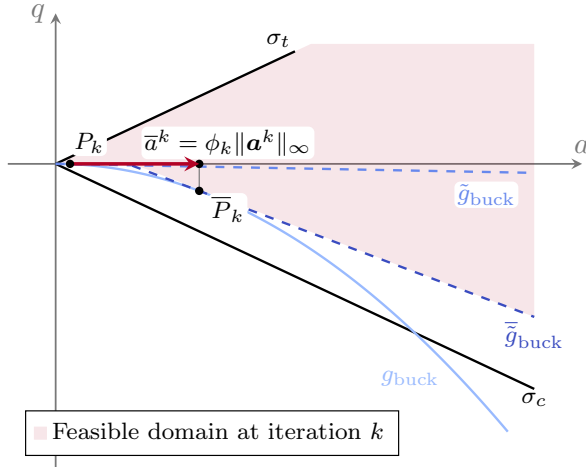


**Figure 3.5:** The reinitialization strategy modifies the linearization point of the members with a small area to promote their reintroduction in the optimization problem.

Subsequently, we propose a heuristic strategy to reinitialize the small cross-sectional area values  $a^k$  used to evaluate the linearized local buckling constraints  $\tilde{g}_{\text{buck}}$  at iteration  $k$ . The strategy is called multiple times during the optimization when the solver converges to a minimum, i.e. when  $\|\Delta x\|_\infty \leq \text{tol}_{slp}$ . It affects only the cross-sectional areas that are smaller than a fraction value  $\tau$  of the maximum value at iteration  $k$ ,  $\|a^k\|_\infty$ . The updated cross-sectional area  $\bar{a}^k$  used to evaluate the linearization point  $\bar{P}_k$  is updated as follows:

$$\bar{a}_i^k := \begin{cases} \phi_n \|a^k\|_\infty & \text{if } a_i^k \leq \tau \|a^k\|_\infty \\ a_i^k & \text{otherwise.} \end{cases} \quad (3.12)$$

The effects of this approach are shown in Fig. 3.5, where it is clear that updating the constraint  $\tilde{g}_{\text{buck}}$  with  $\bar{g}_{\text{buck}}$  reduces the gap between the original and the linearized design space and permits the exploration of new solutions. Additionally, the gradient of the constraint is restored to a non-zero value.

The  $\phi_n$  parameter is used in Equation 3.12 to influence how much the reinitialization heuristic modifies the original formulation. Subsequently, to reach convergence, we propose a continuation scheme on  $\phi_n$  to reduce its impact on the optimization following an exponential decay law:

$$\phi_n = \phi_{n-1}^\beta \quad \forall n \in [1, \dots, n_{\max}], \quad (3.13)$$

where  $n_{\max}$  represent the maximum number of reinitialization calls and the  $\beta$  parameter control the steepness of the exponential progression. In that way, as the number of calls to the reinitialization strategy increases, its influence on the original formulation decreases.

The complete SLP strategy with reinitialization used to solve Problem  $\mathbb{P}_2$  is presented in Fig. 3.6, where the SLP optimized design variable vector is noted as  $\tilde{x}^* = [\tilde{a}^*, \tilde{q}^*]$ .

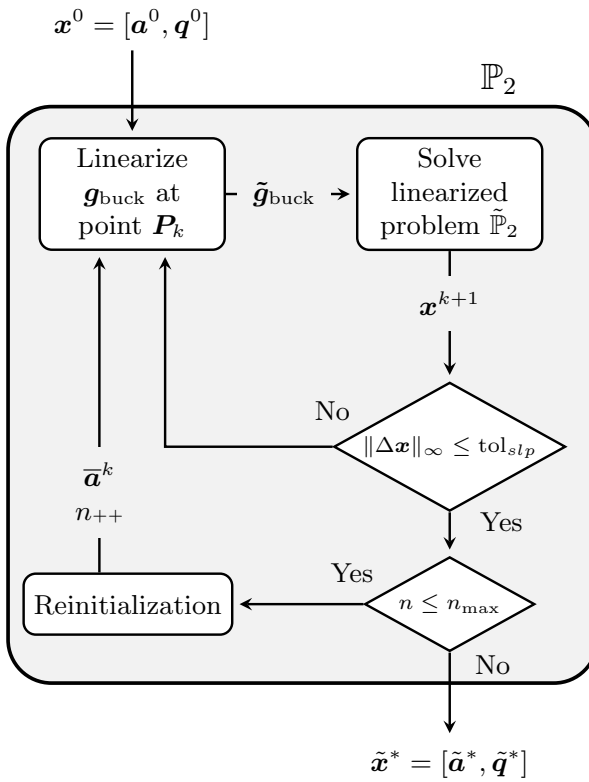


**Figure 3.6:** Flowchart of the SLP strategy with reinitialization used to solve Problem  $\mathbb{P}_2$ .

### 3.2.4 SECOND STEP: NLP OPTIMIZATION

If only one load case and no particular symmetries are imposed on the initial ground structure, the SLP solution  $\tilde{\boldsymbol{x}}^*$  is not statically indeterminate [84, 85]. In that case, it is trivial to evaluate the displacements using 3.10 and the optimization is complete. However, if this is not the case, the stability of the structure is to be tested.

- 84. Kirsch (1989), 'Optimal topologies of truss structures'
- 85. Rozvany et al. (1995), 'Layout Optimization of Structures'

The stability of the SLP-optimized structure is assessed by evaluating the Degree of Static Indeterminacy (DSI) of the truss using Maxwell's criterion:

$$DSI = N_{el} - N_{DOF} - r \quad (3.14)$$

with  $r$  the number of fixed Degrees Of Freedom (DOFs) of the test case. If  $DSI \leq 0$ , the number of equilibrium equations is less than or equal to the number of the internal forces and Equation 3.10 suffices to evaluate the correct displacements of the truss. If, however,  $DSI > 0$ , the truss is potentially statically indeterminate and additional nonlinear constraints must be added to ensure the structure's kinematic compatibility. The optimization is then performed again. We call this second step the NLP step (see Fig. 3.2).

To mitigate the risk of becoming trapped in local minima, the NLP optimizer is employed on a reduced design space. The solution  $\tilde{\boldsymbol{x}}^*$  of the SLP serves the purpose of simplifying the initial ground structure, thereby eliminating elements from the NLP optimization that fall

below the specified threshold value  $a_{\text{thr}}$ :

$$a_i < a_{\text{thr}} \quad \forall i, \text{ with } a_{\text{thr}} = \chi \max(\tilde{\mathbf{a}}^*), \quad (3.15)$$

with the parameter  $\chi$  called the cross-sectional area threshold value.

A linear Finite Element Analysis (FEA) based on the direct stiffness method is performed to provide a correct estimate of forces and displacements caused by the external forces on the solution of Problem  $\mathbb{P}_2$  for the initial point of the optimization. The initial displacement vector  $\mathbf{U}^0$  is calculated as the unique solution to:

$$\mathbf{f} = \mathbf{B}^T \mathbf{q} = \mathbf{B}^T \mathbf{D} \mathbf{e} = \mathbf{B}^T \mathbf{D} \mathbf{B} \mathbf{U}^0 = \mathbf{K} \mathbf{U}^0. \quad (3.16)$$

where  $\mathbf{K}$  is the stiffness matrix of the truss, defined as  $\mathbf{K} = \mathbf{B}^T \mathbf{D} \mathbf{B}$ , with  $\mathbf{D} = \text{diag}(E(\tilde{\mathbf{a}}^* + \delta \mathbf{e})/\ell)$ ,  $\mathbf{e} = [1, \dots, 1]^T$ , and  $\delta = 10^{-12}$ . This last term is added as the structures coming from the SLP step could result in a mechanism with respect to load cases different from the one used for the optimization [37]. Then the initial member forces vector  $\mathbf{q}^0$  is evaluated using 3.10.  $\tilde{\mathbf{a}}^*$ ,  $\mathbf{q}^0$  and  $\mathbf{U}^0$  are used as the starting point of the full NLP formulation where the kinematic compatibility and the exact local buckling formulation are restored. The NLP solver finally outputs the optimized structure variables  $\mathbf{x}^* = [\mathbf{a}^*, \mathbf{q}^*, \mathbf{U}^*]$ .

<sup>37</sup> Dorn et al. (1964), 'Automatic design of optimal structures'

### 3.3 NUMERICAL APPLICATION

In this section, the proposed method is benchmarked against multiple classical and innovative test cases. Firstly, we show how the proposed two-step solution strategy with reinitialization reduces the influence of the starting point on the optimization result compared to the direct NLP optimization of Problem  $\mathbb{P}_1$ . Additionally, as the response surface of the SLP of the proposed method is more regular than the original NLP, the two-step solution strategy generates simple structures i.e. with a low number of active bars, as it is efficient at driving the cross-sectional areas to zero. To show that, we implement and optimize the ten-bar truss and the 2D cantilever beam, two of the most common benchmarks in TTO with buckling constraints. Secondly, to show the ability of the proposed method to work on structures with multiple load cases we implemented a modified ten-bar truss test case where several load cases are applied to the same ground structure. Finally, to assess the computational efficiency and validate the proposed strategy, we optimize a three-dimensional supported beam test case.

The test cases are optimized using different resolution strategies. The proposed method is compared against the direct NLP optimization of Problem  $\mathbb{P}_1$ , denoted in our analysis as NLP. The proposed two-step resolution strategy is implemented with three different maximum numbers of reinitialization calls  $n_{\text{max}}$ : no reinitialization (2S-0R) with

Parameter	Value	Description
$\text{tol}_{\text{slp}}$	$10^{-6}$	Stopping criterion SLP
$\text{tol}_{\text{nlp}}$	$10^{-4}$	Stopping criterion NLP
$\text{max}_{\text{it,SLP}}$	400	Maximum iterations of the SLP algorithm
$\text{max}_{\text{it,NLP}}$	5000	Maximum iterations of the NLP algorithm
$\chi$	$10^{-6}$	Threshold for the ground structure reduction
$\tau$	0.05	Threshold for the reinitialization
$\phi_0$	0.8	Initial reinitialization magnitude parameter
$\beta$	2	Index of the exponential decay law

**Table 3.2:** Values and description of the parameters used for the SLP and NLP optimizations.

$n_{\text{max}} = 0$ , one call of reinitialization (2S-1R) with  $n_{\text{max}} = 1$ , and finally five calls of reinitialization (2S-5R) with  $n_{\text{max}} = 5$ . The reinitialization magnitude parameter  $\phi$  is set up using Equation 3.13 and the parameters listed in Table 3.2, leading to  $\phi = 0.8000$  for the 2S-1R algorithm and to  $\phi = [0.8000, 0.6400, 0.4096, 0.1677, 0.0281]$  for the five reinitialization calls of 2S-5R.

The optimizations are performed using the Python package CVXPY 1.2.2 [178] with the ECOS 2.0.7 [179] solver to solve the relaxed LP Problem  $\tilde{\mathbb{P}}_2$ . The NLP Problem  $\mathbb{P}_1$  is solved using cyipopt [205], a Python wrapper for IPOPT 3.14.11 [35], a large-scale nonlinear optimization package using PARDISO 6.0 [206] as linear solver. The Jacobian and the Hessian of the Lagrangian of the NLP step are calculated at every optimization iteration to allow faster convergence. As every state variable of the optimization is independent of the others, these responses are derived analytically and will not be detailed there. The stopping criteria used for the SLP and NLP optimizations are  $\|\Delta x\|_\infty \leq \text{tol}_{\text{slp}}$ , and  $\|\Delta_{\text{NLP}}\|_\infty \leq \text{tol}_{\text{nlp}}$ , with  $\text{tol}_{\text{slp}} = 10^{-6}$  and  $\text{tol}_{\text{nlp}} = 10^{-4}$  respectively.  $\Delta_{\text{NLP}}$  represents the scaled NLP error, a more comprehensive value used by IPOPT to take into account the optimality of the solution and the constraints violation. The objective function is scaled so that the initial volume is 1000, the areas are in the interval  $[0, 1000]$ , the initial forces in  $[0, 1000]$ , and the displacement in  $[0, 1000]$  for the SLP and the NLP. The full list of parameters used to set up the variable scaling, the SLP optimization, the reinitialization, and the NLP optimization is listed in Table 3.2. Several additional parameters are used in the NLP step for cyipopt and IPOPT:

- ▶ `mu_strategy` is set to `adaptive`
- ▶ `grad_f_constant` is set to `yes`
- ▶ `hessian_constant` is set to `yes`
- ▶ `alpha_for_y` is set to `min-dual-infeas`
- ▶ `linear_solver` is set to `pardiso`
- ▶ `expect_infeasible_problem` is set to `yes`
- ▶ `bound_push` is set to `1e-12`
- ▶ `constr_viol_tol` is set to `1e-6`
- ▶ `nlp_scaling_method` is set to `user-scaling`.

The optimizations presented in this section are performed on a note-

178. Diamond et al. (2016), 'CVXPY: A Python-Embedded Modeling Language for Convex Optimization'

179. Domahidi et al. (2013), 'ECOS: An SOCP solver for embedded systems'

205. Moore et al. (2018), 'cyipopt: Cython interface for the interior point optimizer IPOPT'

35. Wächter et al. (2006), 'On the implementation of an interior-point filter line-search algorithm for large-scale nonlinear programming'

206. Alappat et al. (2020), 'A Recursive Algebraic Coloring Technique for Hardware-efficient Symmetric Sparse Matrix-vector Multiplication'

[207.](#) Stragiotti et al. (2023), 'Truss Topology Optimization with Topological Buckling Constraints Data Set'

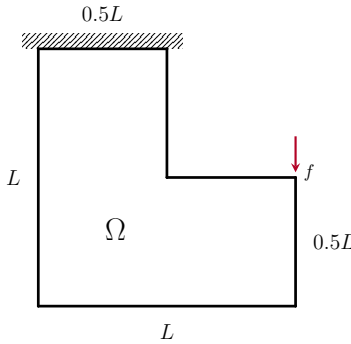


**Figure 3.7:** Boundary conditions of the L-shaped beam test case.

Parameter	Value
$E$	1
$L$	100
$\sigma_L$	[0.20, 1]

**Table 3.3:** Material data used for the optimizations.

book equipped with an Intel Core™ i5-9400H Processor @ 2.50 GHz (4 cores) and 16 GB of RAM. Additionally, the load cases, the starting point, and the result data of all the presented test cases are available in the reference data set [207].

### 3.3.1 L-SHAPED BEAM

To assess the effectiveness of the proposed minimum slenderness limit, we conducted a new round of optimization on the L-shaped beam described in Section 2.2.2 and showed in Fig. 3.7. The material and geometric data are presented in Table 3.3. In the Fig. 3.8, we present the optimized structures obtained using this modified formulation and the stress limits  $\sigma_L$  values of 1, 0.8, 0.3, and 0.2. The first two values have already been used and the results have been presented in Table 2.3. They highlighted the limits of Formulation  $\mathbb{P}_0$  when imposing a specified slenderness limit ( $\lambda < 15$ ). The last two values are introduced here to test how the 3.3 constraints affect the truss topology for extreme cases.

A major focus is put on the shorter bar of the optimized structures to observe how the solution evolved. We observe a redistribution of the same load across multiple smaller bars. More bars became active because there is an upper limit on the cross-sectional area (and thus the force) they can withstand. The four structures present  $N_{el,sl} = 34$ , 38, 56, and 79 active bars, respectively.

In Table 3.4 we compared the new designs limited in minimum slenderness (noted in the table with the 'sl' subscript) to the ones presented in Section 2.2.2 and found that the new designs meet the bar model's slenderness requirements correctly. The number of active bars increases along with the calculation time, but the volume remains nearly the same, indicating there are many solutions with similar volumes. Adding this upper bound constraint, we have extended the domain of application of the TTO. However, we must be careful because very high volumes of fraction solutions can lead to too many bar intersections, resulting in structures with no physical meaning.

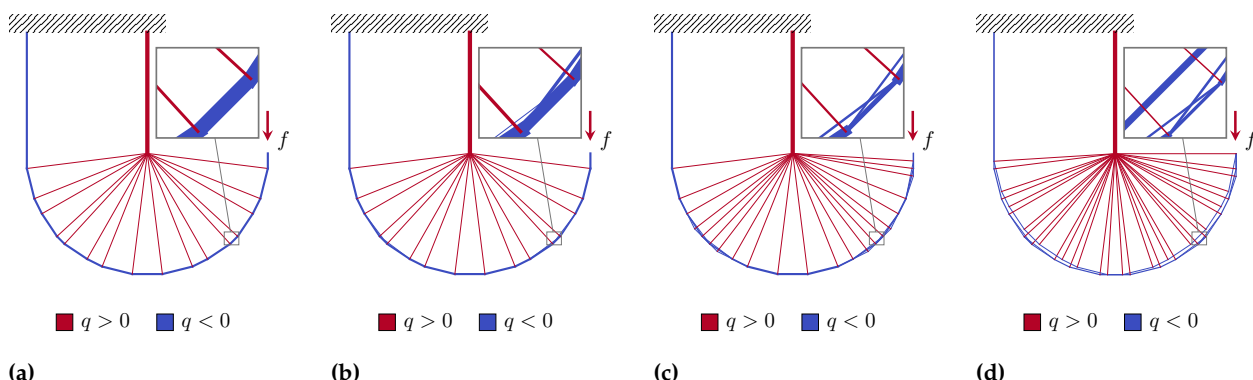


**Figure 3.8:** Topology of the optimized truss structures for different material admissibles  $\sigma_L = 1.0, 0.8, 0.3$  and  $0.2$  with a minimum slenderness limit  $\lambda < 15$ .

**Table 3.4:** Numerical comparison of the effect of the minimum slenderness constraint on the optimization of the 2D L-shaped beam.

$\sigma_L$	$V_f$	<b>Min <math>\lambda</math></b>	$V_{f,sl}$	<b>Min <math>\lambda_{sl}</math></b>	$V_{f,sl}/V_f$	$N_{el,sl}/N_{el}$	$t_{sl}/t$
1.0	6.21 %	15.8	6.21 %	15.8	1.0000	1.00	1.02
0.9	6.90 %	15.0	6.90 %	15.0	1.0000	1.00	1.03
0.8	7.76 %	14.1	7.76 %	15.0	1.0001	1.12	2.27
0.7	8.87 %	13.2	8.87 %	15.0	1.0001	1.12	2.21
0.6	10.35 %	12.2	10.35 %	15.0	1.0002	1.12	1.12
0.5	12.42 %	11.2	12.42 %	15.0	1.0003	1.12	1.07
0.4	–	–	15.53 %	15.0	–	–	–
0.3	–	–	20.71 %	15.0	–	–	–
0.2	–	–	31.06 %	15.0	–	–	–

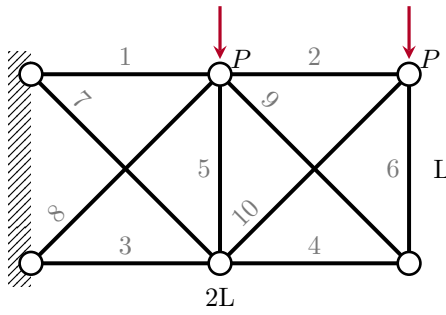


**Figure 3.9:** The ten-bar truss ground structure and load case.

### 3.3.2 TEN-BAR TRUSS

The ten-bar truss is a test case subjected to maximum stress and local buckling constraints proposed by [195] and is shown in Fig. 3.9. It is a small test case with 32 design variables (10 cross-sectional area, 10 internal force, and 12 displacement variables) and 42 constraints (12 force equilibrium, 20 maximum stress, 10 local buckling, and 10 kinematic compatibility constraints) when solved using Formulation  $\mathbb{P}_1$ . The geometry and material data are given in Table 3.5. For simplicity, all numeric values are assumed normalized and dimensionless. We compare the results obtained by our method with those obtained by direct NLP resolution and with the results published by [195] and [196].

The robustness of the optimization algorithms to local minima is evaluated by running 50 optimizations from different initialization points  $a^0$  randomly chosen in the interval  $[0, 100]$ . The first initialization point, denoted  $a_s^0$ , is specifically chosen to match the one used by [196] ( $a_{s,2}^0 = a_{s,8}^0 = a_{s,10}^0 = 0$  and  $a_{s,i}^0 = 50$  elsewhere). This is the starting point from which the authors conclude that the problem is initialization-dependent.

In Fig. 3.10 we show the scatter plot of the optimization of the ten-bar truss for the four considered resolution algorithms, where for every initialization point (X-axis) we show the final volume of the structure. The NLP algorithm converges to different solutions with varying volume values, confirming an abundance of local minima

Parameter	Value
$L$	360
$E$	$1.0 \times 10^4$
$s$	$\pi E/4$
$\sigma_c, \sigma_t$	$\pm 20$
$P$	100

**Table 3.5:** Material data used for the ten-bar truss optimization.

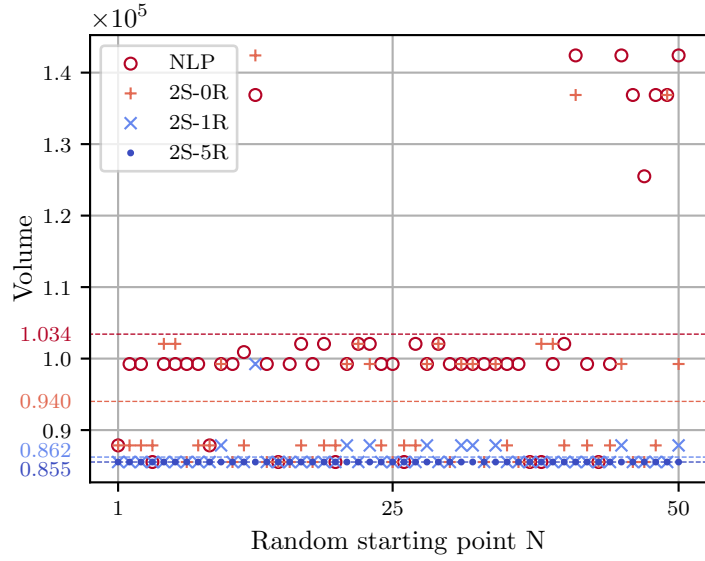


**Figure 3.10:** Scatter plot of the four benchmarked optimization algorithms on the ten-bar truss. The 2S-5R shows a 100 % convergence rate to the lightest structure found. The dashed lines represent the mean of the distributions.

**Table 3.6:** Numerical comparison of the four optimization algorithms on the ten-bar truss for 50 different initial points. The 2S-5R algorithm shows a 100 % convergence rate to the lightest structure found. The iteration count and time are from the first initialization point  $a_s^0$ .

Algorithm	$\bar{V} \pm SD$	Conv.	It.	t [s]
NLP	$(1.03 \pm 0.15) \times 10^5$	14 %	22	0.25
2S-0R	$(9.40 \pm 1.22) \times 10^4$	20 %	4	0.06
2S-1R	$(8.62 \pm 0.21) \times 10^4$	80 %	17	0.24
2S-5R	$(8.55 \pm 0.00) \times 10^4$	100 %	73	1.18
[195]	$8.78 \times 10^4$	-	-	-
[196]	$8.55 \times 10^4$	-	-	-

even for such a small test case with 10 bars. The optimized results are dispersed, and the best design found ( $V = 85534$ ) is only attained 7 times over the 50 optimization runs (14 %). To properly compare the different algorithms, we use two different figures of merit: the mean  $\bar{V}$  and the standard deviation SD of the distribution of the volume of the optimized designs and the ratio of solutions converged to the best result to the total number of initialization points. The numerical results are listed in Table 3.6. The proposed two-step optimization strategy (2S-0R) already reduces  $\bar{V}$  by approximately 9 % compared to NLP, but it is only when we introduce the reinitialization strategy that major improvements are observed, especially when multiple calls of the heuristic are done. The five-calls reinitialization optimization strategy (2S-5R) is not influenced by the initialization point ( $SD = 0$ ), with all solutions successfully converging to the lightest structure.

Let us consider only the first initialization point  $a_s^0$ . In Fig. 3.11 we show the convergence history and the design of the structure throughout the iterations for that specific case. We notice how the initialization point  $a_s^0$  (represented in Fig. 3.11a) corresponds to the topology of the local minimum found by [195]. As extensively shown in Section 3.2.3, if the cross-sectional area of one member is almost or exactly zero the gradient of the local buckling constraint tends to zero and the bar is not considered in the optimization anymore. For that reason, the

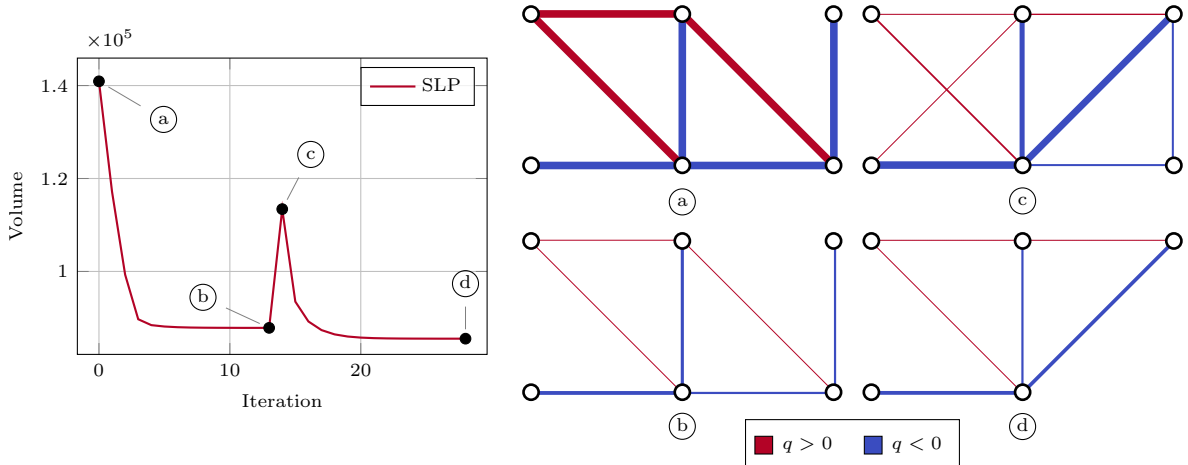


**Figure 3.11:** Volume convergence history for the proposed two-step resolution strategy with one step of reinitialization (2S-1R) for the initialization point  $a_s^0$ . The reinitialization strategy permits to jump from the local minimum (b), with  $V = 87857$ , to the lighter structure (d), with  $V = 85534$ . Only the SLP step is plotted because the solution is statically determinate and kinematic compatibility constraints are already satisfied. In red the members loaded in tension, in blue the members loaded in compression.

optimizer is not able to restore the bars initialized at 0 and promptly converges to a solution that presents the very same topology (see Fig. 3.11b,  $V = 87857$ ). This structure would be the optimization result if no additional steps are done. With a single call of the reinitialization heuristic, the topology is modified as shown in Fig. 3.11c, in which bars 2 and 10 are reintroduced in the set of active members. From this iteration, the optimizer finally converges to the lighter structure shown in Fig. 3.11d with  $V = 85534$ , showing the interest of the reinitialization strategy. We notice how only the SLP step of the proposed two-step strategy is shown here as the optimized structure is statically determinate ( $DSI=0$  and stiffness matrix  $K$  non-singular) and the kinematic compatibility is already satisfied by the optimized design.

It should be mentioned that the proposed heuristic comes with an increase in computational cost. While for the first initialization point, the 2S-0R algorithm converges in only 4 iterations, the single-step 2S-1R and the five-step 2S-5R algorithms converge after 17 and 73 iterations, respectively. The optimization time is slightly more than one second (see the last column of Table 3.6). However, this increase in calculation time is justified by the fact that a single initialization point should suffice to reach an acceptable solution, instead of using a multistart approach.

It is advisable to select the highest number of reinitialization calls (parameter  $n_{\max}$  of Equation 3.13) that is compatible with the user's computational budget. Our research findings suggest that once the parameter  $\phi_k$  (which determines the strength of the heuristic perturbation) drops below 0.01, the reinitialization has no more influence on the result of the linearized problem. Therefore, with the proposed

parameterization of the continuation scheme, pursuing more than five reinitialization calls does not yield additional benefits in the studied test cases.

### 3.3.3 2D CANTILEVER BEAM

The second example we consider is a 2D cantilever beam charged on one extremity as shown in Fig. 3.12. This test case was proposed by Achtziger [189] with the geometry and dimensionless material data given in Table 3.7. The number of the candidate bars of the initial ground structure is  $N_{\text{el}} = 90$ . The complexity of this problem resides in the fact that the geometry and material data are chosen in such a way that the solution with or without local buckling constraints coincides if topological buckling is not considered. The optimized structure shows in this case a volume of  $V = 70.00$ . However, as this structure presents multiple bars in compressive chains, we need to merge them into single bars, recalculate their length, and evaluate their sections to comply with local buckling constraints. By doing so, we would obtain  $V = 99.99$ , an increase of more than 40 % with respect to the optimized structure just found. This load case is built to show the importance of topological buckling and suggests that a lighter solution is to be found between these two bounds.

The 2D cantilever is optimized starting from 100 random points  $\mathbf{a}^0 \in [0, 100]$  and the same four algorithms presented in the previous section. At the end of the optimization, the resulting structures are checked for compressive chains and, if present, they are merged into single bars. The final volume does not change as the effective buckling length  $\ell^*$  is iteratively updated using Equation 3.8 during the optimization. The numerical results are presented in Table 3.8.

**Table 3.7:** Material data used for the 2D cantilever beam optimization.

**189.** Achtziger (1999), ‘Local stability of trusses in the context of topology optimization Part II’

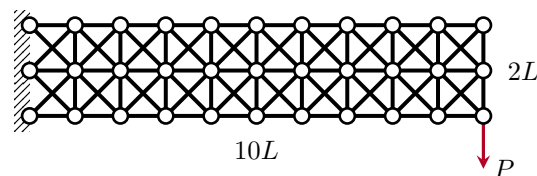


**Figure 3.12:** The 2D cantilever beam load case with a first-order connectivity ground structure. The total number of candidate members is  $N_{\text{el}} = 90$ .

Algorithm	$V_{\min}$	$\bar{V} \pm SD$	$N_{\min}$	$\bar{N}_{\text{el}} \pm SD$
NLP	80.67	$81.34 \pm 2.98$	58	$66.57 \pm 1.13$
2S-0R	79.88	$92.80 \pm 7.45$	10	$25.61 \pm 7.94$
2S-1R	77.78	$88.42 \pm 6.29$	10	$27.86 \pm 6.56$
2S-5R	77.78	$86.72 \pm 6.05$	10	$28.60 \pm 6.44$
[189]	85.58	-	18	-

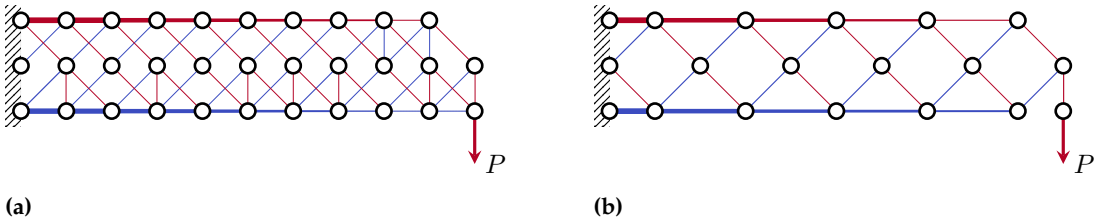


**Figure 3.13:** (a) NLP optimized design of the 2D cantilever beam with a volume of  $V = 80.67$  and high number of active and crossing bars  $N_{\text{el}} = 66$ ; (b) 2S-5R solution  $V = 77.78$  with  $N_{\text{el}} = 31$ . In red the members loaded in tension, in blue the members loaded in compression.

The NLP algorithm shows a good consistency with a mean volume  $\bar{V} = 81.34$  and a low dispersion of the results ( $SD = 2.98$ ), repeatedly converging to a specific solution with  $V = 80.85$ . However, despite the apparent good numerical performance, the solutions always present a high number of active bars, with an average  $\bar{N}_{\text{el}}$  of over 66 bars. As discussed in Section 3.2, the NLP algorithm encounters difficulties in driving the cross-sectional areas to 0. Fig. 3.13a shows the lightest design found using NLP, with  $V = 80.67$  and  $N_{\text{el}} = 66$ .

The proposed two-step formulation without reinitialization 2S-0R drastically reduces the complexity of the structure, with an average number of active bars  $\bar{N}_{\text{el}}$  of around 27, and an absolute minimum of  $N_{\min} = 10$ . However, this simplification of the design comes at the expense of an increased average volume and dispersion ( $\bar{V} = 92.80$  and  $SD = 7.45$ ). This detrimental effect is efficiently counterbalanced with the proposed reinitialization strategy, which reduces the average volume to  $\bar{V} = 86.72$  and  $SD = 6.05$  for 2S-5R. To sum up, the NLP remains stuck in a low-volume local optimum whose volume varies little and that shows a very high number of active bars. With the two-stage strategy, the number of bars of the optimized structures is 58 % lower, resulting in a lighter design in 30 % of cases, and with the best design found that is 3.5 % lighter.

Fig. 3.14 shows how the results of the proposed algorithm are more scattered and do not converge to a single minimum as precedently seen on the ten-bar truss example of Section 3.3.2. A possible explanation for this difference in performance might be the discrete nature of the optimization when topological buckling constraints are taken into account. In some rare cases, we observed that calling the reinitialization makes the optimization converge to a more voluminous design compared to the one we had just before—i.e. the optimizer

**Table 3.8:** Numerical comparison of the 2D cantilever beam of the four algorithms for 100 random initial points. The 2S-5R algorithm shows a good balance between the volume, complexity, and dispersion of the solutions.

$(x_a \ y_a)$	$(x_b \ y_b)$	$\ell$	$q$	$a$	$V$
(0 0)	(1 0)	1.00–5.00	5.00	5.00	
(1 0)	(0 1)	1.41	0.71	0.71	1.00
(1 0)	(2 1)	1.41–0.71	1.02	1.45	
(3 0)	(2 1)	1.41	0.71	0.71	1.00
(3 0)	(4 1)	1.41–0.71	1.02	1.45	
(5 0)	(4 1)	1.41	0.71	0.71	1.00
(5 0)	(6 1)	1.41–0.71	1.02	1.45	
(7 0)	(6 1)	1.41	0.71	0.71	1.00
(7 0)	(8 1)	1.41–0.71	1.02	1.45	
(9 0)	(8 1)	1.41	0.71	0.71	1.00
(9 0)	(10 1)	1.41–0.71	1.02	1.45	
(10 0)	(10 1)	1.00	1.00	1.00	1.00
(0 1)	(1 2)	1.41–0.71	1.02	1.45	
(2 1)	(1 2)	1.41	0.71	0.71	1.00
(2 1)	(3 2)	1.41–0.71	1.02	1.45	
(4 1)	(3 2)	1.41	0.71	0.71	1.00
(4 1)	(5 2)	1.41–0.71	1.02	1.45	
(6 1)	(5 2)	1.41	0.71	0.71	1.00
(6 1)	(7 2)	1.41–0.71	1.02	1.45	
(8 1)	(7 2)	1.41	0.71	0.71	1.00
(8 1)	(9 2)	1.41–0.71	1.02	1.45	
(10 1)	(9 2)	1.41	0.71	0.71	1.00
(0 2)	(1 2)	1.00	5.00	5.00	5.00
(1 0)	(3 0)	2.00–4.00	4.00	8.00	
(3 0)	(5 0)	2.00–3.00	3.00	6.00	
(5 0)	(7 0)	2.00–2.00	2.43	4.87	
(7 0)	(9 0)	2.00–1.00	1.72	3.44	
(1 2)	(3 2)	2.00	4.00	4.00	8.00
(3 2)	(5 2)	2.00	3.00	3.00	6.00
(5 2)	(7 2)	2.00	2.00	2.00	4.00
(7 2)	(9 2)	2.00	1.00	1.00	2.00
				$V_{\text{tot}}$	77.78 <sup>a</sup>

<sup>a</sup>The total volume value is lower than the sum of the member volumes due to the 2 decimal places round-off.

**Table 3.9:** Optimal values of the member forces, areas, and volumes of the 2D cantilever beam.

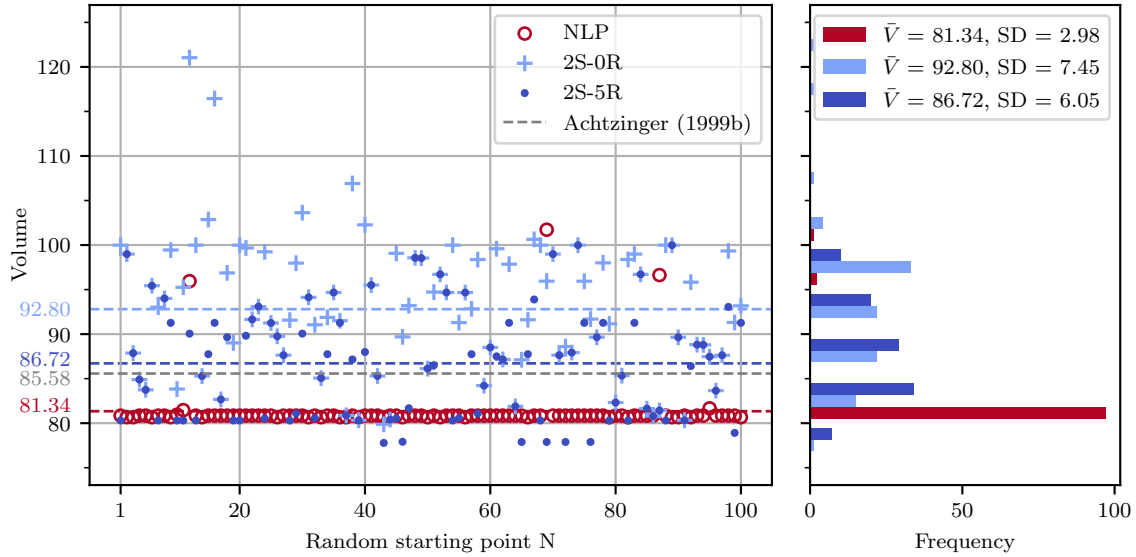


**Figure 3.14:** Left: scatter plot of three of the four benchmarked optimization algorithms on the 2D cantilever beam compared to the solution by Achtziger [189]. The dashed lines represent the mean of distributions. Right: histogram of the distribution of the results of the optimization algorithms.

at the end of the optimization converges to a worse local minimum compared to the ones found just before calling the reinitialization. In these cases, the results presented are the best ones encountered over the optimization steps and not the final ones.

The lightest solution found by 2S-5R with a volume of  $V = 77.78$  and with  $N_{el} = 31$  is presented in Fig. 3.13b. Some of the active members of the optimized design are not present in the original ground structure but are the result of the bar merging process. The optimized design shows a 9 % lower volume with respect to the solution found by Achtziger [189] with  $V = 85.57^1$ . The detailed value of the design variables of the solution can be found in Table 3.9 and in the referenced data set [207]. Approximately 45 % of the solutions of the 2S-5R algorithm are less voluminous than the one found by Achtziger.

189. Achtziger (1999), 'Local stability of trusses in the context of topology optimization Part II'

1: Even if Achtziger [189] reports an optimized volume of  $V = 79.57$ , we use here the value corrected by Tyas [191] of  $V = 85.57$ .

207. Stragiotti et al. (2023), 'Truss Topology Optimization with Topological Buckling Constraints Data Set'

We are aware of the less voluminous solution ( $V = 73.44$ ) found by [191]. The main reason for the difference is that Tyas's method allows the inclusion of bracing-only members that are not required for primary load-carrying purposes to reduce the effective buckling lengths  $\ell$  of internal members. The incorporation of these members is regulated by introducing perturbative forces applied to the structure as additional load cases at unstable nodes. In the specific example of Tyas' structure, the resulting structure is statically admissible, and this ensures that kinematic compatibility is satisfied. However, as demonstrated later in this Chapter, this may not always be the case. Tyas' formulation, in this context, serves only as a lower-bound formulation for minimizing the structure's volume.

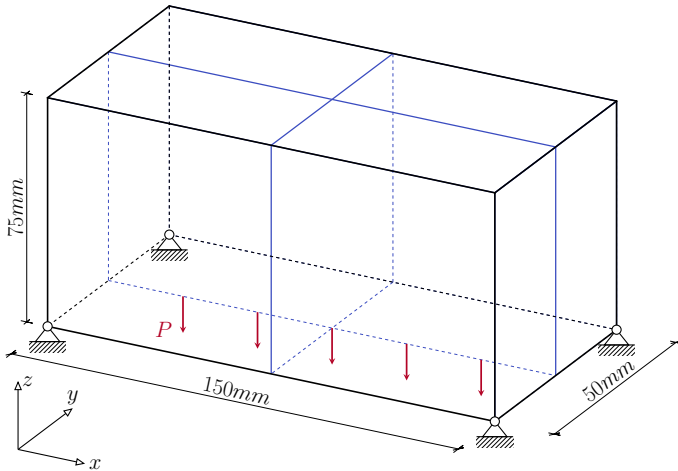


**Figure 3.15:** The simply supported 3D beam example with the load case and boundary conditions. In blue we plot the symmetry planes.

### 3.3.4 SIMPLY SUPPORTED 3D BEAM

In this subsection, we focus on optimizing a simply supported three-dimensional beam. The supports are positioned at all four lower extremities of the design volume, the structure is subjected to five equispaced nodal loads, with each load magnitude set to  $P = 100 \text{ N}$ , applied on the XZ symmetry plane of the structure, as depicted in Fig. 3.15. The volume of the design space is  $150 \text{ mm} \times 50 \text{ mm} \times 75 \text{ mm}$ . These specific dimensions have been selected to accommodate the printing volume of the Creality Halot One, which is an Stereolithography (SLA) 3D printer with maximal printing dimensions of  $127 \text{ mm} \times 80 \text{ mm} \times 160 \text{ mm}$ . The material properties used for the optimization are given in Table 3.10 and mimic a tough SLA resin<sup>2</sup>. The test case exhibits symmetry concerning the XZ and YZ planes (see blue lines of Fig. 3.15), enabling us to mesh and optimize just one-quarter of the structure. This specific portion is meshed using a fully connected ground structure with dimensions of  $4 \times 2 \times 4$  nodes, resulting in a total of 496 elements (or 1984 for the entire structure). For this case, we employ the 2S-5R solving algorithm.

2: The material data has been sourced from [3ds.com/make/solutions/blog/sla-3d-printing-materials-compared](https://3ds.com/make/solutions/blog/sla-3d-printing-materials-compared) and [hubs.com/knowledge-base/sla-3d-printing-materials-compared](https://hubs.com/knowledge-base/sla-3d-printing-materials-compared).

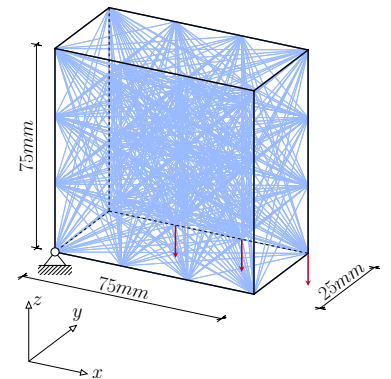


**Figure 3.16:** Ground structure composed of  $N_{\text{el}} = 496$  elements of the symmetric portion used to optimize the simply supported 3D beam.

Table 3.11 and Fig. 3.17 show the numerical results and topology of the optimized structure, respectively. The entire structure features 20 active bars, approximately 1 percent of the original ground structure. In Fig. 3.18, we visualize the stress and buckling constraints applied to the optimized structure. Every compression-loaded bar of the optimized structure activates the buckling constraint, underscoring the critical importance of accounting for this mode of structural failure in a truss. The final structure weights 11.294 g and achieves a volume fraction of 1.761 %. The optimization process is completed within 4 seconds, with only the SLP solved, as the resultant structure is statically determinate and kinematic constraints are inherently satisfied.

Parameter	Value
$E$	2.7 GPa
$\nu$	0.3
$\sigma_c, \sigma_t$	$\pm 55 \text{ MPa}$
$\rho$	$1.14 \text{ g cm}^{-3}$
$P$	100 N

**Table 3.10:** Material data used for the simply supported 3D beam optimization.

**Table 3.11:** Numerical results of the optimization of the simply supported 3D beam.

Quantity	Value
$N_{el}$	1984
$N_{opt}$	20
$V$	$9.907 \text{ cm}^3$
$V\%$	1.761 %
Mass	11.294 g
$a_{max}$	$37.61 \text{ mm}^2$
$C$	3.71 J
$t$	4 s

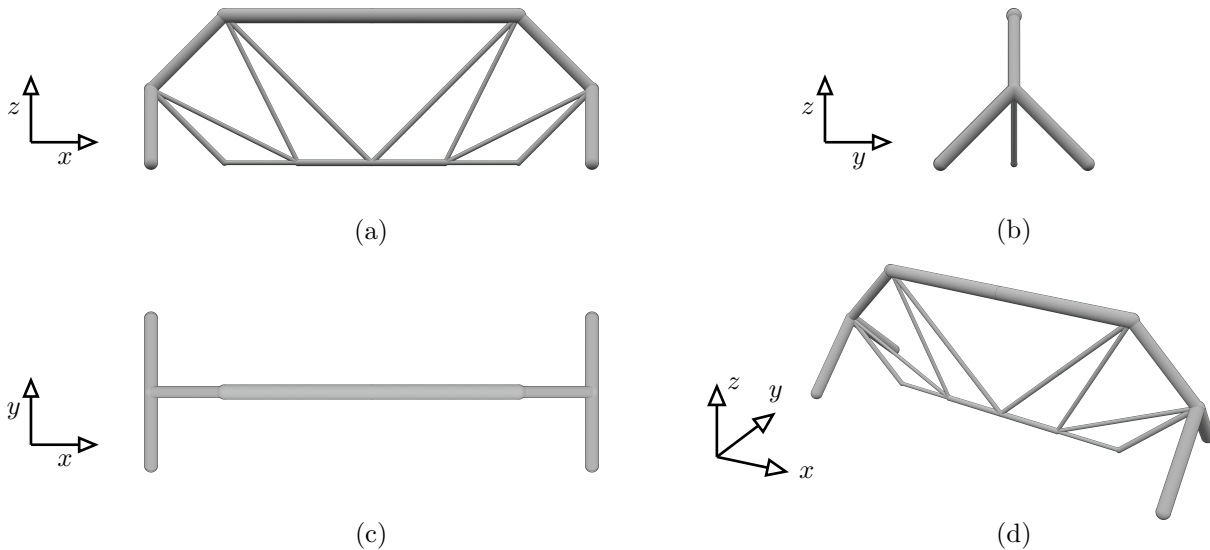


**Figure 3.17:** Orthographic views of the topology of the optimized simply supported 3D beam. (a) XZ plane (b) YZ plane (c) XY plane (d) auxiliary perspective view.

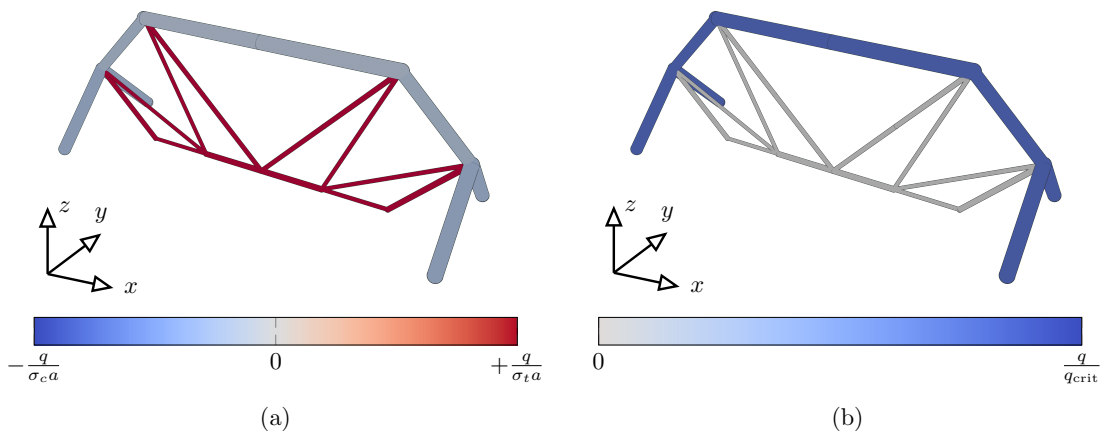


**Figure 3.18:** Maximum stress constraint value (a) and buckling constraint value (b) plotted on the optimized topology of the simply supported 3D beam.

### 3.3.5 TEN-BAR TRUSS WITH MULTIPLE LOAD CASES

We introduce here a more complex example to validate the proposed algorithm on a multiple load cases structure with maximum stress and topological buckling constraints. The test case is obtained by slightly modifying the ten-bar truss presented in Section 3.3.2. The ground structure and the material data are the same, and two load cases  $P_1$  and  $P_2$  are applied at the structure's free extremity symmetrically with respect to the horizontal axis. A graphical presentation of the load case is shown in Fig. 3.19. The loads' magnitude is set to  $P_1 = P_2 = 100$  and the other parameters are listed in Table 3.12.

First, we optimize the structure using the same four algorithms and the starting point presented in Section 3.3.2. Differently from the structures optimized earlier in Sections 3.3.2 and 3.3.3, the solutions of the SLP step are statically indeterminate, as they show a  $DSI > 0$  and a non-singular  $\mathbf{K}$  stiffness matrix. For that reason, the structures undergo the second optimization step in which the kinematic compatibility and the exact buckling constraints are restored (NLP step, see Formulation  $\mathbb{P}_1$ ). The numerical findings of the four algorithms are presented in Table 3.13.

In agreement with previous results, the proposed 2S-5R strategy reduces simultaneously the volume and the dispersion of the solutions. Interestingly, the mean value  $\bar{V}$  of the 2S-0R algorithm is 1.3 % lower with respect to 2S-5R, a fact never observed before. This is due to the 2S-0R algorithm occasionally converging to a heavier solution in the SLP phase that results in a lighter solution once optimized by the NLP, suggesting that the lightest SLP configuration does not always correspond to the lightest NLP design. However, as the difference between the two solutions is low (3.9 %), the 2S-5R algorithm is still preferred thanks to its higher solution consistency (the dispersion  $\sigma$  of 2S-5R is 71 % lower than the dispersion  $\sigma$  of 2S-0R).

We now analyze the lightest solution with a final volume of  $V = 134279.32$ . The optimized design obtained is symmetric. This is consistent with Conjecture 4 made by Rozvany [208], according to which if the boundary conditions and the ground structure are symmetric, and two alternate load conditions are mirror images of each other with respect to the symmetry axis, then at least one globally optimal topology is symmetric. This conjecture has been confirmed in [209] in the case of symmetric convex optimization problems. It is interesting

Parameter	Value
$L$	360
$E$	$1.0 \times 10^4$
$s$	$\pi E / 4$
$\sigma_c, \sigma_t$	$\pm 20$

**Table 3.12:** Material data used for the ten-bar truss optimization.

[208]. Rozvany (2011), 'On symmetry and non-uniqueness in exact topology optimization'

[209]. Guo et al. (2014), 'A confirmation of a conjecture on the existence of symmetric optimal solution under multiple loads'

Algorithm	$\bar{V} \pm SD$
NLP	$1.45 \times 10^5 \pm 1.44 \times 10^4$
2S-0R	$1.33 \times 10^5 \pm 9.56 \times 10^3$
2S-1R	$1.35 \times 10^5 \pm 2.73 \times 10^3$
2S-5R	$1.35 \times 10^5 \pm 2.73 \times 10^3$

**Table 3.13:** Numerical comparison of the four optimization algorithms on the ten-bar truss for 50 different initial points.

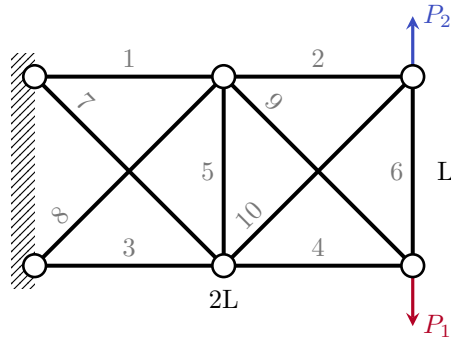


**Figure 3.19:** Ground structure of the ten-bar truss with two applied load cases  $P_1$  and  $P_2$ .

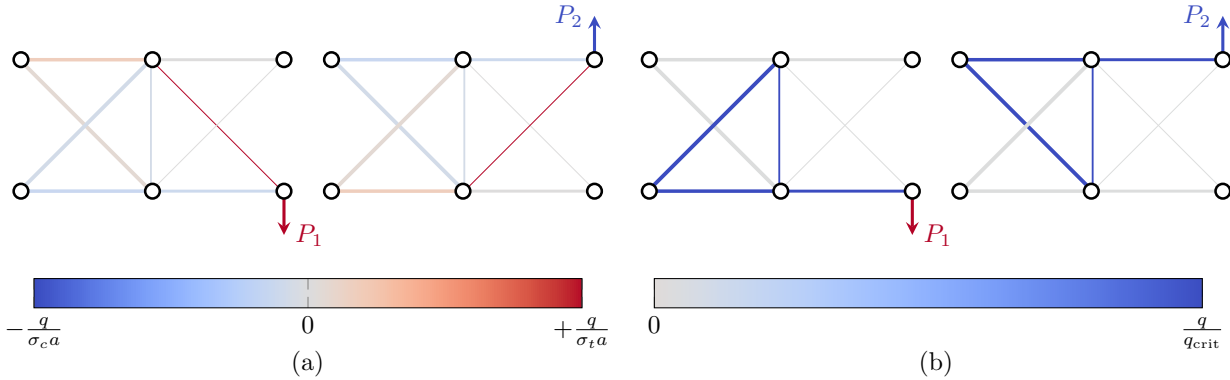


**Figure 3.20:** Maximum stress constraint value (left) and buckling constraint value (right) plotted on the optimized design of the multiple load cases ten-bar truss.

to note that the Conjecture still holds for this specific example even if problem  $\mathbb{P}_1$  is non-linear and non-convex. In Table 3.14 we list the cross-sectional area of the members for the two steps of the proposed solving optimization strategy. The NLP optimized structure presents a volume  $V = 134279.32$ , a 35.15 % increase compared to the predicted volume of the SLP step of  $V = 99084.93$ . Incorporating kinematic constraints to achieve a solution that adheres to elasticity requirements significantly impacts the volume of the optimized solution. The design for the two different load cases  $P_1$  and  $P_2$  is shown in Fig. 3.20, where a side-by-side plot of the maximum stress and buckling constraints is presented. In this example, the bars are constrained by either the buckling or the stress of one of the two load cases. The detailed value of the design variables of the solution is given in Table 3.15, while the iteration history curves of the optimization can be found in Fig. 3.21.

In Fig. 3.21 we provide the iteration history of the objective function and the constraint violation for the SLP and the NLP steps. The graphs on the left depict the evolution of volume during optimization in both the SLP and NLP steps. Looking at the SLP step (red plot), we can see that the SLP reduces the volume and exhibits occasional "spikes," which correspond to the reinitialization heuristic calls. The gradual diminishment of these spikes throughout the optimization is due to the incorporation of the continuation scheme on the parameter  $\phi_k$  of Equation 3.13. Turning our attention to the NLP step, we observe that

Bar	SLP step $\mathbb{P}_2$	NLP step $\mathbb{P}_1$	Difference
$a_1$	57.296	47.987	-16.24 %
$a_2$	40.408	40.621	+0.05 %
$a_3$	57.296	47.987	-16.24 %
$a_4$	40.408	40.621	+0.05 %
$a_5$	40.193	25.547	-36.43 %
$a_6$	0.052	0.000	—
$a_7$	6.997	53.115	+659.11 %
$a_8$	6.997	53.115	+659.11 %
$a_9$	6.997	7.071	+0.01 %
$a_{10}$	6.997	7.071	+0.01 %
V	99084.93	134279.32	+35.51 %

**Table 3.14:** Comparison of the results of the SLP step and NLP step for the multiple load cases ten-bar truss.

$(x_a \ y_a)$	$(x_b \ y_b)$	$\ell$	$q_1$	$q_2$	$\mathbf{a}$	$\mathbf{V}$
(0 360)	(360 360)	360.0	160.5	-139.6	48.0	17 275.4
(360 360)	(720 360)	360.0	0.0	-100.0	40.6	14 623.8
(0 0)	(360 0)	360.0	-139.6	160.5	48.0	17 275.4
(360 0)	(720 0)	360.0	-100.0	0.0	40.6	14 623.8
(360 0)	(360 360)	360.0	-39.6	-39.6	25.6	9197.0
(360 0)	(0 360)	509.1	55.9	-85.5	53.1	27 042.0
(0 0)	(360 360)	509.1	-85.5	55.9	53.1	27 042.0
(720 0)	(360 360)	509.1	141.4	0.0	7.1	3600.0
(360 0)	(720 360)	509.1	0.0	141.4	7.1	3600.0
$V_{\text{tot}}$						134279.32 <sup>a</sup>

**Table 3.15:** Optimal values of the member forces, areas, and volumes of the members of the ten-bar truss with multiple load cases.

<sup>a</sup>The total volume value is lower than the sum of the member volumes due to the one decimal places round-off.

initially the volume is increased and then it descends again, stabilizing at a value that is higher than the one of the NLP starting point. To elucidate this behavior, we refer to the graphs on the right, which present the history of constraint violations in the NLP step. Notably, the starting point of the NLP step always respects equilibrium  $g_{\text{eq}}$  and kinematic compatibility  $g_{\text{comp}}$ , as displacements and forces are evaluated using Equation 3.16. However, stress  $g_{\text{st,c}}$  and  $g_{\text{st,t}}$  and buckling constraints  $g_{\text{buck}}$  are not initially respected, because the force field provided by the SLP does not account for the kinematic compatibility constraint. The NLP optimizer then tries to reduce violations of buckling and stress while temporarily increasing its volume (a phase referred to as the "restoration phase" in the IPOPT algorithm). Ultimately, the optimizer converges to a volume that is slightly higher than what was predicted by the SLP. This aligns with the concept that, by disregarding kinematic compatibility in the SLP step, we have a lower-bound formulation for the volume.

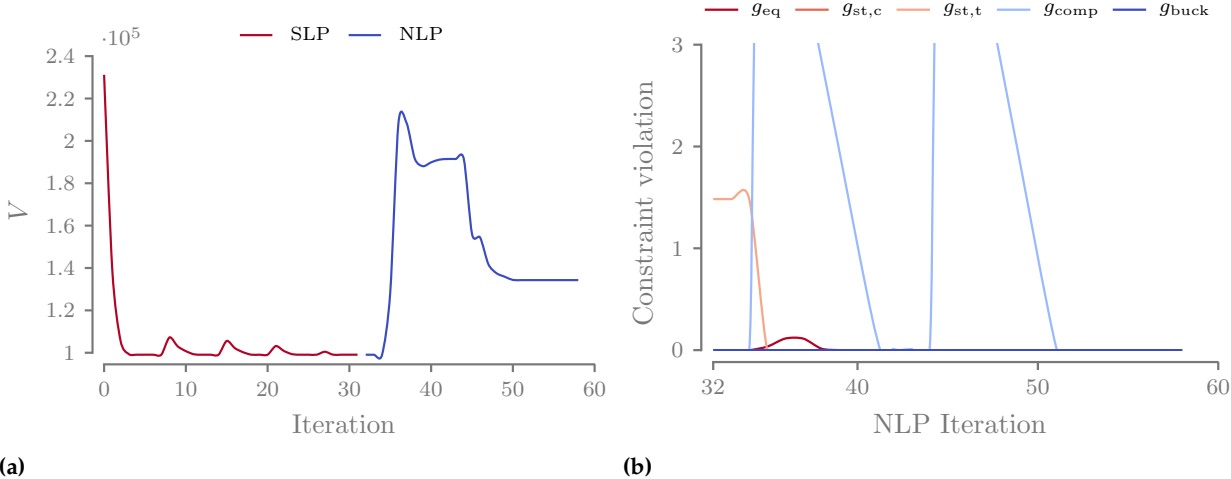


**Figure 3.21:** Iteration history of the ten-bar truss with multiple load cases example solved with the 2S-5R algorithm; (a) objective function history for the SLP and NLP step (b) constraint violation for the NLP step.

### 3.4 CONCLUSION

In this chapter, we presented a structural optimization formulation that minimizes the mass of two- and three-dimensional truss structures subject to multiple load cases, maximum stress, topological buckling, and minimum slenderness constraints. The optimization is solved using an efficient two-step method and shows a reduced influence on the starting point thanks to the proposed reinitialization heuristic. Several numeric examples are presented using the proposed optimization algorithm. Optimized structures display designs with fewer active members compared to traditional optimization methods, leading to lower overall manufacturing complexity. Additionally, thanks to the computational efficiency of the proposed optimization strategy, we show how advanced mechanical constraints such as maximum stress, topological buckling, and kinematic compatibility constraints can be applied and solved on structures with thousands of candidates on a notebook computer.

However, some research questions still remain open. The manufacturing complexity is discussed here only as an outcome of the optimization strategy, but a direct way to impose manufacturing constraints (maximum numbers of bars converging to a single node, minimum section, imposed periodicity of the structure) during the optimization would be beneficial. For that reason, in the next chapters, we study the mechanical behavior of modular structures, exploring the trade-off between mechanical performance and manufacturing complexity.

# OPTIMIZING MODULAR STRUCTURES

Chapter 3 addressed the primary limitations of the classical Truss Topology Optimization (TTO) method by introducing various mechanical constraints such as minimum slenderness of active bars, topological buckling, and kinematic compatibility. However, structures optimized using this algorithm often exhibit complex topologies and regularization methods could enhance the manufacturing phase. This chapter focuses on developing a modular framework for the proposed TTO formulation.

In Section 4.1, we provide a detailed explanation of the modifications needed to apply modular constraints to the TTO. Specifically, we focus on how to model the problem when multiple modules are used and how topological buckling constraints are implemented in modular structures. Finally, in Section 4.2, we evaluate the proposed formulation through various 2D and 3D test cases, aiming to gain a better understanding of modular structures.

## 4.1 FORMULATION OF A MODULAR STRUCTURE OPTIMIZATION ALGORITHM

Assembled modular ultralight structures present an opportunity to greatly improve the performance and cost efficiency of modern aerostructures [117]. The repetitive nature brings various interesting features among which reduced tooling, fast assembly, and short repair time. Additionally, as the mechanical performance of the structure is greatly influenced by the topology and the materials of the repetitive pattern, modular structures are naturally prone to optimization.

In the field of structural optimization, periodic materials are often modeled through asymptotic homogenization [211]. The heterogeneous module topology (also called Representative Volume Element (RVE)) is treated as a homogeneous material with associated mechanical properties i.e. equivalent elastic tensor, shear modulus, etc. The homogenization approach is valid only if the RVE contains enough information about the heterogeneous material and if the structure presents significant periodicity [108, 212].

Nevertheless, our work pertains to structures that frequently exhibit one or more dimensions significantly smaller than the remaining dimensions, such as the thickness of a wingbox or a sandwich panel. In the context of designing modular structures (and not materials), no scale separation is assumed between the repetitive pattern and the structure itself. Consequently, the assumptions of asymptotic

4.1 FORMULATION OF A MODULAR STRUCTURE OPTIMIZATION ALGORITHM . . . . .	77
4.2 OPTIMIZATION OF MODULAR STRUCTURES USING THE VARIABLE LINKING APPROACH . . . . .	82
4.3 CONCLUSION . . . . .	98

Part of the content presented in this chapter has been published and showcased during a conference as: Stragiotti, E. et al. (2022) "Enhanced truss topology optimization (TTO) applied to a cellular wing box", in *ASMO-UK 12, an ISSMO Conference on Engineering Design Optimization*. Book of proceedings. Leeds, United Kingdom [210].

<sup>117</sup>. Cramer et al. (2019), 'Elastic shape morphing of ultralight structures by programmable assembly'

<sup>211</sup>. Zhou et al. (2008), 'Design of graded two-phase microstructures for tailored elasticity gradients'

<sup>108</sup>. Kalamkarov et al. (2009), 'Asymptotic Homogenization of Composite Materials and Structures'  
<sup>212</sup>. Li et al. (2020), 'Anisotropic design and optimization of conformal gradient lattice structures'

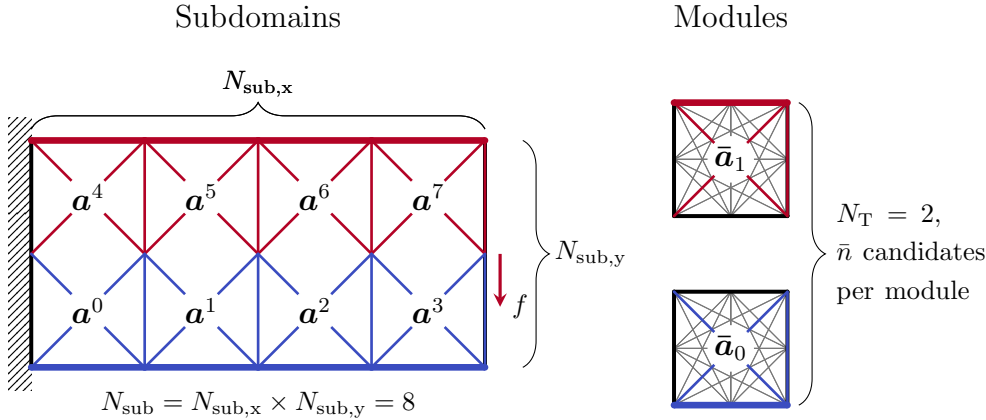


**Figure 4.1:** Notations used for the definition of the variable linking approach used to apply the modularity constraints.

128. Wu et al. (2021), 'Topology optimization of multi-scale structures'

43. Zhang et al. (2006), 'Scale-related topology optimization of cellular materials and structures'

homogenization are not always verified. To address this, full-scale approaches [128] have been developed.

#### 4.1.1 VARIABLE LINKING

The variable linking approach [43] is a full-scale optimization technique that involves first dividing a structure into several subdomains, which are connected in the optimization process – i.e. all subdomains assigned to a given module share the same cross-sectional areas. The primary goal is to make the manufacturing phase simpler and more efficient, allowing to assemble of big structures starting from smaller repetitive modules. With this approach, the optimization perspective shifts. The optimizer design space using the variable linking approach is restricted to the optimization of the topology of the modules, using the whole structure to solely evaluate and impose the necessary mechanical constraints.

We use Fig. 4.1 to illustrate the notation employed in this thesis for modular structures. On the left-hand side of the image, we have the whole test case that we aim to optimize, which is divided into  $N_{\text{sub}}$  subdomains. Each of these subdomains is bound to exhibit the topology of one of the  $N_T$  module topologies presented on the right side of the image. It is assumed for simplicity that each module has the same external shape and an identical ground structure used for discretizing the module volume. Within this framework,  $\bar{n}$  represents the number of candidate bars in one module, and if we assume a fully connected mesh, we can define  $\bar{n} = \bar{m} \cdot (\bar{m} - 1)/2$ , where  $\bar{m}$  stands for the number of nodes in the module. Consequently, for the overall structure, we can write the relationship  $N_{\text{el}} = N_{\text{sub}} \bar{n}$ .

The vector that holds all the cross-sectional areas of the modules is represented by  $\bar{a}$ , and it belongs to the set of positive real numbers  $\mathbb{R}_+^{N_T \bar{n}}$ . This vector is essentially a grouping of individual cross-sectional areas  $\bar{a}_t$  for each of the  $N_T$  modules. In mathematical terms,  $\bar{a}$  is defined as

follows:

$$\bar{\mathbf{a}} := \{\bar{a}_t \in \mathbb{R}_{+}^{\bar{n}} \mid \forall t \in [1, \dots, N_T]\} \quad (4.1)$$

The topology of the entire structure  $\mathbf{a}$ , which originates from the modules' topology  $\bar{\mathbf{a}}$ , is the assembly of the individual cross-sectional areas  $a^j$  of every one of the  $N_{\text{sub}}$  subdomains and is defined as follows:

$$\mathbf{a} := \{a^j \mid \forall j \in [1, \dots, N_{\text{sub}}]\} \quad (4.2)$$

and is evaluated using:

$$\mathbf{a} = \sum_{t=1}^{N_T} \mathbf{h}_t \otimes \bar{\mathbf{a}}_t = \sum_{t=1}^{N_T} \begin{bmatrix} h_{1,t} & \bar{a}_t \\ \vdots & \\ h_{N_{\text{sub}},t} & \bar{a}_t \end{bmatrix} \quad (4.3)$$

where the  $\otimes$  operator represents the Kronecker product. The scalars  $h_{j,t}$  represent binary values, taking either 0 or 1, depending on whether the  $j$ -th subdomain belongs to the  $t$ -th module. These scalars are organized into the column vector  $\mathbf{h}_t$ , which forms the  $t$ -th column of the module mapping matrix  $\mathbf{H} = [\mathbf{h}_0, \dots, \mathbf{h}_{N_T}] \in \mathbb{B}^{N_{\text{sub}} \times N_T}$ , where  $\mathbb{B} = \{0, 1\}$  represents the Boolean domain. The element  $h_{j,t}$  denotes the entry at the  $j$ -th row and  $t$ -th column of the matrix  $\mathbf{H}$ . The module mapping matrix  $\mathbf{H}$  indexes are formally defined as follows:

$$h_{j,t} = \begin{cases} 1 & \text{if the } j\text{-th subdomain belong to the } t\text{-th module,} \\ 0 & \text{otherwise.} \end{cases} \quad (4.4)$$

Lastly, we introduce some notation to denote specific bars within the modules and subdomains. We represent the cross-sectional area of the  $i$ -th bar of the  $t$ -th module as  $\bar{a}_{t,i}$ , while the cross-sectional area of the  $i$ -th bar of the  $j$ -th subdomain as  $a_i^j$ .

#### 4.1.2 TOPOLOGICAL BUCKLING OF MODULAR STRUCTURES

Addressing topological buckling in modular structures is a more complex task compared to monolithic structures. This complexity arises from the fact that we must not only consider bars within a single module's design space but also those connecting different modules. Since the nature of this problem heavily relies on how the modules are arranged within the structure, we have opted for a simplification. We focus only on the assessment of nodal instability within each module: the critical buckling force in Equation 3.4 is evaluated using Equation 3.8, where the topological set  $\mathcal{C}$  only contains the compressive chains of bars that fall inside a module. Additionally, Equation 3.9 is modified as follows:

$$\bar{a}_{t,r} \geq \bar{a}_{t,r=1} \quad r \in \mathcal{C}_{l,r}(\bar{\mathbf{a}}_t) \quad \forall t \in [1, \dots, N_T]. \quad (4.5)$$

In the case of the structure shown in Fig. 4.1 we have:

$$\mathbf{H} = \begin{array}{cc|c} & t=0 & t=1 \\ \begin{array}{c} \mathbf{h}_0 \\ \mathbf{h}_1 \\ \mathbf{h}_2 \\ \mathbf{h}_3 \\ \mathbf{h}_4 \\ \mathbf{h}_5 \\ \mathbf{h}_6 \\ \mathbf{h}_7 \end{array} & \begin{array}{cc} 1 & 0 \\ 1 & 0 \\ 1 & 0 \\ 1 & 0 \\ 0 & 1 \\ 0 & 1 \\ 0 & 1 \\ 0 & 1 \end{array} & \begin{array}{c} j=0 \\ j=1 \\ j=2 \\ j=3 \\ j=4 \\ j=5 \\ j=6 \\ j=7 \end{array} \end{array}$$

as the lower subdomains (numbered from 0 to 3) exhibit the topology of module  $t = 0$ , while the upper subdomains (numbered 4 to 7) show the topology of module  $t = 1$ .

Equation 3.4:

$$q_i + \frac{s_i a_i^2}{\ell_i^{*2}} \geq 0 \quad \forall i \in [1, \dots, N_{\text{el}}],$$

Equation 3.8:

$$\ell_i^*(\mathbf{a}) := \begin{cases} \ell_i & \text{if } i \notin \mathcal{C}_{l,r}(\mathbf{a}) \\ \sum \ell_r \mid r \in \mathcal{C}_{l,r}(\mathbf{a}) & \text{otherwise.} \end{cases}$$

Equation 3.9:

$$a_r \geq a_{r=1}, \quad r \in \mathcal{C}_{l,r}(\mathbf{a}), \quad \forall r \neq 1.$$

We made this choice knowing that the high connectivity of modular structures tends to reduce the occurrence of nodal instability within the structure. Any potential nodal instability in compressive chains at the structure level is addressed in a subsequent post-processing phase.

#### 4.1.3 OPTIMIZATION FORMULATION

The monolithic formulation  $\mathbb{P}_1$  is updated using Equation 4.3 and Equation 4.5 to obtain the modular optimization formulation  $\mathbb{M}_{1,VL}$  that uses the variable linking approach. Formulation  $\mathbb{M}_{1,VL}$  is stated in terms of modular cross-sectional areas  $\bar{\mathbf{a}}$ , member forces  $\mathbf{q}$  and nodal displacements  $\mathbf{U}$  as follows:

$$\begin{aligned}
 \min_{\bar{\mathbf{a}}, \mathbf{q}, \mathbf{U}} \quad & V = \boldsymbol{\ell}^T \mathbf{a} \\
 \text{s.t.} \quad & \mathbf{a} = \sum_{t=1}^{N_T} \mathbf{h}_t \otimes \bar{\mathbf{a}}_t \\
 & \mathbf{B}\mathbf{q} = \mathbf{f} \\
 & \mathbf{q} = \frac{\mathbf{a}E}{\boldsymbol{\ell}} \mathbf{b}^T \mathbf{U} \\
 & \mathbf{q} \geq -\frac{s\mathbf{a}^2}{\boldsymbol{\ell}^*{}^2} \\
 & -\sigma_c \mathbf{a} \leq \mathbf{q} \leq \sigma_t \mathbf{a} \\
 & \bar{\mathbf{a}}_{t,r} \geq \bar{\mathbf{a}}_{t,r=1} \quad r \in \mathcal{C}_{l,r}(\bar{\mathbf{a}}_t), \forall t \\
 & 0 \leq \bar{\mathbf{a}} \leq \frac{4\pi\bar{\ell}^2}{\lambda_{\max}}
 \end{aligned} \tag{\mathbb{M}_{1,VL}}$$

where  $\bar{\boldsymbol{\ell}}$  represents the vector of the lengths of the bars within the modules.

The total number of design variables in the formulation is expressed as  $N_T \bar{n} + N_{\text{sub}} \bar{n} + 2M$  or  $N_T \bar{n} + N_{\text{sub}} \bar{n} + 3M$ , depending on whether the test case is two or three-dimensional. The number of constraints is, however, the same as in the monolithic optimization. This is due to the localized nature of stress, buckling, and compatibility constraints, which are all defined at the structure level and not referred only to individual modules.

The formulation is solved by reusing the proposed two-step optimization algorithm, incorporating the reinitialization heuristic to mitigate dependence on the optimization starting point, as detailed in Section 3.2.1. We state here the formulation  $\mathbb{M}_{2,VL}$  with relaxed compatibility constraints that are solved as the first step of the optimization.

$$\begin{aligned}
\min_{\bar{\alpha}, q, U} \quad & V = \boldsymbol{\ell}^T \boldsymbol{a} \\
\text{s.t.} \quad & \boldsymbol{a} = \sum_{t=1}^{N_T} \boldsymbol{h}_t \otimes \bar{\boldsymbol{a}}_t \\
& \boldsymbol{B}\boldsymbol{q} = \boldsymbol{f} \\
& \boldsymbol{q} \geq -\frac{s\boldsymbol{a}^2}{\boldsymbol{\ell}^{*2}} \tag{\mathbb{M}_{2,VL}} \\
& -\sigma_c \boldsymbol{a} \leq \boldsymbol{q} \leq \sigma_t \boldsymbol{a} \\
& \bar{\boldsymbol{a}}_{t,r} \geq \bar{\boldsymbol{a}}_{t,r=1} \quad r \in \mathcal{C}_{l,r}(\bar{\boldsymbol{a}}_t), \forall t \\
& 0 \leq \bar{\boldsymbol{a}} \leq \frac{4\pi\bar{\boldsymbol{\ell}}^2}{\lambda_{\max}}
\end{aligned}$$

We can solve Formulation  $\mathbb{M}_{2,VL}$  by breaking it down into simpler linearized problems using a Sequential Linear Programming (SLP) algorithm. This is possible because the Kronecker product is a linear operator, and the buckling constraints can be linearized, as previously demonstrated in Section 3.2.1.

#### 4.1.4 SENSITIVITY ANALYSIS

During each iteration of the optimization process, the current state of the structure is determined by the values assigned to the design variables. In structural optimization, the evolution of the structure's design is guided by assessing the sensitivities of both the objective function and constraints with respect to the design variables. In the specific context of the optimization of modular structures, the module (and not the structure divided into subdomains) is identified as the design domain, and for that reason necessitating the derivation of corresponding modular sensitivities.

The approach involves initially computing gradients for all candidates for the full monolithic structure, without considering the modularity. Subsequently, the contributions of each  $i$ -th bar belonging to a specific module topology  $t$  are summed together. Mathematically, this can be expressed as follows:

$$\frac{\partial(\cdot)_i}{\partial \bar{a}_{t,i}} = \sum_{j=0}^{N_{\text{sub}}} \boldsymbol{h}_t^T \frac{\partial(\cdot)_i}{\partial a_i^j} \tag{4.6}$$

where  $(\cdot)$  is a generic quantity for which the sensitivity is calculated. This process is graphically represented in Fig. 4.2.

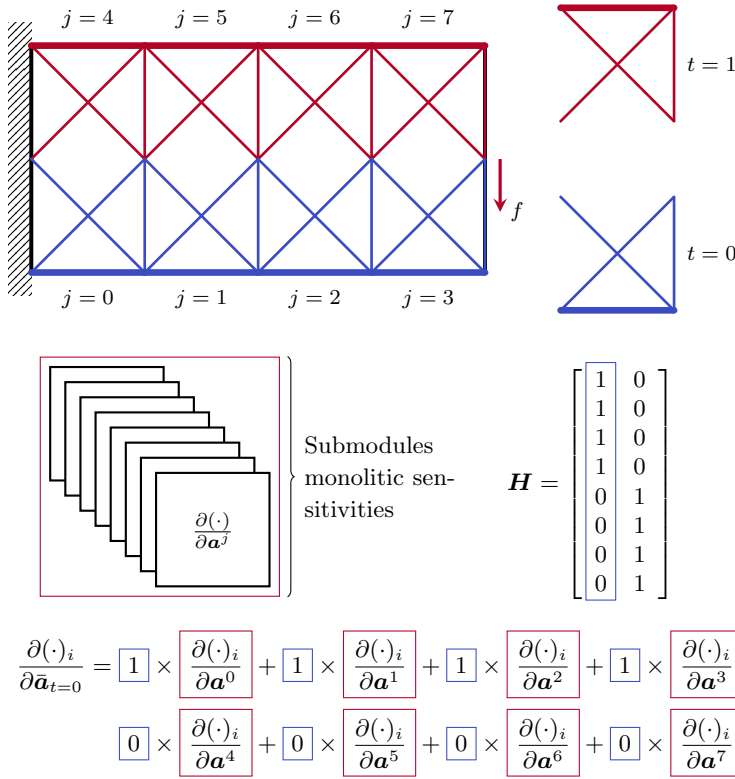


**Figure 4.2:** Notations used for the evaluation of the sensitivities for the optimization of modular structures based on the variable linking scheme.

## 4.2 OPTIMIZATION OF MODULAR STRUCTURES USING THE VARIABLE LINKING APPROACH

Parameter	Value
$\phi_0$	0.8
$\beta$	2

**Table 4.1:** Reminder of the parameters used to set the reinitialization parameters for the modular optimization. The full list of values and tolerances used for the setup of the optimization algorithm can be found in Table 3.2.

178. Diamond et al. (2016), 'CVXPY: A Python-Embedded Modeling Language for Convex Optimization'

179. Domahidi et al. (2013), 'ECOS: An SOCP solver for embedded systems'

205. Moore et al. (2018), 'cyipopt: Cython interface for the interior point optimizer IPOPT'

35. Wächter et al. (2006), 'On the implementation of an interior-point filter line-search algorithm for large-scale nonlinear programming'

In this section, we formulate multiple test cases used to explore the limits and the characteristics of modular structures and the proposed modular structural optimization formulation  $\mathbb{M}_{1,VL}$ .

The test cases are optimized using the two-step resolution strategy implemented with five calls of reinitialization (2S-5R) with  $n_{\max} = 5$ . The reinitialization magnitude parameter  $\phi$  is set up using the same parameters listed in Table 4.1, that leads to  $\phi = [0.8000, 0.6400, 0.4096, 0.1677, 0.0281]$ .

The optimizations are performed using the Python package CVXPY 1.2.2 [178] with the ECOS 2.0.7 [179] solver to solve the relaxed Linear Programming (LP) Problem  $\mathbb{M}_{2,VL}$ . The Non-Linear Programming (NLP) Problem  $\mathbb{M}_{1,VL}$  is solved using cyipopt [205], a Python wrapper for IPOPT 3.14.11 [35], a large-scale nonlinear optimization package using PARDISO 6.0 [206] as linear solver.

### 4.2.1 ON THE EQUIVALENCE OF MULTI-LOAD CASES AND MODULAR STRUCTURES

The first test case we deal with is a two-dimensional bridge structure segment composed of two subdomains ( $n_{\text{sub}} = 2$ ) with symmetric

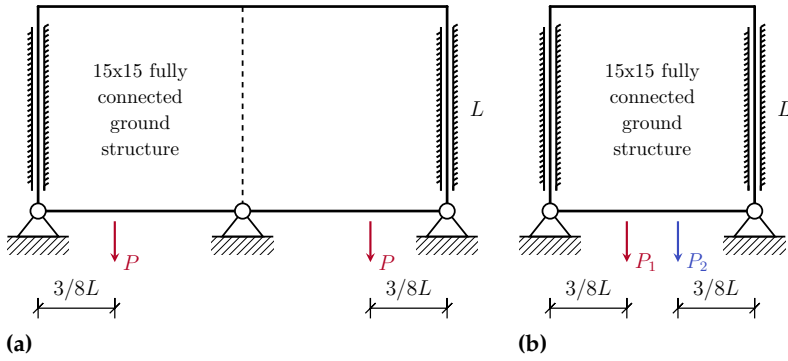


**Figure 4.3:** Boundary conditions of the multi-subdomains (a) and the multi-load cases (b) test cases.

**Table 4.3**

Quantity	Multi-subdomain	Multi-loads
$N_{\text{sub}}$	2	1
$N_{\text{opt}} (N_{\text{el}})$	62 (50400)	31 (25200)
$V$	182.692	91.346

boundary conditions, as illustrated in Fig. 4.3a. In this test case, two vertical loads of magnitude  $P=1$  are applied to the lower side of the design space. The material and geometrical details are given in Table 4.2 and are normalized and adimensional for simplicity. Each subdomain of the structure is discretized using a  $15 \times 15$  fully connected ground structure, with a number of candidates  $\bar{n} = 25200$  per subdomain. It is important to note that, for this example, buckling constraints have been deactivated.

Additionally, a similar structure is optimized, comprised of a single subdomain subjected to two distinct load cases, denoted as  $P_1$  and  $P_2$ . These loads are positioned at precisely the same distance from the support as the structure with multiple subdomains, as illustrated in Fig. 4.3b. The subdomain is discretized using the same  $15 \times 15$  fully connected ground structure.

The optimization is carried out for both structures, utilizing the material data specified in Table 4.2. The joint cost is set at  $s = 0.05$  for the multi-subdomain structure and  $s = 0.1$  for the multi-load case structure. The graphical representation of the optimized structures is given in Fig. 4.4. Remarkably, the resulting subdomain topologies are identical, with the volume of the multi-subdomain structure  $V_1$  being precisely twice the volume of the multi-load cases structure  $V_2$ .

This straightforward example highlights an interesting aspect of optimization of modular structures that aligns with common sense. When a loaded structure is divided into multiple subdomains, each subdomain, when isolated and subjected to appropriate boundary conditions defined by the reaction forces of adjacent bars and supports, experiences multiple loading conditions. By imposing modularity constraints on all these subdomains, the optimization process seeks the optimal structure that simultaneously meets the mechanical needs of all these diverse load cases. Hence, there exists an equivalence between

206. Alappat et al. (2020), 'A Recursive Algebraic Coloring Technique for Hardware-efficient Symmetric Sparse Matrix-vector Multiplication'

Parameter	Value
$L$	100
$E$	1
$\sigma_c, \sigma_t$	$\pm 1$
$P$	1

**Table 4.2:** Material data used for the modular bridge section 2D structure.

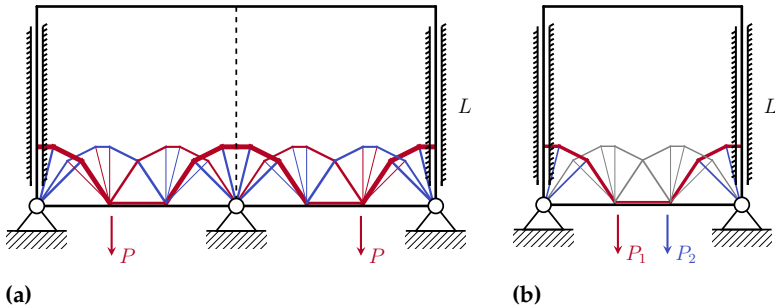


**Figure 4.4:** Optimized structures of the multi-subdomains (a) and the multi-load cases (b) test cases. The resulting module topology is equal for the two cases. In red the bars are in a tensile state, and in blue the bars are in a compressive state.

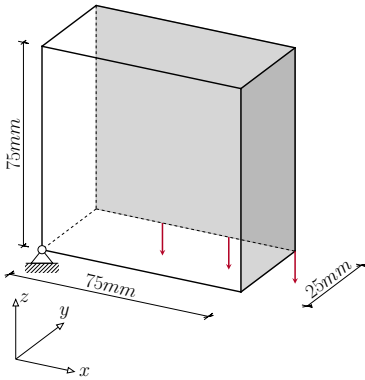


**Figure 4.5:** Symmetric boundary conditions of the simply supported 3D beam. In gray are the symmetry planes of the test case.

Parameter	Value
E	2.7 GPa
$\nu$	0.3
$\sigma_c, \sigma_t$	$\pm 55$ MPa
$\rho$	$1.14 \text{ g cm}^{-3}$
P	100 N

**Table 4.4:** Material data used for the simply supported 3D beam optimization.

optimizing a multi-subdomain structure with modular constraints and performing a multi-load case optimization solely on the module. Consequently, as extensively seen in Section 3.3.5, when dealing with multiple load cases it is necessary to take into account kinematic compatibility in the optimization formulation. This example confirms then the necessity of adding kinematic compatibility constraints when addressing modularity constraints.

#### 4.2.2 PARAMETRIC STUDY ON THE NUMBER OF SUBDOMAINS AND THE COMPLEXITY OF THE MODULE

Here, we perform a parametric study on the modular parameters that are used to optimize the simply supported 3D truss, which was previously analyzed as a monolithic structure in Section 3.3.4. In this study, we focus on a single module  $N_T = 1$ , excluding for the moment the possibility of using multiple module topologies. Additionally, we restrict our investigation to a single module geometry (called also type) with a cubic cell shape. A summary of the loading case, as well as the geometric and material properties of the test case, is presented in Table 4.4 and depicted in Fig. 4.5.

We introduce two new metrics used to enhance our understanding of how modular structures are subjected to loading. The first metric, named the structural efficiency index and denoted as  $\varphi$ , is defined as:

$$\varphi = \frac{N_{\text{opt},f} \times 100}{N_{\text{opt}}}. \quad (4.7)$$

Here,  $N_{\text{opt},f}$  represents the number of bars that activate either the tensile stress, compressive stress, or buckling constraints and is expressed as:

$$N_{\text{opt},f} = \text{card}(\{i \mid c_{f,i} > 0.95\}), \quad (4.8)$$

where  $c_f = \max(-q/\sigma_c a, q/\sigma_t a, q/q_{\text{crit}})$  represent the normalized mechanical failure criterion and  $\text{card}(\{\cdot\})$  represent the cardinality of the set  $\{\cdot\}$ .  $\varphi$  enables a rapid assessment of how close the structure is to the optimal fully stressed state as described by Michell [90]. Since we are accounting for not only tensile and compressive stress but also local buckling, we define a bar as fully stressed when it activates one or more of the three mechanical failure constraints.

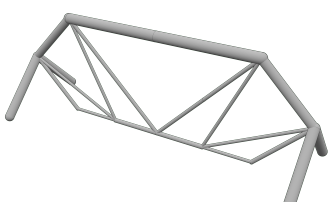


**Figure 4.6:** Perspective view of the monolithic simply supported 3D beam optimized structure with  $V = 9.907 \text{ cm}^3$

90. Michell (1904), 'The limits of economy of material in frame-structures'

The second metric is defined as the mean value of the normalized mechanical failure criterion  $c_f$ , weighted by the volumes of individual bars  $v$ :

$$\psi = \frac{1}{V} \left( \sum_{i=0}^{N_{\text{opt}}} v_i c_{f,i} \right) \quad (4.9)$$

This parameter ranges between 0 and 1, with higher values indicating that, on average, bars are closer to the upper limit of one of the mechanical failure constraints. Notably, greater importance is attributed to more voluminous bars.

**INFLUENCE OF THE NUMBER OF THE SUBDOMAINS** We begin by examining the impact of the number (and consequently, the module scale, interchangeably used here) of subdomains  $N_{\text{sub}}$  in the structure. The structure is partitioned into a varying number of cubic and equally sized subdomains while keeping the test case and material constant. Specifically, the entire structure is subdivided into 6x2x3, 12x4x6, 18x6x9, and 30x10x15 subdomains along the X, Y, and Z axes, and each subdomain is discretized by a 2x2x2 fully connected ground structure with  $n_{\text{bar}} = 28$ . The same analysis is also conducted on a 3x3x3 fully connected ground structure with  $n_{\text{bar}} = 351$  to verify that the trend observed remains consistent across varying cell complexities.

The parametric findings on the impact of the number of subdomains in the structure are summarized in Table 4.5. The table presents numerical results alongside graphical representations of the optimized structures' modules for varying sizes of the repeating module. The first key observation is the significant influence of the module scale on the optimized volume. This relationship is evident in Fig. 4.7, where the volume exhibits an almost linear correlation with the number of subdomains, a trend that persists even for the higher complexity 3x3x3 modules. Regarding computational time, a similar relationship is noted. Despite the number of design variables remaining constant, the increase is attributed to the growing number of mechanical constraints. It is important to highlight that in modular optimization, mechanical constraints are evaluated for every member of the structure, not just within the module. Finally, the number of active bars in the optimized module shows little dependence on the module scale.

A graphical representation of the 3D structures is provided in Fig. 4.9, showing isometric views as well as views on the XZ planes for the case with a module featuring a 2x2x2 ground structure. It is interesting to observe how, as the size of the module increases, the optimizer naturally converges toward solutions that prioritize slender tensile members and thick compressive members to satisfy local buckling constraints. Conversely, for smaller modules, the buckling effective length of the members diminishes and the design transitions to

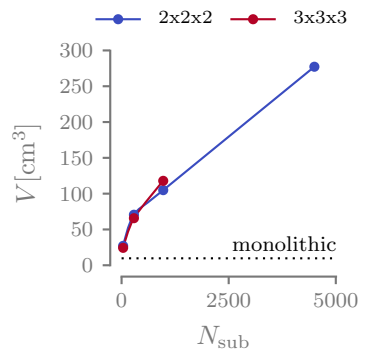


Figure 4.7: Influence of the number of subdomains on the volume of the optimized modular structure.

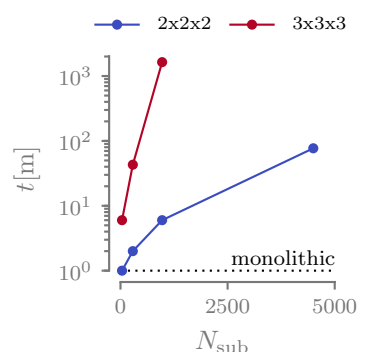


Figure 4.8: Influence of the number of subdomains on the computational time of the optimization.

**Table 4.5:** Numeric results of the parametric study on the influence of the number of subdomains on the optimized structures.

Quantity	7x3x4	2x2x2				3x3x3		
	1x1x1	6x2x3	12x4x6	18x6x9	30x10x15 <sup>a</sup>	6x2x3	12x4x6	18x6x9
—	—							
$\bar{n}_{\text{opt}} (\bar{n})$	1984	9 (28)	9 (28)	8 (28)	8 (28)	19 (351)	15 (351)	16 (351)
$N_{\text{sub}}$	1	36	288	972	4500	36	288	972
$N_{\text{opt}} (N_{\text{el}})$	20 (1984)	(1008)	(8064)	(27216)	(126000)	(12636)	(101088)	(341172)
$V [\text{cm}^3]$	9.907	27.074	70.559	104.891	277.238	24.323	65.723	117.904
$V [\%]$	1.761	4.812	12.544	18.648	49.288	4.324	11.684	20.960
$\bar{\rho} [\text{kg/m}^3]$	80.31	219.48	571.99	850.31	2247.47	197.17	529.55	955.80
$a_{\max} [\text{mm}^2]$	37.61	9.40	5.45	5.45	3.55	5.33	2.60	3.14
$\varphi$	100.00 %	14.81 %	1.85 %	0.67 %	0.12 %	20.51 %	1.46 %	0.62 %
$\psi$	1.000	0.446	0.178	0.105	0.030	0.327	0.127	0.096
t	4 s	6 s	48 s	5 m 6 s	1 h 17 m	5 m 42 s	42 m 50 s	27 h 17 m

<sup>a</sup>In this test case the minimum slenderness limit is relaxed to  $\lambda_{\max} = 10$  instead of 15.

**72.** Sigmund et al. (2016), 'On the (non-)optimality of Michell structures'

a configuration where both tensile and compressive members are equally represented. This observation aligns with the findings of Sigmund on Michell-like structures [72].

In an attempt to understand why the volume is significantly influenced by the number of subdomains, we visualize the trends of the parameters  $\varphi$  and  $\psi$  in Fig. 4.10. As depicted, every bar in the monolithic structure activates either the buckling or the stress constraint, resulting in  $\varphi = 100\%$  and  $\psi = 1$ . However, this is not true for any of the modular structures, as seen in the case of 12x4x6-3x3x3, where numerous bars remain inactive and are represented in gray.

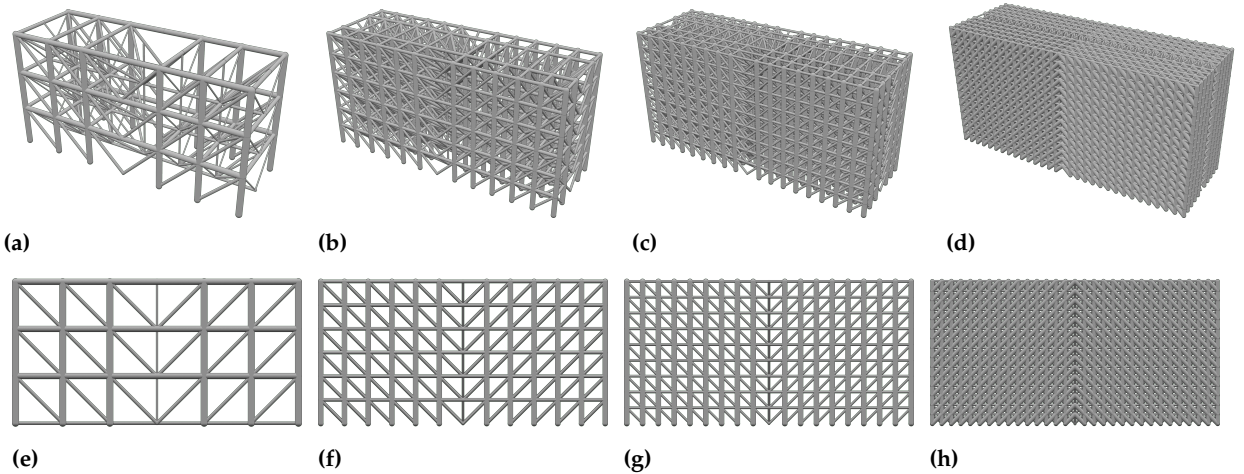


**Figure 4.9:** Rendering of the optimized structures with  $6 \times 2 \times 3$  (a-e),  $12 \times 4 \times 6$  (b-f),  $18 \times 6 \times 9$  (c-g), and  $30 \times 10 \times 15$  (d-h) subdomains. The module presents a  $2 \times 2 \times 2$  complexity.

This phenomenon becomes more apparent in Fig. 4.11, where the stress and buckling constraints are plotted on the optimized structures of both the monolithic and the  $12 \times 4 \times 6$  cases. In this illustration, it is evident that in the  $12 \times 4 \times 6$  case, many bars remain inactive (gray). Examining Fig. 4.11c and d, we notice that the stress and buckling constraints activate only in one subdomain but influence the entire structure. As a result, the modular structure is highly redundant and fail-safe, but this comes at the cost of an increased total volume.

**INFLUENCE OF THE COMPLEXITY OF THE MODULE** We now shift our focus to another parameter of modular structures: the module complexity, defined as the number of candidate members  $\bar{n}$  inside a module. To understand how this parameter influences the optimized structures, we set up an analysis similar to the one previously conducted for the module scale. Utilizing the same test case, we divide the structure into  $6 \times 2 \times 3$  subdomains along the X, Y, and Z axes, respectively. We discretize each module using a  $2 \times 2 \times 2$ , a  $3 \times 3 \times 3$ , a  $4 \times 4 \times 4$ , and a  $5 \times 5 \times 5$  fully connected ground structure ( $\bar{n} = 28$ ,  $\bar{n} = 351$ ,  $\bar{n} = 2016$ ,  $\bar{n} = 7750$ , respectively). The same analysis is conducted on a  $12 \times 4 \times 6$  structure to validate the test on a different modular structure.

The results of the parametric study are presented in a tabular format in Table 4.6, along with the rendering of the module. Once again, we have plotted the most interesting aspects separately. The first aspect we examine is how the volume of the optimized structure is influenced by the module complexity  $\bar{n}$ . In Fig. 4.13, we plot the volume of the optimized structure as a function of  $\bar{n}$ , and observe that, for lower complexities, increasing  $\bar{n}$  has a beneficial effect on volume. However, from the  $4 \times 4 \times 4$  module onwards ( $\bar{n} = 2016$ ), this effect vanishes and the volume appears largely independent from the complexity.

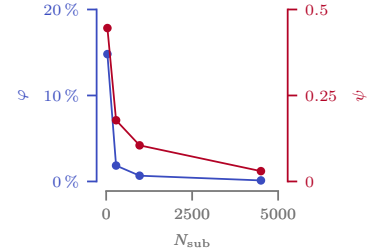


**Figure 4.10:** Influence of the number of subdomains on the loading metrics  $\varphi$  and  $\psi$  of the optimized structures.

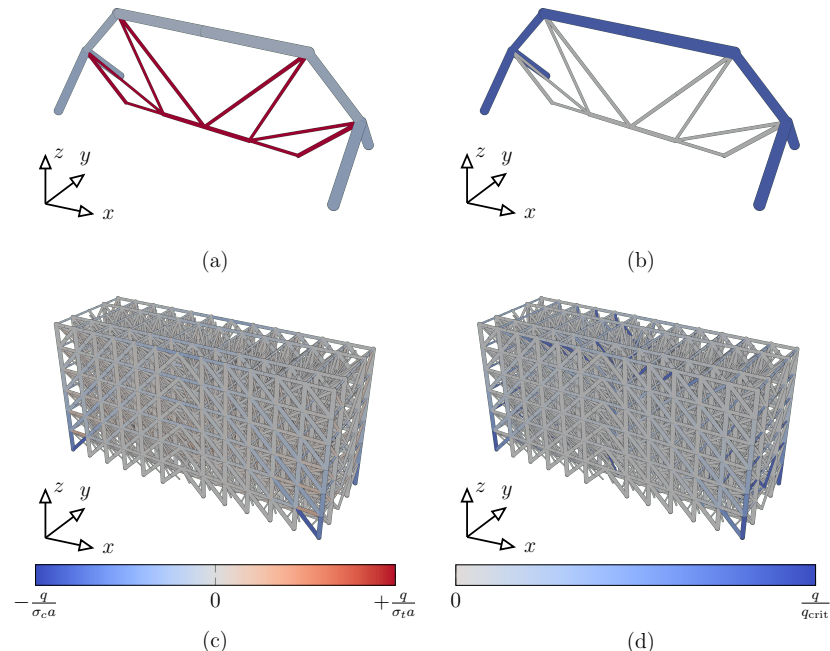


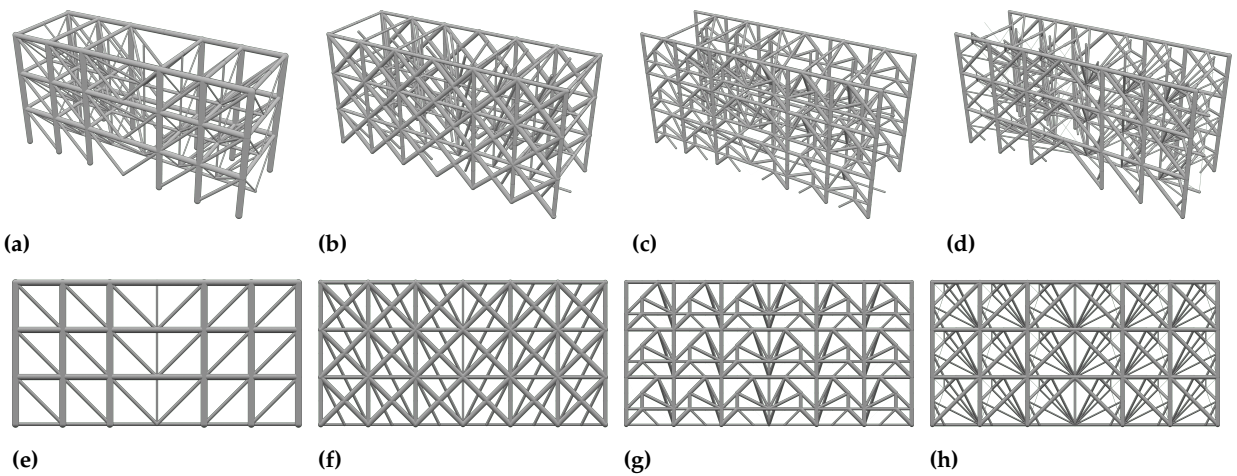
**Figure 4.11:** Stress (a-c) and local buckling (b-d) failure criteria plotted on the monolithic and the 12x4x6-3x3x3 cases.

Regarding computational time (see Fig. 4.14), we notice a relationship similar to the one already observed for the subdomain scale. The computational time goes up as the module complexity increases. This is understandable because in this scenario the number of design variables increases along with the number of candidates and, consequently, the number of constraints as well.

The 3D renderings of the optimized structures for the 6x2x3 subdomains case are presented in Fig. 4.12, allowing the reader to observe the evolution of the module's topology toward greater complexity (from  $\bar{n}_{opt} = 9$  to  $\bar{n}_{opt} = 88$  for the 2x2x2 and 5x5x5 cases, respectively). While in low complexity, the optimizer prioritizes long slender tensile elements, in more complex cases, we observe the apparition of compressive elements less influenced by local buckling because of their shorter buckling length.

**Table 4.6:** Numeric results of the parametric study on the influence of the module complexity on the optimized structures.

Quantity	6x2x3				12x4x6		
	2x2x2	3x3x3	4x4x4	5x5x5	2x2x2	3x3x3	4x4x4
$\bar{n}_{\text{opt}} (\bar{n})$	9 (28)	19 (351)	88 (2016)	88 (7750)	9 (28)	15 (351)	22 (2016)
$N_{\text{sub}}$	36	36	36	36	288	288	288
$N_{\text{opt}} (N_{\text{el}})$	324 (1008)	468 (12636)	792 (72576)	792 (279000)	2592 (8064)	4320 (101088)	6336 (580608)
$V [\text{cm}^3]$	27.074	24.323	17.098	17.083	70.559	65.723	60.368
$V [\%]$	4.812	4.324	3.040	3.036	12.544	11.684	10.732
$\bar{\rho} [\text{kg/m}^3]$	219.48	197.18	138.60	138.49	571.99	532.79	489.38
$a_{\max} [\text{mm}^2]$	9.40	5.33	3.39	3.77	5.45	2.60	2.97
$\varphi$	14.81 %	20.51 %	12.12 %	20.20 %	1.85 %	1.46 %	1.32 %
$\psi$	0.446	0.327	0.414	0.419	0.178	0.127	0.136
$t$	6 s	5 m 42 s	14 m 20 s	3 h 17 m	48 s	42 m 50 s	32 h 4 m

**Figure 4.12:** Rendering of the optimized structures with 2x2x2 (a-e), 3x3x3 (b-f), 4x4x4 (c-g), and 5x5x5 (d-h) module complexity. The number of subdomains is 6x2x3.

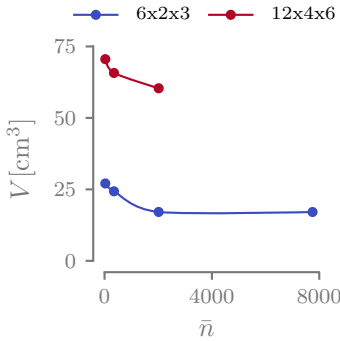


**Figure 4.13:** Influence of the module complexity on the volume of the optimized modular structure.

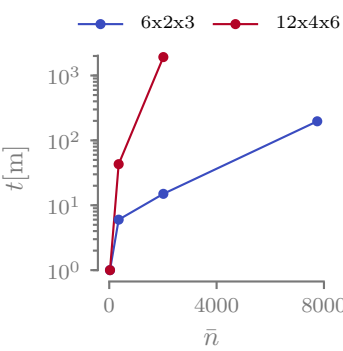


**Figure 4.14:** Influence of the module complexity on the computational time of the optimization.

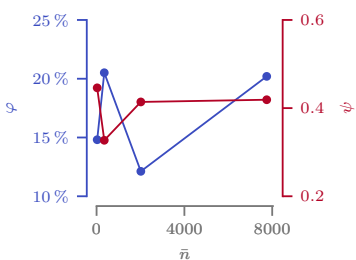


**Figure 4.15:** Influence of the module complexity on the loading metrics  $\varphi$  and  $\psi$  of the optimized structures.

It is interesting to note that the number of active bars in the optimized structure is quite dependent on the complexity of the module. However, in this specific case, we see that it saturates at  $\bar{n} = 88$  in the  $6 \times 2 \times 3$  case, suggesting that we have reached the convergence of the discretization.

Finally, in Fig. 4.15, we present the numerical values of  $\varphi$  and  $\psi$ . Unlike our earlier observations, the trends of these parameters are not monotonic and do not follow an explicit trend. While these indices aid in understanding how much a truss is loaded, they don't necessarily provide clear hints on optimality. A structure loaded up to the material limits contributes to achieving a lighter design but is not sufficient, as this example demonstrates.

**DESIGN OF EXPERIMENTS** With the data gathered thus far, we aim to construct the Design of experiments (DOE) for optimized modular structures. The objective is to monitor how the outcomes vary by introducing a change in the preconditions, represented by one or more independent variables. In our case, the chosen independent variables are the number of subdomains  $N_{\text{sub}}$  ( $x_1$ ) and module complexity  $\bar{n}$  ( $x_2$ ), while the observed responses are the total structural volume  $V$  and the computational time  $t$ . For simplicity, we once again only consider cubic cells.

We chose to use a quadratic model with interaction (the term  $x_1 x_2$ ) in an attempt to capture a potential interference between number of subdomains  $x_1$  and module complexity  $x_2$ , represented as follows:

$$a x_1^2 + b x_2^2 + c x_1 x_2 + d x_1 + e x_2 + f \quad (4.10)$$

The coefficients are determined by solving a least-squares system using the data presented earlier in this section.

We present the outcomes of the DOE for the structure volume  $V$  in Fig. 4.17. In the upper part of the image, we display the surface response along with a scatter plot of the optimized structures (a), and additionally, the isovalue line plot (b). It is noticeable that the volume  $V$  is strongly influenced by the number of subdomains  $N_{\text{sub}}$ , as indicated by the horizontal orientation of the isovalue lines. This suggests that the steeper gradient of the function is in the vertical direction. The modular structures with the lower volume tend to be structures with fewer subdomains characterized by high complexity  $\bar{n}$ . However, when examining subfigures (c) and (d), representing the surface response for computational time  $t$ , it is evident that high module complexity  $\bar{n}$  is associated with an elevated computational time.

Subsequently, we present the main effects plot for the volume and module complexity in Fig. 4.16. The idea of this figure is to visualize, for

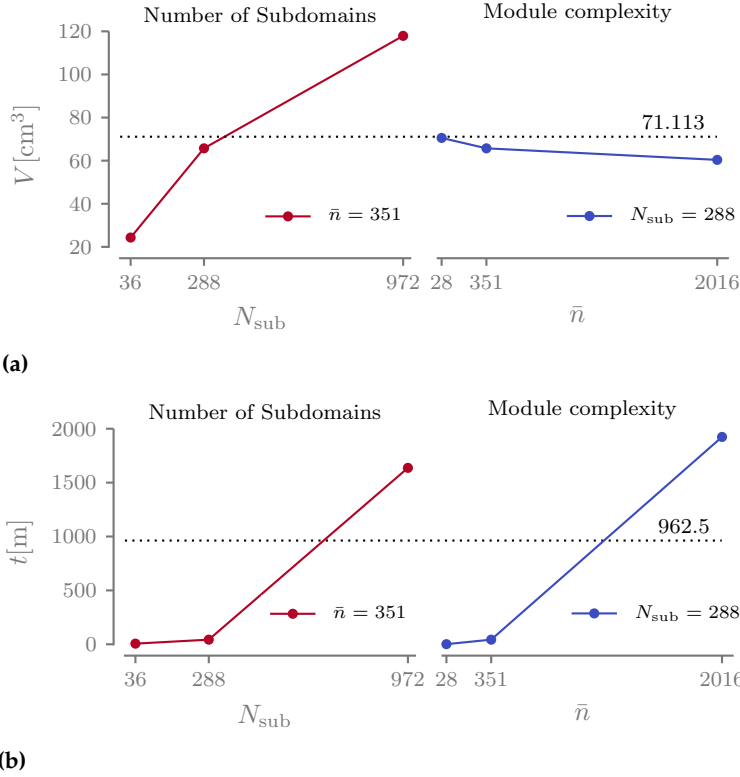


**Figure 4.16:** Main effects plot of volume (a) and computational time (b) as a function of the independent variables.

each independent variable, the effect on the volume and computational time by looking at the slope of the curves. The advantage of this representation is to offer an immediate visualization of the various effects on the observed function.

The coefficients of the quadratic model are listed in Table 4.7 and Table 4.8 for the volume  $V$  and computational time, respectively. Notably, for the volume  $V$ , the coefficient that predominantly influences the behavior of the response surface is  $e$ , which corresponds to the linear term for the number of subdomains  $N_{\text{sub}}$ . The interaction coefficient between the two independent variables, denoted as  $c$ , is low, indicating that the two variables do not significantly contribute when modified together. This is in contrast to computational time, where the interaction coefficient is relevant, along with the two linear terms. In both cases, the quadratic coefficients  $a$  and  $b$  are relatively less important, suggesting a generally linear response.

**DISCUSSION ON THE DOE** We can utilize this DOE as a tool to give general recommendations. While the specific numeric values and their magnitudes are tailored to our specific example, we assume that the observed trends are generally correct and applicable to modular structures as a whole. Therefore, we can conclude that in scenarios where minimizing mass is the primary objective, aiming for the fewest possible number of subdomains is preferred. However,

Coeff.	Value
$a$	$9.00 \times 10^{-8}$
$b$	$-1.02 \times 10^{-5}$
$c$	$-1.77 \times 10^{-6}$
$d$	$-2.64 \times 10^{-3}$
$e$	$1.01 \times 10^{-1}$
$f$	$2.88 \times 10^1$

**Table 4.7:** Coefficients of the quadratic function used to model how the volume  $V$  varies with the number of subdomains  $N_{\text{sub}}$  and the module complexity  $\bar{n}$ .

Coeff.	Value
$a$	$1.55 \times 10^{-3}$
$b$	$-2.87 \times 10^{-4}$
$c$	$2.90 \times 10^{-1}$
$d$	$-2.08 \times 10^1$
$e$	$-5.54$
$f$	$0.00$

**Table 4.8:** Coefficients of the quadratic function used to model how the computational time  $t$  varies with the number of subdomains  $N_{\text{sub}}$  and the module complexity  $\bar{n}$ .

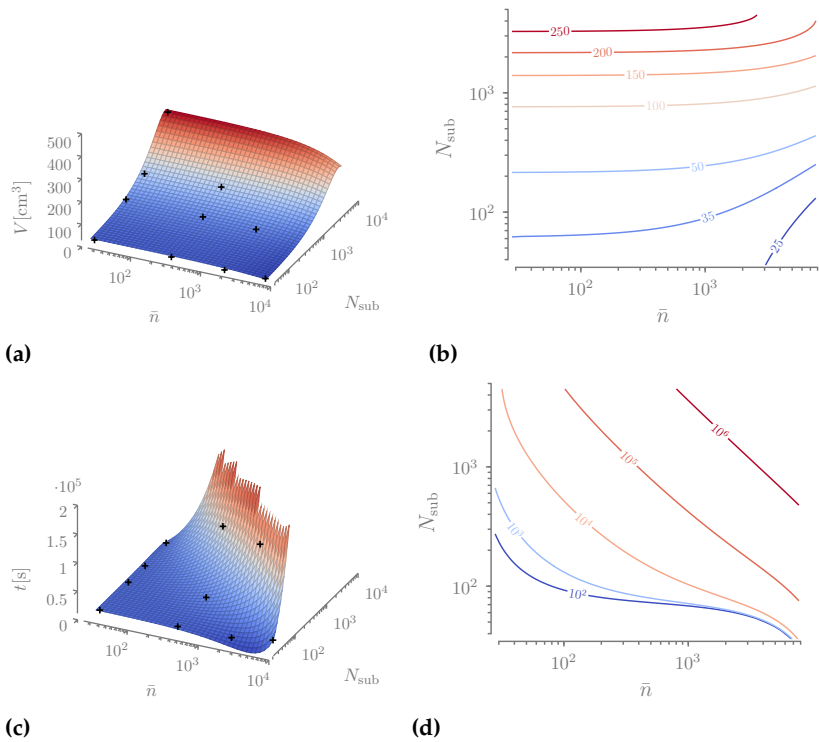


**Figure 4.17:** Design of experiments (DOE) response curves and isocurves plot for the volume (a-b) and computational time (c-d).

additional constraints must be considered. For example, having fewer subdomains implies an increase in the physical size of individual modules. Yet, there is often a manufacturing maximum size that restricts this increase. Consequently, the recommendation is to achieve the largest possible module that can be produced within the limitations of the chosen manufacturing technology.

Although higher complexity significantly impacts computational time, its influence on optimization outcomes is not substantial. Therefore, opting for a medium complexity, such as 3x3x3 nodes in the module (or 4x4 in 2D), strikes a balance between computational cost and optimization effectiveness.

#### 4.2.3 COMPARISON WITH THE OPTIMIZED OCTET-TRUSS

213. Deshpande et al. (2001), 'Effective properties of the octet-truss lattice material'

The proposed modular TTO algorithm is benchmarked against one of the most popular cell topologies found in the literature: the octet-truss (see Fig. 4.18). The octet-truss is a cell known for its highly effective mechanical properties, achieving about half the theoretical values of the upper Hashin-Shtrikman bounds [213] for isotropic materials.

To conduct the benchmark, the simply supported 3D beam is divided into 6x2x3 and 12x4x6 cubic subdomains, which are then populated with the octet-truss topology. The cross-sectional areas of the cell members are all equal, and the numerical value is determined by performing a parametric optimization. The octet-truss structure is constrained by stress, local buckling, and kinematic compatibility

Quantity	6x2x3		12x4x6	
	Octet	3x3x3	Octet	3x3x3
$N_{\text{sub}}$	36	36	288	288
$N_{\text{opt}} (N_{\text{el}})$	1008	(12636)	7488	(101088)
$V [\text{cm}^3]$	65.752	24.323	121.038	65.723
$V [\%]$	11.692	4.324	21.524	11.684
$\bar{\rho} [\text{kg/m}^3]$	533.03	197.18	981.21	532.79
$C [\text{J}]$	1.67	3.63	1.12	1.84
$a_{\max} [\text{mm}^2]$	3.69	5.33	1.83	2.60
$\varphi$	0.39 %	20.51 %	0.05 %	1.46 %
$\psi$	0.075	0.327	0.026	0.127

**Table 4.9:** Numerical results of the comparison between octet-truss and TTO structures.

constraints for every member of the structure. The optimization is performed using Altair OptiStruct.

Fig. 4.19 displays the 3D rendering of the two optimized octet-truss structures (left part of the image) compared to the modular TTO structures (right part of the image). It is noticeable how the TTO algorithm guides the topology of the module toward higher efficiency, creating vertical columns loaded in compression that support thin wires loaded in tension. On the other hand, the octet-truss topology is fixed and exhibits quasi-isotropic mechanical behavior. The octet-truss is a module with good homogenized elastic properties in all directions, thanks to its numerous planes of symmetry. It is, thus, less suitable for structural applications where all the subdomains experience similar loading conditions. In such cases, the module will be equally stiff and strong in every direction, not aligned with the principal stress directions.

We notice that in the octet-truss structure, there are no members oriented exactly along the z axis, while in the TTO optimized cell, they are the ones that show the biggest cross-sectional areas. This tells us that this is the most efficient direction to put the material to obtain a stronger cell. On top of that, the upper and lower faces of the cell present a cross design (see Fig. 4.18) that works well for torque but not for tension and compression loading. A new study exploring what happens if we rotate the cell could be interesting.

The numerical results are presented in Table 4.9 and confirm our observations. The volume of the octet-truss structures is approximately thrice and twice the volume of the modular TTO optimized structures for the 6x2x3 and the 12x4x6 test cases, respectively. This significant gap between the two structures is also evident when examining the values of  $\varphi$  and  $\psi$  of the octet truss structures, significantly lower when compared to the TTO optimized ones. These values drop to very low levels because the cross-sectional area of the entire octet truss structure is determined by the value at which a bar on the structure activates either the stress or the buckling constraints. As the structure is symmetric on the XZ and the YZ planes, a total of four

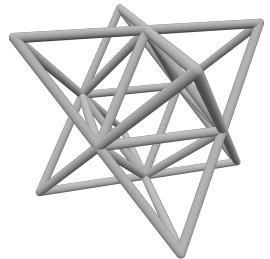


**Figure 4.18:** Rendering of a single octet-truss module.

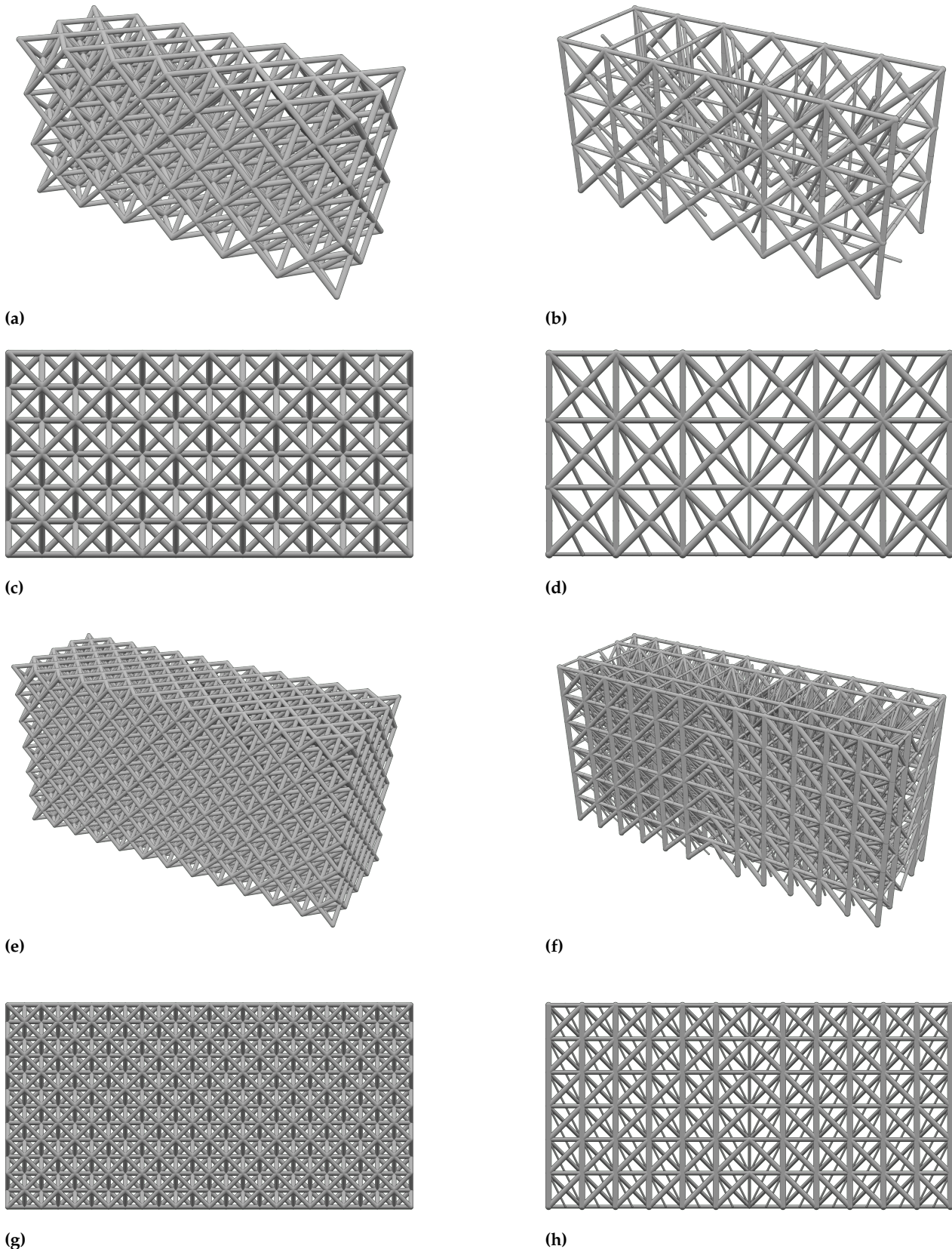


**Figure 4.19:** Comparison of the octet-truss structures (a-c-e-g) and the TTO structures (b-d-f-h) for two different numbers of subdomains, 6x2x3 and 12x4x6.

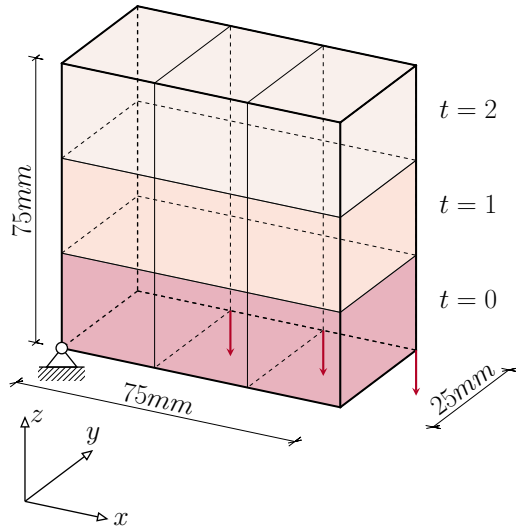


**Figure 4.20:** Graphical representation of the given module layout for the simply supported 3D beam.

bars activate mechanical constraints, resulting in a highly inefficient design. Better results could have been obtained by providing more design freedom to the optimization of the octet-truss, using multiple cross-sectional design variables, but this approach has not been taken here. It is important to note that the comparison presented here does not account for the weight of fasteners and joints necessary to link the cells together.

#### 4.2.4 USING MULTIPLE MODULE TOPOLOGIES

We have explored two extremes so far – the fully modular and the monolithic structures. Now, we aim to investigate the scenarios in between. Up to this point, our study on modular structures has been limited to a single topology of the module, i.e.,  $N_T = 1$ . This is because, when dealing with multiple module topologies, another crucial question arises: how to optimize the module layout? How should the modules be arranged in the structure to minimize the overall volume of the part? This critical question will be discussed in-depth later in the thesis. For now, as we begin to consider multiple module topologies, we make a significant simplification by determining the layout based solely on good engineering common sense, without an additional optimization process.

Let us reconsider the simply supported 3D beam divided into a grid of 6x2x3 subdomains. This time, we optimize the structure using three different modules  $N_T = 3$ . The modules are discretized using an identical fully connected ground structure with 3x3x3 nodes. The module mapping matrix of the structure is provided as an input for the optimization<sup>1</sup> and it represents the module layout shown in Fig. 4.20.

The optimized structure features an interesting design made by two elongated spars that support multiple tensile members responsible for carrying the given loads. The spars exhibit a design that favors long

1: The module mapping matrix is

$$H = \begin{bmatrix} 1 & 0 & 0 \\ 1 & 0 & 0 \\ 1 & 0 & 0 \\ 0 & 0 & 0 \\ 0 & 1 & 0 \\ 0 & 1 & 0 \\ 0 & 1 & 0 \\ 0 & 0 & 1 \\ 0 & 0 & 1 \\ 0 & 0 & 1 \end{bmatrix}$$

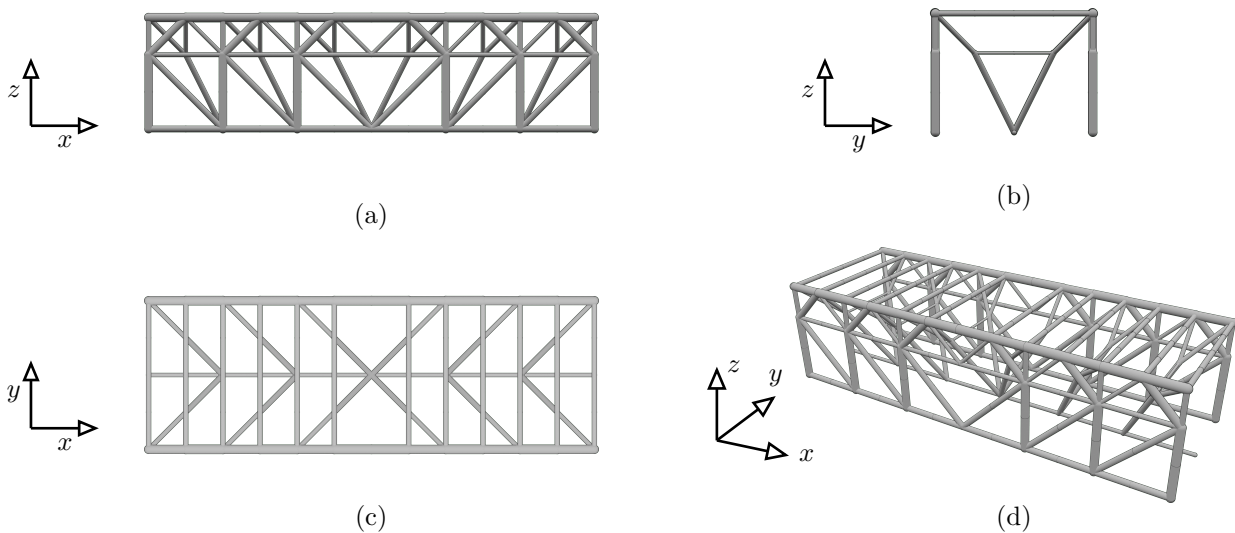


**Figure 4.21:** Orthographic views of the topology of the optimized modular simply supported 3D beam. (a) XZ plane (b) YZ plane (c) XY plane (d) auxiliary perspective view.

tensile members, interconnected by compressive bars. The resulting optimized structure is illustrated in Figure 4.21.

We now examine the modules of the optimized structure. Firstly, we observe that the optimizer sets all the cross-sectional areas of module  $t = 2$  to zero, meaning that the loads are not carried by this part of the structure and thus it is entirely superfluous. This highlights the importance of considering the possibility of an empty topology when optimizing the module layout in the structure. Secondly, we note instances where the module is composed of bars that are disconnected e.g. in  $t = 0$ , potentially necessitating additional post-processing if the goal is to obtain a manufacturable design.

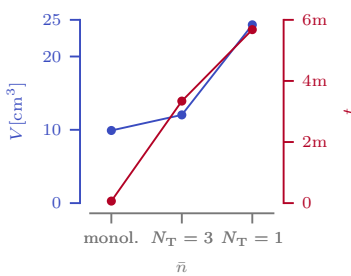


**Figure 4.22:** Comparison of the volume and computational time of the structure with multiple modules with the monolithic and the fully modular structures.

The optimized structure with  $N_T = 3$  is now compared to the reference monolithic structure and the structure with  $N_T = 1$  to assess the difference in mechanical performance due to the increased number of modules topologies. The results are presented in Table 4.10. Interestingly, the computational time of the  $N_T = 1$  solution is lower ( $t = 3 \text{ m } 22 \text{ s}$ ) compared to the  $N_T = 3$  structure ( $t = 5 \text{ m } 42 \text{ s}$ ). This comes as a surprise, considering that the  $N_T = 1$  optimization problem involves more design variables (as three times the number of cross-sectional areas are optimized). However, it turns out that having more design freedom makes the optimization process easier, as the constraints are more straightforward to satisfy. The trends of the volume and computational time are plotted in Fig. 4.22.

The volume reduction is attributed to a more efficient utilization of the subdomain topology, which now varies with the subdomain position. This can be observed by examining the more efficient use of material, with a greater number of bars reaching the mechanical failure limit

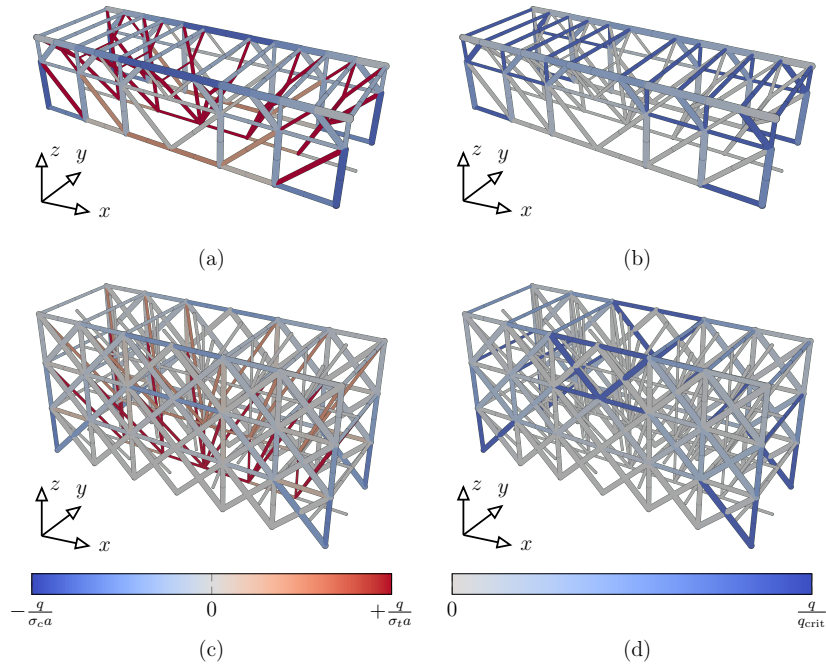


**Figure 4.23:** Stress (a-c) and local buckling (b-d) failure criteria plotted on the multiple and single module modular structures.

( $\varphi = 61.90\%$  for  $N_t = 3$  compared to  $\varphi = 20.51\%$  for  $N_t = 1$ ) and, in general, a more uniform structure loading ( $\psi = 0.716$  vs.  $\psi = 0.327$ ). The stress and buckling failure criteria are plotted in Fig. 4.23 for deeper analysis. It's notable that in subfigures (a) and (b) compared to their counterpart in (c) and (d), a greater number of colored bars are observed. This indicates that more candidates are reaching their maximum mechanical capacity, resulting in increased efficiency and a reduction in the overall volume of the structure.

This study suggests that employing more modules for optimization allows the achievement of less voluminous structures, potentially approaching the performance of monolithic structures. However, this introduces a compromise between volume (and consequently mass) and the ease of manufacturing, a topic we will delve into further in the upcoming chapter.

**Table 4.10:** Numerical results of the comparison between the structure with multiple modules with the monolithic and the fully modular structures.

Quantity	7x3x4	6x2x3-3x3x3- $N_T = 3$			6x2x3 3x3x3 $N_T = 1$
	–	$t = 0$	$t = 1$	$t = 2$	$t = 0$
$\bar{n}_{\text{opt}} (\bar{n})$	1984	10 (351)	18 (351)	– (351)	19 (351)
$N_{\text{sub}}$	1		36		36
$N_{\text{opt}} (N_{\text{el}})$	20 (1984)		336 (12636)		468 (12636)
$V [\text{cm}^3]$	9.907		12.032		24.323
$V [\%]$	1.761		2.139		4.324
$\bar{\rho} [\text{kg/m}^3]$	80.31		97.54		197.18
$\varphi$	100.00 %		61.90 %		20.51 %
$\psi$	1.000		0.716		0.327
$t$	4 s		3 m 22 s		5 m 42 s

### 4.3 CONCLUSION

In this chapter, we introduced an optimization algorithm for modular structures based on the Truss Topology Optimization (TTO) and variable linking. Initially, we investigated the impact of modularity constraints on the topological buckling phenomenon and sensitivity analysis. Subsequently, we adapted the two-step optimization algorithm with reinitialization presented in Chapter 3 to solve the proposed modular formulation.

The modular TTO algorithm is then tested on multiple two- and three-dimensional test cases. Initially, we observe an equivalence between modular structures and structures loaded with multiple load cases. The use of a repeating module throughout the structure significantly impacts the volume, as the module needs to perform well under various loading conditions concurrently. Subsequently, we conducted an extensive parametric analysis of the number of subdomains and module complexity. Based on the results of the Design of experiments (DOE), we provide recommendations: fewer subdomains are generally preferable, with the module as large as manufacturably possible. Module complexity plays a role in volume minimization but has a relatively low impact. Finally, the modular TTO structures are benchmarked against one of the most commonly used module topologies in the literature: the octet-truss lattice.

We finally conducted an optimization using multiple module topologies. The incorporation of multiple modules, some of which may have an entirely empty topology, emerged as a crucial factor that contributes to the reduction of modular structure volume. This in turn allows modular structures to approach the volume of monolithic structures while offering additional ease of manufacturing. However,

the utilization of multiple modules raises a new question: how should the modules be arranged within the different subdomains of the structure?



Chapter 4 introduced the foundational concepts of modular structures and formulated an optimization algorithm designed to optimize structures exhibiting the repetition of a single module topology. Additionally, it presented a design of experiments to gain insights into the general mechanical behavior of modular structures. We observed that, especially in terms of volume, such structures are significantly penalized when compared to monolithic structures. Towards the end of the chapter, we identified two paths we could take to bridge this gap and enhance the mechanical performance of modular structures: to incorporate multiple module topologies and the presence of empty subdomains in the structure where not structurally necessary. In this chapter, we formulate an optimization algorithm that incorporates these two improvements.

The chapter is outlined as follows: In Section 5.1, we present an innovative optimization algorithm for modular structures, which concurrently optimizes both the layout and topology of the modules. The initial layout for the optimization is determined by identifying similarly behaving subdomains through a k-means clustering technique. Section 5.2 tests the proposed formulation on multiple two- and three-dimensional cases, considering both normalized and real engineering dimensions and material data.

## 5.1 OPTIMIZING THE MODULES' LAYOUT USING A MODIFIED DMO ALGORITHM

The objective of this chapter is to address the concurrent optimization of both the layout and topology of multiple modules within a modular structure. The key scientific challenge lies in the discrete nature of the layout optimization problem, i.e. finding the optimal distribution of the different modules within the subdomains of the structure, an inherently discrete problem. Given our intent to employ a gradient descent algorithm, it is necessary to design a methodology for converting the discrete nature of the problem into a continuous one, permitting the application of gradient-based optimization techniques.

### 5.1.1 DEFINITION OF THE SUBDOMAINS CROSS-SECTIONAL AREAS

In this study, our strategy for addressing the discrete layout problem of modules as a continuous one involves defining the variables of the subdomains (i.e., the structure's variables) as a weighted sum of the module variables. This approach draws inspiration from the seminal work of Stegmann and Lund in the Discrete Material Optimization

5.1 OPTIMIZING THE MODULES' LAYOUT USING A MODIFIED DMO ALGORITHM . . . . .	101
5.2 NUMERICAL OPTIMIZATION OF THE TOPOLOGY AND LAYOUT OF MODULAR STRUCTURES . . . . .	108
5.3 CONCLUSION . . . . .	121

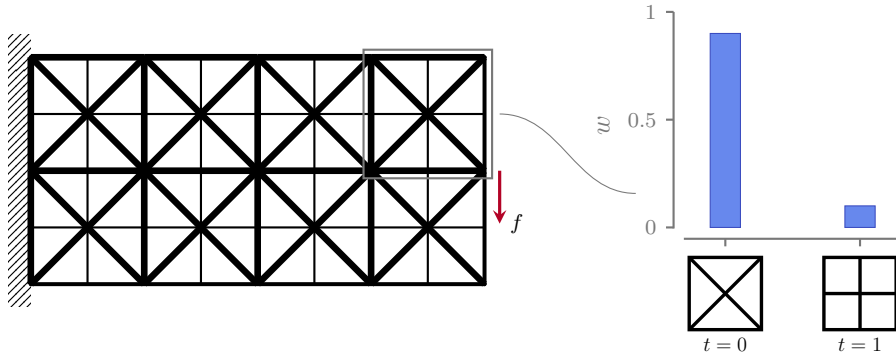


**Figure 5.1:** A modular cantilever beam with  $N_{\text{sub}} = 8$ . The subdomains' topology is defined as the weighted sum of two modules' topologies.

214. Stegmann et al. (2005), 'Discrete material optimization of general composite shell structures'

(DMO) algorithm [214], where an optimizer selects from a set of fixed tensors the optimal homogenized stiffness tensor for each subdomain to minimize the compliance of a given structure. In the scenario of discretizing a ground structure into  $N_{\text{sub}}$  subdomains and utilizing  $N_T$  distinct modules, the cross-sectional areas of subdomain  $j$  are expressed as:

$$\bar{\mathbf{a}}^j = \sum_{t=1}^{N_T} w_t^j \bar{\mathbf{a}}_t \quad (5.1)$$

where  $\bar{\mathbf{a}}_t$  represents the vector of cross-sectional areas of the  $t$ -th module and  $\mathbf{w}^j$  is the vector of weight relatives to the  $j$ -th subdomain, defined as  $\mathbf{w}^j \in [0, 1]^t$ .

Fig. 5.1 illustrates the principle of weighted cell summation for a cantilever beam with  $N_{\text{sub}} = 8$  and  $N_T = 2$ .

### 5.1.2 VARIABLES PENALIZATION SCHEMES

215. Stolpe et al. (2001), 'An alternative interpolation scheme for minimum compliance topology optimization'

When the optimizer converges to a solution, i.e. a set of optimized values of  $\bar{\mathbf{a}}$  and  $\mathbf{w}$ , the weights of all subdomains must converge to either zero or one, with the additional constraint that only one weight per subdomain can be equal to one. This condition is necessary to avoid intermediate weights, which would imply a combination of multiple modules' topologies lacking mechanical significance and proving impractical for manufacturing. However, this result is not achieved if we do not work on the method accordingly. To address this issue, we implement an interpolation scheme that penalizes intermediate weights. Specifically, we opt for the Rational Approximation of Material Properties (RAMP) method [215] instead of the more commonly used Solid Isotropic Material with Penalization Method (SIMP) interpolation scheme. This choice is motivated by RAMP's advantageous property of ensuring that the derivative is never infinite nor zero when the weights approach a value of zero.

We define the design variable  $\alpha \in \mathbb{R}^{j,t}$  as the modules' layout variable, responsible for the module selection within the subdomain  $j$ . Its

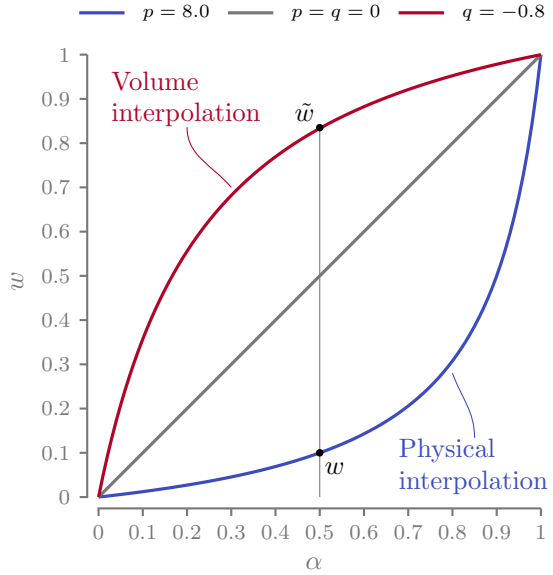


**Figure 5.2:** A dual-phase RAMP interpolation scheme is used to penalize the intermediate weights and promote 0-1 designs.

relationship with the weight  $w$  is the following:

$$w_t^j = \frac{\alpha_t^j}{1 + p(1 - \alpha_t^j)} \quad (5.2)$$

where  $p \in \mathbb{R}^+$  denotes a parameter governing the steepness of the RAMP interpolation. Drawing inspiration from the works of Hvejsel *et al.* [216], we introduce a multi-phase variant of the RAMP interpolation, in which we concurrently penalize mechanical properties while artificially increasing the volume of modules with intermediate densities. To achieve this, we introduce an additional RAMP parameter,  $q$ , always negative ( $q \in \mathbb{R}^-$ ), utilized to assess the augmented weights associated with the volume evaluation  $V$ . We can then write:

$$V = \sum_{j=1}^{N_{\text{sub}}} \tilde{\boldsymbol{\ell}}^T \tilde{\boldsymbol{a}}^j, \quad (5.3)$$

where the vector  $\tilde{\boldsymbol{a}}^j$ , representing the increased cross-sectional areas of the  $j$ -th subdomain is defined as:

$$\tilde{\boldsymbol{a}}^j = \sum_{t=1}^{N_T} \tilde{w}_t^j \bar{\boldsymbol{a}}_t, \quad (5.4)$$

and where  $\tilde{w}$  is:

$$\tilde{w}_t^j = \frac{\alpha_t^j}{1 + q(1 - \alpha_t^j)}. \quad (5.5)$$

So for every design variable  $\alpha_t^j$ , we associate two different weights  $w$  and  $\tilde{w}_t^j$  that are used to evaluate the mechanical properties and the structure volume, respectively (see Fig. 5.2).

216. Hvejsel et al. (2011), 'Material interpolation schemes for unified topology and multi-material optimization'

### 5.1.3 THE OPTIMIZATION FORMULATION AND RESOLUTION ALGORITHM

The objective function of the optimization process is the volume minimization of the modular structure. The members of the structure are subjected to multiple mechanical constraints, namely stress, topological buckling, minimum slenderness, and compatibility constraints. Formulation  $\mathbb{M}_1$  is stated in terms of modules' cross-sectional area  $\bar{a}$ , module selection variables  $\alpha$ , member forces  $q$ , and nodal displacements  $U$  as follows:

$$\begin{aligned}
 \min_{\bar{a}, \alpha, q, U} \quad & V = \sum_{j=1}^{N_{\text{sub}}} \bar{\ell}^T \bar{a}^j \quad (\text{Volume minimization}) \\
 \text{s.t.} \quad & Bq = f \quad (\text{Force equilibrium}) \\
 & q = \frac{aE}{\ell} b^T U \quad (\text{Compatibility constraints}) \\
 & q \geq -\frac{sa^2}{\ell^2} \quad (\text{Euler buckling constraints}) \quad (\mathbb{M}_1) \\
 & -\sigma_C a \leq q \leq \sigma_T a \quad (\text{Stress constraints}) \\
 & \bar{a}_{t,r} \geq \bar{a}_{t,r=1} \quad r \in \mathcal{C}_{l,r}(\bar{a}_t), \forall t \\
 & 0 \leq \bar{a} \leq \frac{4\pi\bar{\ell}^2}{\lambda_{\max}} \quad (\text{Slenderness limit}) \\
 & \sum_{t=1}^{N_T} \alpha_t^j \leq 1, \forall j \quad (\text{One selected module max.})
 \end{aligned}$$

This formulation builds on the classic DMO approach, adding multiple mechanical constraints while operating on a ground structure. Additionally, we are not only selecting the best module for every subdomain by changing the value of  $\alpha$  as classic DMO does, but we are also optimizing the modules' topology simultaneously. This simultaneous optimization is a challenging task. The advantages of this formulation lie in dealing with a discrete problem using continuous design variables and a gradient-based optimizer. However, it comes with the drawback of increasing the problem size, as we are adding numerous additional design variables  $\alpha$  that scale with the number of subdomains and the number of modules i.e. a vector of size  $\alpha^j \in \mathbb{R}^{t^j}$  is defined for every one of the  $j$  subdomains.

The design variables  $\alpha$  are constrained by a set of constraints to be less than or equal to one. It is crucial to note that we treat this constraint as a disequality constraint rather than an equality. This allows the optimizer to set all  $\alpha$  to zero, permitting the removal of the subdomain from the structure. The constraint  $g_{\text{sum}}$  is expressed as follows:

$$g_{\text{sum}} := \sum_{t=1}^{N_T} \alpha_t^j \leq 1, \forall j \quad (5.6)$$

Problem  $\mathbb{M}_1$  is tackled using a modified version of the two-step solving

algorithm proposed in Chapter 3. In this approach, we initially solve a relaxed problem denoted as  $\mathbb{M}_2$ , where kinematic compatibility constraints are omitted. The relaxed formulation  $\mathbb{M}_2$ , expressed in terms of modules' cross-sectional area  $\bar{a}$ , module selection variables  $\alpha$ , and member forces  $q$ , is the following:

$$\begin{aligned}
 \min_{\bar{a}, \alpha, q} \quad & V = \sum_{j=1}^{N_{\text{sub}}} \bar{\ell}^T \bar{a}^j \quad (\text{Volume minimization}) \\
 \text{s.t.} \quad & \mathbf{B}q = f \quad (\text{Force equilibrium}) \\
 & q \geq -\frac{s a^2}{\ell^2} \quad (\text{Euler buckling constraints}) \\
 & -\sigma_C a \leq q \leq \sigma_T a \quad (\text{Stress constraints}) \\
 & 0 \leq \bar{a} \leq \frac{4\pi\bar{\ell}^2}{\lambda_{\max}} \quad (\text{Slenderness limit}) \\
 & \sum_{t=1}^{N_T} \alpha_t^j \leq 1, \forall j \quad (\text{One selected module max.})
 \end{aligned} \tag{\mathbb{M}_2}$$

This relaxed problem is inherently nonlinear due to the introduction of the  $\alpha$  design variable, and we have chosen to solve it using a non-linear gradient-based optimizer that iteratively exploits first and second-order derivatives to achieve convergence. The computation of the Jacobian and Hessian matrices for this problem is not trivial, and the details are elaborated in Appendix 6.3.

Once problem  $\mathbb{M}_2$  is solved, we prepare for the second step, in which the structure's layout is fixed (we remove  $\alpha$  from the second optimization), and the kinematic compatibility constraints are reintroduced. We use the optimized module layout  $\alpha^*$  to establish the fixed module layout on the structure and evaluate the mapping matrix  $H$  used in the variable linking approach of problem  $\mathbb{M}_{1,\text{VL}}$  introduced in Section 4.1.3. The indices of the mapping matrix  $H$  are determined as follows:

$$h_{j,t} = \begin{cases} 1 & \text{if } \alpha_{j,t}^* = \max(\alpha_j^*) \text{ and } \alpha_{j,t}^* > 0.01 \\ 0 & \text{otherwise.} \end{cases} \tag{5.7}$$

Subsequently, the compatibility constraints are reintroduced, and a Finite Element Analysis (FEA) is conducted to evaluate the displacements  $\mathbf{U}$  used in the starting point of the following optimization step. To mitigate the risk of being trapped in local minima, the second step is solved on a reduced design space. The solution  $\bar{a}^*$  of the first optimization is used to simplify the initial ground structure, thereby eliminating elements from the optimization that fall below the specified threshold value  $a_{\text{thr}}$ :

$$\bar{a}_i < a_{\text{thr}} \quad \forall i, \text{ with } a_{\text{thr}} = \chi \max(\bar{a}^*), \tag{5.8}$$

We use a non-linear optimizer to solve  $\mathbb{M}_2$  and not an SLP algorithm as done in Chapter 4 for  $\mathbb{M}_{2,\text{VL}}$ , because the latter was easily linearized by rewriting the local buckling constraints using Taylor's expansion, while  $\mathbb{M}_2$  addition of the layout variable  $\alpha$  makes everything more difficult.

where the parameter  $\chi$  is the cross-sectional area threshold value. The value of  $\chi$  must not be set to a very stringent value, as removing too many bars could create an infeasible problem for the second step of the solving algorithm.

Formulation  $M_{1,VL}$ , defined in Chapter 4 permits to optimize modular structures with fixed module layout using the variable linking approach. It is stated in terms of modular cross-sectional areas  $\bar{a}$ , member forces  $q$  and nodal displacements  $U$  as follows:

$$\begin{aligned} \min_{\bar{a}, q, U} \quad & V = \ell^T a \\ \text{s.t.} \quad & a = \sum_{t=1}^{N_T} h_t \otimes \bar{a}_t \\ & Bq = f \\ & q = \frac{aE}{\ell} b^T U \\ & q \geq -\frac{s a^2}{\ell^{*2}} \\ & -\sigma_c a \leq q \leq \sigma_t a \\ & \bar{a}_{t,r} \geq \bar{a}_{t,r=1} \\ & 0 \leq \bar{a} \leq \frac{4\pi\ell^2}{\lambda_{\max}}, \end{aligned}$$

<sup>159</sup>. Bakker et al. (2021), 'Simultaneous optimization of topology and layout of modular stiffeners on shells and plates'

<sup>136</sup>. Song et al. (2021), 'Investigation on the modelling approach for variable-density lattice structures fabricated using selective laser melting'

<sup>145</sup>. Kumar et al. (2020), 'A density-and-strain-based K-clustering approach to microstructural topology optimization'

<sup>217</sup>. Opgenoord et al. (2019), 'Design for additive manufacturing: cellular structures in early-stage aerospace design'

Now, with all the components in place, we can set up the variable linking formulation  $M_{1,VL}$ , as defined in Chapter 4. This formulation is employed to optimize modular structures with a fixed module layout and provide the final optimized design.

#### 5.1.4 OPTIMIZATION INITIALIZATION: A CLUSTERING ALGORITHM TO IDENTIFY SIMILARLY BEHAVING SUBDOMAINS

Solving the first step of the proposed optimization formulation, we not only adjust the design variable responsible for the modules' layout ( $\alpha$ ) but also optimize the modules' topology ( $\bar{a}$ ). However, a significant challenge arises in this problem due to the strong interdependence between them i.e. the topology of the module is optimized in function of the layout and *vice versa*. It becomes particularly challenging for a gradient-based optimizer to determine the appropriate direction to follow e.g. to reduce the value of the cross-sectional area of a member, the optimizer could play with  $\alpha$ ,  $\bar{a}$  or potentially both at the same time. This is especially true when starting from a completely uniform initial point (as observed in the work of Bakker [159]). To mitigate this challenge, we propose to use a slightly perturbed starting point for the optimization process. We influence the module topology design variable at iteration zero  $\alpha_{\text{init}}$  by privileging a specific module topology for every subdomain as follows:

$$\alpha_{t,\text{init}}^j = \begin{cases} \frac{1}{N_T} \cdot 1.1 & \text{if we privilege the } t\text{-th module on the } j\text{-th subdomain,} \\ \frac{N_T-1.1}{N_T(N_T-1)} & \text{otherwise.} \end{cases} \quad (5.9)$$

The idea behind how to select the best module for a subdomain is to identify the subdomains that show similar mechanical behavior, grouping them based on their stress state. This approach is not new, and it is already been used in the literature of structural optimization [136, 145, 217]. This grouping is assessed using a k-means clustering technique with the number of clusters equal to the number of module topologies  $N_T$ . Given a set of observations  $(x_1, x_2, \dots, x_{N_{\text{sub}}})$ , where each observation is a  $\bar{n}$ -dimensional real vector, k-means clustering aims to partition the  $N_{\text{sub}}$  observations into  $N_T$  sets. In our context, each observation is the vector containing the Finite Element Analysis (FEA) calculated stress distribution on the initial ground structure with a uniform cross-sectional area.

Besides the stress values  $\sigma_i^j$  of the  $i$ -th bar of the  $j$ -th subdomain, we

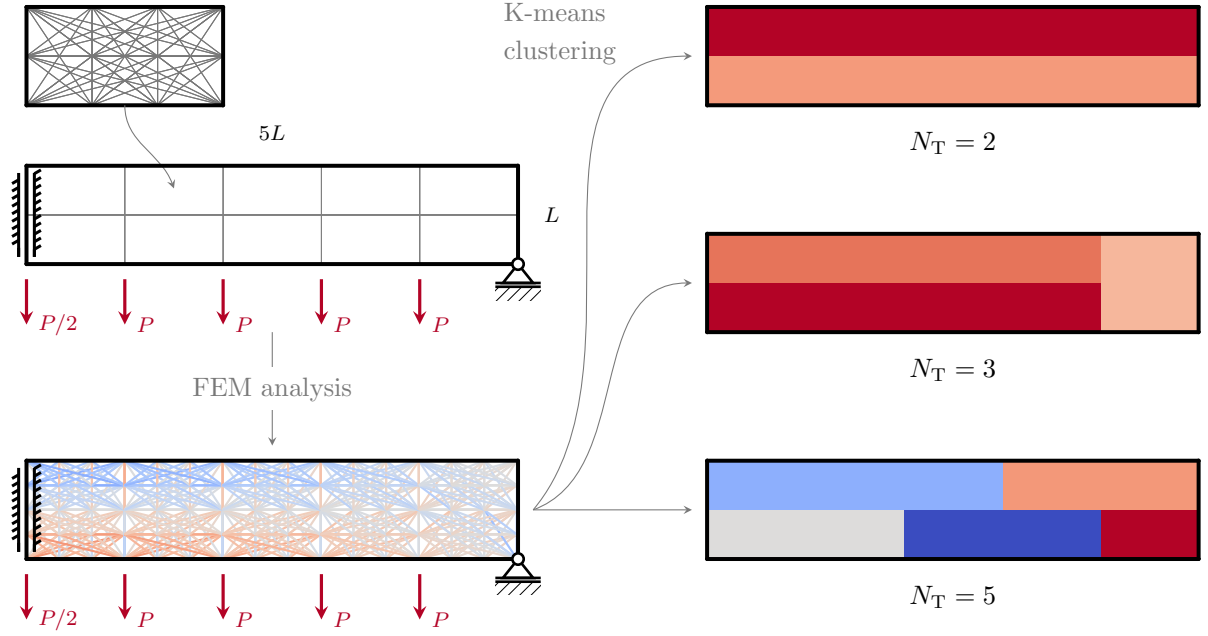


**Figure 5.3:** The stress values of the initial ground structure evaluated using a Finite Element Method (FEM) analysis are used to identify similar behaving subdomains. The sets are calculated using the k-means clustering technique with  $N_T$  number of clusters.

introduce the stress state  $S$  for the  $j$ -th subdomain as:

$$S^j = \sum_{i=0}^{\bar{n}} |\sigma_i^j| \quad (5.10)$$

This addition promotes the clustering not only of subdomains loaded in similar ways but also based on similar magnitudes.

The full clustering process is depicted in Fig. 5.3, showcasing how the grouping is conducted from the same starting point (FEA-calculated stress distribution on the uniform initial ground structure) but with different numbers of clusters ( $N_T = 2, 3$ , and  $5$ ). Finally, Fig. 5.4 illustrates the initial starting point of the optimization, with a uniform initialization of  $\bar{a}$  and the biased weight distribution based on the k-means clustering.

It is essential to highlight that the selection of the number of module topologies  $N_T$  is a critical parameter in the optimization process, predetermined by the designer. While performance metrics such as the average distance or silhouette coefficient may offer insights into the clustering algorithm's efficacy, their applicability here is limited. These metrics typically evaluate the fitness of the clustering based on the stress state of the structure when all subdomains are present, yet during optimization, subdomains may vanish, significantly altering the stress distribution. Moreover, the choice of  $N_T$  emerges as the primary means by which designers can vary the manufacturing complexity of the structure, making it a crucial hyperparameter for user consideration.

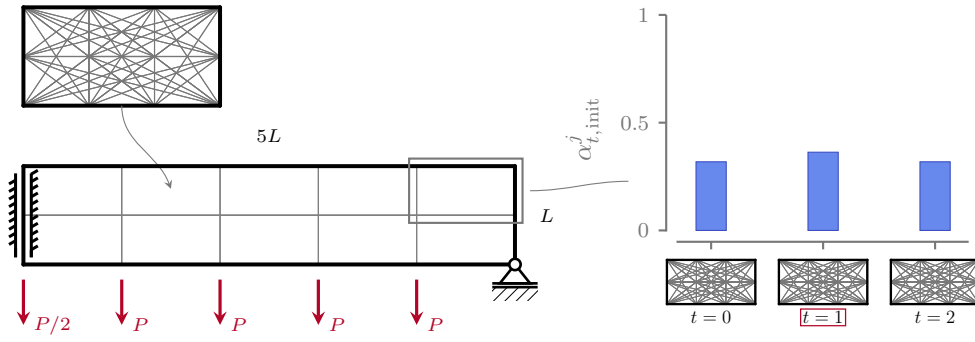


**Figure 5.4:** The proposed starting point for the first step of the optimization: a fully connected ground structure with uniform cross-sectional areas and a biased  $\alpha_{\text{init}}$  distribution, as suggested by the k-means clustering.

## 5.2 NUMERICAL OPTIMIZATION OF THE TOPOLOGY AND LAYOUT OF MODULAR STRUCTURES

The proposed algorithm to optimize the layout and topology of modular structures is tested in this section against multiple two- and three-dimensional test cases. All examples presented are solved using a modified version of the proposed two-step formulation. In the first step, a relaxed formulation (without compatibility constraints) is solved to determine the optimized modules' layout and topology. Subsequently, the layout of the modules is fixed, and the optimization problem is solved again to ensure the compatibility constraints. Both formulations are solved using the nonlinear interior point solver IPOPT.

A continuation scheme is established on the penalization parameter  $q$  of the RAMP interpolation scheme, utilized for evaluating the subdomains' volume. The parameter at the beginning of the optimization is set to zero and is reduced by 0.4 each time the optimizer both satisfies the following criteria: the relative volume difference of two successive iterations  $(V_i - V_{i-1})/V_i$  is less than  $1 \times 10^{-4}$  and the optimizer is not in a restoration phase. The minimum value is set to  $p = -0.8$ . This continuation scheme is implemented only on the  $q$  parameter responsible for the volume evaluation. This is because, as IPOPT is an interior point algorithm, increasing the  $p$  parameter would place the optimizer well outside the feasible region each time it is increased, resulting in a suboptimal situation. The parameter  $\chi$ , referred to as the cross-sectional area threshold value, is set to  $1 \times 10^{-4}$ .

The cross-sectional area threshold value  $\chi$  is used to threshold the bars of the original ground structure to reduce the number of candidates of the second step of the optimization. The candidate bars are the ones that satisfy the following inequality:

$$\bar{a}_i < a_{\text{thr}} \quad \forall i, \text{ with } a_{\text{thr}} = \chi \max(\bar{a}^*)$$

The stopping criterion employed for the first step optimization is  $\|\Delta_{\text{NLP}}\|_\infty \leq \text{tol}_{nlp}$ , where  $\text{tol}_{nlp} = 10^{-8}$ . Here,  $\Delta_{\text{NLP}}$  represents the scaled Non-Linear Programming (NLP) error, a comprehensive value used by IPOPT to consider both the optimality of the solution and constraint violations. The objective function is scaled such that the initial volume is 1000, the cross-sectional area falls within the interval  $[0, 100]$ , the initial forces range within  $[0, 100]$ , and the  $\alpha$  design variable lies within  $[0, 1]$ . The values taken here are taken as normalized

and without units of measure for convenience. Several additional parameters are utilized in the first optimization step for CyIpopt and IPOPT:

- ▶ `mu_strategy` is set to `adaptive`
- ▶ `num_linear_variables` is set to `N`, where  $N$  is the number of bars as the force is linear in this problem
- ▶ `grad_f_constant` is set to `yes`
- ▶ `bound_push` is set to `1e-12`
- ▶ `constr_viol_tol` is set to `1e-6`
- ▶ `nlp_scaling_method` is set to `user-scaling`.

For the settings of the second step optimizer, the reader can refer to Section 4.2.

### 5.2.1 LAYOUT OPTIMIZATION OF FIXED TOPOLOGY MODULES

The proposed optimization formulation is highly versatile, allowing the solution of various optimization problems. We begin by optimizing a straightforward modular structure problem. The objective is to minimize the volume of a structure by optimizing the layout i.e., the distribution, of a single ( $N_T = 1$ ) fixed-topology module within a specified domain. The optimization process involves deciding whether each subdomain should be populated or not. For this scenario, we consider a single fixed module topology, setting  $\bar{a}_i = 0.6$  for all  $i$ . The only degree of freedom granted to the optimizer is, thus, the value of the weights  $w$ , controlled by the layout design variables  $\alpha$ .

The structure to optimize is a two-dimensional cantilever beam with dimensions  $200 \times 100$ , subjected to a center load of magnitude  $P = 1$  directed downward. The optimization domain is divided into  $24 \times 12$  subdomains along the X and Y axes, respectively. Each subdomain is populated with a simple fully connected  $2 \times 2$  nodes ground structure comprising 6 candidate bars, as illustrated in Fig. 5.5. The material and geometrical data of the test case are normalized and dimensionless for convenience, and a list is provided in Table 5.1. In this example we treat a volume minimization problem with symmetrical stress constraints; buckling and compatibility constraints are not taken into account for simplicity and to preserve the solution symmetry.

Before showcasing and discussing the optimization results, we present two extreme cases that help us better understand and contextualize the optimization outcomes. First, we establish a monolithic optimization without considering modularity using the optimization formulation  $\mathbb{P}_1$  described in Chapter 3, setting a maximum cross-sectional area  $a_{\max} = 0.6$ . The optimization is conducted on the same ground structure illustrated in Fig. 5.5. The volume obtained by optimizing the structure that way should represent a lower bound of the optimization, indicating the minimum value towards which modular optimization should tend; the closer to this value, the better. The resulting reference

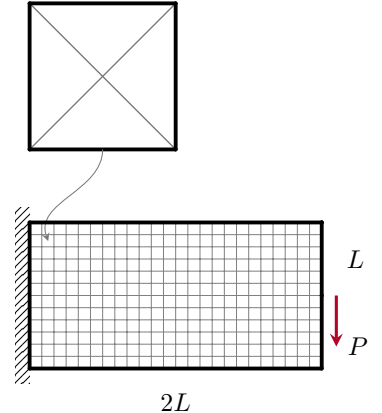


**Figure 5.5:** Boundary conditions of the 2D cantilever beam divided in  $24 \times 12$  subdomains. In the upper part of the image, the ground structure of the module composed of  $\bar{n} = 6$  elements is shown.

Parameter	Value
$L$	100
$\sigma_c, \sigma_t$	$\pm 1$
$P$	1
$a_{\max}$	0.6

**Table 5.1:** Material and geometrical data used for the 2D cantilever beam optimization. The Young's module is not listed as in this problem we temporarily overlook compatibility.

Test case	R1	R2
$\varphi$	100 %	0 %
$\psi$	1.00	0.07

**Table 5.2:** Performance parameters evaluated for the two reference cases R1 and R2.

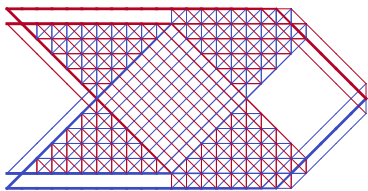


**Figure 5.6:** Monolithic optimized structure labeled R1 for the cantilever beam 2D test case with a maximum cross-sectional area  $a_{\max} = 0.6$ . This solution represents the lower bound solution for this test case with a volume  $V = 832.8$ .

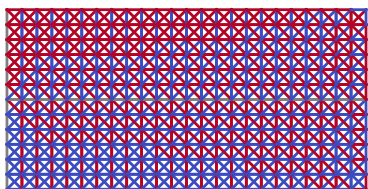


**Figure 5.7:** Fully-modular structure labeled R2 in which every subdomain is populated with a fixed given module. The structural volume is  $V = 9832.9$ .

topology (labeled R1) shown in Fig. 5.6 exhibits a volume  $V = 832.8$  and a structure resembling those obtained in classic topology optimization. Secondly, we present a fully modular structure with a single module topology ( $N_T = 1$ ), where all subdomains adopt the topology of the fixed topology module with all cross-sectional areas set to 0.6. In this case, the structure (labeled R2) demonstrates a volume  $V = 9832.9$  and serves as a reference upper bound for the optimization. The topology of this fully modular structure is depicted in Fig. 5.7.

The structures are examined not just based on volume considerations, but also using the performance metrics for modular designs introduced in Section 4.2.2. Referring to Table 5.2, we observe contrasting characteristics between the monolithic structure R1, which exhibits uniform loading and a fully stressed design, and the fully modular case R2, which presents the diametrically opposite scenario with zero bars that activate mechanical constraints.

Now that we have established a reference for a better understanding of the optimization results, we proceed with the optimization of the layout of the fixed-topology module. For the first example, we decided not to penalize intermediate weights, setting  $p = q = 0$ , and consequently  $w = \alpha$ . We call this modular structure M1. The optimized structure topology is illustrated in Fig. 5.8a and Fig. 5.8b, where we also depict the weight distribution of the solution. At this stage, the optimized structure exhibits a volume  $V = 1567.2$ , a value that is almost two times more voluminous than the monolithic reference R1 ( $V = 832.8$ ). However, this solution is non-physical as many subdomains display intermediate weights (see the weight distribution in Fig. 5.8c), requiring a thresholding operation on the value of the weights  $w$ . The thresholding value is set to 0.01, such that any  $j$  subdomain with a weight  $w^j$  less than this value is considered empty and subdomains with a weight above this value are considered full ( $w^j = 1$ ). The result of the thresholding is presented in Fig. 5.8d, where we observe that all weights are now set either to 1 or 0. The resulting structure has a volume  $V = 8808.6$ , indicating a noticeable volume increase due to the high number of intermediate weights in the solution shown in Fig. 5.8b and close to the volume of the upper bound structure R2 shown in Fig. 5.7. Finally, the structure M1 presents  $\varphi = 0\%$  and  $\psi = 0.121$ , confirming the poor loading condition and efficiency of the structure.

To address this issue, we implement a multi-phase RAMP interpolation where we simultaneously penalize mechanical properties (using the parameter  $p$ ) and artificially increase the volume (using the parameter  $q$ ) of modules with intermediate weights. In this optimization, we set  $p = 8$ ,  $q_0 = 0$ , and  $q_{\min} = -0.8$ , and a continuation scheme is employed on the  $q$  parameter to gradually decrease it to the minimum value, as explained in Section 5.2. We call this example M2. The optimized

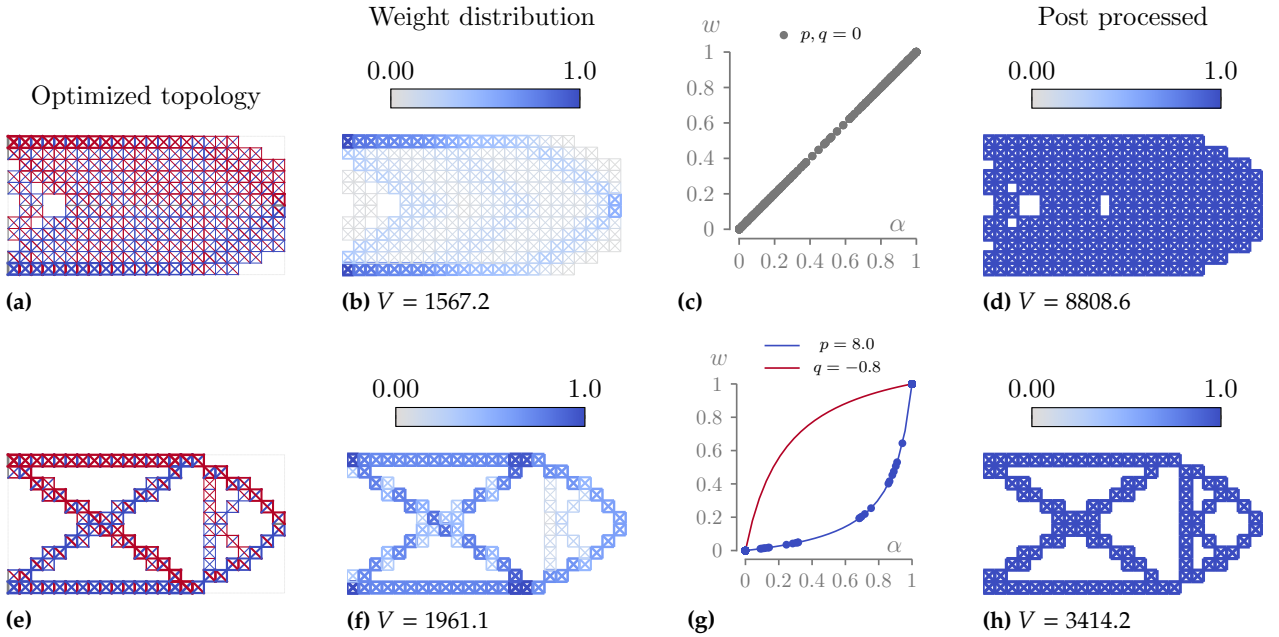


**Figure 5.8:** Optimization of the fixed module topology of the 2D cantilever beam. (a-d) show the solution M1, obtained without penalizing intermediate weights with a final volume  $V = 8808.6$ ; (e-h) show the solution M2, in which the RAMP interpolation helps to reduce intermediate weights. The final structural volume is  $V = 3414.2$ .

structure topology with penalized intermediate weights is depicted in Fig. 5.8e and Fig. 5.8f, with a resulting volume  $V = 1961.175$ , representing a 25 % increase compared to the M1. However, this solution presents fewer subdomains with intermediate weights, as reflected in the thresholding phase shown in Fig. 5.8h, where the volume is now  $V = 3414.2$ , more than 60 % less than M1 and 70 % less than R2. These behaviors are similar to what is observed in classic topology optimization [57, 72]. The M2 structure shows  $\varphi = 5.66 \%$  and  $\psi = 0.342$ , values that are still far from the ones of R1, but that show a remarkable improvement over structure M1.

Now that we have assessed the need for a penalization scheme, we test the proposed optimization formulation with some test cases using multiple fixed modules. As the topology of the module ( $\bar{a}$ ) is not modified, no perturbation is made to the initial starting point, and  $\alpha_{\text{init}}$  at iteration 0 is set to  $\alpha_{t,\text{init}}^j = 0.5, \forall j, t$ .

The first test we conducted was to optimize the layout of two different modules ( $N_T = 2$ ) that present the same connectivity but different cross-sectional areas. We used two 2-nodes fully connected modules with uniform cross-sectional areas set to 0.6 and 0.2 to simulate high and low-density modules for high and low-stress parts of the structure. The results are presented in Fig. 5.9a and b, and the optimized structure has a volume  $V = 2987.4$ . This represents a 12 % improvement over the M2 test case.

Similar results are presented in Fig. 5.9c and d, in which we optimize

57. Bendsøe et al. (1999), 'Material interpolation schemes in topology optimization'

72. Sigmund et al. (2016), 'On the (non-)optimality of Michell structures'

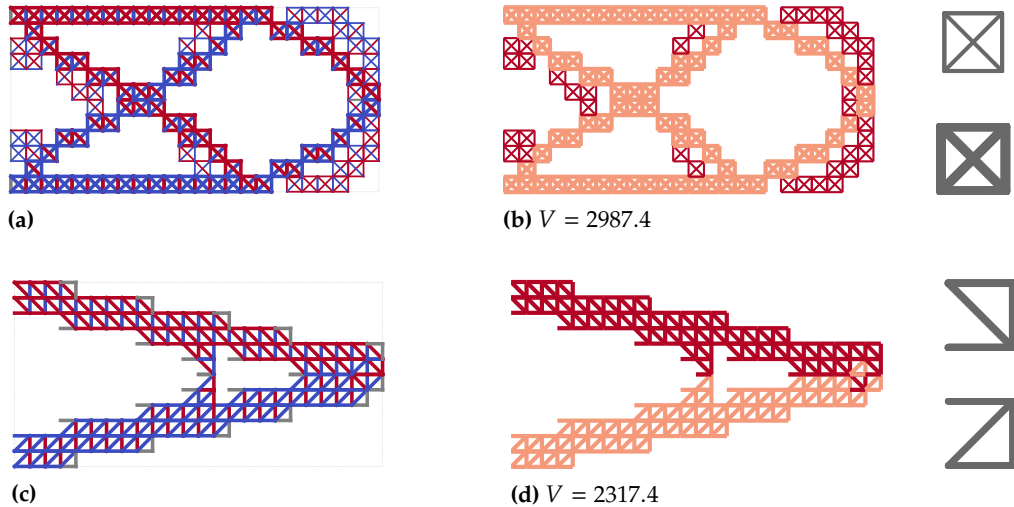
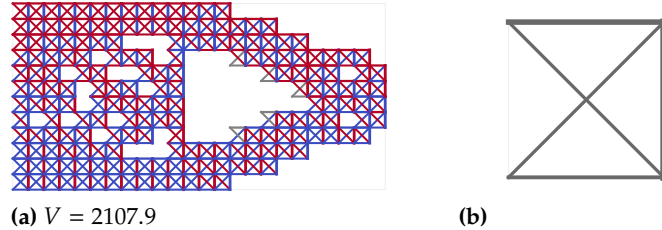


**Figure 5.9:** Two different examples of the optimization of a modular 2D cantilever beam using  $N_T = 2$  fixed topology modules. (a-b) show the topology and the module layout of the structure obtained using two modules with identical topology, but different cross-sectional areas, while the solution shown in (c-d) is obtained using two modules with identical cross-sectional areas, but different topologies. In (a) and (c) red bars are loaded in tension, while blue bars are loaded in compression.

**Figure 5.10:** Optimized topology of the modular structure (a) and the module (b) for the 2D cantilever beam optimized using a single module ( $N_T = 1$ ). Red bars are loaded in tension, while blue bars are loaded in compression.



the module layout of two modules that present different mirrored topologies (see Fig. 5.9d). The structure optimized in this way exhibits a very different module layout and a final volume  $V = 2317.4$ , a 32 % improvement over the M2 test case. These two examples confirm that giving more design freedom to the optimizer can enhance the mechanical performance of the modular structure.

### 5.2.2 MODULES AND LAYOUT OPTIMIZATION

We now optimize a modular structure using multiple modules that can vary their topology (the values of  $\bar{a}$  are no longer fixed). In the case of  $N_T = 1$ , the starting point for the layout variable is  $\alpha_{\text{init}}^j = 1, \forall j$ . The optimized structure, along with the optimized module topology, is shown in Fig. 5.10a and b. The modular structure exhibits a volume  $V = 2107.9$ , the best found until this point, confirming the interest in optimizing both the modules' topology and layout.

Moving on to the layout and topology optimization of modular structures with a number of module topologies  $N_T > 1$ , it becomes necessary to employ k-means clustering to determine the initial values for the layout module variable  $\alpha_{\text{init}}$ . A FEM analysis is conducted on the initial ground structure with uniform cross-sectional areas, and the k-means clustering is used on the stress distribution using

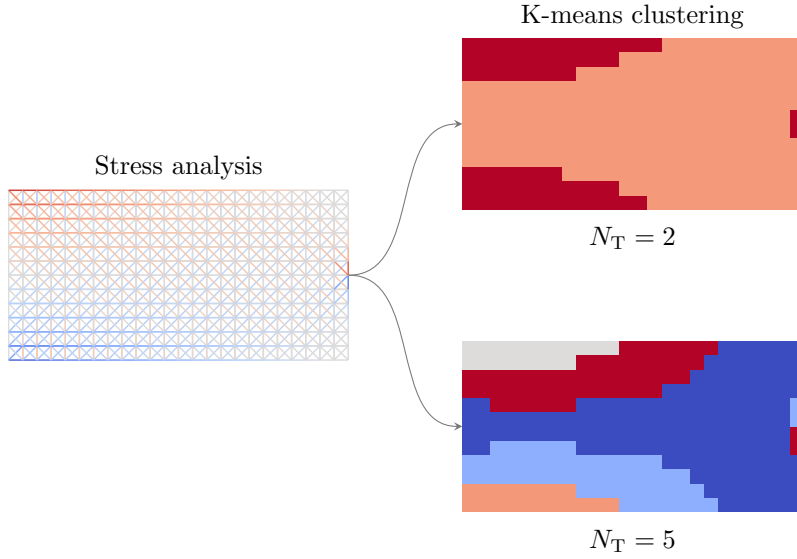


**Figure 5.11:** Similarly stressed sub-domains are identified using the k-means clustering algorithm to suggest a starting point for the first step of the proposed optimization algorithm. In the figure, we show the resulting distribution for  $N_T = 2$  and  $N_T = 5$ , obtained from the FEA stress.

**Table 5.3:** Numeric results of the parametric study on the influence of the number of modules on the optimized 2D cantilever beam.

$N_T$	1	2	3	4	5
$N_{\text{sub}}$	288	288	288	288	288
$N_{\text{sub,e}}$	107	45	72	43	50
$V$	2107.9	1722.6	1730.0	1589.8	1416.0
$a_{\max}$	0.37	0.35	0.48	0.54	0.53
$\varphi$	17.16 %	17.86 %	14.20 %	17.95 %	16.65 %
$\psi$	0.52	0.59	0.57	0.61	0.67
$t$	35 s	18 s	14 s	17 s	26 s

$N_T$  different clusters. This process is shown for  $N_T = 2$  and  $N_T = 5$  in Fig. 5.11, where it is observed that the k-means algorithm tends to regroup together the subdomains more based on their stress state  $S$  than the type of stress solicitation i.e. direction of principal stress. This fact is particularly evident in the  $N_T = 2$  example. It is only when the number of clusters reaches  $N_T = 5$  that a distinction between tension and compression becomes apparent, resulting in a solution that is no longer symmetrical with respect to the neutral axis of the beam.

Starting from the starting point obtained from the k-means clustering, four optimizations are performed for  $N_T$  spanning from 2 to 5. The numerical results of the optimizations are summarized in Table 5.3. Here are the main takeaways: the optimized volume exhibits a decreasing trend with respect to the numbers of modules  $N_T$ , indicating a more efficient allocation of material as the number of module topologies increases. Concurrently, the number of empty subdomains diminishes before reaching a stable value. This behavior could be explained by the increasing specialization of the modules that can shape their topology for more specific load cases and be less general-purpose, increasing the structure efficiency and reducing the redundancies. Indeed, we can observe that the value of the average bar load  $\psi$  is increasing with the number of module topologies. These two effects are illustrated in Fig. 5.12. Additionally, it is interesting how, with an increase in

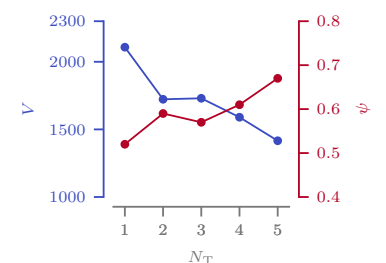


**Figure 5.12:** Influence of the number of modules  $N_T$  on the volume  $V$  and the loading metric  $\psi$  of the optimized 2D cantilever beam.

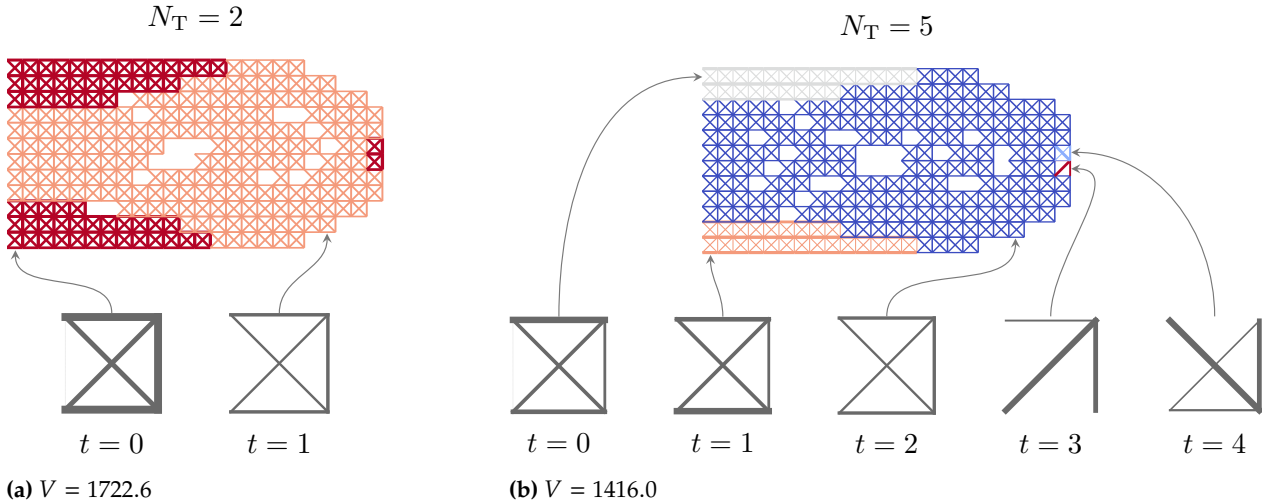


**Figure 5.13:** Visual representation of the optimized modular 2D cantilever beam together with the corresponding module topologies for (a)  $N_T = 2$  and (b)  $N_T = 5$ .

the number of module topologies, the number of empty subdomains  $N_{\text{sub}, e}$  drops from 107 and stabilizes at around 50. This suggests that for this specific test case, increasing the number of modules results in fewer empty subdomains, indicating that it is better to have many light modules rather than a few strong and heavy ones. Concerning the calculation time, we observe no real correlation with the number of modules. We speculate that even if the number of design variables increases with the number of modules  $N_T$ , the problem is often easier to solve, and fewer iterations are necessary to attain convergence. The optimized solutions with  $N_T = 2$  and  $N_T = 5$  are shown together with their optimized modules in Fig. 5.13.

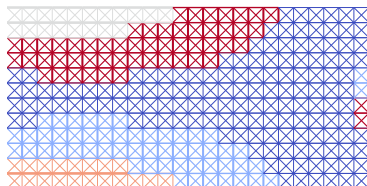


**Figure 5.14:** Optimized 2D cantilever beam obtained using the variable linking formulation with fixed modules' layout and  $N_T = 5$ . The modules' layout is obtained using the k-means clustering technique. The final volume is  $V = 1727.314$ .

The last aspect we want to comment on is a comparison between the optimized structure with  $N_T = 5$  presented in Fig. 5.13b and the structure we would obtain if we used the module layout suggested by the clustering algorithm to set the mapping matrix  $H$  and the variable linking algorithm described in Section 4.1.3. Using this formulation, the structure's layout is fixed, and no changes or empty modules are possible. The optimized structure using this algorithm is shown in Fig. 5.14, and it has a volume  $V = 1727.3$ , more than 20 % greater compared to the proposed method solution. The difference can be explained by two factors: firstly, the proposed formulation allows for empty subdomains, which significantly aids in lightening the structure. Secondly, the proposed formulation uses the clustering results only as a starting point for the layout of the optimization, but the layout can then evolve into a more optimized design. This example verifies the need to consider the module layout as a variable of the optimization that should be optimized simultaneously with the modules' topology.

### 5.2.3 A BENCHMARK CASE STUDY: A SIMPLY SUPPORTED MODULAR BRIDGE

The proposed formulation and optimization method are now benchmarked against benchmarks from the literature. To the knowledge of the authors, to this date, there are no other works that optimize the layout and topology of modular structures using a gradient descent algorithm with continuous design variables. However, similar results have been achieved using Mixed-Integer Programming (MIP), Mixed-Integer Linear Programming (MILP) algorithms, or Simulated Annealing (SA) to optimize modular structures. Examples include the works of Tugilimana *et al.* [158, 160], and we will now compare the results of the proposed formulation with their results.

The considered structure is a large modular structure based on the design of the Bailey bridge [219]. This concept has initially been studied for military purposes and later applied in civil engineering, particularly in temporary bridge structures. Its adaptability, low weight, and rapid erection allowing almost immediate usability for traffic, makes it highly versatile (see Fig. 5.15). The structure consists of 20 modules in length and 2 modules in height. Each module measures 3.050 m in length (10 ft) and 1.525 m in height (5 ft). This configuration results in a total bridge span of 30.50 m (100 ft).

The test case is based on the specifications given by Tugilimana *et al.* [158, 160] and is illustrated in Fig. 5.16, along with the geometrical and material data (normalized) utilized for the optimization (Table 5.4). The optimization is conducted only on the symmetric part of the structure. All constraints from the formulation  $M_1$  are considered in this load case, excluding the buckling constraint, following the approach adopted by Tugilimana *et al.*.

[158]. Tugilimana et al. (2019), 'An integrated design methodology for modular trusses including dynamic grouping, module spatial orientation, and topology optimization'

[160]. Tugilimana et al. (2017), 'Spatial orientation and topology optimization of modular trusses'



**Figure 5.15:** Bailey bridge placed on construction site road over Orava river (Slovakia) [218].

[219]. Department of the Army (1986), 'Field Manual No. 5-277, Panel Bridge, Bailey Type, Washington DC.'

[158]. Tugilimana et al. (2019), 'An integrated design methodology for modular trusses including dynamic grouping, module spatial orientation, and topology optimization'

[160]. Tugilimana et al. (2017), 'Spatial orientation and topology optimization of modular trusses'

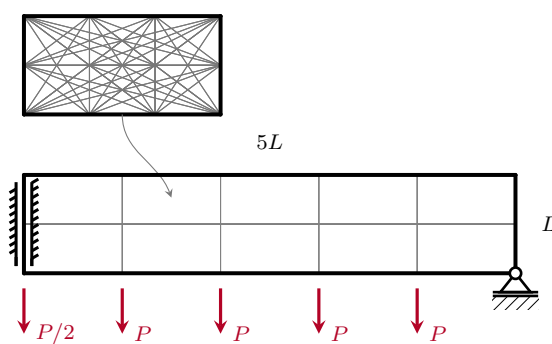


**Figure 5.16:** Graphical representation of the 2D Bailey bridge test case. The structure is divided into  $N_{\text{sub}} = 10$ . The bridge is symmetric, and we are here optimizing only the right part of it.

Parameter	Value
$L$	3.05
$\sigma_c, \sigma_t$	$\pm 1$
$P$	1

**Table 5.4:** Material data used for the 2D Bailey bridge without local buckling constraints test case to compare with the work of Tugilimana *et al.* [158]. The Young's module is not listed as in this problem the authors overlook compatibility and buckling constraints.

The resulting optimized structures are presented in the right part of Fig. 5.17, alongside the topology of the structures optimized by Tugilimana *et al.* [158] on the left part of the image. Below each subfigure, the structure volume is provided, along with the value relative to the Tugilimana solution in square brackets. While the reference images (left part of the image) do not highlight the subdomains with the same module topology using colors, it can be observed that the module layout of the reference and the proposed solution is not always the same, as seen in the cases of  $N_T = 4$  or  $N_T = 5$ . It is noteworthy that the proposed optimization algorithm not only excels in optimizing an intrinsically discrete optimization problem using continuous design variables and a gradient-based optimizer but also improves upon the results found in the literature by up to 3 %. Additionally, the structure obtained with  $N_T = 10$  is the same as what would be achieved by optimizing the structure without considering the modular constraints.

Up to now, we always used normalized material data and dimensions, and we never considered the local buckling of the truss. For this reason, we are interested in testing what happens in this specific test case when we do consider local buckling and use a real load case with realistic dimensions and material data. We are particularly interested in seeing if these changes significantly affect the module's topology and layout in the structure. The material data used for the optimization is presented in Table 5.5 and represents a generic aluminum. The cross-sections are assumed to be circular for the local buckling evaluation. Topological buckling is taken into account inside the modules, as explained in Section 4.1.2.

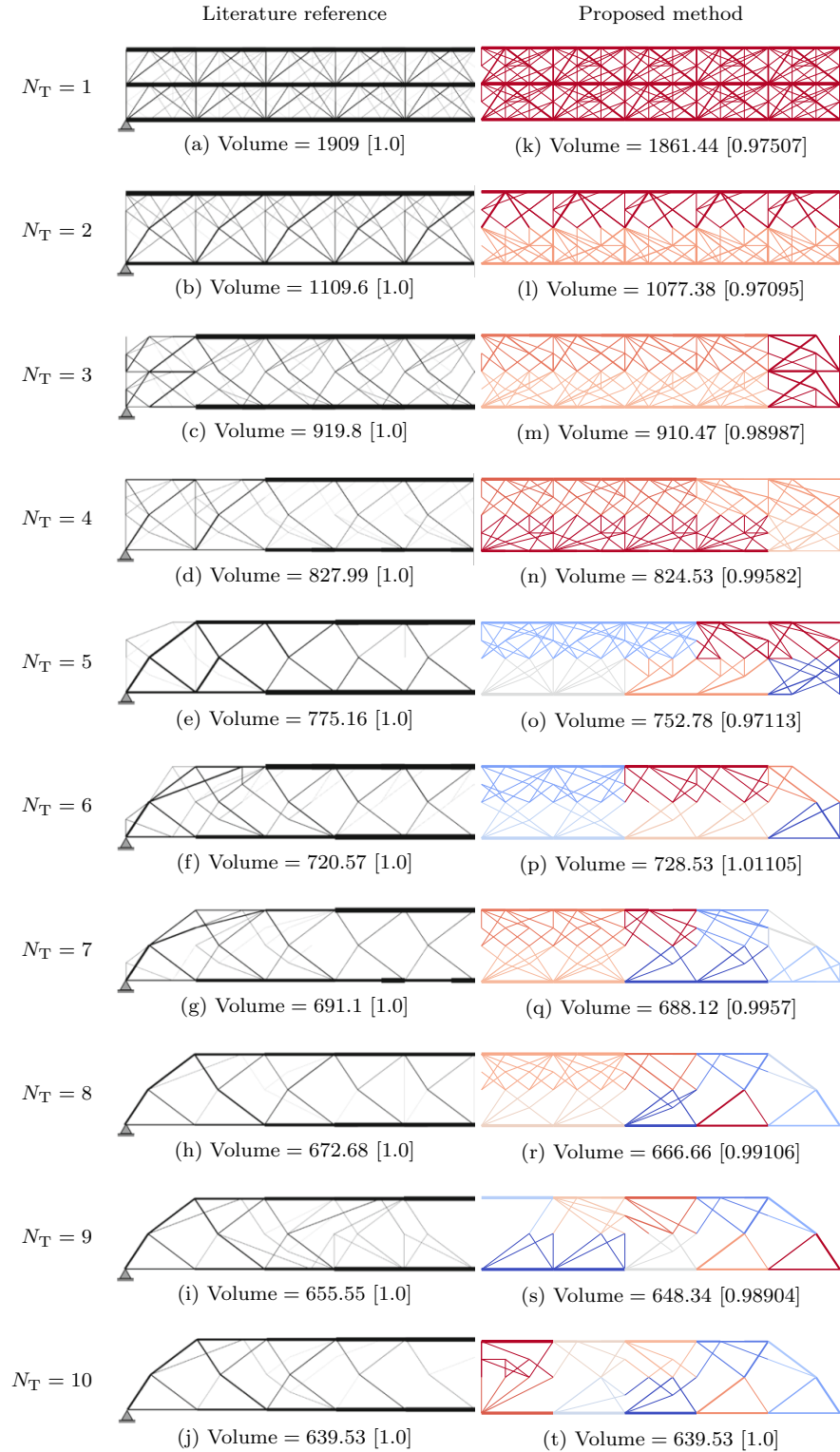


**Figure 5.17:** Visual comparison of the 2D Bailey bridge test case without local buckling constraints proposed by Tugilimana *et al.* [158] obtained for different number of modules  $N_T$ . The images (a-j) represent the optimized structures in [158], while the images (k-t) show the structures obtained with the proposed optimization method. Different colors are used to highlight different modules.

Parameter	Value
$L$	3.05 m
$E$	69 GPa
$\sigma_c, \sigma_t$	$\pm 270$ MPa
$P$	1 MN

**Table 5.5:** Material data used for the 2D Bailey bridge with local buckling constraints test case.

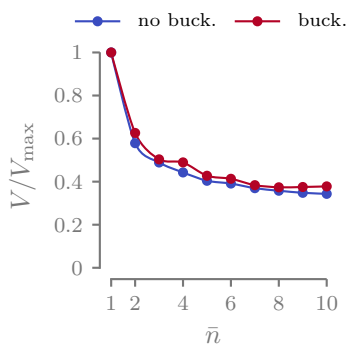


**Figure 5.18:** Normalized volume values plotted against the number of modules  $N_T$  for the simply supported modular bridge. The buckling constraints do not influence the trend of the beneficial effect of using multiple modules  $N_T$  on the structure.

The optimized structures for the Bailey bridge with buckling constraints are shown for different numbers of module topologies ( $N_T = 1$  to 10) in Fig. 5.19. Quickly comparing them with the results without buckling, we notice that for this test case, the layout of the modules remains unchanged. The topology, however, is very different, with generally slightly fewer active bars. The volume can not be directly compared, so we normalize them with respect to the maximum volume ( $N_T = 1$ ) and plot them in Fig. 5.18. We notice that adding multiple module topologies is beneficial in the same way with or without buckling constraints. We can also comment that the biggest reduction in volume from the inclusion of additional modules comes especially at the beginning, e.g., going from  $N_T = 1$  to  $N_T = 2$  or from  $N_T = 2$  to  $N_T = 3$ , while the difference at higher numbers is marginal as the curve approaches a plateau.

Willing to explore how different parameters can influence the resulting volume, topology, and layout, we optimize the same test case with a different number of subdomains and modules. For this exercise, we use a 3x2 nodes fully connected ground structure for faster calculation times.

The results of the optimizations with different numbers of subdomains and modules are shown, together with the value of the structural volume in Fig. 5.20. Looking at the image from left to right, we observe that the trend of volume reduction with the increase in the number of module topologies we have already acknowledged previously is still valid. It is, however, more interesting to see what happens going from top to bottom, i.e. what happens when we change the number of subdomains  $N_{\text{sub}}$  without changing the number of module topologies  $N_T$ . As expected and already observed using the variable linking algorithm (see, for example, Fig. 4.7 in Chapter 4), the volumes increase with the number of subdomains. However, in Fig. 5.21, in this case, we observe a steep increase in the structural volume and then a plateau, different from before. We speculate that this beneficial behavior comes mainly for two reasons: first, the optimization algorithm allows some subdomains to show an empty topology. We observe that when we have a few subdomains, the structure is always filled, with no empty subdomains. But with the increasing number of subdomains, we notice more and more empty subdomains, helping to keep the structure light. Second, by increasing the number of subdomains, the average length of the subdomains' bars decreases. This triggers a change in the failure mode, moving from buckling to stress. For example, we observe that in Fig. 5.20d, the module shows a symmetric topology, meaning that the failure mode is completely changed to stress with equal distribution in compression and tension. This is a very effective use of the material, and consequently, the volume decreases.

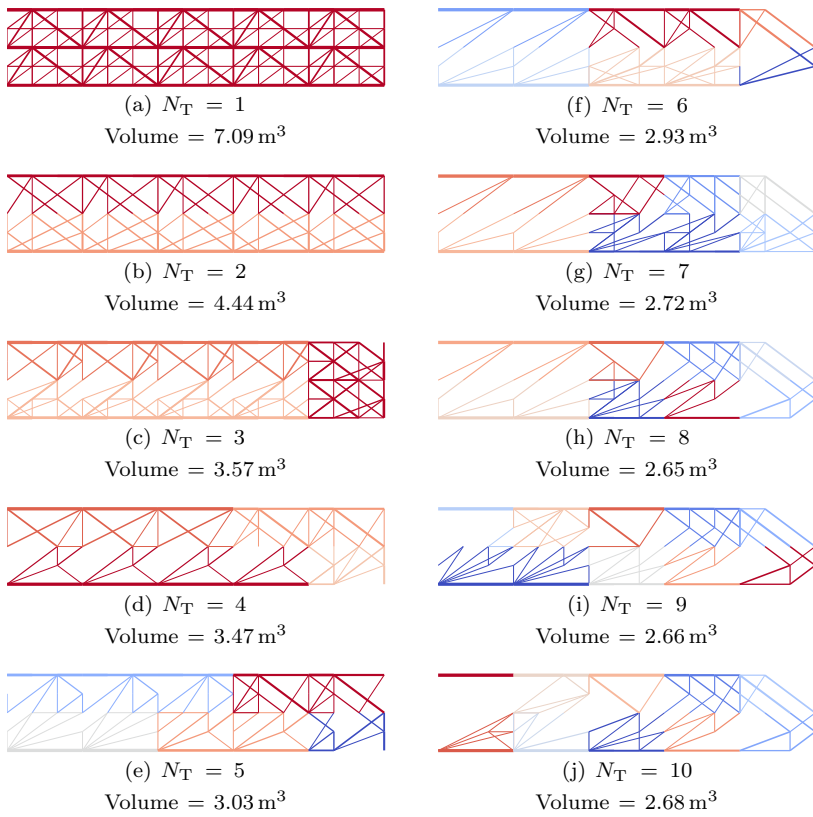


**Figure 5.19:** Visual representation of the optimized structures obtained for different values of  $N_T$  for the 2D Bailey bridge test case with local buckling constraints.

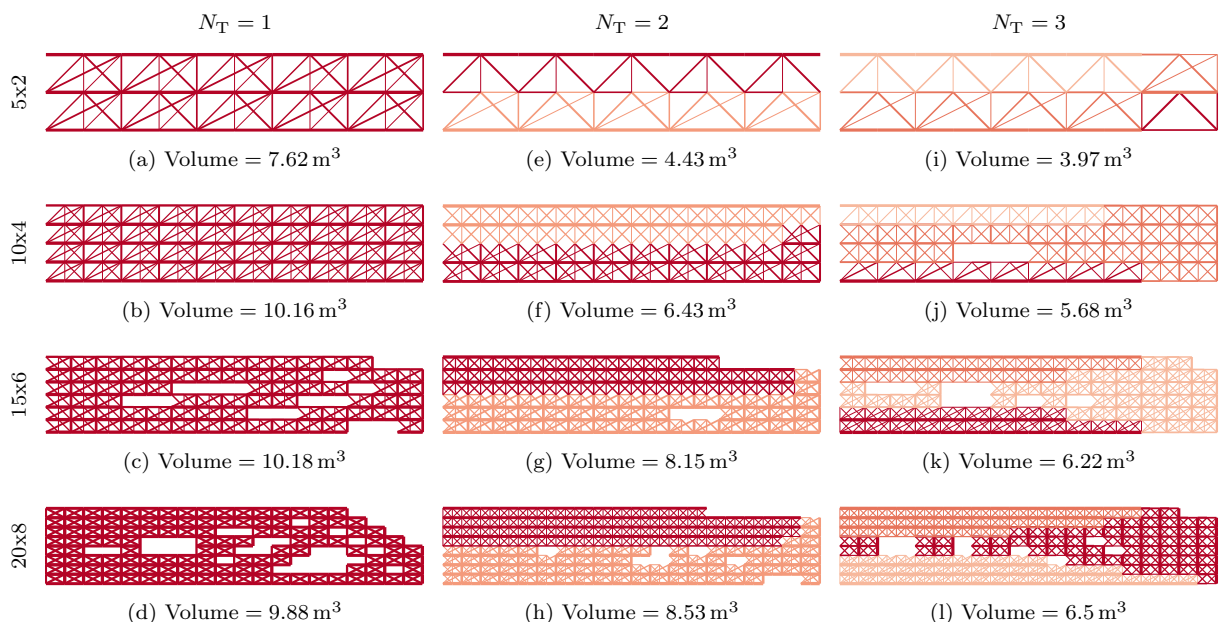


**Figure 5.20:** Study of the influence of the parameters  $N_{\text{sub}}$  and  $N_T$  on the volume and the topology of the 2D Bailey bridge test case.

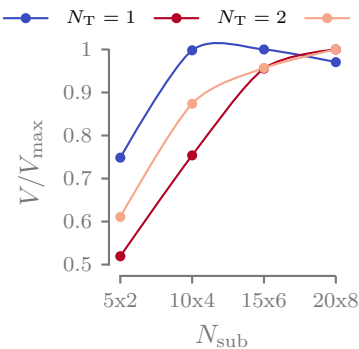


**Figure 5.21:** Normalized volume values plotted against the number of subdomains  $N_{\text{sub}}$  for different values of  $N_T$ .

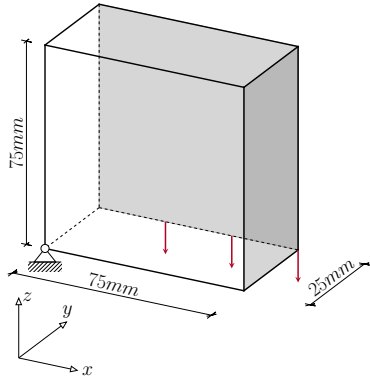


**Figure 5.22:** Symmetric boundary conditions of the simply supported 3D beam. In gray are the symmetry planes of the test case.

Parameter	Value
$E$	2.7 GPa
$\sigma_c, \sigma_t$	$\pm 55$ MPa
$\rho$	$1.14 \text{ g cm}^{-3}$
$P$	100 N

**Table 5.6:** Material data used for the simply supported 3D beam optimization.

Lastly, we observe that the modules' layout is almost invariant with the increasing number of subdomains i.e., the color distribution is not impacted by the module size. This fact is somewhat similar to what we observe in classic topology optimization when we increase the mesh fineness with a fixed distance-based filter. In these cases, the topology remains unchanged with mesh refinement.

#### 5.2.4 SIMPLY SUPPORTED 3D BEAM

The last test we conduct is on the simply supported 3D beam, a test case introduced in Chapter 3 and already used throughout this thesis. We recall the test case and the material and geometric data used for the optimization process in Fig. 5.22 and Table 5.6. We optimize here only one-fourth of the entire structure thanks to its symmetry planes. We conduct the optimization using  $6 \times 2 \times 3$  subdomains on the X, Y, and Z axes, respectively, and every module is discretized using a  $3 \times 3 \times 3$  fully connected ground structure with a total number of candidates  $\bar{n} = 351$  per module. The optimization is conducted using three different numbers of modules,  $N_T = 1, 2, 3$ .

The resulting optimized structures are presented in Fig. 5.23, and the associated numerical results are shown in Table 5.7. An initial observation is that in this specific test case, the optimizer converges to solutions where  $\sum \alpha_t$  for every subdomain equals one. While previously, we observed formulations that led to the creation of empty subdomains with a  $\sum \alpha_t$  equal to zero (as seen in Fig. 5.13 or Fig. 5.20), here the optimizer do not do so. For  $N_T = 2$  and  $N_T = 3$ , the empty subdomains correspond to cases where the cross-sectional areas of one module are set to zero, and the optimizer assigns the value of the corresponding layout variable *alpha* to one. Thus, the solution is still optimized effectively, but using one additional module topology. For instance, examining Fig. 5.23b and e, the solution for  $N_T = 2$  reveals that the optimized structure exhibits only one module topology, with the other being empty. This behavior is acceptable, and the optimized structures show low volumes and good mechanical properties, but from a user perspective is just not desirable.

In our attempts to mitigate this behavior, we experimented with scaling the layout design variable  $\alpha$  and its associated constraints using various factors, yet we consistently obtained identical outcomes. This issue suggests that while the starting point perturbation certainly aids in achieving a well-optimized structure, additional work is needed to develop a whole new resolution strategy. One possible approach could be to separate the topology and layout variables and iteratively solve the two problems independently, one iteration at a time.

A careful examination of the volume  $V$  and mean densities  $\bar{\rho}$  in Table 5.7, however, reveals that the modular structure with  $N_T = 3$  achieves remarkably similar volume (+2.8 %) to the monolithic reference ( $N_{\text{sub}} = 1$ ) depicted in Fig. 5.24. This outcome is particularly

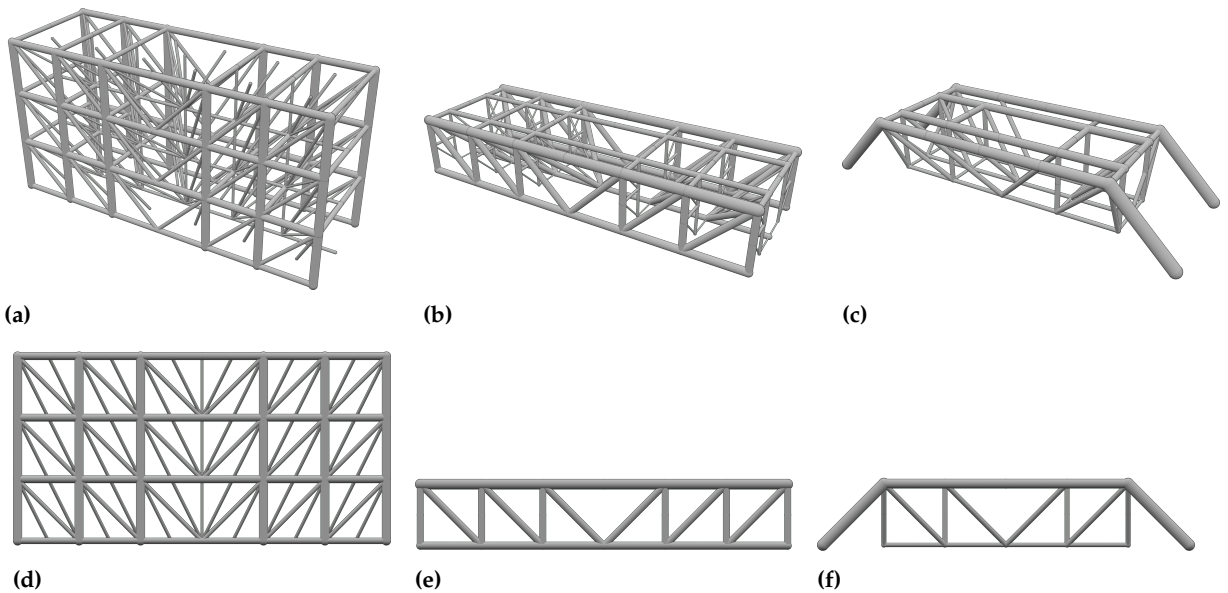


**Figure 5.23:** Rendering of the optimized simply supported 3D beam with  $N_T = 1$  (a,d),  $N_T = 2$  (b,e), and  $N_T = 3$  (c,f).

$N_T$	-	1	2	3
$N_{\text{sub}}$	1	36	36	36
$N_{\text{opt}} (N_{\text{el}})$	20 (1984)	360 (12636)	204 (12636)	104 (12636)
$V [\text{cm}^3]$	9.907	27.958	15.548	10.178
$V [\%]$	1.761	4.970	2.764	1.809
$\bar{\rho} [\text{kg/m}^3]$	80.31	226.65	126.05	82.51
$\varphi$	100.00 %	21.11 %	39.21 %	80.77 %
$\psi$	1.00	0.47	0.66	0.87
$t$	4 s	1 m 18 s	42 s	10 m 22 s

**Table 5.7:** Numeric results of the parametric study on the influence of the number of modules  $N_T$  on the simply supported 3D beam.

significant as it attains the objective of achieving a lightweight structure, almost comparable to the monolithic one, while preserving modularity, highlighting the potential for a light structure with manufacturing advantages due to its modular nature.

### 5.3 CONCLUSION

In this chapter, we introduced an innovative optimization formulation designed to optimize the structural volume of modular structures. The solving algorithm uses the physical information of the model, exploiting analytical derivatives and employing a gradient descent optimization approach. Categorical variables, used to determine module layout, are modeled using a weighted sum of continuous weights that align with the continuous design variables of the optimization scheme. A double penalization scheme is proposed to mitigate the occurrence of non-physical intermediate weights.

The proposed formulation is tested across a variety of two- and three-dimensional test cases sourced from the literature. These tests

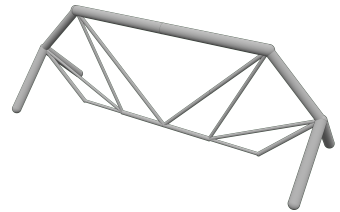


**Figure 5.24:** Perspective view of the monolithic simply supported 3D beam optimized structure with  $V = 9.907 \text{ cm}^3$ .

confirm that the utilization of this optimization formulation enables modular structures to achieve volumes very close to those obtained from monolithic optimization, maintaining modularity and offering a favorable trade-off between optimality and manufacturing complexity. However, the focus has been on simple test cases lacking engineering relevance so far. In the next chapter, we address this limitation by applying the presented optimization formulations in the aerospace context.

Ultralight trusses offer a compelling solution for the development of innovative aerostructures due to their exceptional aeroelastic properties and high stiffness-to-weight ratio. These structures align well with the optimization formulations discussed in previous chapters. Opgenoord [116, 217] proposed a two-step sequential optimization approach to reduce the weight of truss wings. Initially, they generated a ground structure with varying nodal densities based on the stress field, followed by a sizing optimization algorithm to determine the cross-sectional areas, considering stress, local buckling, and aeroelastic constraints. Shahabsafa [220], on the other hand, took a different approach, employing discrete cross-sectional areas and a Mixed-Integer Linear Optimization (MILP) sizing optimization algorithm to address the complexities of the problem. However, by solely focusing on modifying the component sizes, the opportunity to optimize the overall truss topology is missed, limiting the potential for further weight savings. Moreover, none of these studies evaluated the fabricability of the proposed designs, highlighting the potential benefits of modularity in addressing these aspects.

In the preceding chapters, our focus was on the development of optimization methods for both monolithic and modular structures, which were then applied to two- and three-dimensional academic load cases. In this chapter, we aim to validate the proposed optimization algorithms by applying them to real-world engineering problems in the aeronautical domain. Firstly, to evaluate computational efficiency and validate the strategy outlined in Chapter 3 on a large-scale structure, we optimize a monolithic three-dimensional wingbox test case based on the NASA Common Research Model (CRM), considering multiple load cases and two discretization refinements. Subsequently, we apply the modular algorithm introduced in Chapter 5 to a drone-sized wing utilizing an extruded NACA 0012 profile.

The optimizations presented in this section are performed on a notebook equipped with an Intel Core™ i5-9400H Processor @ 2.50 GHz (4 cores) and 16 GB of RAM.

## 6.1 3D CRM WINGBOX WITH MULTIPLE LOAD CASES

In this section, the monolithic optimization strategy presented in Chapter 3 is used to optimize a real-size wingbox, to validate its ability to work on large, three-dimensional structures with more candidate members compared to the precedent test cases. The structure is based

6.1 3D CRM WINGBOX WITH MULTIPLE LOAD CASES . . . . .	123
6.2 NACA 0012 MODULAR DRONE WING . . . . .	134
6.3 CONCLUSION . . . . .	143
<b>116.</b> Opgenoord et al. (2018), 'Aeroelastic Tailoring using Additively Manufactured Lattice Structures'	
<b>217.</b> Opgenoord et al. (2019), 'Design for additive manufacturing: cellular structures in early-stage aerospace design'	
<b>220.</b> Shahabsafa et al. (2018), 'A novel approach to discrete truss design problems using mixed integer neighborhood search'	

[221.](#) Brooks et al. (2018), 'Benchmark Aerostructural Models for the Study of Transonic Aircraft Wings'

[222.](#) Fakhimi et al. (2021), 'Discrete multi-load truss sizing optimization'

[207.](#) Stragiotti et al. (2023), 'Truss Topology Optimization with Topological Buckling Constraints Data Set'

Parameter	Value
$E$	69 GPa
$\sigma_c, \sigma_t$	$\pm 270$ MPa
$\rho$	$2.7 \text{ g cm}^{-3}$

**Table 6.1:** Material data used for the CRM optimization.

[178.](#) Diamond et al. (2016), 'CVXPY: A Python-Embedded Modeling Language for Convex Optimization'

[179.](#) Domahidi et al. (2013), 'ECOS: An SOCP solver for embedded systems'

[205.](#) Moore et al. (2018), 'cyipopt: Cython interface for the interior point optimizer IPOPT'

[35.](#) Wächter et al. (2006), 'On the implementation of an interior-point filter line-search algorithm for large-scale nonlinear programming'

[206.](#) Alappat et al. (2020), 'A Recursive Algebraic Coloring Technique for Hardware-efficient Symmetric Sparse Matrix-vector Multiplication'

Equation 3.13 reads:

$$\phi_n = \phi_{n-1}^\beta \quad \forall n \in [1, \dots, n_{\max}],$$

with  $\phi_0 = 0.8$  and  $\beta = 2$ .

Equation 3.15 reads:

$$a_i < a_{\text{thr}} \quad \forall i, \text{ with } a_{\text{thr}} = \chi \max(\tilde{a}^*)$$

on the jig (undeformed) shape of the wingbox of the NASA CRM [221]. The structure is submitted to three different load cases: +2.5 g maneuver (LC\_1), -1 g maneuver (LC\_2), and cruise with gust +1.3 g (LC\_3). The nodes of the bounding volume and the loads used are provided by Fakhimi *et al.* [222], where a detailed discussion on how they are evaluated can be found. The ground structure of the test case is presented in Fig. 6.1a. Additionally, the load cases and the starting point, of all the presented test cases are available in the reference data set [207].

The material used for the optimization is an aluminum alloy with Young's modulus of 69 GPa, density of  $2.7 \text{ g/cm}^3$ , and yield stress equal to  $\pm 270$  MPa (see Table 6.1). To ensure a conservative design, we incorporated safety factors ( $sf$ ) associated with each load case. These safety factors are integrated into the formulation by reducing the maximum stress and buckling allowables by factors of 1.5, 1.5, and 2.67 for the three considered load cases, respectively. The cross-sections are assumed circular with the cross-sectional buckling parameter  $s = \pi E/4$ . The optimization is carried only on the wingbox, the internal structure of the wing, and there is no influence of the skin on the optimization.

The optimizations are performed using the Python package CVXPY 1.2.2 [178] with the ECOS 2.0.7 [179] solver to solve the relaxed Linear Programming (LP) Problem Equation  $\tilde{\mathbb{P}}_2$ . The Non-Linear Programming (NLP) Problem Equation  $\mathbb{P}_1$  is solved using cyipopt [205], a Python wrapper for IPOPT 3.14.11 [35], a large-scale nonlinear optimization package using PARDISO 6.0 [206] as the linear solver. The stopping criterion used for the Sequential Linear Programming (SLP) and NLP optimisations are  $\|\Delta x\|_\infty \leq \text{tol}_{slp}$ , and  $\|\Delta_{NLP}\|_\infty \leq \text{tol}_{nlp}$ , with  $\text{tol}_{slp} = 10^{-6}$  and  $\text{tol}_{nlp} = 10^{-4}$  respectively.  $\Delta_{NLP}$  represents the scaled NLP error, a more comprehensive value used by IPOPT to take into account the optimality of the solution and the constraints violation. The reinitialization magnitude parameter  $\phi$  is set up using Equation 3.13, leading to  $\phi = [0.8000, 0.6400, 0.4096, 0.1677, 0.0281]$  for the five reinitialization calls of 2S-5R. The full list of parameters used to set up the variable scaling, the SLP optimization, the reinitialization, and the NLP optimization is the same used in Chapter 3 listed in Table 3.2.

### 6.1.1 ADVANCED THRESHOLDING

As the CRM is a large and thin structure that presents a noticeable difference in load magnitude between the tip and the root of the wingbox, the quantities of interest of the optimization span different orders of magnitude (from  $\text{m}^2$  to  $\text{mm}^2$ , and from MN to N). For that reason, the choice of the cross-sectional area threshold value  $\chi$  defined in Equation 3.15 and used to simplify the initial NLP ground structure is crucial. Taking a high value (such as  $\chi = 10^{-4}$ , restraining

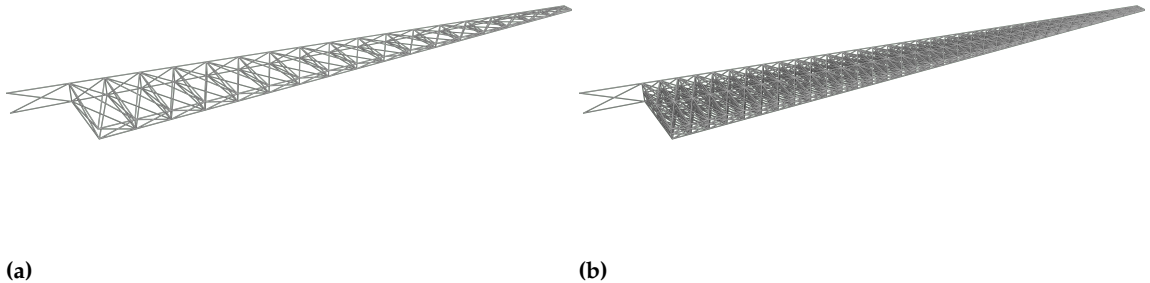


**Figure 6.1:** (a) Ground structure of the CRM-315 test case; (b) Ground structure of the CRM-2370 test case. The cross-sectional areas shown in the two sub-figures represent the starting point of the optimizations.

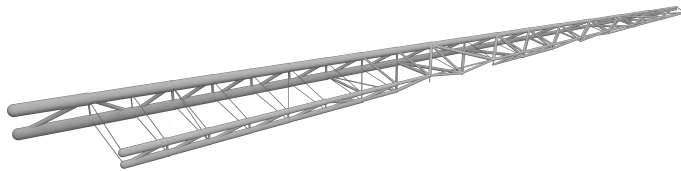


**Figure 6.2:** Optimized topology of the CRM-315 with 257 active bars.

the solution from  $\text{m}^2$  to  $\text{cm}^2$ ) would mean possibly canceling out bars fundamental for the nodal force equilibrium in the less loaded part of the wing (wing tip and the central part of the wing's sections near the root). By contrast, a low value (such as  $\chi = 10^{-9}$ ) would permit the correct simulation of the mechanical response of the structure, but it would lead to a very high number of candidate bars and, thus, longer optimizations and convergence difficulty for the NLP phase. For that reason,  $\chi$  is set to an average value ( $\chi = 10^{-6}$ ), eliminating all the bars under the value  $a_{\text{thr}} = \chi \max(\mathbf{a})$ , but an additional check is performed before proceeding to the thresholding. The bars under the threshold  $a_{\text{thr}}$  are sorted in ascending order of cross-sectional area and, starting from the smallest one, we iteratively check via a Finite Element Analysis (FEA) that the difference between the force and displacement fields before and after the bar removal is below than a certain bound. In the present study we used the following:  $\|\Delta q\|_\infty < 10 \text{ N}$  and  $\|\Delta U\|_\infty < 1 \text{ cm}$ .

### 6.1.2 NUMERICAL OPTIMIZATION OF THE CRM WINGBOX

Two different discretizations are considered for the optimization. The proposed algorithm is firstly tested on the same ground structure provided by Fakhimi *et al.* [222], composed of  $N_{\text{el}} = 315$  candidate members (CRM-315). The second discretization is obtained by refining

222. Fakhimi et al. (2021), 'Discrete multi-load truss sizing optimization'

the 315-bar ground structure, evaluating the midpoints of every member, and connecting them with first-order connectivity. We obtain  $N_{el} = 2370$  candidate members (CRM-2370). The loads and the boundary conditions are applied on the same nodes of the ground structure for the two studied ground structures. The cross-sectional areas of the starting point of the CRM-315 and the CRM-2370 are set to  $0.0001 \text{ m}^2$  and they are shown in Fig. 6.1. Only one single start point is used for these two examples as the proposed two-step strategy with reinitialization already proved in Chapter 3 to reduce the starting point influence on the optimization result. The resolution algorithm used is 2S-5R. The numerical results of the optimization for the two different discretizations are reported in Table 6.2.

[222.](#) Fakhimi et al. (2021), 'Discrete multi-load truss sizing optimization'

The optimized CRM-315 structure shows a mass of 21.342 t, a 27.01 % reduction compared to the solution with discrete cross-section areas found by Fakhimi *et al.* [222] (29.238 t). Other than the substantial difference in the modelization of the cross-section areas, the mass reduction could be explained by the fact that the proposed algorithm has a zero lower bound on cross-sectional areas, thus permitting the topology of the structure to change: the 2S-5R solution shows 257 active bars out of 315 at convergence (see Fig. 6.2). In contrast, the MILO problem solved by Fakhimi *et al.* [222] is employed as a sizing optimization algorithm with fixed topology (and thus 315 active members in the optimized design). A more detailed comparison could not be performed as the authors did not share the values of the cross-sectional areas of their solution.

The volume fraction of the solution is 1.313 % and the minimum slenderness ratio  $\lambda$  (ratio between the length and the radius of gyration of the bar) of a bar is 14.96, which is compatible with the truss modelization used to discretize the wingbox volume. The execution time of the optimization is 19 s for the SLP step and 128 s for the NLP step, for a total of 147 s on a regular notebook, compared to the over four days of optimization of Fakhimi [222] on a desktop workstation. The iteration history curves of the optimization are plotted in Figure 6.3a, where we notice the multiple sharp volume increases due to the reinitialization heuristic in the SLP step. Figure 6.3b, on the other hand, shows the constraint violation curves for the NLP phase. The starting point coming from the relaxed SLP step violates the stress and buckling constraints as the predicted force field does not account for kinematic compatibility, necessary due to the multiple loading conditions of this test case. From the graph, we can observe how the kinematic compatibility constraint is extremely challenging to satisfy.

**MAXIMUM DISPLACEMENT CONSTRAINTS** The designer of an aircraft may wish to restrict the maximum Z displacement of the wingtip  $Z_{t,\ell}$  to prevent excessive flexing of the wing, which could significantly

Quantity	CRM-315	CRM-2370
$N_{el}$	315	2370
$N_{opt}$	257	1127
$V [m^3]$	7.90	7.44
$V [\%]$	1.309 %	1.232 %
Mass [t]	21.342	20.092
$a_{max} [m^2]$	0.198	0.208
$C_{LC\_1} [MJ]$	3.23	3.17
$C_{LC\_2} [MJ]$	1.28	1.27
$C_{LC\_3} [MJ]$	0.76	0.74
$t [s]$	147	3189

**Table 6.2:** Numerical results of the optimization of the CRM with two different ground structures.

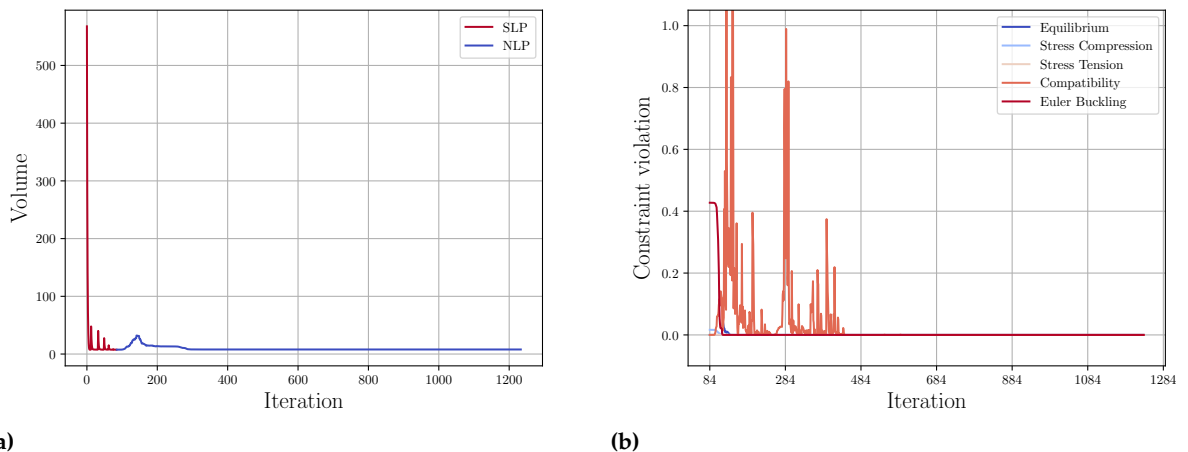


**Figure 6.3:** Iteration history of the CRM-315 test case solved with the 2S-5R algorithm. (a) objective function history for the SLP and NLP step. The sharp increases in the objective function during the SLP step correspond to the reinitialization calls. (b) constraint violation for the NLP step.

affect the aerodynamic performance of the wing. It is important to note that by controlling the maximum displacements of the structure, we can effectively influence its compliance, even if compliance minimization is not explicitly included in the objective function. Additionally, imposing such constraints can passively enhance the stiffness of the wing and mitigate aeroelastic phenomena such as flutter instability.

Having observed that in the unconstrained version the maximum tip displacement of the optimized CRM-315 structure, which has a half wing span of 29.4 m, is  $Z_t = 4.11$  m, we set three different maximum wingtip displacement values  $Z_{t,\ell} = [1 \text{ m}, 2 \text{ m}, 3 \text{ m}]$  in the NLP step, intending to explore how sensitive the optimized structure is with respect to this constraint. These constraints are simply put as bound constraints on the displacement design variable in the NLP step. The optimizations are conducted using the same material, geometrical, and load data as in the previous example.

We run the three additional optimizations and we plot the displacements in the XZ plane in Fig. 6.4 and the numerical values of the

**Table 6.3:** Numerical results of the optimization of the CRM-315 model with three different maximum displacement constraints ( $Z_{t,\ell} = 1\text{ m}$ ,  $Z_{t,\ell} = 2\text{ m}$ ,  $Z_{t,\ell} = 3\text{ m}$ ) and no maximum displacement constraints.

$Z_{t,\ell} [\text{m}]$	1	2	3	-
$V [\text{m}^3]$	26.70	13.78	9.39	7.90
$V [\%]$	4.421 %	2.283 %	1.556 %	1.309 %
Mass [t]	72.086	37.218	25.363	21.342
$a_{\max} [\text{m}^2]$	0.615	0.293	0.197	0.198
$C_{LC\_1} [\text{MJ}]$	1.05	1.96	2.79	3.23
$C_{LC\_2} [\text{MJ}]$	0.37	0.71	1.04	1.28
$C_{LC\_3} [\text{MJ}]$	0.26	0.47	0.67	0.76

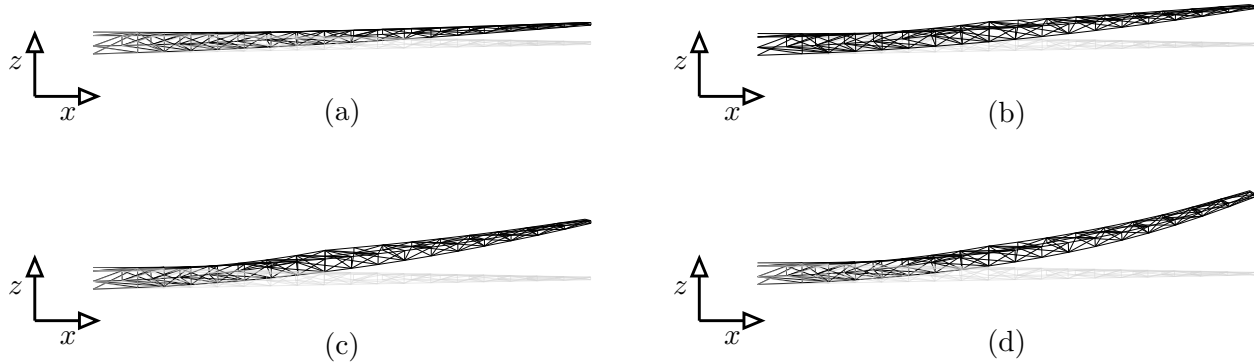


**Figure 6.4:** Undeformed (gray) and deformed (black) shapes of the optimized CRM-315 structures with a half wing span of 29.4 m for different values of maximum Z displacement  $Z_{t,\ell}$  of the wing tip constraints for the LC\_1 load case. (a)  $Z_{t,\ell} = 1\text{ m}$ ; (b)  $Z_{t,\ell} = 2\text{ m}$ ; (c)  $Z_{t,\ell} = 3\text{ m}$ ; (d) no maximum displacement constraints.

We note that the CRM has a half wing span of 29.4 m.

optimization in Table 6.3. Firstly, we notice how effectively the optimizer limited the maximum displacement and converged to a solution even with a hard-to-satisfy constraint such as  $Z_{t,\ell} = 1\text{ m}$ . Secondly, we observe that constraint satisfaction doesn't come for free. The added rigidity needed to comply with the maximum displacement constraint comes from a significant increase in material, representing a 19%, 75%, and 237% increase compared to the unconstrained case for  $Z_{t,\ell} = [3\text{ m}, 2\text{ m}, 1\text{ m}]$ , respectively. Finally, as already mentioned, the constraints on maximum displacements significantly influence the compliance of the structure, and we can see how, even if the proposed formulation does not explicitly account for it, we can indirectly reduce the compliance of the structure.

**MULTIPLE MATERIALS** The proposed formulation utilizes material data as input for the optimization, and until this point, we have not investigated how the material data could influence the topology and the final volume of the optimized structure. However, we recognize the importance of the choice of material properties, and here, we aim to examine their influence on the CRM-315 test case.

We utilized four different materials commonly used in the aerospace domain: an aluminum alloy, titanium alloy, inox steel, and pultruded Carbon Fiber Reinforced Polymer (CFRP), each with mechanical properties as reported in Table 6.4. In addition to classic material properties such as Young's modulus, yield stress, and density, we

Material	Aluminium	Titanium	Steel	Pultruted CFRP
$E$	69 GPa	120 GPa	210 GPa	150 GPa
$\sigma_c, \sigma_t$	$\pm 270 \text{ MPa}$	$\pm 880 \text{ MPa}$	$\pm 355 \text{ MPa}$	$+1200, -880 \text{ MPa}$
$\rho$	$2.7 \text{ g cm}^{-3}$	$4.5 \text{ g cm}^{-3}$	$7.8 \text{ g cm}^{-3}$	$1.6 \text{ g cm}^{-3}$
$\text{kgCO}_e^2/\text{kg}$	12.5	47.0	5.0	34.5
\$/\text{kg}\$	2.2	23.5	6.3	40.5

Material	Aluminium	Titanium	Steel	Pultruted CFRP
$V [\text{m}^3]$	7.90	4.53	5.88	3.67
$V [\%]$	1.309 %	0.749 %	0.974 %	0.607 %
Mass [t]	21.342	20.372	46.168	5.868
$a_{\max} [\text{m}^2]$	0.198	0.088	0.153	0.086
$C_{LC\_1} [\text{MJ}]$	3.23	4.88	1.33	4.39
$C_{LC\_2} [\text{MJ}]$	1.28	1.94	0.53	1.73
$C_{LC\_3} [\text{MJ}]$	0.76	1.15	0.31	1.03
$Z_t [\text{m}]$	4.10	5.97	1.70	5.31
Cost [ $\text{tCO}_e^2$ ]	266.7	957.5	230.8	202.4
Cost [k\$]	46.9	478.7	290.8	237.6

also considered the environmental cost, i.e., the mass of equivalent  $\text{CO}_2$  emitted to produce a unit mass of the material, as well as the economic cost in dollars. These values were sourced from Ashby's book [223].

The numerical results of the optimizations are presented in Table 6.5, and several observations can be made. First, we confirm that the mass of the optimized structure is highly influenced by the choice of material, particularly by the specific resistance ( $\sigma_L/\rho$ ) and specific stiffness ( $E/\rho$ ) of the material. Second, we notice that the values of compliance  $C$  and maximum tip displacement  $Z_t$  are also greatly influenced by material data, specifically by the ratio between strength and Young's modulus of the material ( $\sigma_L/E$ ). This is because a stronger material leads to smaller cross-sectional areas and thus lower global rigidity. Third, the volume behavior follows a hyperbolic law with respect to the strength of the material, as in this specific case, the most voluminous elements are constrained by stress rather than buckling (see the constraints' analysis later in the chapter). Finally, we present the deformed structures in Fig. 6.5, where it is evident how titanium and pultruded CFRP exhibit high deformation shapes due to their superior resistance properties.

We then observe the environmental and economic cost of the four structures. Upon inspection of Fig. 6.6, we notice that, apart from titanium, the structures exhibit almost the same environmental cost for material production. This is unexpected given the significantly different specific  $\text{CO}_2$  emissions of the four materials; for instance, there is nearly a seven-fold difference between steel and CFRP. However, the CFRP solution demonstrates a massive weight reduction, ultimately favoring it over steel and even aluminum. A similar trend

**Table 6.4:** Material data of the four materials used for the CRM-315 optimization.

**Table 6.5:** Numerical results of the CRM-315 optimized using four different materials.

223. Ashby (1999), 'Materials selection in mechanical design'

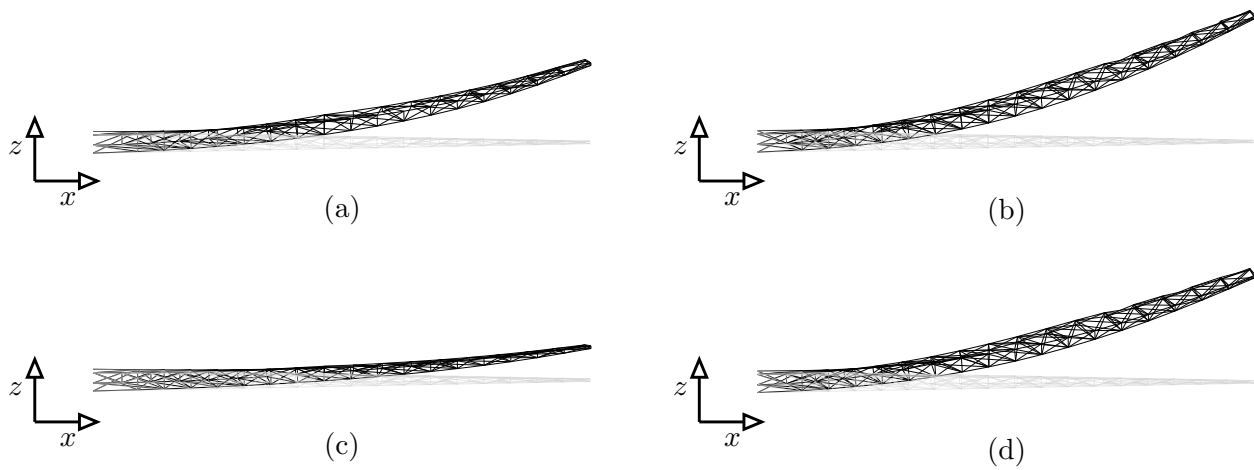


**Figure 6.5:** Undeformed (gray) and deformed (black) shapes of the optimized CRM-315 structures with four different materials for the LC\_1 load case; (a) aluminum with  $Z_t = 4.10$  m; (b) titanium with  $Z_t = 5.97$  m; (c) inox steel with  $Z_t = 1.70$  m; (d) pultruded CFRP with  $Z_t = 5.31$  m.

is observed in terms of cost, although the very low production cost favors aluminum over all other materials. It appears that, for this specific load case, CFRP, despite costing more than aluminum, represents the best compromise between excellent mechanical properties, environmental impact, and economic cost. Finally, it should be noted that here we only consider the material cost, but the lower weight on an aircraft leads to much greater savings compared to the cost of material production alone. This further favors the pultruded CFRP case.

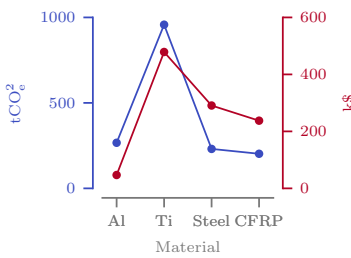


**Figure 6.6:** Environmental and economic cost of the CRM-315 structure optimized using four different materials: aluminum, titanium, inox steel, and pultruded CFRP.

**ENRICHING THE MESH** As described earlier in the chapter, we now aim to assess the influence of the initial ground structure on the volume and topology of the optimized structure. We utilize the refined ground structure, referred to as CRM-2370, which was optimized for the same three load cases used previously and employs aluminum as the material.

The mass of the optimized CRM-2370 structure is 20.092 t, a 1.318 t reduction compared to the CRM-315 (−6.2%). Additionally, if we compare the compliance of the three load cases (see Table 6.2), we notice how the solution of CRM-2370 is not only lighter but also stiffer, suggesting in general a more efficient structure topology. The maximum tip deflection of the wingbox  $Z_t$  is 4.167 m, −2.953 m, 1.948 m for the three considered load cases, respectively. There are 1127 active bars in the optimized design, and the whole optimization took 3189 s (1911 s for the SLP step, 1278 s for the NLP step). The iteration history curves of the optimization are plotted in Fig. 6.8. In Fig. 6.7 the normalized maximum stress and buckling constraints are plotted on the deformed shape of the three load cases. We notice how in general the topology of the two external "spars" is shaped after

	<b>LC_1</b>	<b>LC_2</b>	<b>LC_3</b>	<b>Tot.</b>
<b>Buckling</b>	281	145	143	569
<b>Tension</b>	56	3	4	63
<b>Compression</b>	286	6	6	298
<b>Tot.</b>	623	154	153	930

**Table 6.6:** Number of active mechanical failure constraints for the CRM-2370 optimized design per type of constraint (rows) and per load case (columns).

the +2.5 g load case, while the interior of the wingbox is made by a thinner truss constrained by buckling.

**ACTIVE MECHANICAL CONSTRAINTS** To better understand which mechanical phenomena is the most constraining for the bars of the solution, we present in Fig. 6.9 a graph where the normalized stress criterion  $c_s = \max(-q sf/\sigma_c a, q sf/\sigma_t a)$  and the normalized buckling criterion  $c_b = q sf/q_{crit}$  are plotted against each other. Every point in the scatter plot represents the members of the solution of the SLP and the NLP steps that show at least a charge of 1N (931 out of 1127 members). This threshold is applied as at the end of the NLP step some members present a very small section, creating numerical problems when evaluating the stress and buckling criteria. All the SLP members activate either the maximum stress or buckling limit, while 68 out of 931 NLP members are located in the center of the graph ( $c_s < 0.95$  and  $c_b < 0.95$ ). We speculate that this behavior is due to the inclusion of the kinematic compatibility constraint in the NLP algorithm: the cross-sectional area of these bars is chosen to comply with the global displacements. In Table 6.6, a summary of the active mechanical failure constraints (buckling, tensile stress, and compressive stress) present in the NLP solution. The table showcases the number of active constraints categorized by constraint type and load case. The optimized design encompasses a total of 930 active mechanical failure constraints for 863 bars (931 minus the 68 bars constrained by kinematic compatibility). This suggests that certain members are concurrently subject to multiple failure constraints across different load cases. An additional observation is that the design of the solution is primarily influenced by local buckling and compressive failures, especially under the +2.5 g load case (LC\_1).

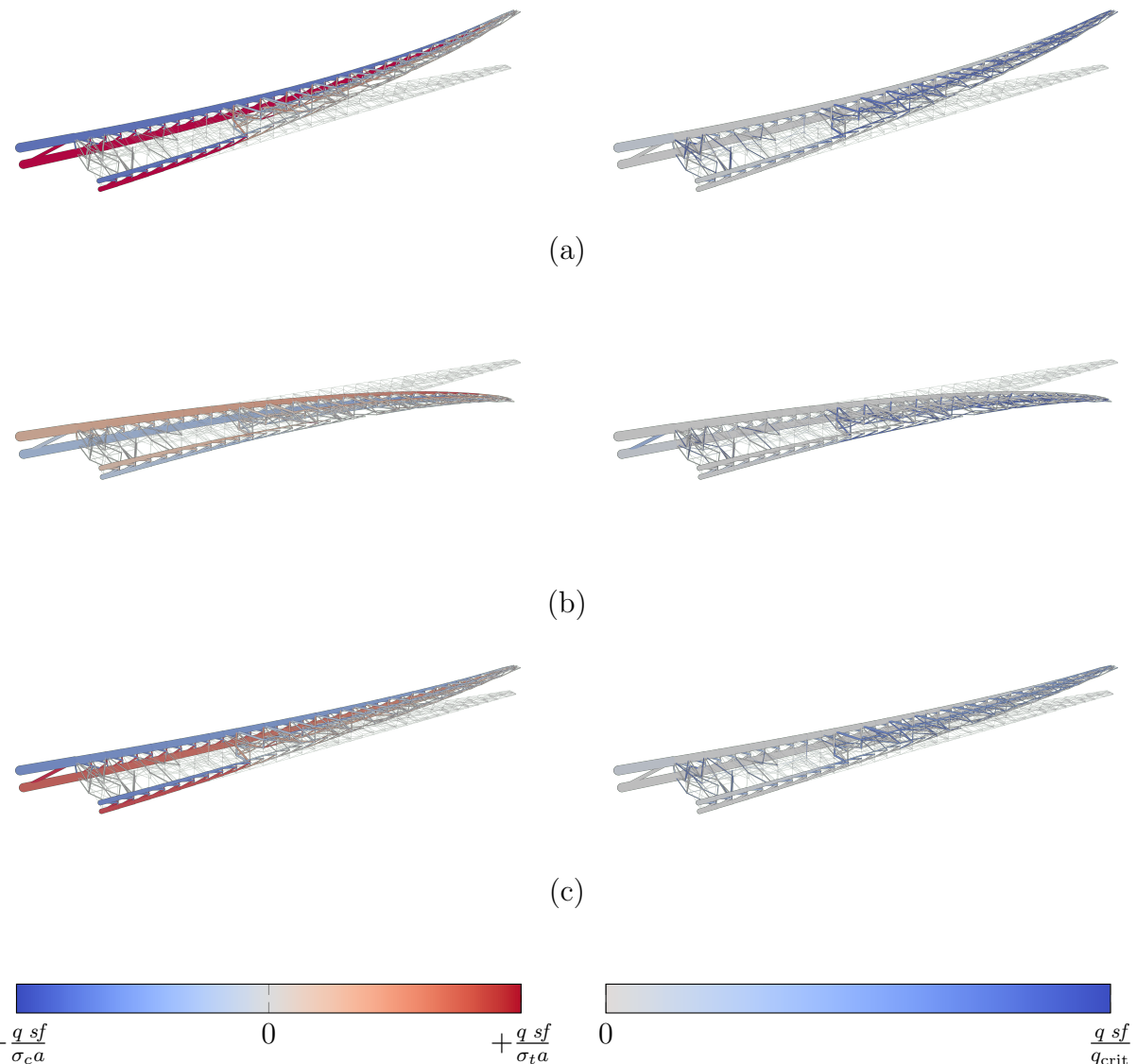


**Figure 6.7:** Maximum stress constraint value (left) and buckling constraint value (right) plotted on the deformed shape of the optimized design (undeformed shape in light grey) of CRM-2370 for the three load cases: +2.5 g maneuver (a), -1 g maneuver (b), and cruise with gust (+1.3 g) (c). The maximum  $z$  tip deflection is 4.167 m, -2.953 m, and 1.948 m, respectively.

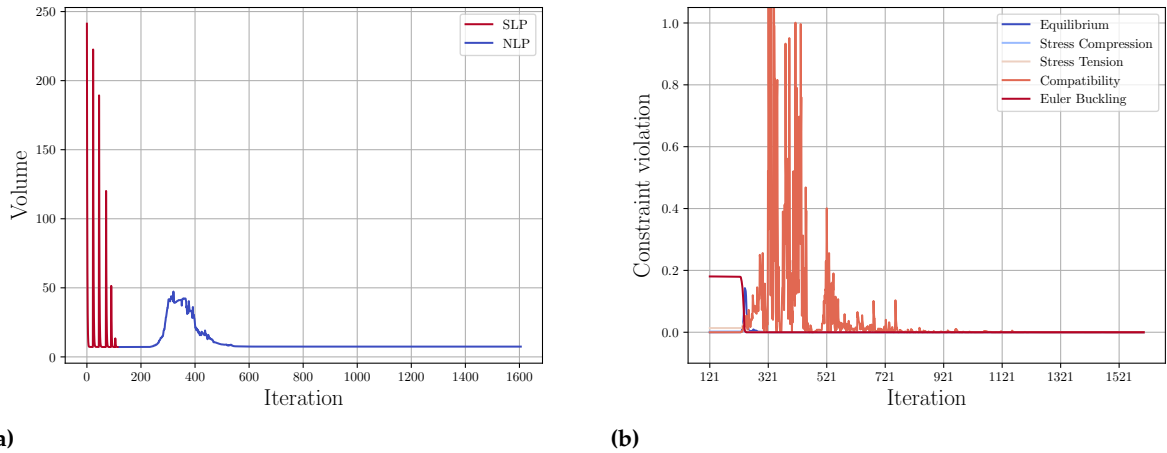


**Figure 6.8:** Iteration history of the CRM-2370 example solved with the 2S-5R algorithm. (a) objective function history for the SLP and NLP step. The sharp increases in the objective function during the SLP step correspond to the reinitialization calls. (b) constraint violation for the NLP step.

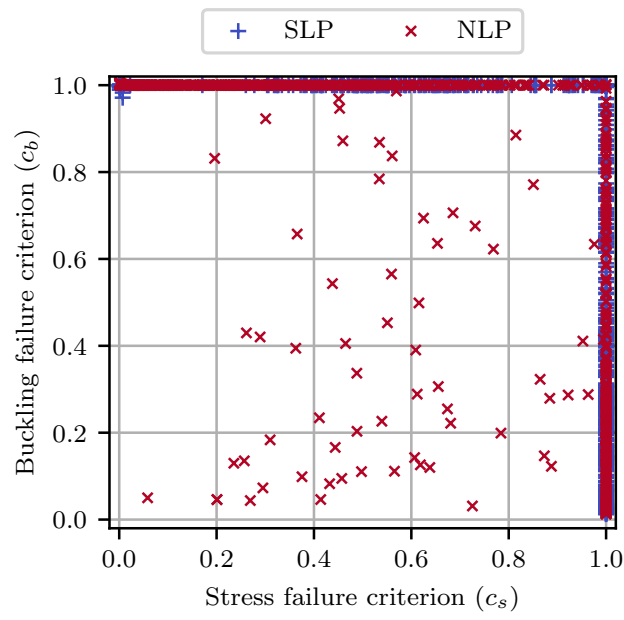


**Figure 6.9:** Normalized buckling and maximum stress constraint values for the optimized CRM-2370 structure after the SLP and the NLP optimization steps.

## 6.2 NACA 0012 MODULAR DRONE WING

Parameter	Value
$E$	6.8 GPa
$\sigma_c, \sigma_t$	$\pm 140$ MPa
$\rho$	$1.42 \text{ g cm}^{-3}$

**Table 6.7:** Material data of the Ultem 2200 used for the NACA 0012 optimization.

We now turn our attention to another aeronautical test case. One of the most suitable applications for modular structures is their use in small fixed-wing drones. This is due to the inherent ease of field deployment, easiness of repair and transport, and extremely lightweight properties of modular structures. Jenett and his working group at NASA developed an experimental platform for studying active morphing wings using lattices, the dimensions of which are shown in Figure 6.10. The platform's wing volume is obtained by extruding a NACA 0012 airfoil with a chord of  $c = 305 \text{ mm}$  by a span of  $b = 580 \text{ mm}$ . For our modular optimization, we adopt the same volume and focus on optimizing the internal structure rather than aerodynamic and aeroelastic properties. As the platform was not designed for flight, additional data on the internal structure requirements is not provided by the authors. Therefore, we conservatively assume a maximum takeoff weight of MTOW = 10 kg and design the structure to withstand a maximum loading factor of  $n_z = 2$ . The wing has a rectangular planform on the XY plane, and we assume a constant lift distribution along the X-axis (span of the extruded profile). Additionally, we simplify by assuming the lift distribution is constant along the Y-plane (chord plane). The lift distribution is then integrated to evaluate the concentrated nodal loads required for our optimization. In this setup, all nodes on the upper skin are equally loaded in the Z-direction. Similar to the CRM test case, we neglect the effect of the skin on the mechanical model. The wing is fixed at the root points ( $X = 0$ ). Finally, we employ Ultem 2200 as the material for optimization, a high-performance thermoplastic material filled with 20 % glass fiber, known for its exceptional strength, heat resistance, chemical resistance, and suitability for applications requiring durability. The mechanical properties are summarized in Table 6.7.

### 6.2.1 MODULAR GROUND STRUCTURE GENERATION FOR IRREGULAR VOLUMES

Compared to the academic test cases presented in Chapter 4 and Chapter 5, the extruded NACA 0012 profile does not have a regular

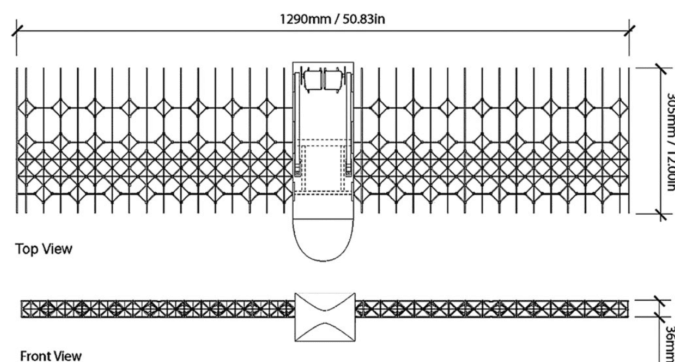


**Figure 6.10:** The Digital Morphing Wing Platform developed at NASA [125].

parallelepiped shape that can be easily partitioned into cubic subdomains. The simplest solution in this scenario would be to partition the structure into equal sections by performing multiple cuts on the YZ plane. However, this strategy may not apply to more complex external shapes. For this reason, we developed a ground structure generation strategy that maximizes the generation of modular domains on complex volumes.

First, we generate a cloud of nodes equally distributed in the three axes. The distance between nodes on the three axes represents a hyperparameter for the user, who can use this parameter to choose the size of the repeating module's geometry. Then, the points are tested for their position inside the volume using a winding number algorithm. This algorithm determines whether a point is inside or outside a volume by counting the number of times a ray from the point crosses the volume boundary. If the winding number is non-zero, the point is inside the volume; otherwise, it is outside. The points that are inside the volume are grouped into sets of eight and used as the vertices of the parallelepiped used as subdomains of the structure. At this point, additional equispaced nodes are added inside the newly generated subdomains depending on the chosen module complexity. This process results in a modular subdivision of a complex volume, minimizing the non-modular volume. All these phases are visually presented in the top row of Fig. 6.11.

Remember, we define module complexity as the number of nodes used to generate the modules' ground structure.

Once the subdomains and additional nodes have been identified within the structure, we can compute the modular ground structure. For each subdomain, a fully connected ground structure is built. The ground structure for the remaining volume that was not filled with subdomains is generated using the Delaunay triangulation algorithm. This algorithm uses the edges of the generated tetrahedra as members of the ground structure. The role of this ground structure is to transfer loads from the external boundary to the modular structure, and it can be optimized concurrently with the modular structure. Since the Delaunay triangulation algorithm uses the nodes of the modular ground structure as seeds for the mesh generation, the two discretizations are conformal. The final ground structure is obtained by superimposing the two discretizations, ensuring that the members of the non-modular part lying on the faces of the modular part are removed beforehand. An example of the generation of the two conformal discretizations is shown in the bottom row of Fig. 6.11.

### 6.2.2 NUMERICAL OPTIMIZATION OF THE MODULAR NACA 0012 DRONE WING

The algorithm described above is employed to create the ground structure used to optimize the modular NACA 0012 drone wing. In the case of the NACA 0012 wing, the non-modular part is very regular due to the extruded nature of the wing volume. Therefore,

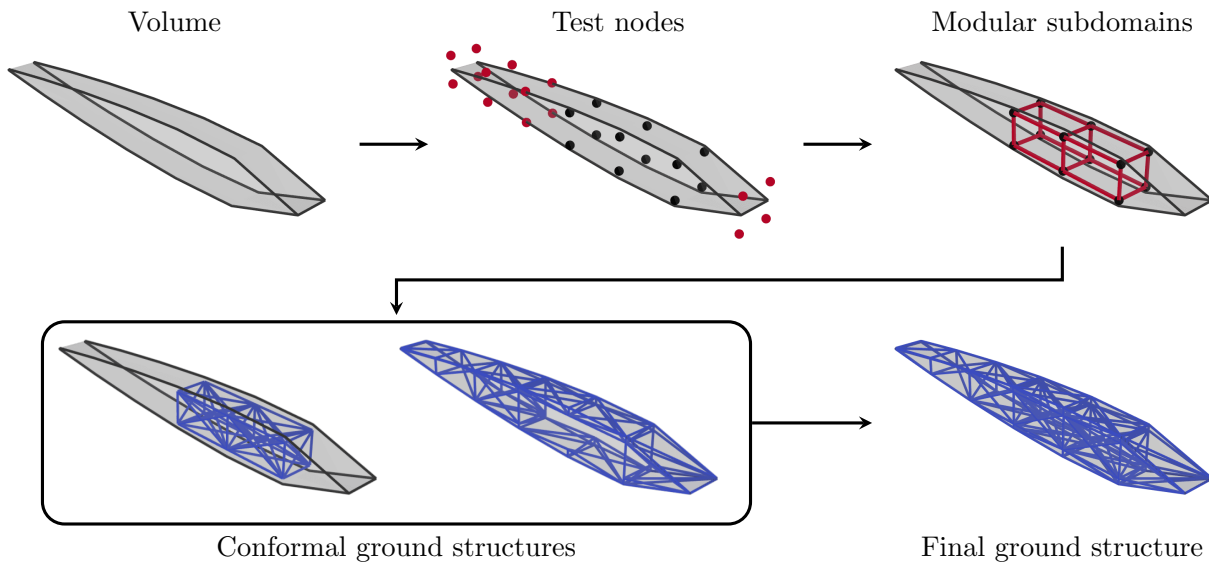


**Figure 6.11:** Ground structure generation flow chart of the proposed algorithm used to discretize irregular volumes and maximize the modular part.

1: When referring to different module types, we are discussing distinct module geometries and their corresponding bar connectivity configurations.

the Delaunay triangulation algorithm can easily output a modular ground structure. In this example, we define, thus, two different module types<sup>1</sup>: the internal structure of the wing profile, referred to as the wingbox type, as it acts as the wingbox of the wing and is made up of parallelepipedic-shaped subdomains, and the profile type, which subdivides the original volume into wing sections.

The inter-distance between cloud points used for the wingbox-type ground structure generation is chosen in such a manner as to obtain 10 subdomains on the X-axis, 1 on Y, and 1 on Z. Each subdomain is made up of  $2 \times 2 \times 2$  nodes and a fully connected ground structure, totaling 28 candidate elements per module. Concerning the profile-type module, the extruded volume is divided into 5, 1, and 1 subdomains on the X, Y, and Z axes, respectively. Each module has a total of 175 candidates per module. A graphical representation of the two conformal ground structures is presented in Fig. 6.12, while a comprehensive view of the full ground structure is shown in Fig. 6.13. This ground structure configuration is referred to as Configuration A.

The Configuration A ground structure, as presented, is used as the discretization for solving three different optimization problems. We set up all the problems using Ultem 2200 material and the wing dimensions, loading conditions, and boundary conditions described earlier in Section 6.2. The difference between the problems lies in the use of a different number of module topologies  $N_T$  for the three optimizations. We will start by analyzing the optimized structure behavior using a single topology  $N_T = 1$  for the two module types, and then we will increment to  $N_T = 2$  and  $N_T = 3$ .

Table 6.8 presents the numerical results of the optimization. Instead of reporting the volume, we focus on the mass and mass density in this

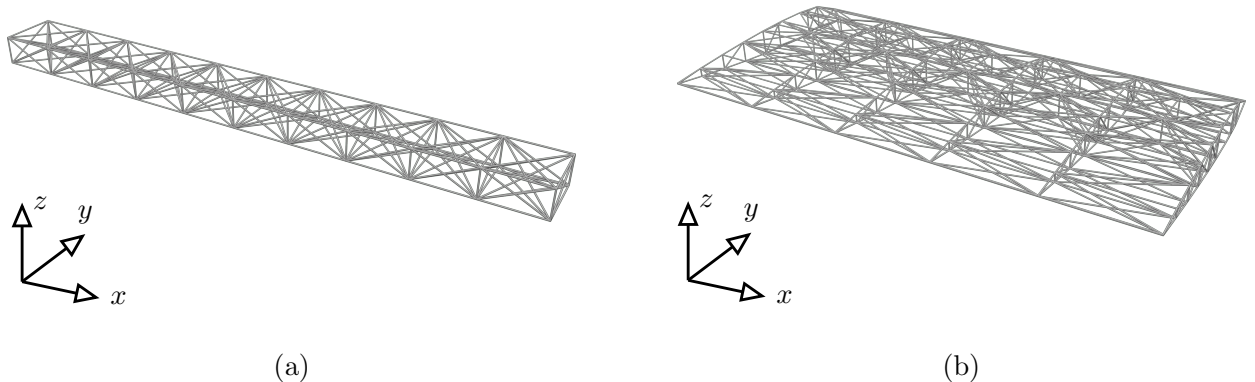


**Figure 6.12:** (a) wingbox type and (b) section type ground structures used for the optimization of the NACA 0012 drone wing.

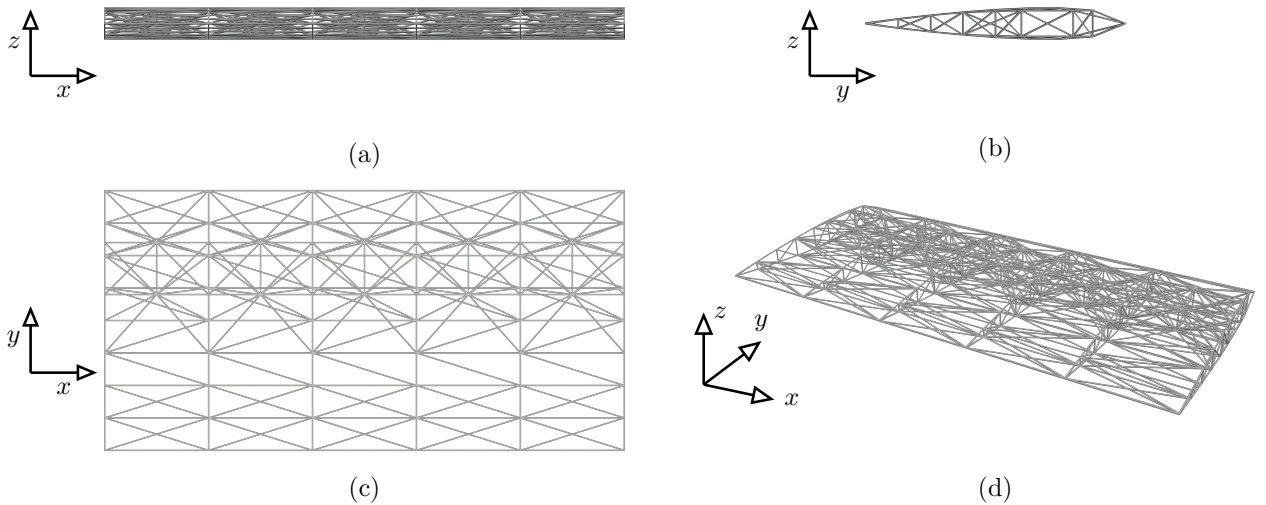


**Figure 6.13:** Rendering of the complete ground structure used for the optimization of the NACA 0012 drone wing seen from different viewing angles. This ground structure is formed by the superposition of two conformal ground structures: the wingbox and the section type.

**Table 6.8:** Numeric results of the parametric study on the influence of the number of modules  $N_T$  on the NACA 0012 drone wing.

$N_T$	Configuration A			Configuration B		
	1	2	3	1	2	3
$N_{\text{opt}} (N_{\text{el}})$	425 (1155)	503 (1155)	366 (1155)	620 (1675)	539 (1675)	454 (1675)
Mass [g]	49.0	33.3	29.5	37.3	23.8	22.9
$V$ [%]	0.81	0.55	0.48	0.62	0.39	0.37
$\bar{\rho}$ [kg/m <sup>3</sup> ]	11.53	7.84	6.93	8.76	5.59	5.38
$\varphi$	22.5 %	37.9 %	56.0 %	19.0 %	36.9 %	50.0 %
$\psi$	0.45	0.69	0.73	0.46	0.70	0.72
t	39 s	5 m 6 s	2 m 3 s	2 m 28 s	3 m 32 s	5 m 1 s

[223.](#) Ashby (1999), 'Materials selection in mechanical design'

[117.](#) Cramer et al. (2019), 'Elastic shape morphing of ultralight structures by programmable assembly'

table, as they are more easily understandable and have greater physical significance. Additionally, these values follow the same trends as the volume, multiplied by a factor. In the columns corresponding to configuration A, we observe that the trends identified in Chapter 5 persist: both the mass density and the mass of the structure decrease monotonically with the number of different module topologies, reaching a minimum of  $M = 29.5 \text{ g}$  and  $\bar{\rho} = 6.93 \text{ kg/m}^3$ . This specific mass density  $\bar{\rho}$  value is typical of aerogels [223], and comparable to values observed in NASA's MADCAT experimental platform [117]. Similar trends are evident in the performance parameters  $\varphi$  and  $\psi$ , which tend towards 100 % and 1.00 respectively with the increase of  $N_T$ , indicating a more efficient use of the material in the solution. The number of active bars in the optimized solution,  $N_{\text{opt}}$ , is approximately 40 % of the members of the initial ground structure. Additionally, the execution times never exceeded six minutes.

We will now provide a detailed commentary on the topology of the least voluminous solution obtained for  $N_T = 3$ , with a mass of  $M = 29.5 \text{ g}$ . Fig. 6.14 visually presents the most noteworthy aspects of the modular structure. Subfigures (a) to (d) depict the structure from four different angles. Starting from the root (left part of the images) and progressing towards the tip, we observe distinct features of the topology. Near the root of the wing, the algorithm minimizes the number of members as all nodes are encasted. Moving towards the central part of the wing, the topology resembles a classic wing configuration consisting of spars and ribs. A large spar runs along the entire span of the wing, in the upper half chord. In the initial sections, this spar is composed of voluminous bars due to high compression loads on the upper skin of the wing. However, towards the wing tip, the single massive spar is split into two lighter spars as the loads decrease.

Examining the ribs, we note that their thickness remains mostly constant regardless of their position on the X-axis. This uniform thickness is because the ribs primarily transfer loads to the larger spars and do not bear additional loads from subsequent sections, as the spars do. However, for wings with different planforms and lift distributions along the X-axis, this uniformity in rib thickness may not be optimal. Shorter ribs, experiencing lower loads, may require thinner dimensions. Notably, in subfigure (a), we observe that the topology of the modules near the root is more constrained by buckling, favoring tension elements. Conversely, near the wing tip, the topology becomes increasingly symmetric.

Regarding the layout of the modules, subfigures (e) and (f) illustrate how the algorithm suggests similar but not identical layout strategies for the two module types. For the wingbox type (subfigure (e)), there is an almost uniform distribution of different module topologies over the wing span, with one notable exception: the fourth subdomain from the

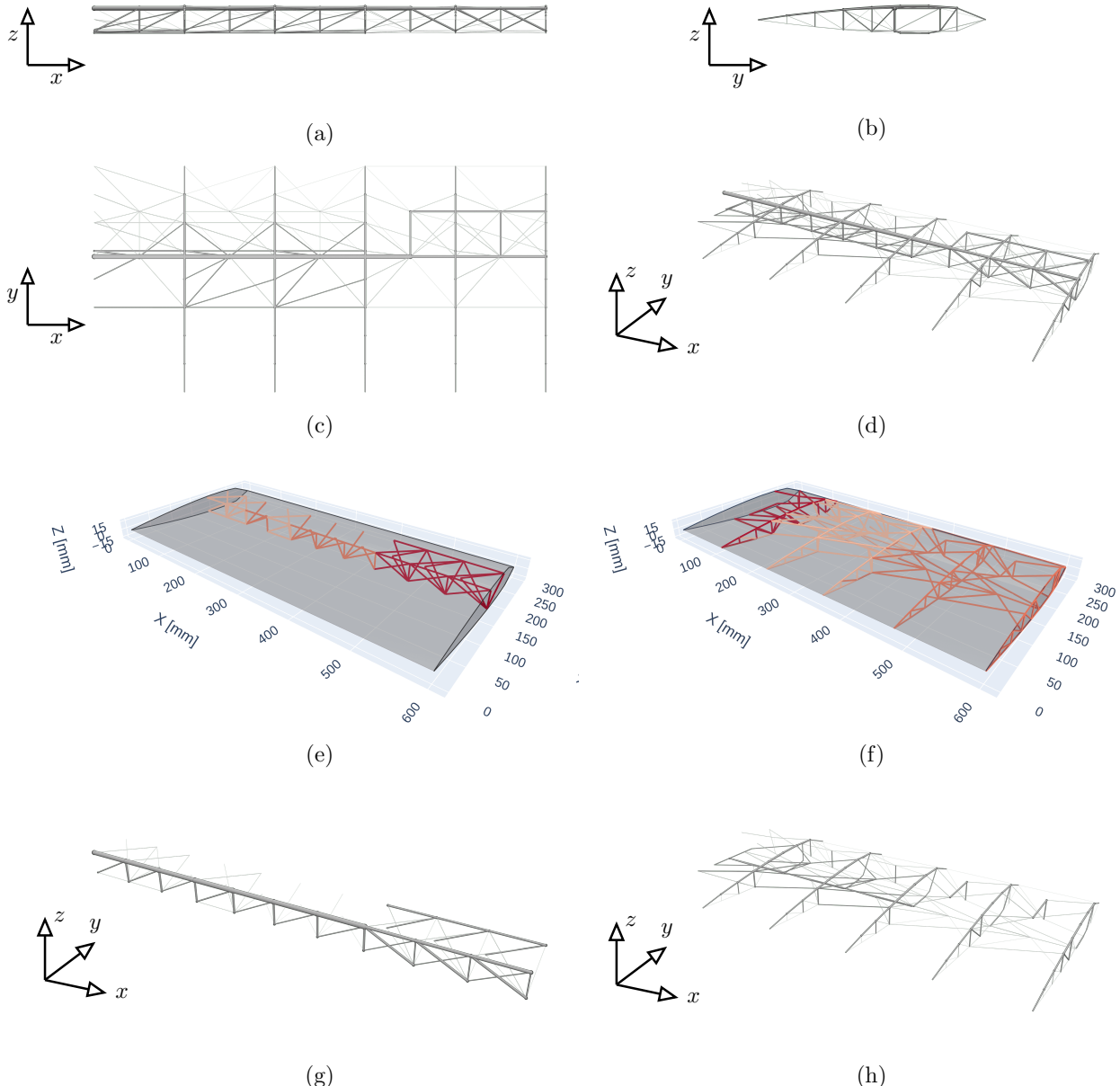


**Figure 6.14:** Subfigures (a) to (d) present different views on the resulting optimized structure obtained for configuration A with  $N_T = 3$  different topologies for the wingbox and the section type modules. The structure has a total mass of  $M = 29.5\text{ g}$  and a mass density of  $\bar{\rho} = 6.93\text{ kg/m}^3$ ; (e) and (f) illustrates the modules' layout in the structure for the wingbox and section modules type; (g) and (h) present the modules' topology for the wingbox and section modules type.

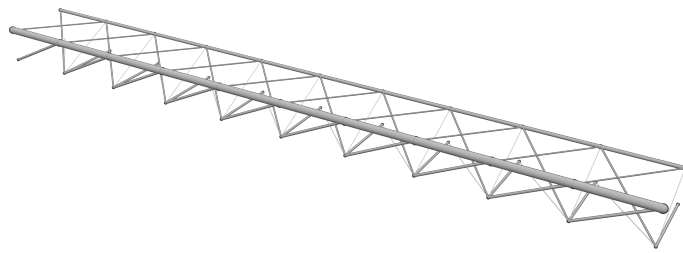


**Figure 6.15:** Rendering of the wingbox type subdomains of the resulting optimized structure obtained for configuration A with  $N_T = 1$ . The most voluminous bars could be lightened by splitting them into shorter components, reducing the free buckling length.

root displays a different topology. This deviation could be attributed to either resolving a connectivity issue with neighboring subdomains or the optimizer converging to a local minimum. In the case of the section type (subfigure (f)), the first subdomains near the root exhibit a distinct topology compared to the others. This variation is understandable as these subdomains typically experience different load states due to their proximity to the boundary conditions. This phenomenon aligns with our previous observations, as seen in Fig. 5.13, where subdomains near the loads exhibited different topologies. The remaining module topologies are more evenly distributed across the wing span.

Finally, in subfigures (g) and (h), we present the optimized structure divided into the wingbox type and the section type subdomains. It is especially interesting to note that in subfigure (g), the most voluminous component is the upper part of the long compressive spar, consisting of the first seven submodules. This observation becomes even clearer when examining the wingbox type optimized structure for the case with  $N_T = 1$ , as shown in Fig. 6.15. Considering that the cross-sectional area of this component is particularly sensitive to the length of the members composing it, we wonder if modifying the ground structure could be beneficial for this specific load case.

For that reason, we decided to test a different ground structure configuration in which, instead of having 10 different wingbox-type submodules, we have 20, thereby halving the length of the most voluminous buckling-constrained bars. The new wingbox ground structure is shown in Fig. 6.16. The section type ground structure generation parameters used are the same, and the ground structure only differs to accommodate the nodes generated by the new wingbox ground structure. We refer to this ground structure configuration as configuration B.

The numerical results of the optimizations for configuration B are presented in the right-hand side part of Table 6.8. As correctly predicted, reducing the free effective buckling length of the members that compose the main wing spar helped considerably reduce the mass of the structure. We observe a 23 %, 28 %, and 22 % reduction in

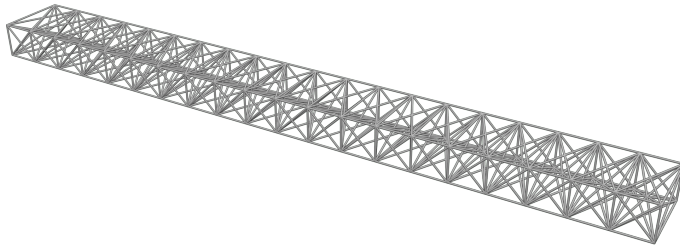


**Figure 6.16:** Visual representation of the ground structure of the 20 wingbox type submodules of configuration B.

mass compared to configuration A for the three numbers of topologies considered. The volume trends for the two configurations are plotted in Fig. 6.17. Despite the increase in candidate members, the optimization time remained the same, with no optimization exceeding five minutes of calculation time. It is important to remember that in Section 4.2.2, we observed that increasing the number of subdomains tends to increase the volume of the solution, but in this specific test case, we observe a different behavior. This fact confirms how choosing the correct ground structure is critical to obtaining a good solution.

Finally, in Fig. 6.18, we present the resulting optimized structure obtained for configuration B with  $N_T = 3$  different topologies for the wingbox and the section type modules. The structure has a total mass of  $M = 22.9$  g and a mass density of  $\bar{\rho} = 5.38$  kg/m<sup>3</sup>. Subfigure (a) shows the isometric view of the optimized topology. The structure exhibits similar characteristics to the configuration case A, with uniform ribs and a single large spar that splits into two towards the end of the span. However, the difference becomes apparent when observing the wingbox type subdomains in subfigures (b) and (d). Here, we observe how the reduced buckling length of the bars, given by the higher number of submodules, helps in reducing the cross-sectional area of the large spar. The layout of the modules is depicted in subfigures (b) and (c) for the two module types. Compared to the results of configuration A, we notice a more even distribution, indicating that the optimization runs correctly.

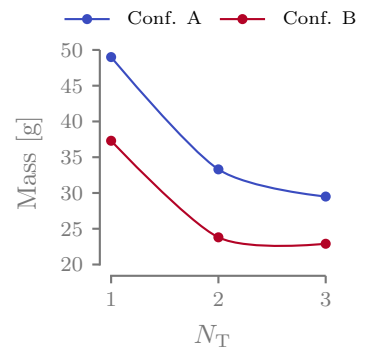


**Figure 6.17:** Evolution of the mass of the NACA 0012 drone wing structure for configuration A and B and different number of modules' topologies  $N_T$ .

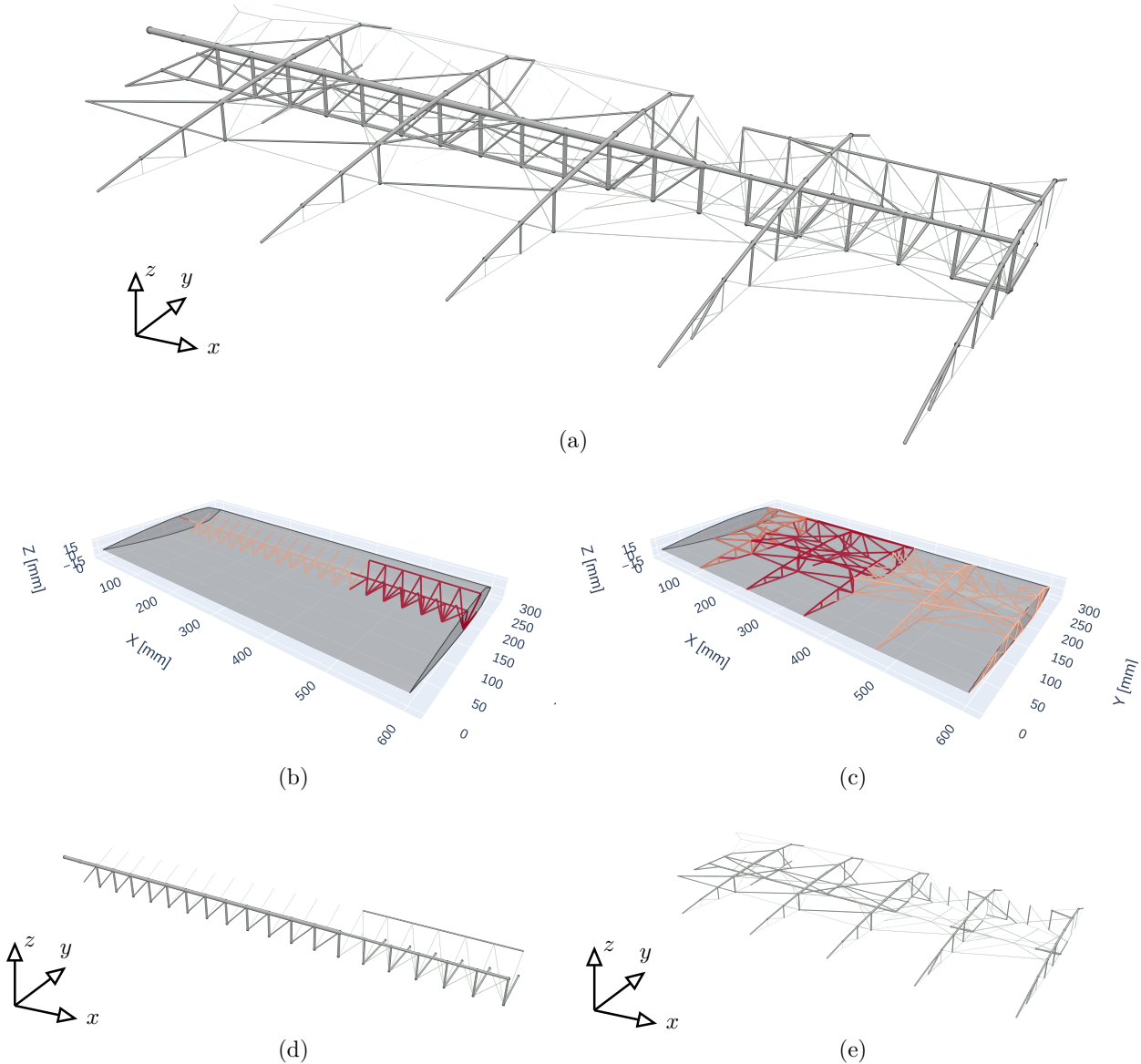


**Figure 6.18:** Subfigures (a) presents the resulting optimized structure obtained for configuration B with  $N_T = 3$  different topologies for the wingbox and the section type modules. The structure has a total mass of  $M = 22.9$  g and a mass density of  $\bar{\rho} = 5.38$  kg/m<sup>3</sup>; (b) and (c) illustrates the modules' layout in the structure for the wingbox and section modules type; (d) and (e) present the modules' topology for the wingbox and section modules type.

### 6.3 CONCLUSION

In this chapter, we focused on studying the applicability of the optimization algorithms proposed in this thesis in real engineering test cases, with real dimensions, loads, and materials. Firstly, we benchmarked the monolithic optimization algorithm proposed in Chapter 3 using a three-load-case test case on the CRM structure. We achieved a 27 % lighter structure compared to the literature, employing a gradient-based optimizer that solved the problem in minutes instead of days. Additionally, we performed further tests on the structure, evaluating the influence of displacement constraints, material data, and the fineness of the initial ground structure.

Secondly, we dedicated ourselves to the optimization of a modular drone wing structure based on the NACA 0012 profile. We developed an algorithm that allows the generation of modular ground structures starting from any volume. Then, we used this algorithm to generate the ground structure of the NACA 0012 volume, subdividing the structure into two module types. We studied how the optimized structure changed with the variation of the number of topologies. Additionally, we proposed a better ground structure configuration based on engineering observations and confirmed that the starting ground structure can influence the solution.



# CONCLUSION AND PERSPECTIVES

## CONCLUSION

In the aerospace sector, weight reduction plays a fundamental role due to the intricate relationship between weight and lift. The need to reduce aircraft weight is essential as it directly influences wing loading, thereby enhancing aerodynamic efficiency, maneuverability, and fuel efficiency. Beyond its economic significance, weight reduction has become a pressing environmental concern. In response to these challenges, innovative concepts such as the Blended-Wing Body (BWB) or the utilization of transonic truss-braced wings with high elongation have been proposed. These concepts share a common requirement for thin, lightweight wings with High Aspect Ratio (HAR). A potential design solution fitting well within this context is the application of modular lattice structures as the primary structure for these wings. The inherent low mass and modular construction benefits make these structures an attractive choice. However, the challenge lies in the absence of a standardized method for the design and optimization for this kind of structure. Addressing these considerations, this thesis introduces the development of a design and optimization methodology tailored for ultralight modular structures.

In Chapter 2, we conducted a comprehensive comparison between two optimization frameworks for designing ultralight structures: density-based topology optimization and Truss Topology Optimization (TTO). Initially, we formulated a shared volume minimization problem with material resistance constraints for both methods. Then, we explored the differences and similarities in their modeling, especially focusing on the disparities between the Nested Analysis and Design (NAND) and Simultaneous Analysis and Design (SAND) approaches. We performed numerical tests using a two-dimensional L-shaped beam as a test case, where we gradually adjusted the material properties to achieve various volume fractions—i.e. high strength is associated with low volume fraction. The results revealed two critical limitations in the applicability of these methods: density-based topology optimization faced challenges at low volume fractions due to the continuous discretization needing mesh refinement, leading to increased computational costs. Conversely, TTO encountered issues at moderately high volume fractions, where the cross-sectional area radius became too large, impacting the applicability of the truss idealization. Computational time observations highlighted TTO's linear nature, providing clear advantages in this regard. Another important finding is that with continuous discretization, achieving finer details in the optimized structure demands more elements. In contrast, TTO

with ground structure discretization eliminates this need, making the optimization process more straightforward and efficient. Considering these findings, we decided to focus our work on TTO, aligning well with our goal of optimizing ultralight structures.

In Chapter 3, we tackle the main limitations of the classical TTO method. Initially, we introduce a constraint on the minimum slenderness of active bars in optimized structures, expanding the method's range of applicability. We then focus on incorporating local buckling constraints, crucial for lightweight structures, additionally addressing the nodal stability of compressed bars, known as buckling chains or topological buckling. We then model kinematic compatibility constraints to handle more complex scenarios resulting in statically inadmissible structures, such as multiple load cases or imposed symmetries. We propose then a comprehensive TTO formulation with these additions, together with its extension to multiple load cases. However, naively solving the proposed formulation on a Non-Linear Programming (NLP) solver proves challenging due to the problem's multimodality. To overcome this, we proposed an innovative two-step optimization algorithm. The first step consists of the resolution of a relaxed problem to generate an initial approximate solution for subsequent complete optimization. The reinitialization heuristic reduces the starting point's influence on results. Through this approach, we demonstrate the algorithm's effectiveness on benchmark problems, showcasing its robustness and versatility in handling complex structures under various load cases. Remarkably, in specific case studies like the ten-bar truss, we demonstrated the algorithm's robustness, revealing negligible starting point influence through 100 random initializations. Additionally, when applied to the 2D cantilever beam problem proposed by Achtziger, the algorithm consistently found improved solutions, leading to a 9 % lower volume with respect to the best solution found in literature. Furthermore, we extended the testing to more complex scenarios, including a two-dimensional truss subjected to multiple load cases. This highlighted the need to incorporate kinematic constraints into the formulation for accurate optimization. Finally, the algorithm showcased its versatility by successfully optimizing a three-dimensional structure, illustrating its adaptability to diverse engineering challenges.

Chapter 4 is devoted to the development of the modular framework for the proposed TTO formulation. We opted for a full-scale method, a method that does not assume physical scale separation between the module and the whole structure, called variable linking, in which the periodicity of the structure is created by linking the design variables of different subdomains of the structure. The subsequent section of the chapter involves a examination of the formulation through various numerical optimizations to show the limits and trends of modular TTO optimization. First, we highlight the close relationship

between multi-load cases and modular structures, emphasizing the need for kinematic compatibility constraints in modular structures. Then, a parametric study investigates two key hyperparameters of the optimization: the number of subdomains and the complexity of the module. Based on the numerical findings, a Design of experiments (DOE) is constructed, leading to recommendations such as favoring fewer subdomains with modules as large as manufacturably possible. Module complexity, while impacting volume minimization, exhibits a relatively low overall impact. To conclude, the modular TTO structures undergo benchmarking against the widely used octet-truss lattice, and showing how structures with optimized module topology reduces considerably the structure mass.

Modular structures show a mass increase compared to their monolithic counterparts due to the repetition of the same module across the design space, where varying loading conditions may exist. To narrow the gap between modular and monolithic structures, in Chapter 5 we introduce a new design variable: the layout of modules in space. The problem is reformulated to concurrently optimize the topology of multiple modules and their arrangement in the design domain. This task is significantly more challenging due to the strong connection between module topology and layout, compounded by the inherently discrete nature of the layout problem. The discrete design space is firstly relaxed by employing a continuous model and then is optimized by applying the proposed optimization method based on a modified Discrete Material Optimization (DMO). To prevent convergence towards non-physical solutions, a dual-phase penalization scheme based on the Rational Approximation of Material Properties (RAMP) method is developed. Finding an appropriate starting point is non-trivial, and we use the k-means clustering approach on the stress distribution of the unoptimized initial structure to provide an initial module layout. The proposed formulation is tested across various two and three-dimensional cases, demonstrating superior results compared to the literature. We show that controlling the number of module topologies and the presence of subdomains effectively reduces the gap between monolithic and modular structures. Remarkably, on the simply supported 3D beam we achieved a similar volume (+2.8 %) to the monolithic reference while preserving the manufacturing advantages inherent to the modular nature. However, it is essential to note that having more modules is associated with increased manufacturing complexity, and the user must decide the optimal value for their specific application by using a Pareto front analysis.

In Chapter 6, we extend our analysis to real-world applications from the aerospace domain. Initially, we employ the monolithic optimization algorithm to reduce the weight of the wingbox of the NASA Common Research Model (CRM), a standard benchmark in aeronautic

research. The test case is subjected to multiple load cases (+2.5g, -1g, and cruise loads) with respective safety factors. The optimization, conducted with various materials and discretizations, results in structures lighter (-27%) and achieved in less time compared to existing literature (minutes instead of days). Additionally, we performed additional tests, such as quantitative studies on the influence of the material, the addition of maximum displacement constraints, and the influence of the initial ground structure on the optimized structure. Subsequently, the modular optimization formulation introduced in Chapter 5 is applied to a drone-sized wing based on the 0012 NACA wing profile. This showcases the versatility of the proposed algorithm in addressing complex real-world scenarios and test cases within the aerospace domain.

## PERSPECTIVES

The research opens up various possibilities and potential directions for future exploration. We can categorize these prospects based on the respective chapters.

In Chapter 2, we focused on the comparison between TTO and solely the generic density-based topology optimization. It would have been intriguing to compare the results with feature-mapping optimization methods. While we can only speculate, likely, the outcomes would not significantly differ since these methods also depend on continuous discretization for finite element analysis and sensitivity analysis as density-based methods. Any variations, especially in terms of computational time, may not be substantial.

Regarding Chapter 3, we primarily addressed local buckling constraints, but it would be valuable to explore the implementation of global buckling constraints. Additionally, we consistently used bar elements instead of beam elements, neglecting the impact of joint stiffness in the optimization. While our assumptions are valid for high slenderness values of bars, it would be interesting to investigate the effects of this switch. Then, while multiple mechanical constraints were incorporated into the optimization, the discussion on manufacturing complexity is presented only as an outcome of the optimization strategy. It would be interesting to consider additional manufacturing constraints, such as a maximum number of bars converging to a single node, or minimum section requirements of the structure during the optimization process. lastly, materials have thus far been treated solely as inputs for optimization. Further research is required to explore methods for integrating material selection into the optimization loop, as demonstrated in prior work [224].

<sup>224</sup> Duriez et al. (2022), 'On some properties of the compliance-volume fraction Pareto front in topology optimization useful for material selection'

In Chapter 4, we consistently used cubic modules; however, the external shape of the modules—i.e. the ratio between dimensions

or alternative shapes such as pyramidal or dodecahedral—could significantly influence the mechanical properties of the module. Investigating this additional design variable in the modular problem is important, striking a balance between shape complexity, mass, and manufacturing complexity. It's worth noting that numerous studies on the tessellation of 2D and 3D space could serve as inspiration for exploring this direction [225, 226]. Additionally, our focus on topological buckling was limited to within the module, and further exploration on algorithmically implementing topological buckling at the structure level would be intriguing.

Chapter 5 has emphasized the significant challenge of concurrently optimizing the topology and layout of modules. Although the proposed perturbation of the starting point has proven effective in addressing this issue, a more complex heuristic could enhance the optimization process. For instance, an alternating formulation could be employed, where the layout and topology are optimized sequentially in a repetitive manner until convergence, offering an alternative approach to the intricacies of concurrent optimization.

Finally, in Chapter 6, it was observed that the choice of the initial ground structure significantly impacts the optimization of real-sized structures. Extensive studies should be conducted to determine the most effective approach for conceiving the optimal ground structure tailored to specific problems. Additionally, up to this point, we have primarily discussed environmental costs as an outcome of optimization. However, it is crucial to consider them during the optimization process. Incorporating environmental costs into the optimization formulation could offer compelling opportunities for eco-design initiatives [227–229].

225. Coxeter (1973), 'Regular Polytopes'

226. Loeb (1991), 'Space-filling Polyhedra'

227. Duriez et al. (2022), 'Ecodesign with topology optimization'

228. Duriez et al. (2023), 'CO<sub>2</sub> footprint minimization of solar-powered HALE using MDO and eco-material selection'

229. Duriez et al. (2023), 'A fast method of material, design and process eco-selection via topology optimization, for additive manufactured structures'



# COMMUNICATIONS

## JOURNAL ARTICLES

- [A1] Stragiotti, E., Irisarri, F.-X., Julien, C., and Morlier, J., 'Efficient 3D truss topology optimization for aeronautical structures (in press)', *Structural and Multidisciplinary Optimization* (Jan. 2024).

DOI: [10.1007/s00158-024-03739-5](https://doi.org/10.1007/s00158-024-03739-5)

## CONFERENCE PROCEEDINGS

- [C1] Stragiotti, E., Irisarri, F.-X., Julien, C., and Morlier, J., 'Towards manufactured lattice structures: a comparison between layout and topology optimization', *AeroBest 2021 International Conference on Multidisciplinary Design Optimization of Aerospace Systems. Book of proceedings*, Lisbon, Portugal: ECCOMAS, July 2021, pp. 229–244.
- [C2] Stragiotti, E., Irisarri, F.-X., Julien, C., and Morlier, J., 'Enhanced truss topology optimization (TTO) applied to a cellular wing box', *ASMO-UK 12 / ASMO-Europe 1 / ISSMO Conference on Engineering Design Optimization* (2022), Leeds, United Kingdom, July 2022.
- [C3] Stragiotti, E., Irisarri, F.-X., Julien, C., and Morlier, J., 'Optimisation des structures lattices : une comparaison entre le layout optimization et l'optimisation topologique', *CSMA 2022 15ème Colloque National en Calcul des Structures*, Presqu'île de Giens, France, May 2022.

## OTHERS

- [M1] Stragiotti, E., Irisarri, F.-X., Julien, C., and Morlier, J., 'Truss Topology Optimization with Topological Buckling Constraints Data Set', May 2023.

DOI: [10.17632/BW7XB2W6ST.1](https://doi.org/10.17632/BW7XB2W6ST.1)



# BIBLIOGRAPHY

- [1] Carrier, G., Atinault, O., Dequand, S., and Toussaint, C., 'Investigation of a Strut-Braced Wing Configuration for Future Commercial Transport', 2012, p. 16. cited on page 3
- [2] Carrier, G. G., Arnoult, G., Fabbiane, N., Schotte, J.-S., David, C., Defoort, S., Benard, E., and Delavenne, M., 'Multidisciplinary analysis and design of strut-braced wing concept for medium range aircraft', *AIAA SCITECH 2022 Forum*, AIAA SciTech Forum, American Institute of Aeronautics and Astronautics, Dec. 2021. cited on page 3  
DOI: [10.2514/6.2022-0726](https://doi.org/10.2514/6.2022-0726)
- [3] Airbus, 'Airbus reveals new zero-emission concept aircraft | Airbus', Oct. 2021. cited on page 3  
URL: <https://www.airbus.com/en/newsroom/press-releases/2020-09-airbus-reveals-new-zero-emission-concept-aircraft>
- [4] Belvin, W. K., Doggett, W. R., Watson, J. J., Dorsey, J. T., Warren, J. E., Jones, T. C., Komendera, E. E., Mann, T., and Bowman, L. M., 'In-Space Structural Assembly: Applications and Technology', *3rd AIAA Spacecraft Structures Conference*, AIAA SciTech Forum, American Institute of Aeronautics and Astronautics, Jan. 2016. cited on page 4  
DOI: [10.2514/6.2016-2163](https://doi.org/10.2514/6.2016-2163)
- [5] Cheung, K. C. and Gershenfeld, N., 'Reversibly Assembled Cellular Composite Materials', *Science* 341.6151 (Sept. 2013), pp. 1219–1221. cited on pages 4, 23, 24  
DOI: [10.1126/science.1240889](https://doi.org/10.1126/science.1240889)
- [6] Costa, A., Jenett, B., Kostitsyna, I., Abdel-Rahman, A., Gershenfeld, N., and Cheung, K., 'Algorithmic Approaches to Reconfigurable Assembly Systems', *arXiv:2008.11925 [cs]* (Aug. 2020). cited on pages 4, 23, 24  
DOI: [10.1109/AERO.2019.8741572](https://doi.org/10.1109/AERO.2019.8741572)
- [7] Bendsøe, M. P. and Sigmund, O., 'Topology Optimization'. Berlin, Heidelberg: Springer Berlin Heidelberg, 2004. cited on pages 7, 12, 15, 19, 35, 37, 43  
ISBN: [978-3-642-07698-5](#) [978-3-662-05086-6](#)
- [8] Martins, J. and Ning, A., 'Engineering Design Optimization'. Cambridge University Press, 2021. cited on pages 8, 12, 36, 179  
ISBN: [978-1-108-83341-7](#)
- [9] Prager, W. and Taylor, J. E., 'Problems of Optimal Structural Design', *Journal of Applied Mechanics* 35.1 (Mar. 1968), pp. 102–106. cited on page 9  
DOI: [10.1115/1.3601120](https://doi.org/10.1115/1.3601120)

- cited on page 9
- [10] Prager, W., 'Optimality Criteria in Structural Design', *Proceedings of the National Academy of Sciences of the United States of America* 61.3 (1968), pp. 794–796.
- cited on pages 9, 12, 24, 25, 41
- [11] Bendsøe, M. P. and Kikuchi, N., 'Generating optimal topologies in structural design using a homogenization method', *Computer Methods in Applied Mechanics and Engineering* 71.2 (Nov. 1988), pp. 197–224.  
DOI: [10.1016/0045-7825\(88\)90086-2](https://doi.org/10.1016/0045-7825(88)90086-2)
- cited on pages 9, 53
- [12] Bendsøe, M. P., 'Optimization of Structural Topology, Shape, and Material'. Berlin, Heidelberg: Springer Berlin Heidelberg, 1995.  
ISBN: [978-3-662-03117-9](https://doi.org/978-3-662-03117-9) [978-3-662-03115-5](https://doi.org/978-3-662-03115-5)
- cited on page 9
- [13] Sigmund, O., 'A 99 line topology optimization code written in Matlab', *Structural and Multidisciplinary Optimization* 21.2 (Apr. 2001), pp. 120–127.  
DOI: [10.1007/s001580050176](https://doi.org/10.1007/s001580050176)
- cited on page 9
- [14] Allaire, G., Belhachmi, Z., and Jouve, F., 'The homogenization method for topology and shape optimization. Single and multiple loads case', *Revue Européenne des Éléments Finis* 5.5-6 (Jan. 1996), pp. 649–672.  
DOI: [10.1080/12506559.1996.10511241](https://doi.org/10.1080/12506559.1996.10511241)
- cited on page 9
- [15] Li, W., Suryanarayana, P., and Paulino, G. H., 'Accelerated fixed-point formulation of topology optimization: Application to compliance minimization problems', *Mechanics Research Communications* 103 (Jan. 2020), p. 103469.  
DOI: [10.1016/j.mechrescom.2019.103469](https://doi.org/10.1016/j.mechrescom.2019.103469)
- cited on pages 9, 39, 40
- [16] Ferrari, F. and Sigmund, O., 'A new generation 99 line Matlab code for compliance topology optimization and its extension to 3D', *Structural and Multidisciplinary Optimization* 62.4 (Oct. 2020), pp. 2211–2228.  
DOI: [10.1007/s00158-020-02629-w](https://doi.org/10.1007/s00158-020-02629-w)
- cited on page 9
- [17] Anderson, D. G., 'Iterative Procedures for Nonlinear Integral Equations', *Journal of the ACM* 12.4 (Oct. 1965), pp. 547–560.  
DOI: [10.1145/321296.321305](https://doi.org/10.1145/321296.321305)
- cited on page 10
- [18] Conn, A. R., Scheinberg, K., and Vicente, L. N., 'Introduction to Derivative-Free Optimization'. Society for Industrial and Applied Mathematics, Jan. 2009.  
ISBN: [978-0-89871-668-9](https://doi.org/978-0-89871-668-9) [978-0-89871-876-8](https://doi.org/978-0-89871-876-8)
- cited on page 10
- [19] Audet, C. and Hare, W., 'Derivative-Free and Blackbox Optimization', Springer Series in Operations Research and Financial Engineering. Cham: Springer International Publishing, 2017.  
ISBN: [978-3-319-68912-8](https://doi.org/978-3-319-68912-8) [978-3-319-68913-5](https://doi.org/978-3-319-68913-5)

- [20] Simon, D., 'Evolutionary optimization algorithms: biologically-inspired and population-based approaches to computer intelligence', 1. ed. Hoboken, NJ: Wiley, 2013.  
ISBN: 978-1-118-65950-2 978-0-470-93741-9      cited on page 10
- [21] Balamurugan, R., Ramakrishnan, C. V., and Swaminathan, N., 'A two phase approach based on skeleton convergence and geometric variables for topology optimization using genetic algorithm', *Structural and Multidisciplinary Optimization* 43.3 (Mar. 2011), pp. 381–404.  
DOI: 10.1007/s00158-010-0560-4      cited on page 10
- [22] Sigmund, O., 'On the usefulness of non-gradient approaches in topology optimization', *Structural and Multidisciplinary Optimization* 43.5 (May 2011), pp. 589–596.  
DOI: 10.1007/s00158-011-0638-7      cited on page 10
- [23] Luh, G.-C. and Lin, C.-Y., 'Structural topology optimization using ant colony optimization algorithm', *Applied Soft Computing* 9.4 (Sept. 2009), pp. 1343–1353.  
DOI: 10.1016/j.asoc.2009.06.001      cited on page 10
- [24] Luh, G.-C., Lin, C.-Y., and Lin, Y.-S., 'A binary particle swarm optimization for continuum structural topology optimization', *Applied Soft Computing*, The Impact of Soft Computing for the Progress of Artificial Intelligence 11.2 (Mar. 2011), pp. 2833–2844.  
DOI: 10.1016/j.asoc.2010.11.013      cited on page 10
- [25] Stolpe, M., 'Global optimization of minimum weight truss topology problems with stress, displacement, and local buckling constraints using branch-and-bound', *International Journal for Numerical Methods in Engineering* 61.8 (2004), pp. 1270–1309.  
DOI: <https://doi.org/10.1002/nme.1112>      cited on pages 10, 52
- [26] Mattheck, C. and Burkhardt, S., 'A new method of structural shape optimization based on biological growth', *International Journal of Fatigue* 12.3 (May 1990), pp. 185–190.  
DOI: 10.1016/0142-1123(90)90094-U      cited on page 10
- [27] Xie, Y. M. and Steven, G. P., 'A simple evolutionary procedure for structural optimization', *Computers & Structures* 49.5 (Dec. 1993), pp. 885–896.  
DOI: 10.1016/0045-7949(93)90035-C      cited on page 10
- [28] Manickarajah, D., Xie, Y. M., and Steven, G. P., 'An evolutionary method for optimization of plate buckling resistance', *Finite Elements in Analysis and Design* 29.3 (June 1998), pp. 205–230.  
DOI: 10.1016/S0168-874X(98)00012-2      cited on page 10
- [29] Young, V., Querin, O. M., Steven, G. P., and Xie, Y. M., '3D and multiple load case bi-directional evolutionary structural optimization (BESO)', *Structural optimization* 18.2 (Oct. 1999), pp. 183–192.      cited on page 10

- cited on page 11
- cited on pages 11, 39
- cited on page 11
- cited on page 11
- cited on pages 11, 63, 82, 124
- cited on page 11
- cited on pages 11, 17–19, 37, 43, 52, 62
- cited on pages 11, 18
- cited on pages 11, 17, 18, 43, 52
- cited on pages 12, 56
- cited on pages 12, 13, 24, 25, 38, 49
- DOI: [10.1007/BF01195993](https://doi.org/10.1007/BF01195993)
- [30] Kraft, D., 'A software package for sequential quadratic programming', *Tech. Rep. DFVLR-FB 88-28, DLR German Aerospace Center — Institute for Flight Mechanics, Koln, Germany.* (1988).
- [31] Svanberg, K., 'The method of moving asymptotes—a new method for structural optimization', *International Journal for Numerical Methods in Engineering* 24.2 (1987), pp. 359–373.  
DOI: <https://doi.org/10.1002/nme.1620240207>
- [32] Svanberg, K., 'A Class of Globally Convergent Optimization Methods Based on Conservative Convex Separable Approximations', *SIAM Journal on Optimization* 12.2 (Jan. 2002), pp. 555–573.  
DOI: [10.1137/S1052623499362822](https://doi.org/10.1137/S1052623499362822)
- [33] Bruyneel, M., Duysinx, P., and Fleury, C., 'A family of MMA approximations for structural optimization', *Structural and Multidisciplinary Optimization* 24.4 (Oct. 2002), pp. 263–276.  
DOI: [10.1007/s00158-002-0238-7](https://doi.org/10.1007/s00158-002-0238-7)
- [34] Fleury, C. and Braibant, V., 'Structural optimization: A new dual method using mixed variables', *International Journal for Numerical Methods in Engineering* 23.3 (1986), pp. 409–428.  
DOI: [10.1002/nme.1620230307](https://doi.org/10.1002/nme.1620230307)
- [35] Wächter, A. and Biegler, L. T., 'On the implementation of an interior-point filter line-search algorithm for large-scale nonlinear programming', *Mathematical Programming* 106.1 (Mar. 2006), pp. 25–57.  
DOI: [10.1007/s10107-004-0559-y](https://doi.org/10.1007/s10107-004-0559-y)
- [36] Rojas Labanda, S. and Stolpe, M., 'Benchmarking optimization solvers for structural topology optimization', *Structural and Multidisciplinary Optimization* 52 (Sept. 2015).  
DOI: [10.1007/s00158-015-1250-z](https://doi.org/10.1007/s00158-015-1250-z)
- [37] Dorn, W. S., Gomory, R. E., and Greenberg, H., 'Automatic design of optimal structures', *J. Mécanique* (1964).
- [38] Chan, H. S. Y., 'Optimum structural design and linear programming', *College of Aeronautics Report Aero* 175 (1964).
- [39] Hemp, W. S., 'Optimum Structures'. Clarendon Press, 1973, Google-Books-ID: cJhpAAAAMAAJ.  
ISBN: [978-0-19-856110-1](https://www.googleapis.com/books/v1/books/9780198561101)
- [40] Sankaranarayanan, S., Haftka, R. T., and Kapania, R. K., 'Truss topology optimization with simultaneous analysis and design', *AIAA Journal* 32.2 (Feb. 1994), pp. 420–424.  
DOI: [10.2514/3.12000](https://doi.org/10.2514/3.12000)
- [41] Bendsøe, M. P., 'Optimal shape design as a material distribution problem', *Structural optimization* 1.4 (Dec. 1989), pp. 193–202.

DOI: [10.1007/BF01650949](https://doi.org/10.1007/BF01650949)

- [42] Sigmund, O., 'Materials with prescribed constitutive parameters: An inverse homogenization problem', *International Journal of Solids and Structures* 31.17 (Sept. 1994), pp. 2313–2329.  
DOI: [10.1016/0020-7683\(94\)90154-6](https://doi.org/10.1016/0020-7683(94)90154-6) cited on page 12
- [43] Zhang, W. and Sun, S., 'Scale-related topology optimization of cellular materials and structures', *International Journal for Numerical Methods in Engineering* 68.9 (2006), pp. 993–1011.  
DOI: [10.1002/nme.1743](https://doi.org/10.1002/nme.1743) cited on pages 12, 27, 28, 78
- [44] Collet, M., Noël, L., Bruggi, M., and Duysinx, P., 'Topology optimization for microstructural design under stress constraints', *Structural and Multidisciplinary Optimization* 58.6 (Dec. 2018), pp. 2677–2695.  
DOI: [10.1007/s00158-018-2045-9](https://doi.org/10.1007/s00158-018-2045-9) cited on page 12
- [45] Borrvall, T. and Petersson, J., 'Topology optimization of fluids in Stokes flow', *International Journal for Numerical Methods in Fluids* 41.1 (2003), pp. 77–107.  
DOI: [10.1002/fld.426](https://doi.org/10.1002/fld.426) cited on page 12
- [46] Bruyneel, M. and Duysinx, P., 'Note on topology optimization of continuum structures including self-weight', *Structural and Multidisciplinary Optimization* 29.4 (Apr. 2005), pp. 245–256.  
DOI: [10.1007/s00158-004-0484-y](https://doi.org/10.1007/s00158-004-0484-y) cited on page 12
- [47] Sigmund, O., 'Manufacturing tolerant topology optimization', *Acta Mechanica Sinica* 25.2 (Apr. 2009), pp. 227–239.  
DOI: [10.1007/s10409-009-0240-z](https://doi.org/10.1007/s10409-009-0240-z) cited on page 12
- [48] Brackett, D., Ashcroft, I., and Hague, R., 'Topology Optimization for Additive Manufacturing' (2011), p. 15.  
DOI: [10.26153/tsw/15300](https://doi.org/10.26153/tsw/15300) cited on pages 12, 15
- [49] Sigmund, O., 'On the Design of Compliant Mechanisms Using Topology Optimization\*', *Mechanics of Structures and Machines* 25.4 (Jan. 1997), pp. 493–524.  
DOI: [10.1080/08905459708945415](https://doi.org/10.1080/08905459708945415) cited on pages 12, 14
- [50] Bruns, T. E. and Tortorelli, D. A., 'Topology optimization of non-linear elastic structures and compliant mechanisms', *Computer Methods in Applied Mechanics and Engineering* 190.26 (Mar. 2001), pp. 3443–3459.  
DOI: [10.1016/S0045-7825\(00\)00278-4](https://doi.org/10.1016/S0045-7825(00)00278-4) cited on page 12
- [51] Wang, W., Munro, D., Wang, C. C. L., Keulen, F. van, and Wu, J., 'Space-time topology optimization for additive manufacturing', *Structural and Multidisciplinary Optimization* 61.1 (Jan. 2020), pp. 1–18.  
DOI: [10.1007/s00158-019-02420-6](https://doi.org/10.1007/s00158-019-02420-6) cited on page 12

- cited on page 12
- [52] Allaire, G., Jouve, F., and Toader, A.-M., 'A level-set method for shape optimization', *Comptes Rendus Mathematique* 334.12 (Jan. 2002), pp. 1125–1130.  
DOI: [10.1016/S1631-073X\(02\)02412-3](https://doi.org/10.1016/S1631-073X(02)02412-3)
- cited on page 12
- [53] Wang, M. Y., Wang, X., and Guo, D., 'A level set method for structural topology optimization', *Computer Methods in Applied Mechanics and Engineering* 192.1 (Jan. 2003), pp. 227–246.  
DOI: [10.1016/S0045-7825\(02\)00559-5](https://doi.org/10.1016/S0045-7825(02)00559-5)
- cited on page 12
- [54] Allaire, G., Jouve, F., and Toader, A.-M., 'Structural optimization using sensitivity analysis and a level-set method', *Journal of Computational Physics* 194.1 (Feb. 2004), pp. 363–393.  
DOI: [10.1016/j.jcp.2003.09.032](https://doi.org/10.1016/j.jcp.2003.09.032)
- cited on page 12
- [55] Tortorelli, D. A. and Michaleris, P., 'Design sensitivity analysis: Overview and review', *Inverse Problems in Engineering* 1.1 (Oct. 1994), pp. 71–105.  
DOI: [10.1080/174159794088027573](https://doi.org/10.1080/174159794088027573)
- cited on pages 13, 15, 39
- [56] Wang, F., Lazarov, B. S., and Sigmund, O., 'On projection methods, convergence and robust formulations in topology optimization', *Structural and Multidisciplinary Optimization* 43.6 (June 2011), pp. 767–784.  
DOI: [10.1007/s00158-010-0602-y](https://doi.org/10.1007/s00158-010-0602-y)
- cited on pages 13, 14, 111
- [57] Bendsøe, M. P. and Sigmund, O., 'Material interpolation schemes in topology optimization', *Archive of Applied Mechanics* 69.9 (Nov. 1999), pp. 635–654.  
DOI: [10.1007/s004190050248](https://doi.org/10.1007/s004190050248)
- cited on page 14
- [58] Hashin, Z. and Shtrikman, S., 'A variational approach to the theory of the elastic behaviour of multiphase materials', *Journal of the Mechanics and Physics of Solids* 11.2 (Mar. 1963), pp. 127–140.  
DOI: [10.1016/0022-5096\(63\)90060-7](https://doi.org/10.1016/0022-5096(63)90060-7)
- cited on page 14
- [59] Díaz, A. and Sigmund, O., 'Checkerboard patterns in layout optimization', *Structural optimization* 10.1 (Aug. 1995), pp. 40–45.  
DOI: [10.1007/BF01743693](https://doi.org/10.1007/BF01743693)
- cited on page 14
- [60] Sigmund, O., 'Design of Material Structures using Topology Optimization', PhD thesis, Technical University of Denmark, DK-2800 Lyngby, 1994.
- cited on pages 14, 39, 41
- [61] Sigmund, O., 'Morphology-based black and white filters for topology optimization', *Structural and Multidisciplinary Optimization* 33.4 (Apr. 2007), pp. 401–424.  
DOI: [10.1007/s00158-006-0087-x](https://doi.org/10.1007/s00158-006-0087-x)

- [62] Allaire, G. and Francfort, G. A., 'A Numerical Algorithm for Topology and Shape Optimization', *Topology Design of Structures*, NATO ASI Series, ed. by Bendsøe, M. P. and Soares, C. A. M., Dordrecht: Springer Netherlands, 1993, pp. 239–248, ISBN: 978-94-011-1804-0.  
DOI: [10.1007/978-94-011-1804-0\\_16](https://doi.org/10.1007/978-94-011-1804-0_16)
- [63] Allaire, G. and Kohn, R. V., 'Topology Optimization and Optimal Shape Design Using Homogenization', *Topology Design of Structures*, NATO ASI Series, ed. by Bendsøe, M. P. and Soares, C. A. M., Dordrecht: Springer Netherlands, 1993, pp. 207–218, ISBN: 978-94-011-1804-0.  
DOI: [10.1007/978-94-011-1804-0\\_14](https://doi.org/10.1007/978-94-011-1804-0_14)
- [64] Rozvany, G. I. N., 'A critical review of established methods of structural topology optimization', *Structural and Multidisciplinary Optimization* 37.3 (Jan. 2009), pp. 217–237.  
DOI: [10.1007/s00158-007-0217-0](https://doi.org/10.1007/s00158-007-0217-0)
- [65] Petersson, J. and Sigmund, O., 'Slope constrained topology optimization', *International Journal for Numerical Methods in Engineering* 41.8 (1998), pp. 1417–1434.  
DOI: [10.1002/\(SICI\)1097-0207\(19980430\)41:8<1417::AID-NME344>3.0.CO;2-N](https://doi.org/10.1002/(SICI)1097-0207(19980430)41:8<1417::AID-NME344>3.0.CO;2-N)
- [66] Rojas-Labanda, S. and Stolpe, M., 'Automatic penalty continuation in structural topology optimization', *Structural and Multidisciplinary Optimization* 52.6 (Dec. 2015), pp. 1205–1221.  
DOI: [10.1007/s00158-015-1277-1](https://doi.org/10.1007/s00158-015-1277-1)
- [67] Zhou, M., Fleury, R., Shyy, Y.-K., Thomas, H., and Brennan, J., 'Progress in Topology Optimization with Manufacturing Constraints', *9th AIAA/ISSMO Symposium on Multidisciplinary Analysis and Optimization*, Atlanta, Georgia: American Institute of Aeronautics and Astronautics, Sept. 2002, ISBN: 978-1-62410-120-5.  
DOI: [10.2514/6.2002-5614](https://doi.org/10.2514/6.2002-5614)
- [68] Liu, J., Gaynor, A. T., Chen, S., Kang, Z., Suresh, K., Takezawa, A., Li, L., Kato, J., Tang, J., Wang, C. C. L., Cheng, L., Liang, X., and To, A. C., 'Current and future trends in topology optimization for additive manufacturing', *Structural and Multidisciplinary Optimization* 57.6 (June 2018), pp. 2457–2483.  
DOI: [10.1007/s00158-018-1994-3](https://doi.org/10.1007/s00158-018-1994-3)
- [69] Aage, N., Andreassen, E., Lazarov, B. S., and Sigmund, O., 'Giga-voxel computational morphogenesis for structural design', *Nature* 550.7674 (Oct. 2017), pp. 84–86.  
DOI: [10.1038/nature23911](https://doi.org/10.1038/nature23911)

- cited on page 16
- [70] Salazar de Troya, M. A. and Tortorelli, D. A., 'Adaptive mesh refinement in stress-constrained topology optimization', *Structural and Multidisciplinary Optimization* 58.6 (Dec. 2018), pp. 2369–2386.  
DOI: [10.1007/s00158-018-2084-2](https://doi.org/10.1007/s00158-018-2084-2)
- cited on page 16
- [71] Zhang, S., Gain, A. L., and Norato, J. A., 'Adaptive mesh refinement for topology optimization with discrete geometric components', *Computer Methods in Applied Mechanics and Engineering* 364 (June 2020), p. 112930.  
DOI: [10.1016/j.cma.2020.112930](https://doi.org/10.1016/j.cma.2020.112930)
- cited on pages 16, 17, 21, 41, 49, 53, 86, 111
- [72] Sigmund, O., Aage, N., and Andreassen, E., 'On the (non-)optimality of Michell structures', *Structural and Multidisciplinary Optimization* 54.2 (Aug. 2016), pp. 361–373.  
DOI: [10.1007/s00158-016-1420-7](https://doi.org/10.1007/s00158-016-1420-7)
- cited on page 16
- [73] Wein, F., Dunning, P. D., and Norato, J. A., 'A review on feature-mapping methods for structural optimization', *Structural and Multidisciplinary Optimization* 62.4 (Oct. 2020), pp. 1597–1638.  
DOI: [10.1007/s00158-020-02649-6](https://doi.org/10.1007/s00158-020-02649-6)
- cited on page 16
- [74] Guo, X., Zhang, W., and Zhong, W., 'Doing Topology Optimization Explicitly and Geometrically—A New Moving Morphable Components Based Framework', *Journal of Applied Mechanics* 81.8 (May 2014).  
DOI: [10.1115/1.4027609](https://doi.org/10.1115/1.4027609)
- cited on page 16
- [75] Zhang, W., Li, D., Yuan, J., Song, J., and Guo, X., 'A new three-dimensional topology optimization method based on moving morphable components (MMCs)', *Computational Mechanics* 59.4 (Apr. 2017), pp. 647–665.  
DOI: [10.1007/s00466-016-1365-0](https://doi.org/10.1007/s00466-016-1365-0)
- cited on page 16
- [76] Norato, J. A., Bell, B. K., and Tortorelli, D. A., 'A geometry projection method for continuum-based topology optimization with discrete elements', *Computer Methods in Applied Mechanics and Engineering* 293 (Aug. 2015), pp. 306–327.  
DOI: [10.1016/j.cma.2015.05.005](https://doi.org/10.1016/j.cma.2015.05.005)
- cited on page 16
- [77] Zhang, S., Norato, J. A., Gain, A. L., and Lyu, N., 'A geometry projection method for the topology optimization of plate structures', *Structural and Multidisciplinary Optimization* 54.5 (Nov. 2016), pp. 1173–1190.  
DOI: [10.1007/s00158-016-1466-6](https://doi.org/10.1007/s00158-016-1466-6)
- cited on page 16
- [78] Coniglio, S., Morlier, J., Gogu, C., and Amargier, R., 'Generalized Geometry Projection: A Unified Approach for Geometric Feature Based Topology Optimization', *Archives of Computational Methods in Engineering* 27.5 (Nov. 2020), pp. 1573–1610.  
DOI: [10.1007/s11831-019-09362-8](https://doi.org/10.1007/s11831-019-09362-8)

- [79] Kazemi, H., Vaziri, A., and Norato, J. A., 'Multi-material topology optimization of lattice structures using geometry projection', *Computer Methods in Applied Mechanics and Engineering* 363 (May 2020), p. 112895.  
DOI: [10.1016/j.cma.2020.112895](https://doi.org/10.1016/j.cma.2020.112895)
- [80] Cheng, G. D. and Guo, X., ' $\varepsilon$ -relaxed approach in structural topology optimization', *Structural optimization* 13.4 (June 1997), pp. 258–266.  
DOI: [10.1007/BF01197454](https://doi.org/10.1007/BF01197454)
- [81] Rozvany, G., 'On design-dependent constraints and singular topologies', *Structural and Multidisciplinary Optimization* 21.2 (Apr. 2001), pp. 164–172.  
DOI: [10.1007/s001580050181](https://doi.org/10.1007/s001580050181)
- [82] Gao, X. and Ma, H., 'Topology optimization of continuum structures under buckling constraints', *Computers & Structures* 157 (Sept. 2015), pp. 142–152.  
DOI: [10.1016/j.compstruc.2015.05.020](https://doi.org/10.1016/j.compstruc.2015.05.020)
- [83] He, L., Gilbert, M., and Song, X., 'A Python script for adaptive layout optimization of trusses', *Structural and Multidisciplinary Optimization* 60.2 (Aug. 2019), pp. 835–847.  
DOI: [10.1007/s00158-019-02226-6](https://doi.org/10.1007/s00158-019-02226-6)
- [84] Kirsch, U., 'Optimal topologies of truss structures', *Computer Methods in Applied Mechanics and Engineering* 72.1 (Jan. 1989), pp. 15–28.  
DOI: [10.1016/0045-7825\(89\)90119-9](https://doi.org/10.1016/0045-7825(89)90119-9)
- [85] Rozvany, G. I. N., Bendsøe, M. P., and Kirsch, U., 'Layout Optimization of Structures', *Applied Mechanics Reviews* 48.2 (Feb. 1995), pp. 41–119.  
DOI: [10.1115/1.3005097](https://doi.org/10.1115/1.3005097)
- [86] Kirsch, U., 'Optimal design of trusses by approximate compatibility', *Computers & Structures* 12.1 (July 1980), pp. 93–98.  
DOI: [10.1016/0045-7949\(80\)90097-8](https://doi.org/10.1016/0045-7949(80)90097-8)
- [87] Cheng, G., 'Some aspects of truss topology optimization', *Structural Optimization* 10.3-4 (Dec. 1995), pp. 173–179.  
DOI: [10.1007/BF01742589](https://doi.org/10.1007/BF01742589)
- [88] Achtziger, W., 'Local stability of trusses in the context of topology optimization Part I: Exact modelling', *Structural Optimization* 17.4 (Dec. 1999), pp. 235–246.  
DOI: [10.1007/BF01206999](https://doi.org/10.1007/BF01206999)
- [89] Maxwell, J. C., 'I.—On Reciprocal Figures, Frames, and Diagrams of Forces', *Earth and Environmental Science Transactions of The Royal Society of Edinburgh* 26.1 (1870), pp. 1–40.  
DOI: [10.1017/S0080456800026351](https://doi.org/10.1017/S0080456800026351)

- cited on pages 18, 20, 42, 84
- [90] Michell, A. G. M., 'The limits of economy of material in frame-structures', *The London, Edinburgh, and Dublin Philosophical Magazine and Journal of Science* 8.47 (Nov. 1904), pp. 589–597.  
DOI: [10.1080/14786440409463229](https://doi.org/10.1080/14786440409463229)
- cited on pages 19, 20
- [91] Gilbert, M. and Tyas, A., 'Layout optimization of large-scale pin-jointed frames', *Engineering Computations* 20.8 (Dec. 2003), pp. 1044–1064.  
DOI: [10.1108/02644400310503017](https://doi.org/10.1108/02644400310503017)
- cited on page 19
- [92] Pedersen, P., 'Optimal Joint Positions for Space Trusses', *Journal of the Structural Division* 99.12 (Dec. 1973), pp. 2459–2476.  
DOI: [10.1061/JSDEAG.0003669](https://doi.org/10.1061/JSDEAG.0003669)
- cited on page 19
- [93] Achtziger, W., 'On simultaneous optimization of truss geometry and topology', *Structural and Multidisciplinary Optimization* 33.4 (Apr. 2007), pp. 285–304.  
DOI: [10.1007/s00158-006-0092-0](https://doi.org/10.1007/s00158-006-0092-0)
- cited on page 19
- [94] Descamps, B. and Filomeno Coelho, R., 'A lower-bound formulation for the geometry and topology optimization of truss structures under multiple loading', *Structural and Multidisciplinary Optimization* 48.1 (July 2013), pp. 49–58.  
DOI: [10.1007/s00158-012-0876-3](https://doi.org/10.1007/s00158-012-0876-3)
- cited on page 19
- [95] He, L. and Gilbert, M., 'Rationalization of trusses generated via layout optimization', *Structural and Multidisciplinary Optimization* 52.4 (Oct. 2015), pp. 677–694.  
DOI: [10.1007/s00158-015-1260-x](https://doi.org/10.1007/s00158-015-1260-x)
- cited on page 19
- [96] Lu, H. and Xie, Y. M., 'Reducing the number of different members in truss layout optimization', *Structural and Multidisciplinary Optimization* 66.3 (Feb. 2023), p. 52.  
DOI: [10.1007/s00158-023-03514-y](https://doi.org/10.1007/s00158-023-03514-y)
- cited on page 19
- [97] Savine, F., Irisarri, F.-X., Julien, C., Vincenti, A., and Guerin, Y., 'A component-based method for the optimization of stiffener layout on large cylindrical rib-stiffened shell structures', *Structural and Multidisciplinary Optimization* 64.4 (Oct. 2021), pp. 1843–1861.  
DOI: [10.1007/s00158-021-02945-9](https://doi.org/10.1007/s00158-021-02945-9)
- cited on pages 20, 37
- [98] Parkes, E., 'Joints in optimum frameworks', *International Journal of Solids and Structures* 11.9 (Sept. 1975), pp. 1017–1022.  
DOI: [10.1016/0020-7683\(75\)90044-X](https://doi.org/10.1016/0020-7683(75)90044-X)
- cited on pages 20, 22
- [99] Schaedler, T. A. and Carter, W. B., 'Architected Cellular Materials', *Annual Review of Materials Research* 46.1 (July 2016), pp. 187–210.  
DOI: [10.1146/annurev-matsci-070115-031624](https://doi.org/10.1146/annurev-matsci-070115-031624)
- cited on pages 20, 24, 25
- [100] Kohn, R. V. and Strang, G., 'Optimal design and relaxation of variational problems', *Communications on Pure and Applied Mathematics* 39.1 (1986), pp. 113–137.  
DOI: [10.1002/cpa.3160390107](https://doi.org/10.1002/cpa.3160390107)

- [101] Allaire, G. and Aubry, S., 'On optimal microstructures for a plane shape optimization problem', *Structural optimization* 17.2 (Apr. 1999), pp. 86–94.  
DOI: [10.1007/BF01195933](https://doi.org/10.1007/BF01195933)
- [102] Fleck, N. A., Deshpande, V. S., and Ashby, M. F., 'Micro-architected materials: past, present and future', *Proceedings of the Royal Society A: Mathematical, Physical and Engineering Sciences* 466.2121 (Sept. 2010), pp. 2495–2516.  
DOI: [10.1098/rspa.2010.0215](https://doi.org/10.1098/rspa.2010.0215)
- [103] NZ, B. S., 'Hypholoma fasciculare,' Apr. 2023.  
URL: <https://www.flickr.com/photos/volvob12b/52833345708/>
- [104] LIBRARY, S. G. P., 'Leaf structure, SEM'.  
URL: <https://www.sciencephoto.com/media/30288/view/leaf-structure-sem>
- [105] gripspix (mostly off, health issues), 'Wing of a dragonfly, detail', Aug. 2007.  
URL: <https://www.flickr.com/photos/gripspix/1233292309/>
- [106] Archimorph, 'bone\_03'.  
URL: [https://archimorph.files.wordpress.com/2010/01/bone\\_03.jpg](https://archimorph.files.wordpress.com/2010/01/bone_03.jpg)
- [107] Dai, G. M. and Zhang, W. H., 'Size effects of basic cell in static analysis of sandwich beams', *International Journal of Solids and Structures* 45.9 (May 2008), pp. 2512–2533.  
DOI: [10.1016/j.ijsolstr.2007.12.007](https://doi.org/10.1016/j.ijsolstr.2007.12.007)
- [108] Kalamkarov, A. L., Andrianov, I. V., and Danishevs'kyy, V. V., 'Asymptotic Homogenization of Composite Materials and Structures', *Applied Mechanics Reviews* 62.3 (Mar. 2009).  
DOI: [10.1115/1.3090830](https://doi.org/10.1115/1.3090830)
- [109] Coelho, P. G., Amiano, L. D., Guedes, J. M., and Rodrigues, H. C., 'Scale-size effects analysis of optimal periodic material microstructures designed by the inverse homogenization method', *Computers & Structures*, CIVIL-COMP 174 (Oct. 2016), pp. 21–32.  
DOI: [10.1016/j.compstruc.2015.10.001](https://doi.org/10.1016/j.compstruc.2015.10.001)
- [110] Zhang, Y., Xiao, M., Li, H., Gao, L., and Chu, S., 'Multiscale concurrent topology optimization for cellular structures with multiple microstructures based on ordered SIMP interpolation', *Computational Materials Science* 155 (Dec. 2018), pp. 74–91.  
DOI: [10.1016/j.commatsci.2018.08.030](https://doi.org/10.1016/j.commatsci.2018.08.030)
- [111] Deshpande, V. S., Ashby, M. F., and Fleck, N. A., 'Foam topology: bending versus stretching dominated architectures', *Acta Materialia* 49.6 (Apr. 2001), pp. 1035–1040.  
DOI: [10.1016/S1359-6454\(00\)00379-7](https://doi.org/10.1016/S1359-6454(00)00379-7)

- cited on pages 22, 24, 25
- [112] Ashby, M., 'The properties of foams and lattices', *Philosophical Transactions of the Royal Society A: Mathematical, Physical and Engineering Sciences* 364.1838 (Jan. 2006), pp. 15–30.  
DOI: [10.1098/rsta.2005.1678](https://doi.org/10.1098/rsta.2005.1678)
- cited on page 22
- [113] Evans, A. G., He, M. Y., Deshpande, V. S., Hutchinson, J. W., Jacobsen, A. J., and Barvosa-Carter, W., 'Concepts for Enhanced Energy Absorption Using Hollow Micro-Lattices', *International Journal of Impact Engineering* (2010).  
DOI: [10.1016/j.ijimpeng.2010.03.007](https://doi.org/10.1016/j.ijimpeng.2010.03.007)
- cited on page 22
- [114] Schaedler, T. A., Ro, C. J., Sorensen, A. E., Eckel, Z., Yang, S. S., Carter, W. B., and Jacobsen, A. J., 'Designing Metallic Microlattices for Energy Absorber Applications', *Advanced Engineering Materials* 16.3 (2014), pp. 276–283.  
DOI: [10.1002/adem.201300206](https://doi.org/10.1002/adem.201300206)
- cited on page 22
- [115] Ozdemir, Z., Hernandez-Nava, E., Tyas, A., Warren, J. A., Fay, S. D., Goodall, R., Todd, I., and Askes, H., 'Energy absorption in lattice structures in dynamics: Experiments', *International Journal of Impact Engineering* 89 (Mar. 2016), pp. 49–61.  
DOI: [10.1016/j.ijimpeng.2015.10.007](https://doi.org/10.1016/j.ijimpeng.2015.10.007)
- cited on pages 23, 123
- [116] Opgenoord, M. M. and Willcox, K. E., 'Aeroelastic Tailoring using Additively Manufactured Lattice Structures', *2018 Multidisciplinary Analysis and Optimization Conference*, Atlanta, Georgia: American Institute of Aeronautics and Astronautics, June 2018.  
DOI: [10.2514/6.2018-4055](https://doi.org/10.2514/6.2018-4055)
- cited on pages 23, 24, 77, 138
- [117] Cramer, N. B., Cellucci, D. W., Formoso, O. B., Gregg, C. E., Jenett, B. E., Kim, J. H., Lendraitis, M., Swei, S. S., Trinh, G. T., Trinh, K. V., and Cheung, K. C., 'Elastic shape morphing of ultralight structures by programmable assembly', *Smart Materials and Structures* 28.5 (Apr. 2019), p. 055006.  
DOI: [10.1088/1361-665X/ab0ea2](https://doi.org/10.1088/1361-665X/ab0ea2)
- cited on page 23
- [118] Hutmacher, D. W., 'Scaffolds in tissue engineering bone and cartilage', *Biomaterials, Orthopaedic Polymeric Biomaterials: Applications of Biodegradables* 21.24 (Dec. 2000), pp. 2529–2543.  
DOI: [10.1016/S0142-9612\(00\)00121-6](https://doi.org/10.1016/S0142-9612(00)00121-6)
- cited on page 23
- [119] Mota, C., Puppi, D., Chiellini, F., and Chiellini, E., 'Additive manufacturing techniques for the production of tissue engineering constructs', *Journal of Tissue Engineering and Regenerative Medicine* 9.3 (Mar. 2015), pp. 174–190.  
DOI: [10.1002/term.1635](https://doi.org/10.1002/term.1635)
- cited on page 23
- [120] Nikolova, M. P. and Chavali, M. S., 'Recent advances in biomaterials for 3D scaffolds: A review', *Bioactive Materials* 4 (Oct. 2019), pp. 271–292.  
DOI: [10.1016/j.bioactmat.2019.10.005](https://doi.org/10.1016/j.bioactmat.2019.10.005)

- [121] Lu, T. J., Stone, H. A., and Ashby, M. F., 'Heat transfer in open-cell metal foams', *Acta Materialia* 46.10 (June 1998), pp. 3619–3635.  
DOI: [10.1016/S1359-6454\(98\)00031-7](https://doi.org/10.1016/S1359-6454(98)00031-7)
- [122] Wadley, H. N. G. and Queheillalt, D. T., 'Thermal Applications of Cellular Lattice Structures', *Materials Science Forum* 539-543 (2007), pp. 242–247.  
DOI: [10.4028/www.scientific.net/MSF.539-543.242](https://doi.org/10.4028/www.scientific.net/MSF.539-543.242)
- [123] AirShowConsultants, 'The REAL monster from Loch Ness – Vickers Wellington', June 2013.  
URL: <https://shortfinals.org/2013/06/15/the-real-monster-from-loch-ness-vickers-wellington-r-for-robert/>
- [124] Bensoussan, A., Lions, J.-L., and Papanicolaou, G., 'Asymptotic analysis for periodic structures', *Studies in mathematics and its applications* v. 5. Amsterdam ; New York : New York: North-Holland Pub. Co. ; sole distributors for the U.S.A. and Canada, Elsevier North-Holland, 1978.  
ISBN: [978-0-444-85172-7](https://doi.org/10.1017/CBO9780511541299)
- [125] Jenett, B., Calisch, S., Cellucci, D., Cramer, N., Gershenfeld, N., Swei, S., and Cheung, K. C., 'Digital Morphing Wing: Active Wing Shaping Concept Using Composite Lattice-Based Cellular Structures', *Soft Robotics* 4.1 (Mar. 2017), pp. 33–48.  
DOI: [10.1089/soro.2016.0032](https://doi.org/10.1089/soro.2016.0032)
- [126] Dong, L., Deshpande, V., and Wadley, H., 'Mechanical response of Ti–6Al–4V octet-truss lattice structures', *International Journal of Solids and Structures* 60-61 (May 2015), pp. 107–124.  
DOI: [10.1016/j.ijsolstr.2015.02.020](https://doi.org/10.1016/j.ijsolstr.2015.02.020)
- [127] Stolpe, M., 'Fail-safe truss topology optimization', *Structural and Multidisciplinary Optimization* 60.4 (Oct. 2019), pp. 1605–1618.  
DOI: [10.1007/s00158-019-02295-7](https://doi.org/10.1007/s00158-019-02295-7)
- [128] Wu, J., Sigmund, O., and Groen, J. P., 'Topology optimization of multi-scale structures: a review', *Structural and Multidisciplinary Optimization* (Mar. 2021).  
DOI: [10.1007/s00158-021-02881-8](https://doi.org/10.1007/s00158-021-02881-8)
- [129] Hunt, C. J., Wisnom, M. R., and Woods, B. K. S., 'WrapToR composite truss structures: Improved process and structural efficiency', *Composite Structures* 230 (Dec. 2019), p. 111467.  
DOI: [10.1016/j.compstruct.2019.111467](https://doi.org/10.1016/j.compstruct.2019.111467)
- [130] Gershenfeld, N., Carney, M., Jenett, B., Calisch, S., and Wilson, S., 'Macrofabrication with Digital Materials: Robotic Assembly', *Architectural Design* 85.5 (2015), pp. 122–127.  
DOI: [10.1002/ad.1964](https://doi.org/10.1002/ad.1964)

- cited on pages 23, 24
- [131] Jenett, B. and Cheung, K., 'BILL-E: Robotic Platform for Locomotion and Manipulation of Lightweight Space Structures', *25th AIAA/AHS Adaptive Structures Conference*, Grapevine, Texas: American Institute of Aeronautics and Astronautics, Jan. 2017.  
DOI: [10.2514/6.2017-1876](https://doi.org/10.2514/6.2017-1876)
- cited on pages 23, 24
- [132] Niehs, E., Schmidt, A., Scheffer, C., Biediger, D. E., Yannuzzi, M., Jenett, B., Abdel-Rahman, A., Cheung, K. C., Becker, A. T., and Fekete, S. P., 'Recognition and Reconfiguration of Lattice-Based Cellular Structures by Simple Robots', *2020 IEEE International Conference on Robotics and Automation (ICRA)*, May 2020, pp. 8252–8259.  
DOI: [10.1109/ICRA40945.2020.9196700](https://doi.org/10.1109/ICRA40945.2020.9196700)
- cited on page 24
- [133] Opgenoord, M., 'Transonic Flutter Prediction and Aeroelastic Tailoring for Next-Generation Transport Aircraft', PhD thesis, Aug. 2018.
- cited on page 24
- [134] Park, K.-M., Min, K.-S., and Roh, Y.-S., 'Design Optimization of Lattice Structures under Compression: Study of Unit Cell Types and Cell Arrangements', *Materials* 15.1 (Jan. 2022), Number: 1 Publisher: Multidisciplinary Digital Publishing Institute, p. 97.  
DOI: [10.3390/ma15010097](https://doi.org/10.3390/ma15010097)
- cited on pages 24, 25
- [135] Xu, S., Shen, J., Zhou, S., Huang, X., and Xie, Y. M., 'Design of lattice structures with controlled anisotropy', *Materials & Design* 93 (Mar. 2016), pp. 443–447.  
DOI: [10.1016/j.matdes.2016.01.007](https://doi.org/10.1016/j.matdes.2016.01.007)
- cited on pages 24, 25, 106
- [136] Song, J., Tang, Q., Feng, Q., Ma, S., Guo, F., and Han, Q., 'Investigation on the modelling approach for variable-density lattice structures fabricated using selective laser melting', *Materials & Design* 212 (Dec. 2021), p. 110236.  
DOI: [10.1016/j.matdes.2021.110236](https://doi.org/10.1016/j.matdes.2021.110236)
- cited on pages 24, 25
- [137] Zhou, M. and Rozvany, G. I. N., 'The COC algorithm, Part II: Topological, geometrical and generalized shape optimization', *Computer Methods in Applied Mechanics and Engineering*, Second World Congress on Computational Mechanics 89.1 (Aug. 1991), pp. 309–336.  
DOI: [10.1016/0045-7825\(91\)90046-9](https://doi.org/10.1016/0045-7825(91)90046-9)
- cited on page 25
- [138] Rodrigues, H., Guedes, J., and Bendsoe, M., 'Hierarchical optimization of material and structure', *Structural and Multi-disciplinary Optimization* 24.1 (Aug. 2002), pp. 1–10.  
DOI: [10.1007/s00158-002-0209-z](https://doi.org/10.1007/s00158-002-0209-z)
- cited on page 25
- [139] Partz, O. and Trabelsi, K., 'A Post-Treatment of the Homogenization Method for Shape Optimization', *SIAM Journal on Control and Optimization* 47.3 (Jan. 2008), pp. 1380–1398.  
DOI: [10.1137/070688900](https://doi.org/10.1137/070688900)

- [140] Groen, J. P. and Sigmund, O., 'Homogenization-based topology optimization for high-resolution manufacturable microstructures', *International Journal for Numerical Methods in Engineering* 113.8 (2018), pp. 1148–1163.  
DOI: [10.1002/nme.5575](https://doi.org/10.1002/nme.5575) cited on pages 25–27
- [141] Wang, C., Gu, X., Zhu, J., Zhou, H., Li, S., and Zhang, W., 'Concurrent design of hierarchical structures with three-dimensional parameterized lattice microstructures for additive manufacturing', *Structural and Multidisciplinary Optimization* 61.3 (Mar. 2020), pp. 869–894.  
DOI: [10.1007/s00158-019-02408-2](https://doi.org/10.1007/s00158-019-02408-2) cited on page 26
- [142] Guedes, J. and Kikuchi, N., 'Preprocessing and postprocessing for materials based on the homogenization method with adaptive finite element methods', *Computer Methods in Applied Mechanics and Engineering* 83.2 (Oct. 1990), pp. 143–198.  
DOI: [10.1016/0045-7825\(90\)90148-F](https://doi.org/10.1016/0045-7825(90)90148-F) cited on page 25
- [143] Allaire, G., Geoffroy-Donders, P., and Pantz, O., 'Topology optimization of modulated and oriented periodic microstructures by the homogenization method', *Computers & Mathematics with Applications, Simulation for Additive Manufacturing* 78.7 (Oct. 2019), pp. 2197–2229.  
DOI: [10.1016/j.camwa.2018.08.007](https://doi.org/10.1016/j.camwa.2018.08.007) cited on page 26
- [144] Geoffroy-Donders, P., Allaire, G., and Pantz, O., '3-d topology optimization of modulated and oriented periodic microstructures by the homogenization method', *Journal of Computational Physics* 401 (Jan. 2020), p. 108994.  
DOI: [10.1016/j.jcp.2019.108994](https://doi.org/10.1016/j.jcp.2019.108994) cited on page 26
- [145] Kumar, T. and Suresh, K., 'A density-and-strain-based K-clustering approach to microstructural topology optimization', *Structural and Multidisciplinary Optimization* 61.4 (Apr. 2020), pp. 1399–1415.  
DOI: [10.1007/s00158-019-02422-4](https://doi.org/10.1007/s00158-019-02422-4) cited on pages 26, 106
- [146] Xia, L. and Breitkopf, P., 'Multiscale structural topology optimization with an approximate constitutive model for local material microstructure', *Computer Methods in Applied Mechanics and Engineering* 286 (Apr. 2015), pp. 147–167.  
DOI: [10.1016/j.cma.2014.12.018](https://doi.org/10.1016/j.cma.2014.12.018) cited on page 26
- [147] Wang, C., Zhu, J. H., Zhang, W. H., Li, S. Y., and Kong, J., 'Concurrent topology optimization design of structures and non-uniform parameterized lattice microstructures', *Structural and Multidisciplinary Optimization* 58.1 (July 2018), pp. 35–50.  
DOI: [10.1007/s00158-018-02009-0](https://doi.org/10.1007/s00158-018-02009-0) cited on pages 26, 27

- cited on pages 26, 27
- [148] Imediegwu, C., Murphy, R., Hewson, R., and Santer, M., 'Multi-scale structural optimization towards three-dimensional printable structures', *Structural and Multidisciplinary Optimization* 60.2 (Aug. 2019), pp. 513–525.  
DOI: [10.1007/s00158-019-02220-y](https://doi.org/10.1007/s00158-019-02220-y)
- cited on pages 26, 27
- [149] Duriez, E., Morlier, J., Charlotte, M., and Azzaro-Pantel, C., 'A well connected, locally-oriented and efficient multi-scale topology optimization (EMTO) strategy', *Structural and Multidisciplinary Optimization* 64.6 (Dec. 2021), pp. 3705–3728.  
DOI: [10.1007/s00158-021-03048-1](https://doi.org/10.1007/s00158-021-03048-1)
- cited on pages 26, 27
- [150] Kim, C., Lee, J., and Yoo, J., 'Machine learning-combined topology optimization for functionary graded composite structure design', *Computer Methods in Applied Mechanics and Engineering* 387 (Dec. 2021), p. 114158.  
DOI: [10.1016/j.cma.2021.114158](https://doi.org/10.1016/j.cma.2021.114158)
- cited on pages 26, 27
- [151] White, D. A., Arrighi, W. J., Kudo, J., and Watts, S. E., 'Multi-scale topology optimization using neural network surrogate models', *Computer Methods in Applied Mechanics and Engineering* 346 (Apr. 2019), pp. 1118–1135.  
DOI: [10.1016/j.cma.2018.09.007](https://doi.org/10.1016/j.cma.2018.09.007)
- cited on pages 26, 27
- [152] Chandrasekhar, A. and Suresh, K., 'Multi-Material Topology Optimization Using Neural Networks', *Computer-Aided Design* 136 (July 2021), p. 103017.  
DOI: [10.1016/j.cad.2021.103017](https://doi.org/10.1016/j.cad.2021.103017)
- cited on pages 26, 27
- [153] Wang, L., Liu, Z., Da, D., Chan, Y.-C., Chen, W., and Zhu, P., 'Enhancing Data-driven Multiscale Topology Optimization with Generalized De-homogenization', Dec. 2021.  
URL: <https://arxiv.org/abs/2112.02506v2>
- cited on page 27
- [154] Sigmund, O., 'On benchmarking and good scientific practise in topology optimization', *Structural and Multidisciplinary Optimization* 65.11 (Oct. 2022), p. 315.  
DOI: [10.1007/s00158-022-03427-2](https://doi.org/10.1007/s00158-022-03427-2)
- cited on pages 27, 28
- [155] Cheng, L., Bai, J., and To, A. C., 'Functionally graded lattice structure topology optimization for the design of additive manufactured components with stress constraints', *Computer Methods in Applied Mechanics and Engineering* 344 (Feb. 2019), pp. 334–359.  
DOI: [10.1016/j.cma.2018.10.010](https://doi.org/10.1016/j.cma.2018.10.010)
- cited on pages 27, 28
- [156] Wu, J., Aage, N., Westermann, R., and Sigmund, O., 'Infill Optimization for Additive Manufacturing—Approaching Bone-Like Porous Structures', *IEEE Transactions on Visualization and Computer Graphics* 24.2 (Feb. 2018), pp. 1127–1140.  
DOI: [10.1109/TVCG.2017.2655523](https://doi.org/10.1109/TVCG.2017.2655523)

- [157] Huang, X. and Xie, Y. M., 'Optimal design of periodic structures using evolutionary topology optimization', *Structural and Multidisciplinary Optimization* 36.6 (Nov. 2008), pp. 597–606.  
DOI: [10.1007/s00158-007-0196-1](https://doi.org/10.1007/s00158-007-0196-1) cited on pages 27, 28
- [158] Tugilimana, A., Coelho, R. F., and Thrall, A. P., 'An integrated design methodology for modular trusses including dynamic grouping, module spatial orientation, and topology optimization', *Structural and Multidisciplinary Optimization* 60.2 (Aug. 2019), pp. 613–638.  
DOI: [10.1007/s00158-019-02230-w](https://doi.org/10.1007/s00158-019-02230-w) cited on pages 28, 115–117
- [159] Bakker, C., Zhang, L., Higginson, K., and Keulen, F. v., 'Simultaneous optimization of topology and layout of modular stiffeners on shells and plates', *Structural and Multidisciplinary Optimization* 64.5 (Nov. 2021), pp. 3147–3161.  
DOI: [10.1007/s00158-021-03081-0](https://doi.org/10.1007/s00158-021-03081-0) cited on pages 28, 106
- [160] Tugilimana, A., Thrall, A. P., Descamps, B., and Coelho, R. F., 'Spatial orientation and topology optimization of modular trusses', *Structural and Multidisciplinary Optimization* 55.2 (Feb. 2017), pp. 459–476.  
DOI: [10.1007/s00158-016-1501-7](https://doi.org/10.1007/s00158-016-1501-7) cited on pages 28, 115
- [161] Liu, Y., Wang, Z., Lu, H., Ye, J., Zhao, Y., and Min Xie, Y., 'Layout optimization of truss structures with modular constraints', *Structures* 55 (Sept. 2023), pp. 1460–1469.  
DOI: [10.1016/j.istruc.2023.06.071](https://doi.org/10.1016/j.istruc.2023.06.071) cited on page 28
- [162] Stromberg, L. L., Beghini, A., Baker, W. F., and Paulino, G. H., 'Application of layout and topology optimization using pattern gradation for the conceptual design of buildings', *Structural and Multidisciplinary Optimization* 43.2 (Feb. 2011), pp. 165–180.  
DOI: [10.1007/s00158-010-0563-1](https://doi.org/10.1007/s00158-010-0563-1) cited on page 28
- [163] Wu, J., Dick, C., and Westermann, R., 'A System for High-Resolution Topology Optimization', *IEEE Transactions on Visualization and Computer Graphics* 22.3 (Mar. 2016), pp. 1195–1208.  
DOI: [10.1109/TVCG.2015.2502588](https://doi.org/10.1109/TVCG.2015.2502588) cited on page 28
- [164] Stragiotti, E., Irisarri, F.-X., Julien, C., and Morlier, J., 'Towards manufactured lattice structures: a comparison between layout and topology optimization', *AeroBest 2021 International Conference on Multidisciplinary Design Optimization of Aerospace Systems. Book of proceedings*, Lisbon, Portugal: ECCOMAS, July 2021, pp. 229–244.  
cited on page 29
- [165] Achtziger, W. and Kanzow, C., 'Mathematical programs with vanishing constraints: optimality conditions and constraint qualifications', *Mathematical Programming* 114.1 (July 2008), pp. 69–99.  
DOI: [10.1007/s10107-006-0083-3](https://doi.org/10.1007/s10107-006-0083-3) cited on page 30

- cited on page 30
- [166] Cheng, G. and Jiang, Z., 'Study on Topology Optimization with Stress Constraints', *Engineering Optimization* 20.2 (Nov. 1992), pp. 129–148.  
DOI: [10.1080/03052159208941276](https://doi.org/10.1080/03052159208941276)
- cited on pages 31–33, 39
- [167] Verbart, A., Langelaar, M., and Keulen, F. v., 'A unified aggregation and relaxation approach for stress-constrained topology optimization', *Structural and Multidisciplinary Optimization* 55.2 (Feb. 2017), pp. 663–679.  
DOI: [10.1007/s00158-016-1524-0](https://doi.org/10.1007/s00158-016-1524-0)
- cited on pages 31, 38
- [168] Duysinx, P. and Bendsøe, M. P., 'Topology optimization of continuum structures with local stress constraints', *International Journal for Numerical Methods in Engineering* 43.8 (1998), pp. 1453–1478.  
DOI: [10.1002/\(SICI\)1097-0207\(19981230\)43:8<1453::AID-NME480>3.0.CO;2-2](https://doi.org/10.1002/(SICI)1097-0207(19981230)43:8<1453::AID-NME480>3.0.CO;2-2)
- cited on pages 31, 32, 38
- [169] Le, C., Norato, J., Bruns, T., Ha, C., and Tortorelli, D., 'Stress-based topology optimization for continua', *Structural and Multidisciplinary Optimization* 41.4 (Apr. 2010), pp. 605–620.  
DOI: [10.1007/s00158-009-0440-y](https://doi.org/10.1007/s00158-009-0440-y)
- cited on page 32
- [170] Holmberg, E., Torstenfelt, B., and Klarbring, A., 'Stress constrained topology optimization', *Structural and Multidisciplinary Optimization* 48.1 (2013), pp. 33–47.  
DOI: [10.1007/s00158-012-0880-7](https://doi.org/10.1007/s00158-012-0880-7)
- cited on page 32
- [171] Silva, G. A. da, Beck, A. T., and Sigmund, O., 'Stress-constrained topology optimization considering uniform manufacturing uncertainties', *Computer Methods in Applied Mechanics and Engineering* 344 (Feb. 2019), pp. 512–537.  
DOI: [10.1016/j.cma.2018.10.020](https://doi.org/10.1016/j.cma.2018.10.020)
- cited on page 32
- [172] Stolpe, M., 'On Models and Methods for Global Optimization of Structural Topology', PhD thesis, 2003.
- cited on page 32
- [173] Sved, G. and Ginos, Z., 'Structural optimization under multiple loading', *International Journal of Mechanical Sciences* 10.10 (Oct. 1968), pp. 803–805.  
DOI: [10.1016/0020-7403\(68\)90021-0](https://doi.org/10.1016/0020-7403(68)90021-0)
- cited on page 33
- [174] Silva, G. A. da, Aage, N., Beck, A. T., and Sigmund, O., 'Local versus global stress constraint strategies in topology optimization: A comparative study', *International Journal for Numerical Methods in Engineering* 122.21 (2021), pp. 6003–6036.  
DOI: [10.1002/nme.6781](https://doi.org/10.1002/nme.6781)
- cited on page 33
- [175] Kreisselmeier, G. and Steinhauser, R., 'Systematic Control Design by Optimizing a Vector Performance Index', *IFAC Proceedings Volumes*, IFAC Symposium on computer Aided Design of Control Systems, Zurich, Switzerland, 29-31 August 12.7 (Sept. 1979), pp. 113–117.  
DOI: [10.1016/S1474-6670\(17\)65584-8](https://doi.org/10.1016/S1474-6670(17)65584-8)

- [176] Watts, S., Arrighi, W., Kudo, J., Tortorelli, D. A., and White, D. A., 'Simple, accurate surrogate models of the elastic response of three-dimensional open truss micro-architectures with applications to multiscale topology design', *Structural and Multidisciplinary Optimization* 60.5 (Nov. 2019), pp. 1887–1920.  
DOI: [10.1007/s00158-019-02297-5](https://doi.org/10.1007/s00158-019-02297-5)
- [177] Johnson, S. G., 'The NLOpt nonlinear-optimization package', <https://github.com/stevengj/nlopt>, 2007.
- [178] Diamond, S. and Boyd, S., 'CVXPY: A Python-Embedded Modeling Language for Convex Optimization', 2016.
- [179] Domahidi, A., Chu, E., and Boyd, S., 'ECOS: An SOCP solver for embedded systems', *2013 European Control Conference (ECC)*, Zurich: IEEE, July 2013, pp. 3071–3076, ISBN: 978-3-033-03962-9.  
DOI: [10.23919/ECC.2013.6669541](https://doi.org/10.23919/ECC.2013.6669541)
- [180] Lewiński, T., Zhou, M., and Rozvany, G. I. N., 'Extended exact solutions for least-weight truss layouts—Part I: Cantilever with a horizontal axis of symmetry', *International Journal of Mechanical Sciences* 36.5 (1994), pp. 375–398.  
DOI: [10.1016/0020-7403\(94\)90043-4](https://doi.org/10.1016/0020-7403(94)90043-4)
- [181] Munro, D. and Groenwold, A., 'Local stress-constrained and slope-constrained SAND topology optimisation', *International Journal for Numerical Methods in Engineering* 110.5 (May 2017), pp. 420–439.  
DOI: [10.1002/nme.5360](https://doi.org/10.1002/nme.5360)
- [182] Bruggi, M. and Duysinx, P., 'Topology optimization for minimum weight with compliance and stress constraints', *Structural and Multidisciplinary Optimization* 46.3 (Sept. 2012), pp. 369–384.  
DOI: [10.1007/s00158-012-0759-7](https://doi.org/10.1007/s00158-012-0759-7)
- [183] París, J., Navarrina, F., Colominas, I., and Casteleiro, M., 'Block aggregation of stress constraints in topology optimization of structures', *Advances in Engineering Software, Advances in optimum engineering design* 41.3 (Mar. 2010), pp. 433–441.  
DOI: [10.1016/j.advengsoft.2009.03.006](https://doi.org/10.1016/j.advengsoft.2009.03.006)
- [184] Norato, J. A., Smith, H. A., Deaton, J. D., and Kolonay, R. M., 'A maximum-rectifier-function approach to stress-constrained topology optimization', *Structural and Multidisciplinary Optimization* 65.10 (Sept. 2022), p. 286.  
DOI: [10.1007/s00158-022-03357-z](https://doi.org/10.1007/s00158-022-03357-z)
- [185] Stragiotti, E., Irisarri, F.-X., Julien, C., and Morlier, J., 'Efficient 3D truss topology optimization for aeronautical structures (in press)', *Structural and Multidisciplinary Optimization* (Jan. 2024).  
DOI: [10.1007/s00158-024-03739-5](https://doi.org/10.1007/s00158-024-03739-5)

- cited on pages 52, 57
- [186] Reinschmidt, K. F. and Russell, A. D., 'Applications of linear programming in structural layout and optimization', *Computers & Structures* 4.4 (Aug. 1974), pp. 855–869.  
DOI: [10.1016/0045-7949\(74\)90049-2](https://doi.org/10.1016/0045-7949(74)90049-2)
- cited on page 52
- [187] Oberndorfer, J. M., Achziger, W., and Hornlein, H. R. E. M., 'Two approaches for truss topology optimization: a comparison for practical use', *Structural Optimization* 11.3-4 (June 1996), pp. 137–144.  
DOI: [10.1007/BF01197027](https://doi.org/10.1007/BF01197027)
- cited on page 52
- [188] Silva Smith, O., 'Topology optimization of trusses with local stability constraints and multiple loading conditions? a heuristic approach', *Structural Optimization* 13.2-3 (Apr. 1997), pp. 155–166.  
DOI: [10.1007/BF01199235](https://doi.org/10.1007/BF01199235)
- cited on pages 52, 55, 68–70
- [189] Achziger, W., 'Local stability of trusses in the context of topology optimization Part II: A numerical approach', *Structural optimization* 17.4 (Dec. 1999), pp. 247–258.  
DOI: [10.1007/BF01207000](https://doi.org/10.1007/BF01207000)
- cited on page 52
- [190] Pritchard, T., Gilbert, M., and Tyas, A., 'Plastic Layout Optimization of Large-Scale Frameworks Subject to Multiple Load Cases, Member Self-Weight and with Joint Length Penalties' (Jan. 2005).
- cited on pages 52, 53, 70
- [191] Tyas, A., Gilbert, M., and Pritchard, T., 'Practical plastic layout optimization of trusses incorporating stability considerations', *Computers & Structures* 84.3 (Jan. 2006), pp. 115–126.  
DOI: [10.1016/j.compstruc.2005.09.032](https://doi.org/10.1016/j.compstruc.2005.09.032)
- cited on page 52
- [192] Descamps, B. and Filomeno Coelho, R., 'The nominal force method for truss geometry and topology optimization incorporating stability considerations', *International Journal of Solids and Structures* 51.13 (June 2014), pp. 2390–2399.  
DOI: [10.1016/j.ijsolstr.2014.03.003](https://doi.org/10.1016/j.ijsolstr.2014.03.003)
- cited on pages 52, 58
- [193] Schwarz, J., Chen, T., Shea, K., and Stanković, T., 'Efficient size and shape optimization of truss structures subject to stress and local buckling constraints using sequential linear programming', *Structural and Multidisciplinary Optimization* 58.1 (July 2018), pp. 171–184.  
DOI: [10.1007/s00158-017-1885-z](https://doi.org/10.1007/s00158-017-1885-z)
- cited on page 52
- [194] Cai, Q., Feng, R., and Zhang, Z., 'Topology optimization of trusses incorporating practical local buckling stability considerations', *Structures* 41 (July 2022), pp. 1710–1718.  
DOI: [10.1016/j.istruc.2022.05.109](https://doi.org/10.1016/j.istruc.2022.05.109)
- cited on pages 53, 65, 66
- [195] Guo, X., Cheng, G., and Yamazaki, K., 'A new approach for the solution of singular optima in truss topology optimization with stress and local buckling constraints', *Structural and Multidisciplinary Optimization* 22.5 (Dec. 2001), pp. 364–373.

- DOI: [10.1007/s00158-001-0156-0](https://doi.org/10.1007/s00158-001-0156-0)
- [196] Stolpe, M. and Svanberg, K., 'A note on stress-constrained truss topology optimization', *Structural and Multidisciplinary Optimization* 25.1 (Mar. 2003), pp. 62–64.  
DOI: [10.1007/s00158-002-0273-4](https://doi.org/10.1007/s00158-002-0273-4)
- [197] Zhou, M., 'Difficulties in truss topology optimization with stress and local buckling constraints', *Structural optimization* 11.2 (Apr. 1996), pp. 134–136.  
DOI: [10.1007/BF01376857](https://doi.org/10.1007/BF01376857)
- [198] Rozvany, G. I. N., 'Difficulties in truss topology optimization with stress, local buckling and system stability constraints', *Structural optimization* 11.3 (June 1996), pp. 213–217.  
DOI: [10.1007/BF01197036](https://doi.org/10.1007/BF01197036)
- [199] Ben-Tal, A., Jarre, F., Kočvara, M., Nemirovski, A., and Zowe, J., 'Optimal Design of Trusses Under a Nonconvex Global Buckling Constraint', *Optimization and Engineering* 1.2 (July 2000), pp. 189–213.  
DOI: [10.1023/A:1010091831812](https://doi.org/10.1023/A:1010091831812)
- [200] Kočvara, M., 'On the modelling and solving of the truss design problem with global stability constraints', *Structural and Multidisciplinary Optimization* 23.3 (Apr. 2002), pp. 189–203.  
DOI: [10.1007/s00158-002-0177-3](https://doi.org/10.1007/s00158-002-0177-3)
- [201] Neves, M. M., Rodrigues, H., and Guedes, J. M., 'Generalized topology design of structures with a buckling load criterion', *Structural optimization* 10.2 (Oct. 1995), pp. 71–78.  
DOI: [10.1007/BF01743533](https://doi.org/10.1007/BF01743533)
- [202] Ferrari, F., Sigmund, O., and Guest, J. K., 'Topology optimization with linearized buckling criteria in 250 lines of Matlab', *Structural and Multidisciplinary Optimization* 63.6 (June 2021), pp. 3045–3066.  
DOI: [10.1007/s00158-021-02854-x](https://doi.org/10.1007/s00158-021-02854-x)
- [203] Mela, K., 'Resolving issues with member buckling in truss topology optimization using a mixed variable approach', *Structural and Multidisciplinary Optimization* 50.6 (Dec. 2014), pp. 1037–1049.  
DOI: [10.1007/s00158-014-1095-x](https://doi.org/10.1007/s00158-014-1095-x)
- [204] Kirsch, U., 'Effect of Compatibility and Prestressing on Optimized Trusses', *Journal of Structural Engineering* 115.3 (Mar. 1989), pp. 724–737.  
DOI: [10.1061/\(ASCE\)0733-9445\(1989\)115:3\(724\)](https://doi.org/10.1061/(ASCE)0733-9445(1989)115:3(724))
- [205] Moore, J. K. and Mechmotum, 'cyipopt: Cython interface for the interior point optimizer IPOPT', 2018.  
URL: <https://github.com/mechmotum/cyipopt>

- cited on pages 63, 82, 83, 124
- [206] Alappat, C., Basermann, A., Bishop, A. R., Fehske, H., Hager, G., Schenk, O., Thies, J., and Wellein, G., 'A Recursive Algebraic Coloring Technique for Hardware-efficient Symmetric Sparse Matrix-vector Multiplication', *ACM Transactions on Parallel Computing* 7.3 (2020), 19:1–19:37.  
DOI: [10.1145/3399732](https://doi.org/10.1145/3399732)
- cited on pages 64, 70, 124
- [207] Stragiotti, E., Irisarri, F.-X., Julien, C., and Morlier, J., 'Truss Topology Optimization with Topological Buckling Constraints Data Set', May 2023.  
DOI: [10.17632/BW7XB2W6ST.1](https://doi.org/10.17632/BW7XB2W6ST.1)
- cited on page 73
- [208] Rozvany, G. I. N., 'On symmetry and non-uniqueness in exact topology optimization', *Structural and Multidisciplinary Optimization* 43.3 (Mar. 2011), pp. 297–317.  
DOI: [10.1007/s00158-010-0564-0](https://doi.org/10.1007/s00158-010-0564-0)
- cited on page 73
- [209] Guo, X., Du, Z., and Cheng, G., 'A confirmation of a conjecture on the existence of symmetric optimal solution under multiple loads', *Structural and Multidisciplinary Optimization* 50.4 (Oct. 2014), pp. 659–661.  
DOI: [10.1007/s00158-014-1089-8](https://doi.org/10.1007/s00158-014-1089-8)
- cited on page 77
- [210] Stragiotti, E., Irisarri, F.-X., Julien, C., and Morlier, J., 'Enhanced truss topology optimization (TTO) applied to a cellular wing box', *ASMO-UK 12 / ASMO-Europe 1 / ISSMO Conference on Engineering Design Optimization* (2022), Leeds, United Kingdom, July 2022.
- cited on page 77
- [211] Zhou, S. and Li, Q., 'Design of graded two-phase microstructures for tailored elasticity gradients', *Journal of Materials Science* 43.15 (Aug. 2008), pp. 5157–5167.  
DOI: [10.1007/s10853-008-2722-y](https://doi.org/10.1007/s10853-008-2722-y)
- cited on page 77
- [212] Li, D., Liao, W., Dai, N., and Xie, Y. M., 'Anisotropic design and optimization of conformal gradient lattice structures', *Computer-Aided Design* 119 (Feb. 2020), p. 102787.  
DOI: [10.1016/j.cad.2019.102787](https://doi.org/10.1016/j.cad.2019.102787)
- cited on page 92
- [213] Deshpande, V. S., Fleck, N. A., and Ashby, M. F., 'Effective properties of the octet-truss lattice material', *Journal of the Mechanics and Physics of Solids* 49.8 (Aug. 2001), pp. 1747–1769.  
DOI: [10.1016/S0022-5096\(01\)00010-2](https://doi.org/10.1016/S0022-5096(01)00010-2)
- cited on page 102
- [214] Stegmann, J. and Lund, E., 'Discrete material optimization of general composite shell structures', *International Journal for Numerical Methods in Engineering* 62.14 (Apr. 2005), pp. 2009–2027.  
DOI: [10.1002/nme.1259](https://doi.org/10.1002/nme.1259)
- cited on page 102
- [215] Stolpe, M. and Svanberg, K., 'An alternative interpolation scheme for minimum compliance topology optimization', *Structural and Multidisciplinary Optimization* 22.2 (Sept. 2001), pp. 116–124.

DOI: [10.1007/s001580100129](https://doi.org/10.1007/s001580100129)

- [216] Hvejsel, C. F. and Lund, E., 'Material interpolation schemes for unified topology and multi-material optimization', *Structural and Multidisciplinary Optimization* 43.6 (June 2011), pp. 811–825.  
DOI: [10.1007/s00158-011-0625-z](https://doi.org/10.1007/s00158-011-0625-z) cited on page 103
- [217] Opgenoord, M. M. J. and Willcox, K. E., 'Design for additive manufacturing: cellular structures in early-stage aerospace design', *Structural and Multidisciplinary Optimization* 60.2 (Aug. 2019), pp. 411–428.  
DOI: [10.1007/s00158-019-02305-8](https://doi.org/10.1007/s00158-019-02305-8) cited on pages 106, 123
- [218] Prokop, J., Odrobiňák, J., Farbák, M., and Novotný, V., 'Load-Carrying Capacity of Bailey Bridge in Civil Applications', *Applied Sciences* 12.8 (Jan. 2022), p. 3788.  
DOI: [10.3390/app12083788](https://doi.org/10.3390/app12083788) cited on page 115
- [219] Department of the Army, 'Field Manual No. 5-277, Panel Bridge, Bailey Type, Washington DC.' 1986 cited on page 115
- [220] Shahabsafa, M., Mohammad-Nezhad, A., Terlaky, T., Zuluaga, L., He, S., Hwang, J. T., and Martins, J. R. R. A., 'A novel approach to discrete truss design problems using mixed integer neighborhood search', *Structural and Multidisciplinary Optimization* 58.6 (Dec. 2018), pp. 2411–2429.  
DOI: [10.1007/s00158-018-0999-8](https://doi.org/10.1007/s00158-018-0999-8) cited on page 123
- [221] Brooks, T. R., Kenway, G. K. W., and Martins, J. R. R. A., 'Benchmark Aerostructural Models for the Study of Transonic Aircraft Wings', *AIAA Journal* 56.7 (July 2018), pp. 2840–2855.  
DOI: [10.2514/1.J056603](https://doi.org/10.2514/1.J056603) cited on page 124
- [222] Fakhimi, R., Shahabsafa, M., Lei, W., He, S., Martins, J. R. R. A., Terlaky, T., and Zuluaga, L. F., 'Discrete multi-load truss sizing optimization: model analysis and computational experiments', *Optimization and Engineering* (Sept. 2021).  
DOI: [10.1007/s11081-021-09672-6](https://doi.org/10.1007/s11081-021-09672-6) cited on pages 124–126
- [223] Ashby, M. F., 'Materials selection in mechanical design', 2nd ed. Oxford, OX ; Boston, MA: Butterworth-Heinemann, 1999.  
ISBN: [978-0-7506-4357-3](https://doi.org/978-0-7506-4357-3) cited on pages 129, 138
- [224] Duriez, E., Charlotte, M., Azzaro-Pantel, C., and Morlier, J., 'On some properties of the compliance-volume fraction Pareto front in topology optimization useful for material selection', Nov. 2022.  
DOI: [10.48550/arXiv.2211.15358](https://arxiv.org/abs/2211.15358) cited on page 148
- [225] Coxeter, H. S. M., 'Regular Polytopes'. Courier Corporation, Jan. 1973, Google-Books-ID: iWvXsVInpgMC.  
ISBN: [978-0-486-61480-9](https://doi.org/978-0-486-61480-9) cited on page 149

- cited on page 149
- [226] Loeb, A. L., 'Space-filling Polyhedra', *Space Structures, Design Science Collection*, ed. by Loeb, A. L., Boston, MA: Birkhäuser, 1991, pp. 127–132, ISBN: 978-1-4612-0437-4.  
DOI: [10.1007/978-1-4612-0437-4\\_16](https://doi.org/10.1007/978-1-4612-0437-4_16)
- cited on page 149
- [227] Duriez, E., Morlier, J., Azzaro-Pantel, C., and Charlotte, M., 'Ecodesign with topology optimization', *Procedia CIRP*, 32nd CIRP Design Conference (CIRP Design 2022) - Design in a changing world 109 (Jan. 2022), pp. 454–459.  
DOI: [10.1016/j.procir.2022.05.278](https://doi.org/10.1016/j.procir.2022.05.278)
- cited on page 149
- [228] Duriez, E., Guadaño Martín, V. M., and Morlier, J., 'CO<sub>2</sub> footprint minimization of solar-powered HALE using MDO and eco-material selection', *Scientific Reports* 13.1 (July 2023), p. 11994.  
DOI: [10.1038/s41598-023-39221-3](https://doi.org/10.1038/s41598-023-39221-3)
- cited on page 149
- [229] Duriez, E., Azzaro-Pantel, C., Morlier, J., and Charlotte, M., 'A fast method of material, design and process eco-selection via topology optimization, for additive manufactured structures', *Cleaner Environmental Systems* 9 (June 2023), p. 100114.  
DOI: [10.1016/j.cesys.2023.100114](https://doi.org/10.1016/j.cesys.2023.100114)

## **APPENDIX**



# SENSITIVITY ANALYSIS OF THE MODULAR STRUCTURE OPTIMIZATION ALGORITHM

In this appendix, we demonstrate how the gradient, Jacobian, and Hessian matrices of the objective function and the optimization constraints are evaluated for the layout and topology optimization formulation  $\mathbb{M}_2$  presented in Chapter 5. This step, called sensitivity analysis, is crucial for gradient descent optimization algorithms, as it allows for faster and more accurate convergence compared to using finite differences. We remind the reader that the index  $i$  is relative to the number of bars in a module  $\bar{n}$ , the index  $j$  is relative to the number of subdomains  $N_{\text{sub}}$  in which the structure is divided, and the index  $t$  is relative to the number of different modules' topologies  $N_T$ . The indexes are summarized in Table 1 for added clarity.

More information on sensitivity analysis can be found in the book by Martins and Ning [8].

## 1 OPTIMIZATION FORMULATION, OBJECTIVE FUNCTION AND CONSTRAINTS

The relaxed formulation  $\mathbb{M}_2$  for which we want to perform the sensitivity analysis is expressed in terms of modules' cross-sectional area  $\bar{a}$ , module selection variables  $\alpha$ , and member forces  $q$  as:

$$\begin{aligned}
 \min_{\bar{a}, \alpha, q} \quad & V = \sum_{j=1}^{N_{\text{sub}}} \bar{\ell}^T \tilde{a}^j \quad (\text{Volume minimization}) \\
 \text{s.t.} \quad & Bq = f \quad (g_{\text{eq}}) \\
 & q \geq -\frac{s\alpha^2}{\ell^2} \quad (g_{\text{buck}}) \\
 & -\sigma_C \alpha \leq q \leq \sigma_T \alpha \quad (g_{\text{st,t}}, g_{\text{st,c}}) \\
 & 0 \leq \bar{a} \leq \frac{4\pi\bar{\ell}^2}{\lambda_{\max}} \quad (g_{\text{slend}}) \\
 & \sum_{t=1}^{N_T} \alpha_t^j \leq 1, \quad \forall j \quad (g_{\text{sum}}),
 \end{aligned} \tag{\mathbb{M}_2}$$

in which

$$V = \sum_{j=1}^{N_{\text{sub}}} \bar{\ell}^T \tilde{a}^j, \tag{1}$$

represents the structural volume of the modular structure and acts as the objective function to minimize for the optimization. The vector  $\tilde{a}^j$ , representing the increased cross-sectional areas of the  $j$ -th subdomain, is defined as follows:

$$\tilde{a}^j = \sum_{t=1}^{N_T} \tilde{w}_t^j \bar{a}_t, \tag{2}$$

Index	Interval	Expl.
$i$	$[0, \bar{n}[$	# of bars in a module
$j$	$[0, N_{\text{sub}}[$	# of sub-domains # of modules'
$t$	$[0, N_T[$	topologies

**Table 1:** Reminder of the indexes used for the sensitivity analysis of the layout and topology optimization of modular structures.

and where  $\tilde{w}$  is evaluated using the RAMP interpolation scheme with the  $q$  parameter as follows:

$$\tilde{w}_t^j = \frac{\alpha_t^j}{1 + q(1 - \alpha_t^j)}. \quad (3)$$

The cross-sectional areas vector  $\mathbf{a}^j$  of subdomain  $j$  used for the constraints evaluation is expressed as:

$$\mathbf{a}^j = \sum_{t=1}^{N_T} w_t^j \bar{\mathbf{a}}_t, \quad (4)$$

where  $\bar{\mathbf{a}}_t$  represent the vector of cross-sectional areas of the  $t$  module and  $w^j$  is the vector of weight relatives to the  $j$  subdomain, defined as  $w^j \in \mathbb{R}^t | w_j^t \in [0, 1]$ . Its relationship with the weight  $w$  is as follows:

$$w_t^j = \frac{\alpha_t^j}{1 + p(1 - \alpha_t^j)}, \quad (5)$$

where  $p \in \mathbb{R}^+$  denotes a parameter governing the steepness of the RAMP interpolation.

## 2 COMMON DERIVATIVES

We introduce here some important derivatives that we use all along the Chapter.

$$\frac{\partial \mathbf{a}^j}{\partial \bar{\mathbf{a}}_t} = w_t^j, \quad (6)$$

$$\frac{\partial \mathbf{a}^j}{\partial \alpha_t^j} = \frac{\partial \mathbf{a}^j}{\partial w_t^j} \frac{\partial w_t^j}{\partial \alpha_t^j}, \quad (7)$$

where

$$\frac{\partial \mathbf{a}^j}{\partial w_t^j} = \bar{\mathbf{a}}_t, \quad (8)$$

and

$$\frac{\partial w_t^j}{\partial \alpha_t^j} = \frac{1 + (\cdot)}{\left(1 + (\cdot)(1 - \alpha_t^j)\right)^2}, \quad (9)$$

where  $(\cdot)$  is either equal to  $p$  or  $q$ .

$$\frac{\partial^2 w_t^j}{\partial (\alpha_t^j)^2} = \frac{2(\cdot)(1 + (\cdot))}{\left(1 + (\cdot)(1 - \alpha_t^j)\right)^3}. \quad (10)$$

### 3 GRADIENT

The gradient of the objective function  $V$  is non-zero only for the design variables  $\bar{\alpha}$  and  $\alpha$ . It is evaluated for  $\bar{\alpha}$  as following:

$$\frac{\partial V}{\partial \bar{\alpha}_t} = \bar{\ell}^T \sum_{j=1}^{N_{\text{sub}}} \tilde{w}_t^j, \text{ with } t \in [1, \dots, N_T]. \quad (11)$$

The gradient with respect to  $\alpha$  can be written as:

$$\frac{\partial V}{\partial \alpha_t^j} = \frac{\partial V}{\partial w_t^j} \frac{\partial w_t^j}{\partial \alpha_t^j}, \quad (12)$$

where

$$\frac{\partial V}{\partial w_t^j} = \bar{\ell}^T \bar{\alpha}_t, \quad (13)$$

and evaluated using Equation 9 and the parameter  $q$ . As already mentioned, the gradient is zero with respect to the member forces  $q$ :

$$\frac{\partial V}{\partial q} = 0. \quad (14)$$

### 4 JACOBIAN MATRIX

We focus now on the evaluation of the Jacobian matrix of the optimization constraints with respect to the design variables.

**EQUILIBRIUM CONSTRAINTS** The equilibrium constraint  $g_{\text{eq}}$  is linear on  $q$  and not dependent on  $\bar{\alpha}$  and  $\alpha$ . For that reason we can write:

$$\frac{\partial g_{\text{eq}}}{\partial \bar{\alpha}} = 0, \quad (15)$$

$$\frac{\partial g_{\text{eq}}}{\partial \alpha} = 0, \quad (16)$$

$$\frac{\partial g_{\text{eq}}}{\partial q} = B. \quad (17)$$

**STRESS CONSTRAINTS** Knowing that:

$$\frac{\partial g_{\text{st,t}}^j}{\partial \alpha^j} = -\sigma_t, \quad (18)$$

and

$$\frac{\partial g_{\text{st,c}}^j}{\partial \alpha^j} = \sigma_c, \quad (19)$$

the Jacobian for the stress constraints  $g_{st,t}$  and  $g_{st,c}$  can be evaluated using Equation 6 and Equation 7 as follows:

$$\frac{\partial g_{st,*}^j}{\partial \bar{a}_t} = \frac{\partial g_{st,*}^j}{\partial a^j} \frac{\partial a^j}{\partial \bar{a}_t}, \quad (20)$$

and

$$\frac{\partial g_{st,*}^j}{\partial \alpha^j} = \frac{\partial g_{st,*}^j}{\partial a^j} \frac{\partial a^j}{\partial \alpha^j}, \quad (21)$$

where the asterisk \* refers to either the compression and the tension constraints. The stress constraints are linear with respect to  $q$ :

$$\frac{\partial g_{st,*}}{\partial q} = \mathbf{1}, \quad (22)$$

in which  $\mathbf{1}$  represent a vector of all ones.

**BUCKLING CONSTRAINTS** Knowing that:

$$\frac{\partial g_{buck}^j}{\partial a^j} = 2 \frac{s a^j}{\ell^2}, \quad (23)$$

the Jacobian for the buckling constraints  $g_{buck}$  with respect to  $\bar{a}$  can be evaluated using Equation 6 as:

$$\frac{\partial g_{buck}^j}{\partial \bar{a}_t} = \frac{\partial g_{buck}^j}{\partial a^j} \frac{\partial a^j}{\partial \bar{a}_t}. \quad (24)$$

Using Equation 7 we evaluate the derivative with respect to  $\alpha$  as:

$$\frac{\partial g_{buck}^j}{\partial \alpha^j} = \frac{\partial g_{buck}^j}{\partial a^j} \frac{\partial a^j}{\partial \alpha^j}. \quad (25)$$

**MAXIMUM SUM ALPHA CONSTRAINTS** The constraint  $g_{sum}$  on the maximal value of  $\alpha$  in every subdomain is linear with respect to  $\alpha$  and it does not depend on the other design variables. For that reason we can write:

$$\frac{\partial g_{sum}}{\partial \bar{a}} = 0, \quad (26)$$

$$\frac{\partial g_{sum}}{\partial \alpha} = \mathbf{1}, \quad (27)$$

$$\frac{\partial g_{sum}}{\partial q} = 0. \quad (28)$$

## 5 HESSIAN MATRIX

For the evaluation of the hessian matrix, we list here only the nonzero contributions, assuming that all the remaining are zero.

**VOLUME** The only nonzero contributions to the Hessian matrix are:

$$\frac{\partial^2 V}{\partial \bar{a}_t \partial \alpha_t^j} = \bar{\ell}^T \frac{\partial \tilde{w}_t^j}{\partial \alpha_t^j}, \quad (29)$$

and

$$\frac{\partial^2 V}{\partial (\alpha_t^j)^2} = \bar{\ell}^T \bar{a}_t \frac{\partial^2 w_t^j}{\partial (\alpha_t^j)^2}, \quad (30)$$

that can be evaluated using Equation 9 and Equation 10

**EQUILIBRIUM CONSTRAINTS** All terms are zero for the equilibrium constraints.

## STRESS CONSTRAINTS

$$\frac{\partial^2 g_t^j}{\partial \bar{a}_t \partial \alpha_t^j} = -\sigma_t \frac{\partial w_t^j}{\partial \alpha_t^j}, \quad (31)$$

$$\frac{\partial^2 g_t^j}{\partial (\alpha_t^j)^2} = -\sigma_t \bar{a}_t \frac{\partial^2 w_t^j}{\partial (\alpha_t^j)^2}. \quad (32)$$

**BUCKLING CONSTRAINTS** To evaluate the Hessian of buckling constraints we need to define two additional indexes,  $l$  and  $m$  that are spanning from 0 to  $N_T - 1$  as the index  $t$ . We can then write:

$$\frac{\partial^2 g_{\text{buck}}^j}{\partial \bar{a}_l \partial \bar{a}_m} = 2 \frac{s}{\ell^2} w_l^j w_m^j. \quad (33)$$

The mixed term is evaluated as follow:

$$\frac{\partial^2 g_{\text{buck}}^j}{\partial \bar{a}_l \partial \alpha_m^j} = 2 \frac{s}{\ell^2} w_l^j \frac{\partial a^j}{\partial \alpha_m^j} + 2 \frac{s a^j}{\ell^2} \frac{\partial w_l^j}{\partial \alpha_m^j}, \quad (34)$$

$$\frac{\partial^2 g_{\text{buck}}^j}{\partial \bar{a}_l \partial \alpha_m^j} = 2 \frac{s}{\ell^2} w_l^j \frac{\partial w_m^j}{\partial \alpha_m^j} \bar{a}_m + 2 \frac{s a^j}{\ell^2} \frac{\partial w_l^j}{\partial \alpha_m^j}, \quad (35)$$

$$\frac{\partial^2 g_{\text{buck}}^j}{\partial \bar{a}_l \partial \alpha_m^j} = \begin{cases} 2 \frac{s}{\ell^2} \frac{\partial w_t^j}{\partial \alpha_t^j} (w_t^j \bar{a}_t + a^j) & \text{if } l = m = t \\ 2 \frac{s}{\ell^2} w_l^j \frac{\partial w_m^j}{\partial \alpha_m^j} \bar{a}_m & \text{otherwise.} \end{cases} \quad (36)$$

And finally the quadratic term in  $\alpha$ :

$$\frac{\partial^2 g_{\text{buck}}^j}{\partial \alpha_l^j \partial \alpha_m^j} = 2 \frac{s}{\ell^2} \bar{a}_l \frac{\partial a^j}{\partial \alpha_m^j} \frac{\partial w_l^j}{\partial \alpha_l^j} + 2 \frac{s a^j}{\ell^2} \bar{a}_l \frac{\partial^2 w_l^j}{\partial \alpha_l^j \partial \alpha_m^j}, \quad (37)$$

$$\frac{\partial^2 g_{\text{buck}}^j}{\partial \alpha_l^j \partial \alpha_m^j} = \begin{cases} 2 \frac{s}{\ell^2} \bar{a}_t^2 \left( \frac{\partial w_t^j}{\partial \alpha_t^j} \right)^2 + 2 \frac{s a^j}{\ell^2} \bar{a}_t \frac{\partial^2 w_t^j}{\partial (\alpha_t^j)^2} & \text{if } l = m = t \\ 2 \frac{s}{\ell^2} \bar{a}_l \bar{a}_m \left( \frac{\partial w_m^j}{\partial \alpha_m^j} \right) \left( \frac{\partial w_l^j}{\partial \alpha_l^j} \right) & \text{otherwise.} \end{cases} \quad (38)$$

**MAXIMUM SUM ALPHA CONSTRAINTS** All terms are zero for the  $g_{\text{sum}}$  constraint.